Clumped and intramolecular isotopic perspectives on the behavior of organic and inorganic carbon in the shallow crust and deep biosphere

Thesis by
Max Kaufmann Lloyd

In Partial Fulfillment of the Requirements for the
degree of
Doctor of Philosophy

CALIFORNIA INSTITUTE OF TECHNOLOGY
Pasadena, California

2018
Defended December 1, 2017

© 2018

Max Kaufmann Lloyd
ORCID: 0000-0001-9367-2698

All rights reserved

ACKNOWLEDGEMENTS

A frillion and one thanks to John, who made this all possible. John, you have the uncanny ability to do everything, and be the everything-advisor, all the time. It's a wonder your neck isn't constantly sore from all the hats you wear. Thank you for encouraging me to follow my interests, even when they were seven disciplines and six oxidation states away from what I was NSF-ordained to work on. Thank you for being the kind of advisor who will support sending a lab-based geochemist to Switzerland to put a capstone on a body of work and collect enough samples to support three hypothetical students of my own someday. Plenty of folks have described how Caltech GPS is a special place to go to grad school. It's clear to me that even within that realm, the Eiler Lab is uniquely fortunate. Thank you for working so hard to make it all happen.

A tar-tainted thank you to Alex, for welcoming a isotope geochemist with a metamorphic petrology problem into your lab and life. It has been an absolute delight, and a career-altering experience, being exposed to the world and opportunities in organic geochemistry. Thank you for bringing me on as a TA and into the Geobiology fold, Everything that comes next, both professional and personal, is due in large part to you. Also, still waiting for that replacement pair of swim trunks, just so you know.

Thank you as well to my other committee members, Victoria and George. Your insight and suggestions, from opposite ends of the geochemistry spectrum, have been invaluable. I am a substantially more well-rounded scientist because of your influences.

No (happy) geochemist is an island. A litany of late nights in lab are only possible with the support of others going through the same. Thank you to Hayden, Stephen, Alison, Uri, Camilo, Elizabeth, Kat, Hank, Paul, John, Nithya, Brooke, Elle, Laurence, Tony, Peter, Daniel, Lewis, Katie, Seb, Lizzy, Kristin, and Nami for doing it with me. Graduate school is not supposed to be this gratifying.

Finally, thank you to my family, to Mom, Dad, and Maya. Happy families are ostensibly all the same, but I still think we're still special.

ABSTRACT

Although the upper crust is the most accessible swath of the subsurface, the geochemical processes therein are challenging to observe. Here, I use site-specific and 'clumped' isotope analyses (where multiple rare, heavy isotopes are bound in single molecules) of carbonates and organic solids to explore petrology, brittle tectonics, diagenesis, and biodegradation in the shallow crust. In carbonates, I employ contact aureoles, regional metamorphic terranes, thermal and geochemical models, and high-pressure experiments, to extract nuanced thermal and chemical histories. In the organic realm, I develop new methods to measure the clumped $^{13}C-^{2}H$ composition of methoxyl groups ($R-O-CH_3$) from kerogen, lignin, and other complex organic substrates. This work expands the field of clumped isotope geochemistry into the realm of solid compounds, and enables new, site-specific isotopic perspectives on the shallow crustal transformations of organic carbon substrates and the microbial assemblages that live on them.

PUBLISHED CONTENT AND CONTRIBUTIONS

Lloyd, Max K, John M Eiler, and Peter I Nabelek (2017). "Clumped isotope thermometry of calcite and dolomite in a contact metamorphic environment". In: *Geochimica et Cosmochimica Acta* 197, pp. 323–344. DOI: 10.1016/j.gca.2016.10.037.

I designed the study with input from J.M.E., acquired the data, analyzed the data, and performed the modeling. I wrote the paper with input from J.M.E., and P.K.N.

TABLE OF CONTENTS

Acknowledgements . . . iii
Abstract . . . iv
Published Content and Contributions . . . v
Table of Contents . . . vi
List of Illustrations . . . viii
List of Tables . . . xviii
Chapter I: Introduction . . . 1
1.1 Kinetic and analytical impedances to studying shallow crustal geochemistry . . . 1
1.2 A path forward in novel isotopic techniques . . . 3
Chapter II: Clumped isotope thermometry of calcite and dolomite in a contact metamorphic environment . . . 9
2.1 Introduction . . . 10
2.2 Background . . . 11
2.3 Geologic overview of the Notch Peak aureole: A natural laboratory for clumped isotope reordering processes . . . 19
2.4 Samples and methods . . . 22
2.5 Results . . . 27
2.6 Discussion . . . 32
2.7 Conclusions . . . 47
2.8 Supplementary data tables . . . 49
Chapter III: Experimental determination of the preservation potential of the dolomite clumped isotope thermometer . . . 60
3.1 Abstract . . . 60
3.2 Introduction . . . 61
3.3 Materials and methods . . . 65
3.4 Results of dolomite reordering experiments . . . 72
3.5 Extracting dolomite Δ_{47} reordering rate constants from experimental data . . . 74
3.6 Discussion . . . 86
3.7 Conclusions . . . 96
3.8 Supplementary Materials . . . 98
Chapter IV: A preliminary investigation of carbonate clumped isotope compositions in a major fold-and-thrust belt . . . 114
4.1 Introduction . . . 114
4.2 Methods . . . 121
4.3 Results and exploratory discussion . . . 125
4.4 Synthesis and suggestions for focus of future work . . . 144
4.5 Supplementary data tables . . . 150

Chapter V: Extraction and detemination of combined $^{13}C-{}^{2}H$ and $^{2}H_2$ clumping of methoxyl groups from organic monomers, plant tissues, and coal . . 157
5.1 Introduction 157
5.2 Background 159
5.3 Methods for chemical extraction and purification 164
5.4 Methods for dual-mass spectrometric measurement 172
5.5 Results and Discussion 187
Chapter VI: The thermal and bio-degration of methoxyl groups in coals: implications for isotopic heterogeneity of complex organic compounds and the support of the deep biosphere 200
6.1 Introduction 200
6.2 Background 202
6.3 Methods 206
6.4 Results 212
6.5 Discussion 215
6.6 Conclusions 222
6.7 Supplementary data 223

LIST OF ILLUSTRATIONS

Number *Page*

2.1 Apparent equilibrium blocking temperatures of single isotope and bulk isotope thermometers in calcite and dolomite. Carbon-13, and dry ($X_{CO_2} = 1$) oxygen-18 lines are derived from the calcite diffusion experiments of Labotka et al. (2011). Wet oxygen-18 parameters are from the calcite data of Farver (1994). Following the convention of Labotka et al. (2011), all three single isotope exchange apparent equilibrium blocking temperature relations are calculated using the Dodson-style equation of Lasaga (1998), assuming linear cooling rates and a grain size of 100 μm: $T_c = \frac{E_a/R}{\ln?[2K_0T_c^2/(a^2SE_a/R)]}$, where E_a, R, K_0, T_c, a, and S are the activation energy, gas constant, frequency factor, apparent equilibrium blocking temperature, grain radius, and cooling rate, respectively. These curves implicitly assume that self-diffusion in calcite is the rate-limiting step to re-equilibration, which is consistent with results from limited measurements of dolomite single-isotope diffusion (Anderson, 1972). The calcite Δ_{47} curve is calculated using the optical calcite data and eqn. (14) of Passey and Henkes (2012). No dolomite Δ_{47}reordering parameters are yet published, but clumped isotope measurements of dolomite from the Predazzo contact aureole (Ferry et al., 2011) and the Notch Peak aureole (this study) suggest that it should preserve apparent equilibrium temperatures ~100 °C above calcite. Cooling rates for these data are estimated from a thermal model of the Notch Peak aureole developed in section 2.6, and a similar model reflecting the geometry, depth, and sample location in the Predazzo aureole, and uncertainties therein (Ferry et al., 2002). 13

2.2 Schematic diagram of the behavior of case-1, 2, and 3 exchange thermometers in a representative thermal metamorphic event. The four key events are 1) peak crystallization, 2) cooling down from peak temperature to the ambient/burial temperature, 3) incubation at ambient temperature, and 4) exhumation to surface. A case-1 thermometer ($T_{peak} < T_c$) records the temperature of peak metamorphism. A case-2 thermometer ($T_{ambient} < T_c < T_{peak}$) records an apparent equilibrium blocking temperature dependent on the cooling rate near this value (T_c). The case-3 ($T_c \leq T_{ambient}$) thermometer fully re-equilibrates with the ambient temperature of the system, and records this value, provided exhumation is rapid enough to quench the system to further exchange. 17

2.3 Sample locations in the Notch Peak aureole, Utah, USA (modified after Hintze and Davis, 2002) 20

2.4 Assessment of the accuracy of the bulk $\delta^{13}C$ and $\delta^{18}O$ exchange thermometers. Measured dolomite – calcite fractionations are compared to those predicted from equilibrium crystallization at the temperatures predicted by published thermal models of the Big Horse Ls Member (Table 2.2). Errors are 2σ standard errors, generated by propagation of mean dolomite and calcite $\delta^{13}C$ or $\delta^{18}O$ errors, assuming dolomite and calcite measurements are uncorrelated (not strictly true, see Methods section). Equilibrium temperature-bulk isotope relationships for carbon-13 and oxygen-18 are derived from Sheppard and Schwarcz (1970) and Horita (2014), respectively. . . . 30

2.5 Δ_{47} values for calcite and dolomite in the Notch Peak aureole. Errors on individual points are 1σ standard errors of the weighted average of replicates. Blue line is the weighted average of all calcite Δ_{47} measurements in the aureole, with dashed lines denoting the 2σ error envelope on this value. Model peak T values are derived from the equations in John M Ferry and Dipple (1992) and Theodore C Labotka, Peter I Nabelek, and Papike (1988). Dashed gold lines denote the approximate locations of the main metamorphic isograds in the unit. Semitransparent points at 2.63 km are for sample 12–NPK–11b, where abundant secondary cross-cutting carbonate veining has overprinted the primary dolomite and calcite temperature signals (See section 2.6 for details). 32

2.6 Models for calcite Δ_{47} reordering during cooling in the aureole of the Notch Peak pluton. Calcite apparent equilibrium temperatures approach the ambient temperature of the system during the 100 Ma after intrusion, but whether full re-equilibration occurs depends on the residence temperature and the reordering model used (A). Solid lines were generated using the exchange-diffusion model of Stolper and J M Eiler (2015), and dotted lines using the first-order approximation model for optical calcite from Passey and Henkes (2012). Arrhenian parameters were varied by up to 1σ of their reported values and uncertainties to examine the sensitivity of final calcite Δ_{47} temperature to the exact rate constants used (B, C). Symbols are included for clarity, and do not necessarily represent locations where calculations were performed. 42

3.1 Error-weighted global least squares fit to dolomite heating experiments using the transient defect/equilibrium defect model of Henkes et al. (2014) (Eqn. 10). Red star is the mean unheated initial composition. Other symbols are mean of replicate measurements of heating experiments, with 1σ standard errors. Solid lines are the global fit to the data. Dashed lines are equilibrium Δ_{47} values for every temperature. 77

3.2 Error-weighted global least squares fit to dolomite heating experiments using the exchange-diffusion model of D. A. Stolper and J M Eiler (2015) (Eqns. 12–14). Red star is the mean unheated initial composition. Other symbols are mean of replicate measurements of heating experiments, with 1σ standard errors. Solid lines are the global fit to the data. Dashed lines are equilibrium Δ_{47} values for every temperature. 82

3.3 Predicted dependence of dolomite Δ_{47} apparent equilibrium blocking temperature on cooling rate, and the measured apparent equilibrium blocking temperatures of natural dolomite marbles. Blue, red, and green shaded regions denote 2σ uncertainties on predictions of the first order approximation to the transient defect/equilibrium defect model, and the exchange-diffusion model using two different T–D47 calibrations. Cooling rates with uncertainties for the Notch Peak and Predazzo contact aureoles were estimated from conductive cooling models described in Lloyd et al. (2017). Low temperature cooling rates from regionally exhumed terranes are rarely known with useful precision, and the range of apparent equilibrium temperatures measured in such systems is larger than would be expected if regional exhumation was the sole determining variable (c.f., Ryb et al. 2017). Thus, we plot only the rough region over which these processes are likely to operate. 87

3.4 Arrhenius plots for the rate constants for the exchange and diffusion components of the D. A. Stolper and J M Eiler (2015) model. Dolomite rate constants (and uncertainties) from this study are compared with optical calcite rate constants from this publication. 90

3.5 Arrhenius plots for the rate constants for the equilibrium component, transient component, and annealing rate on the transient component, for the Δ_{47} reordering model of Henkes et al. (2014)Henkes et al. (2014). These are compared to the parameters for optical calcite and brachiopod calcite reported therein. 91

3.6 'Box car' heating models of dolomite Δ_{47} reordering. Solid lines denote the true temperature-time path of each run. Dashed lines are dolomite Δ_{47} apparent equilibrium temperatures predicted using the exchange-diffusion model for each T-t path. Dotted lines are the dolomite Δ_{47} temperatures predicted using the transient defect/equilibrium defect model. 109

3.7 Expected reordering behaviors of the dolomite and calcite Δ_{47} thermometers using the exchange-diffusion model in a simple burial-exhumation scenario. Shaded areas denote 1σ confidence limits for the respective thermometer. Here, calcite is initially formed in equilibrium at 25 °C, and dolomite at 50 °C later on the burial path. This setup assumes no recrystallization after initial dolomite and calcite formation. 110

3.8 Photographs of the Eugui crystal aggregate used for this study. Prior to imaging, sample was bisected using a hammer and chisel to reveal internal structure and layering. Outlined portions denote approximate sections that were removed, powdered, and measured to test the cm-scale isotopic homogeneity of the sample. The entire sample is apparently homogeneous with respect to Δ_{47} and δ^{13}C, but the colorless crystal aggregate is ~3 ‰ heavier in δ^{18}O than the massive while base. All mm-sized fragments used for the heating experiments were taken from protruding, faceted crystals from the colorless crystal aggregate. 110

3.9 Weighted global least squares fit to dolomite heating experiments using the simple, first order reordering model (Eqn. 8, Main Text). Complex reordering behaviors evident in these data are not captured by the simple model. 111

3.10 Univariate and bivaraite density plots for the Monte Carlo simulation of the six parameter transient defect/equilibrium defect model. Kernel density estimates were generated using the kdeplot function from the seaborn statistical data visualization package. 112

3.11 Univariate and bivaraite density plots for the Monte Carlo simulation of the five parameter exchange-diffusion model. Kernel density estimates were generated using the kdeplot function from the seaborn statistical data visualization package. 113

4.1 Simplified map of the units, major faults, and trends in anchimetamorphic grade in the Glarus alps (Wang, FREY, and STERN, 1996). 119

4.2 Contrasting predictions for temperature profiles across distinctive textures of a schematic of the Lochsite shear zone. Modified from Ebert, Herwegh, and A. Pfiffner (2007). 119

4.3 Cartoon demonstrating the procedure for the graphical determination of the relationship between terminal motion on the Glarus thrust and the doming/rotation of the fault plane using dolomite Δ_{47} temperatures. Estimates of peak conditions along N–S transect from Ebert, Herwegh, and A. Pfiffner (2007) and references therein. Red, green, and blue lines are hypothesized positions and orientations of measurements of final temperatures along the same transect. Coldest (blue) line assumes a dip angle of 8° (similar to the present-day orientation) and a geothermal gradient of 25 °C/km. 121
4.4 Tectonic map of the Glarus alps, showing approximate locations of all samples obtained in the September 2016 campaign. Generated using Tectonics 500 base map from `https://map.geo.admin.ch/`. 123
4.5 Calcite δ^{13}C values from the Helvetic nappes and Infrahelvetic flysch 126
4.6 Calcite δ^{18}O values from the Helvetic nappes and Infrahelvetic flysch 127
4.7 Cross-plot of calcite δ^{13}C and δ^{18}O values from the Helvetic nappes and Infrahelvetic flysch 128
4.8 Calcite Δ_{47}-temperatures from the Helvetic nappes and Infrahelvetic flysch 130
4.9 Calcite locations and Δ_{47}-temperatures in the northern Helvetic nappes. Approximate sample locations plotted on the regional cross section of O Adrian Pfiffner (1993). 131
4.10 Calcite locations and Δ_{47}-temperatures in the southern Helvetic nappes and Infrahelvetic complex. Approximate sample locations plotted on the regional cross section of O Adrian Pfiffner (1993). Due to doming of the fault plane, some Helvetic nappe samples are inaccurately projected into this section. 132
4.11 Triple-plot of calcite δ^{18}O, $T_{\Delta 47}$, and theoretical equilibrium water δ^{18}O in the Helvetic nappes and Infrahelvetic complex. $\delta^{18}O_{H2O}$ calculated from the empirical calibration of Friedman and O'neil (1977). Error-weighted linear regressions of temperature and fluid data were calculated using York, 1968 fits. 134

4.12 Paired dolomite and calcite Δ_{47} values and temperatures from the Infrahelvetic flysch (16SCH01B, 16EN1A, and 16W01) and parautochthonous cover of the Aar massif (16–VP–11,–50). With one exception, stepped dolomite extractions have not been replicated, so dolomite Δ_{47} values are highly uncertain. Locations of three flysch samples are unknown, so here all samples are simply ordered by their dolomite $T_{\Delta47}$ value. 135
4.13 Triple-plot of calcite and dolomite $\delta^{18}O$, $T_{\Delta47}$, and theoretical equilibrium water $\delta^{18}O$ in the North- and South-helvetic flysch. $\delta^{18}O_{H2O}$ values calculated from the empirical calibrations of Friedman and O'neil (1977) and Horita (2014) for calcite and dolomite, respectively. Error-weighted linear regression of calcite temperature and fluid data was calculated using a York, 1968 fit. 138
4.14 Pictures of high-grade outcrops of the Lochsiten calc-tectonite and enveloping units in the southernmost exposures of the Glarus fault plane. 139
4.15 Calcite $T_{\Delta47}$, $\delta^{13}C$, and $\delta^{18}O$ in the Piz Segans section. 140
4.16 Calcite $T_{\Delta47}$, $\delta^{13}C$, and $\delta^{18}O$ at the Vorab Pign outcrop. 140
4.17 Calcite $T_{\Delta47}$, $\delta^{13}C$, and $\delta^{18}O$ at the new Vorab contact. Individual data points at the same distance are texture-specific powders subsampled by micro-drilling. 141
4.18 The Glarus thrust contact exposed on the north flank of Kärpf (SCS: 726740/199933). 142
4.19 Calcite $T_{\Delta47}$, $\delta^{13}C$, and $\delta^{18}O$ at the Kärpf outcrop. 143
4.20 Photographs and isotopic data for microdrilled carbonate fabrics of the Lochsiten calc-tectonite at Nagens, where peak conditions exceeded 300 °C. 144
4.21 Photographs and isotopic data for microdrilled carbonate fabrics from low-temperature sections of the Lochsiten calc-tectonite. 145
4.22 Calcite C – O reordering model for T-t paths in the Infrahelvetic complex. 147
4.23 Synthesis of peak temperatures, measured and modeled calcite Δ_{47} temperatures in the Infrahelvetic complex. 148
5.1 Schematic of the vacuum line setup for extracting and purifying iodomethane 164

5.2 Schematic of the experimental setup for evolving and concentrating CH_3I in a reflux reactor in a continuous N_2 stream 167
5.3 Mass spectrum of fluoromethane, acquired on a Thermo DFS IRMS, with electron energy at 55 eV, filament current at 1.5 mA, on a 1e5 SEM amplifier. Peaks are labeled by the most abundant unsubstituted species at each cardinal mass. 172
5.4 Mass spectrum of methyl fragment isotopologues and other isobaric interferences at mass 17 Da. Mass scan acquired on the prototype Thermo MAT 253 Ultra, 2.0 mA filament current, 100 eV electron energy, medium resolution entrance slit, on a Faraday cup with a 10^{12} Ω amplifier. Low-mass edge of major isotopologues are labeled. $^{12}CH_2D_2$ is not resolvable at this scale. 173
5.5 Hysteresis in intensity of unsubstituted methyl fragment $^{12}CH_3^+$ vs. bellows pressure for CH_3F working gas, over the course of ~1 hour. Mean intensities integrated for 3 minutes, and allowed to equilibrate for 1 minute after each change in bellows compression. Data acquired on the Thermo DFS, 1.49 mA filament current, -80 eV electron energy, an SEM with 10^5 amplification. Arrows denote direction in which data points were collected. 175
5.6 Drift in adduction rate of methyl groups when CH_3Cl is the analyte. Runs were each acquired by constantly measuring reference gas over the course of an hour. During the 2 hr break in between, all that was changed about the instrument state was the compression percentage of the bellows. 177
5.7 Inverse dependence of methyl fragment adduction rate on methyl fragment intensity when CH_3F is the analyte gas. 178
5.8 Mass spectrum of mass 34 of fluoromethane on the MAT 253 Ultra. Star denotes location of measurement. 179
5.9 Mass spectrum of mass 35 of fluoromethane on the MAT 253 Ultra. Star denotes location of measurement. 179
5.10 Mass spectrum of mass 36 of fluoromethane on the MAT 253 Ultra. Star denotes location of measurement. 180
5.11 Example adduct line of $r35$ vs. $i34$ of fluoromethane on the MAT 253 Ultra. 180

5.12 Example adduct line of $r36$ vs. $i35$ of fluoromethane on the MAT 253 Ultra. Note that for this relationship to be accurate, the adduct contribution to the intensity on mass 35 must first be subtracted. . . . 181
5.13 Dependence of fragmentation rate ($i33/i34$) on intensity of mass 34. Note that our correction scheme assumes that the fragmentation rate is effectively constant over the intensity range of actual measurements. 181
5.14 Example off-peak background line near mass 35 vs. $i34$ of fluoromethane on the MAT 253 Ultra. 182
5.15 Example off-peak background line near mass 36 vs. $i34$ of fluoromethane on the MAT 253 Ultra. 182
5.16 Example off-peak background line near mass 34 vs. $i34$ of fluoromethane on the MAT 253 Ultra. 183
5.17 Example of peak shape and model fit of methyl fragment isotopologues at mass 35. 184
5.18 Example of peak shape and model fit of methyl fragment isotopologues at mass 16. 185
5.19 Sample measured 1σ standard errors, and expected shot noise limits, for the described DFS measurements at masses 35 and 16. 186
5.20 Accuracy tests for δ^{13}C measurements of methoxyl groups in methanol and iodomethane standards. 189
5.21 Accuracy tests for δ^{2}H measurements of methoxyl groups in methanol and iodomethane standards. 190
5.22 Reproducibility of Δ_{36} measurements of methoxyl groups in methanol and iodomethane standards across multiple analytical sessions. 192
5.23 Reproducibility of Δ_{36} measurements of methoxyl groups in methanol and iodomethane standards across multiple analytical sessions, relative to $\delta_{36,wg}$. 192
5.24 Variation in Δ_{36} values among natural and synthetic methoxyl-bearing monomers and polymers, compared to δ^{2}H. 193
5.25 Variation in Δ_{36} values among natural and synthetic methoxyl-bearing monomers and polymers, compared to $\delta_{36,wg}$. 193
6.1 Variation in methoxyl δ^{13}C with vitrinite reflectance. Vitrinite reflectances of undegraded materials were not measured, but are assigned a nominal value of 0.2 in order to be shown here. 215

6.2 Variation in methoxyl δ^{13}C with methoxyl concentration. Dashed pink line denotes the expected trend of a Rayleigh fractionation model, given an initial composition of poplar wood and an isotope effect of $-12.3‰$. Green boxes denote hypothesized demethoxylation process endmembers, which could be mixed in single samples to explain the variance among degraded samples (see text for details). 216
6.3 Thermal de-methoxylation experiments of poplar wood, showing the total mass loss, apparent enrichment in methoxyl groups of residues, and methoxyl δ^{13}Cvalues in these residues. 223
6.4 A Rayleigh model for the poplar thermal stress experiments 227
6.5 Calibration line used to relate CH_3I peak areas measured by GC-combustion-IRMS to true methoxyl concentrations obtained by offline reflux condense procesures. 228
6.6 Discrepancies and agreements in measured vs. predicted methoxyl content, and methoxyl δ^{13}C, for samples measured by both methods. . 229
6.7 Methoxyl sampling sites, concentrations, and δ^{13}C values from a living Jacaranda branch. 230
6.8 Methoxyl sampling sites, concentrations, and δ^{13}C values from the compound leaf of a living Jacaranda tree. 231
6.9 Covariation in methoxyl content and δ^{13}C values of specific tissues within a single Jacaranda tree. 232

LIST OF TABLES

Number *Page*

2.1 Average ($n = 2 - 3$) fractionation factors for partial recovery of CO_2 from calcite and dolomite during stepped acid digestion procedure. Errors are 1σ standard errors of the fractionations, derived by propagating the standard errors of the replicate measurements of the partial recovery, and complete recovery methods. These measurements are in Table 2.9. Δ_{47} values of calcite and dolomite standards obtained using the stepped digestion procedure were indistinguishable from their unfractionated values outside of uncertainty, so no corrections were applied. 25

2.2 Average values of $\delta^{13}C$ and $\delta^{18}O$ in calcite and dolomite. Reported calcite values (calcite, total) are the unweighted mean of all individual offline calcite digestions and online bulk digestions with the dolomite $\delta^{13}C$ and $\delta^{18}O$ contributions removed (see Methods section for details). Errors are 1σ standard errors of the mean of multiple analyses, or the 1σ typical external reproducibility for offline digestion where only one replicate was used (0.05‰ and 0.1‰ for $\delta^{13}C$ and $\delta^{18}O$, respectively; individual measurements available in the electronic annex). Oxygen-18 and carbon-13 equilibrium fractionation temperatures are calculated using the equations of Horita (2014) and Sheppard and Schwarcz (1970), respectively. Model peak temperatures are from the distance–T relation of John M Ferry and Dipple (1992), except for sample 12H-122, which is beyond 4 km, where the 4th-order equation is no longer valid. Here, peak temperature was estimated based on the burial depth of the unit and a reasonable upper crustal geotherm (see section 2.6). Actual distance of sample 20H-99 (*) is 0.23 km, however this rock is from a different set of outcrops (in Contact Canyon) than the rest of the sample suite, where isograds are compressed. To more accurately compare sample 20H-99 to the others, it was projected to the distance it would lie at along the main transect in North Canyon 28

2.3 Average Δ_{47} values of online bulk powder measurements, and offline calcite, dolomite digestions. Total calcite values were obtained by averaging all offline measurements of calcite fractions and online bulk measurements with the dolomite contribution removed (see Methods section for details). Errors in bulk, calcite, total calcite, and dolomite Δ_{47} values are 1σ standard errors of the mean of multiple analyses, or 1σ measurement errors where only one replicate was used. The Δ_{47}–temperature calibration is based on a second-order polynomial fit in Δ_{47} vs. $1/T^2$-space to the data of Ghosh et al. (2006), Guo et al. (2009), Bonifacie et al. (2011), and Stolper and J M Eiler (2015) (see Methods for details). Actual distance of sample 20H-99 (*) is 0.23 km, however this rock is from a different set of outcrops (in Contact Canyon) than the rest of the sample suite, where isograds are compressed. To more accurately compare sample 20H-99 to the others, it was projected to the distance it would lie at along the main transect in North Canyon. 29
2.4 Description of the values used to numerically solve the thermal diffusion equation in the model Notch Peak aureole. 41
2.5 Individual measurements of calcite clumped isotopes using the offline stepped acid digestion procedure. 50
2.6 Individual measurements of dolomite clumped isotopes using the offline stepped acid digestion procedure. 51
2.7 Individual clumped isotope measurements of bulk powders using an online common acid bath (mixed calcite and dolomite). 52
2.8 Individual clumped isotope measurements of two high-grade dolomite marbles from the Western US. Gabbs-17 is a massive, buff, crystalline dolomite marble from Gabbs, NV, that was regionally metamorphosed as part of Tertiary fold and thrust belt, with additional contact metamorphism due to intrusion of granitic plutons (Humphrey and Wyatt, 1958; Cathles, Erendi, and Barrie, 1997). ML-INYO is a white, crystalline dolomite marble from Inyo Range, CA regionally metamorphosed due to burial beneath ~10 km of section Cambrian and younger (Nelson, 1962). Gabbs-17 is part of the Caltech Working Mineral Collection, sampler unknown. ML-INYO was collected by G.R. Rossman. 52

2.9 Individual measurements of the calcite standard Carrara marble, an in-house dolomite standard (SS-07), and mixtures of the two subjected to the stepped extraction procedure described in section 2.4 of the main text. Offline extractions of calcite or dolomite from mixtures of the standards were only compared to online (i.e., common acid bath) measurements of pure phases from the same analytical session in order to minimize the effect of instrumental drift on $\delta^{13}C$ and $\delta^{18}O$ values. For these offline extractions, the two standards were mixed in proportions comparable to those observed in the natural samples(i.e., X_{dolomite} values of 0.02 – 0.1 by moles). 53

2.10 Individual measurements used to determine the Δ_{47} acid digestion fractionation of dolomite when reacted at 50 °C in McCrea (1950)-style vessels, by comparison with the mean Δ_{47} value of the same standard (SS07) when reacted by the common acid bath technique at 90 °C. With an acid digestion fractionation correction of 0.040‰, the mean of the offline 50 °C measurements agrees with the mean of the online 90 °C measurements (with the accepted fractionation correction of 0.092‰). 54

3.1 Mean $\delta^{13}C$, $\delta^{18}O$, and Δ_{47} values of dolomite from all heating experiments and the unheated starting material. Reported uncertainties on $\delta^{13}C$ and $\delta^{18}O$ are 1σ standard deviations of individual measurements. Uncertainties on Δ_{47} values are 1σ standard errors. ^{18}O compositions of dolomite fragments are calculated from $\delta^{18}O$ values of CO_2 using a 90 °C dolomite–CO_2 common acid bath fractionation of: $\alpha^{18} = 1.009218$ (see Section 2.3). Δ_{47} are reported in the CO_2-equilibrated absolute reference frame, and corrected to the 25 °C acid scale by adding a fractionation factor of 0.092 ‰. Asterix denotes an experiment where aberrant $\delta^{13}C$, $\delta^{18}O$, and Δ_{47} values all suggest minor contamination by a secondary carbonate, so this sample is omitted from analyses and model fits. 73

3.2 Dolomite Δ_{47} reordering parameters for the Henkes et al. (2014) transient defect/equilibrium defect model. 'Best fit' parameters were generated using an error-weighted least squares global fit to the mean measured data reported in Table 1. Mean and 1σ s.d. of acceptable fits are the averages and standard deviations for each parameter based on fits to ~10,000 Monte Carlo simulations of the underlying Δ_{47} measurements. Activation energies are all reported in kJ/mol. Pre-exponential factors are reported in s^{-1}. 79
3.3 Dolomite Δ_{47} reordering parameters for the D. A. Stolper and J M Eiler (2015) exchange–diffusion model. Sources of fits, and units, are summarized in Table 3.2. 85
3.4 Major and minor element contents of two crystal fragments of the starting material of this study, determined on a JEOL JXA-8200 electron probe micro-analyzer with a KeV beam, 20 nA beam current, and a 10 μm spot size. CO_2 content was not measured; reported CO_2 values assume material has perfect carbonate stoichiometry. 98
3.6 Individual single and clumped isotope measurements of dolomite samples from each heating experiment. Uncertainties on $\delta^{13}C$ and $\delta^{18}O$ values are 1σ standard deviations of replicate measurements. Uncertainties on Δ_{47} are 1σ standard errors of the mean. Note that here, reported temperatures are furnace setpoints, which were converted to actual temperatures in the sample chamber using the calibration described in Section 2.3 101
3.5 Individual measurements of unheated fragments of the Eugui dolomite crystal aggregate, from disparate locations of the sample. 102
3.7 Pearson correlation coefficients for the families of Arrhenius parameters for the transient defect/equilibrium defect model generated using the Monte Carlo scheme described in Section 4.3 103
3.8 Pearson correlation coefficients for the families of Arrhenius parameters and m_p for the exchange-diffusion model, generated using the Monte Carlo scheme described in Section 4.4 103
3.9 Calcite Δ_{47} reordering parameters for the data of D. A. Stolper and J M Eiler (2015) exchange–diffusion model. Sources of fits, and units, are summarized in Table 2. 104
4.1 Mean calcite Δ_{47} data for the Glarus alps. 151
4.2 Mean dolomite Δ_{47} data for the Glarus alps. 152

4.3 Mean calcite Δ_{47} data for the Lochsited calc-tectonite 153
5.1 Iodomethane yields from methoxyl extractions of pure compounds. 'V' samples used the reaction vessel method. 'C' samples used the reflux condenser. 188
5.2 Adduct-corrected, background-corrected δ^{35}, δ^{36}, and $\delta D/^{13}C$ measurements, relative to the working gas composition. 188
5.3 Derived $\delta^{13}C$ (vs. VPDB), $\delta^{2}H$ (vs. VSMOW), and Δ_{36} (vs. wg) measurements of methoxyl groups from synthetic and natural materials. 189
6.1 Thermal maturities, methoxyl concentrations, and methoxyl $\delta^{13}C$ values, determined using the Gas Bench bottle reaction + GC-combustion-IRMS method. 212
6.2 Iodomethane $\delta^{13}C$ values samples purified by the reflux condenser procedure but analyzed by GC-combustion-IRMS 213
6.3 Methoxyl contents and $\delta^{13}C$ values determined by offline reflux condenser reaction + sealed tube combustion/IRMS. 214
6.4 Individual iodomethane measurements by GC-combustion-IRMS . . 226
6.5 Individual iodomethane measurements by reflux reaction + offline sealed-tube combustion 227

Chapter 1

INTRODUCTION

1.1 Kinetic and analytical impedances to studying shallow crustal geochemistry

Despite being the most accessible swath of the solid earth, the shallow crust is also the least well-understood. When probing the processes that modify minerals and molecules, geochemical investigators are commonly after the answers to *Who*, *What*, and *Where*: *who* are the chemical species that reacted?; *what* reaction occurred (and thus, what was produced?); and *where* did it all happen? At the earth's surface, reactants and products can commonly be accounted for, and the environmental conditions are well-constrained. So even though reaction mechanisms (e.g., biologic metabolisms, mineral-surface chemistry) can be cryptic, the inputs and outputs of such biologic 'black boxes' can be observed in real-time. Samples of the deep lithosphere and asthenosphere are harder to obtain, but whether exhumed in core complexes or entrained in magmas, these contain discernible, interpretable records of processes in their mineral textures and chemical compositions. From deeper regions where no surface samples exist, much can still be learned from models and experiments because at these elevated temperatures and pressures, the attainment of thermodynamic equilibrium can reasonably be assumed. If the deep earth is in thermodynamic equilibrium and its spatial chemical heterogeneities are minor, then our knowledge of this realm is limited largely by the accuracy of our equations of state.

Studying shallow crustal processes is comparatively challenging both because reaction products can be imperceptible and solid phases are rarely in equilibrium. The onset of metamorphism is traditionally pegged at the formation of the first metamorphic mineral, often a hydrous sheet silicate like talc or chlorite, at temperatures at or near ~350 °C. Below this temperature, phase transformations do occur, but these are difficult to observe and idiosyncratic by nature. Fluid activities and compositions, which catalyze modifications, can vary at all relevant scales. Chemical gradients of reactive species, too, depend on the environment and evolve in space and time. By the time a rock is studied at the surface, the instigators of a reaction are long gone, and the products hard to observe. For example, stable mineral recrystallization is

a process by which phases are dissolved an reprecipitated on an atomic scale. Diagenesis can modify key paleoenvironmental proxies in carbonate rocks (e.g., δ^{34}S of calcium-associated sulfate (Present et al., 2015), Δ_{47} (Cummins et al., 2014)) in ways that are often cryptic and may appear random. One of the principal questions regarding the evolution of our planet—whether the ancient oceans were hot, depleted in δ^{18}O, or neither—can be reduced to an argument of whether diagenesis (and associated isotopic modification) is intrinsic or avoidable in ancient carbonates (Grossman, 2012; Veizer and Prokoph, 2015).

Even when transformations are documented, accurately characterizing them can be prohibitive. Kerogen, the principal form of organic matter that survives early degradation and persists in subsurface environments, is polymeric, insoluble in most solvents, and recalcitrant to separation and analysis by conventional organic geochemical techniques. When it comes to studying the conditions of organic matter maturation, we are severely limited by what we can measure. After all, the two main proxies for thermal maturity, vitrinite reflectance and Rock-Eval, amount to empirical observations that, essentially, 'hotter kerogen is shinier and harder to burn.' Unsurprisingly, such thermal maturity indicators are impossible to interpret quantitatively because any calibrations to useful parameters (e.g., temperature and time) are valid only for the exact same materials subjected to similar pressures and maturation environments. The same is true for the equivalent proxies in carbonate and silicate systems, like the conodont alteration index and illite crystallinity.

Shallow crustal processes occur far from thermodynamic equilibrium, making it difficult to design and interpret models and laboratory experiments of these processes. Surface-born organic molecules and inorganic minerals are only meta-stable at shallow crustal conditions, and will transform through kinetic reactions for which no simple free-energy equations can be written. The reaction rates of these commonly Arrhenian processes are highly sensitive to the temperature and depth at which they occur. Moreover, the products of these processes are sensitive to specific thermal history because myriad reactions with unique Arrhenius relationships act on the same substrate at a molecular level. When it comes to kinetic reactions, 'fast and hot' does not replicate 'low and slow.' After all, a steak pan-seared to medium rare does not have the same properties as a steak simmered for a day. Similarly, the products of artificial organic matter maturation experiments, run 'hot' on laboratory timescales, do not sufficiently replicate the oils and gases produced when these materials mature at moderate temperatures for millions of years.

Overcoming these hindrances to shallow crustal geochemistry is necessary because of the major processes that occur here. Because it is the long-term 'storage locker' for ancient sedimentary sections, we need to know how prolonged residences modify the geochemical proxies we rely on for studying past surface environments. Can we reliably detect when diagenesis and recrystallization have compromised our proxies? If so, what are the mechanisms of such modification? Shallow crustal sections are also subjected to low-pressure, low-temperature analogs of major tectonic processes like orogenesis and subduction. Magmas are intruded, hydrothermal fluids are circulated, and fold-and-thrust belts are emplaced. The transition from ductile to brittle tectonics results in major earthquakes or more enigmatic shallow slow slip events. How are such events recorded in sections where no obvious new mineral growth occurs? Can we reconstruct past brittle deformational histories given more sensitive techniques?

The shallow crust also houses a major component of the global carbon cycle. The delivery, modification, and preservation of reduced carbon compounds in the subsurface are critical controls on the oxidation state of the earth. The form of these compounds (i.e., kerogen, oil, and gas) is not only important economically, but also for the current and past life on this planet. By mass, the subsurface biosphere is the greatest reservoir of life on earth. These deep biosphere microbes thrive (relatively speaking) on the organic carbon substrates delivered from the surface above. Understanding the activity and evolution of this environment, including the potential for similar ones to host life on other planets, requires understanding the processes, both biotic and abiotic, that act on and modify carbon in the shallow crust.

1.2 A path forward in novel isotopic techniques

In this thesis, I develop and apply new techniques to study processes acting on the two major pools of carbon in the shallow crust. Carbonate rocks, containing oxidized carbon in the form carbonate minerals like calcite and dolomite ($CaCO_3$ and $CaMg(CO_3)_2$), are a ubiquitous component of the sedimentary record and the principal archive of ancient environments. Nonetheless, these lithologies are overlooked for studies of shallow crustal processes because they are devoid of the accessory minerals and organic molecules and polymers conventionally required for such work. The 'clumped' isotope composition of carbonate is a relatively new proxy for the conditions (T, $\delta^{18}O_{fluid}$) of carbonate crystallization. Because carbonate minerals precipitate out of aqueous solutions where isotopic exchange is rapid, they can preserve isotopic configurations, reported as Δ_{47} values, that are in

homogeneous equilibrium with the ambient conditions of their formation environment. This technique has myriad applications as a geochemical proxy, but to date its use has been largely restricted to the formation temperatures of primary carbonate fabrics and surface processes. However, for the same reason that this thermometer appears to reliably record, e.g., the temperatures of the ancient ocean, carbonate clumped isotope compositions of recrystallized carbonate fabrics should be uniquely well-suited for constraining the conditions of sub-greenschist grade metamorphism in the shallow crust. Moreover, because dolomite and calcite clumped isotope compositions have distinct susceptibilities to recrystallization and reordering in the solid-state, even these 'simplest' two-phase carbonate rocks have the potential to record detailed, surprisingly nuanced thermal histories below 300 °C. If successful, these techniques would enable wide application to shallow crustal processes where unsuitable conditions (i.e., temperatures too cold) or lack of specialized lithologies (e.g., no pristine apatites) precluded previous work. If simple calcite–dolomite carbonates can be used accurately reconstruct fluid, crystallization, and thermal histories at conditions between 25 and 300 °C, then virtually no shallow-crustal section is off-limits to future study.

In the first half of this thesis, I describe efforts to validate, calibrate, and apply calcite and dolomite clumped isotope isotope thermometers to the study of shallow crustal metamorphism and deformation. Doing so requires understanding the conditions under which carbonate grains recrystallize in order to relate the temperatures recorded by carbonate clumped isotope compositions to discrete geologic events. In Chapter 2, I observe the behavior of these proxies in response to contact metamorphism in the Notch Peak aureole, Utah. Because this metamorphic aureole is well-studied, well-exposed, and simple to model, it serves as the ideal 'natural laboratory' to test the hypothesis that carbonate clumped isotopes can record the conditions of peak crystallization below the nominal onset of metamorphism beyond the mineralogically-defined contact auroele. I find that dolomite clumped isotope temperatures agree with expected peak temperatures in regions exposed to 300 to 150 °C, while co-existing calcite Δ_{47} values fully re-equilibrate back to the ambient burial conditions of the unit. Importantly, these records of peak temperature and retrograde cooling can be found even in samples where no obvious grain coarsening or heterogeneous metamorphic mineral reactions have occurred. That is, with this technique, it appears possible to distinguish between carbonates exposed to subtly different anchimetamorphic conditions in which no other textural or geochemical distinctions exist. This work lays the groundwork for application of these new ther-

mometers to a wide range of problems in shallow crustal petrology that have been intractable with solely conventional thermal maturity indicators.

In Chapter 3, I use a high-pressure heating experiments to measure the rate of dolomite Δ_{47} reordering in the solid state. This work enables predictions of the conditions under which dolomite formation temperatures can be preserved during burial and exhumation. While this goal is useful alone, I attempt to extend this work beyond a simple 'measure, fit, and model' exercise. Because the clumped isotope composition of a mineral is a measure of the intramolecular arrangement of its constituent atoms, solid-state changes in clumped isotope composition are a direct record of the breakage and formation of ionic bonds and the diffusion of atoms through the crystal lattice. Previous work on the solid-state reordering of the clumped isotope composition of calcite indicates that the intramolecular diffusion of carbon and oxygen is more complex and much faster than what ion probe-based ^{13}C and ^{18}O diffusion measurements would predict. My work on the kinetics of $^{13}C-^{18}O$ bond reordering in dolomite demonstrates that although the non-Arrhenian nature of this phenomenon is shared by all carbonates, the rates are phase-specific. By linking differences in the rates of $C-O$ bond reordering in these two phases to differences in the structure of their crystal lattices, I can entertain hypotheses for the fundamental mechanisms by which this reordering (and diffusion/exchange in general) occurs. This permits distinguishing between the two existing, mathematically-distinct models for solid state Δ_{47} reordering based on their proposed mechanistic groundings. Ultimately I argue for favoring one over the other based on these findings.

Despite the knowledge of the recrystallization and reordering behavior of carbonates gleaned from Chapters 2, 3 and previous work, critical questions remain: how do these results replicate when 'scaled-up' to low-grade regional metamorphic terranes? What aspects of orogeny are recorded when strata experience protracted histories of regional strain, fluid flow, burial, and exhumation during the emplacement of major fold and thrust belts? Chapter 4 describes ongoing work to address these questions by characterizing clumped isotope geochemistry of a classic study area of low-grade regional metamorphism, the Helvetic nappes in the Swiss Alps. Here, extensive previous work with thermal maturity indicators has made explicit predictions for the km-scale trends in metamorphic grade, and which deformation features do and do not perturb metamorphic isograds. My regional survey encompassing ~150 km^2 of exposed Mesozoic carbonates examines when these predictions hold true for

this novel geothermometer. Initial results indicate that while peak conditions are reliably recorded in the clumped isotope compositions of carbonates above ~150 °C, stress magnitude, fluid content, and mineralogy (calcite vs. dolomite) are principal controls on the timing of recrystallization below this temperature.

In addition, in Chapter 4, I use the sheared carbonate fabrics from the basal thrust of the Helvetic nappes to begin to constrain the depth and timing of tens of km of fault motion and the mechanism by which this 'megathrust' moved. Although it is widely recognized that thrusting along the Glarus fault persisted into the retrograde metamorphic phase, the amount of motion accommodated by the fault during exhumation, and the kinematic behavior of materials during this deformation, are still debated. By linking subsequent generations of dynamically recrystallized fault fabrics to specific temperatures, depths, and fluid sources, I am working to reconstruct the thermal and rheological evolution of this enigmatic, out-of-sequence megathrust.

The second half of this thesis concerns the development and application of new isotopic proxies to study the other major carbon pool of the shallow crust: the organic carbon reservoir. The carbon isotope composition of sedimentary organic matter is our principal record of the coevolution of the carbon cycle and life on Earth. Because conventional carbon isotope measurements require combustion to CO_2 for analysis, however, our understanding of the $\delta^{13}C$ records in organic compounds unavoidably average all carbon sites in molecules. This is problematic because everywhere we look, organic molecules have heterogeneous intramolecular isotopic structures, reflecting the litany of site-specific processes by which lipids, proteins, carbohydrates, and kerogens are assembled, modified, and consumed. *All carbon is not created (isotopically) equal*, and the disconnect between the atomic-scale nature of organic chemistry and our present (at best) compound-scale ability to observe it results in major outstanding questions about how carbon is cycled in surface and subsurface environments.

Chapter 5 describes the development of chemical and mass spectrometric techniques to characterize the $\delta^{13}C$, $\delta^{2}H$, and clumped $^{13}C-^{2}H$ composition of O-bound methyl groups in simple organic monomers and solid organic polymers. This is a two-part problem. First, I describe the chemical techniques required to extract, purify, and derivatize these methyl groups, intact, for analysis by isotope-ratio mass spectrometry. This is non-trivial work because conventional techniques in organic chemistry for these kinds of procedures are not concerned with the attainment of quantitative yields or high-purity samples, which are critical requirements for making meaning-

ful isotopic analyses. Thus, considerable effort went into adapting, designing, and testing procedures that would be suitable for high-precision stable isotope work. In many instances I describe the rationale behind certain steps to assist the development of similar procedures by future workers. Second, I detail the efforts to accurately, precisely measure the isotopic structure of these methyl groups, derivatized as fluoromethane CH_3F. Such a mass spectrometric measurement should be conceptually similar to existing techniques for the clumped $^{13}C-^{2}H$ isotope measurement of methane CH_4 that have been developed on the same instrument. In practice, however, there are unforeseen complications that, in hindsight, make methane unusually amenable to direct clumped isotopic measurement but methyl groups unusually challenging. The development cycle for this mass-spectrometric procedure required work over three years with two attempted analytes, and ultimately requires two separate mass spectrometers and multiple working days for a single measurement. Again, to assist with future development of similar techniques, I describe major efforts that did not succeed in addition to those that do. By exploring why some strategies, such as the the direct analysis of methyl fragments, can be problematic, I hope to give a better sense of the possibilities and limits of clumped isotopic measurements by sector-style isotope-ratio mass spectrometry. Finally, I describe initial applications of this procedure to the forensic discrimination of natural and synthetic vanillin, and discuss whether these methyl groups are likely to be assembled in equilibrium with their formation environment by metabolisms in higher plants.

Finally, in Chapter 6, I use the chemical extraction procedure developed in Chapter 5 and a simpler complementary technique to explore the variation of the $\delta^{13}C$ of methoxyl groups in during the synthesis of terrestrial plant lignin and its progressive degradation to kerogen and coal. I find massive ($\leq 55‰$) enrichments in the site-specific carbon isotope composition of these moieties in relatively immature coals relative to the composition of their undegraded counterparts. I argue that these enrichments are generated by normal kinetic isotope effects associated with the progressive loss of these sites during the thermal and bio-degradation of terrestrial organic matter in the shallow crust. This study appears to resolve an outstanding paradox regarding isotopic mass balance of early thermogenic methane and its sources, and opens the door for future work tracking specific C1 compounds through the full maturation cycle, and detecting integrated past activities and metabolisms of deep biosphere microbes. In addition, it serves as an initial demonstration of the promise of site-specific isotopic records of lignin kerogen sub-units. When also considering methoxyl $\delta^{13}C$ measurements I have made of other components

in higher plants, this body of work demonstrates that methoxyl $\delta^{13}C$ values vary by more than 100‰ in natural materials that all have unremarkable, 'normal' bulk $\delta^{13}C$ compositions. These massive signals reflect the rich archives that site-specific organic carbon measurements preserve, as long as we're patient enough to uncover them.

References

Cummins, Renata C et al. (2014). "Carbonate clumped isotope constraints on Silurian ocean temperature and seawater d". In: 140.C, pp. 241–258.

Grossman, E L (2012). "Applying oxygen isotope paleothermometry in deep time". In: . . . *Earth's Deep-Time Climate: The State of the . . .*

Present, Theodore M et al. (2015). "Large Carbonate Associated Sulfate isotopic variability between brachiopods, micrite, and other sedimentary components in Late Ordovician strata". In: *Earth and Planetary Science Letters* 432.Supplement C, pp. 187–198.

Veizer, Ján and Andreas Prokoph (2015). "Earth-Science Reviews". In: *Earth-Science Reviews* 146.C, pp. 92–104.

Chapter 2

CLUMPED ISOTOPE THERMOMETRY OF CALCITE AND DOLOMITE IN A CONTACT METAMORPHIC ENVIRONMENT

Clumped isotope compositions of slowly-cooled calcite and dolomite marbles record apparent equilibrium temperatures of roughly 150 – 200 °C and 300 – 350 °C, respectively. Because clumped isotope compositions are sensitive to the details of T-t path within these intervals, measurements of the Δ_{47} values of coexisting calcite and dolomite can place new constraints on thermal history of low-grade metamorphic rocks over a large portion of the upper crust (from ~5 to ~15 km depth). We studied the clumped isotope geochemistry of coexisting calcite and dolomite in marbles from the Notch Peak contact metamorphic aureole, Utah. Here, flat-lying limestones were intruded by a pluton, producing a regular, zoned metamorphic aureole. Calcite Δ_{47} temperatures are uniform, 156 ± 12 °C (2σ s.e.), across rocks varying from high-grade marbles that exceeded 500 °C to nominally unmetamorphosed limestones >5 km from the intrusion. This result appears to require that the temperature far from the pluton was close to this value; an ambient temperature just 20 °C lower would not have permitted substantial re-equilibration, and should have preserved depositional or early diagenetic Δ_{47} values several km from the pluton. Combining this result with depth constraints from overlying strata suggests the country rock here had an average regional geotherm of 22.3 – 27.4 °C/km from the late Jurassic Period until at least the middle Paleogene Period. Dolomite Δ_{47} in all samples above the talc+tremolite-in isograd record apparent equilibrium temperatures of 328^{+13}_{-12} °C (1σ s.e.), consistent with the apparent equilibrium blocking temperature we expect for cooling from peak metamorphic conditions. At greater distances, dolomite Δ_{47} records temperatures of peak (anchi)metamorphism or pre-metamorphic diagenetic conditions. The interface between these domains is the location of the 330 °C isotherm associated with intrusion. Multiple-phase clumped isotope measurements are complemented by bulk δ^{13}C and δ^{18}O dolomite-calcite thermometry. These isotopic exchange thermometers are largely consistent with peak temperatures in all samples within 4 km of the contact, indicating that metamorphic recrystallization can occur even in samples too low-grade to produce growth of conventional metamorphic index minerals (i.e., talc and tremolite). Altogether, this work demonstrates the potential of these methods to quantify the conditions of metamorphism at sub-

greenschist facies.

2.1 Introduction

There are relatively few quantitative geothermometers that can be used to investigate the thermal histories and temperatures of chemical processes occurring in the upper ~15 km of the crust. Below ~300 °C, most heterogeneous equilibria, including the cation and stable isotope exchange reactions upon which most geothermometers are based, proceed too slowly to reach thermodynamic equilibrium. Some established thermometers, such as oxygen isotope fractionation in quartz – calcite veins (Kirschner, Sharp, and Masson, 1995) or fluid inclusion phase equilibria and microthermometry (Mullis et al., 1994), are applicable in this range of relatively low temperatures, but only to narrow types of samples. Other methods are more widely applicable but yield only semi-quantitative constraints, such as a relative ranking of thermal maturity (e.g., illite crystallinity; conodont color alteration; vitrinite reflectance; Frey (1987)). One method of thermometry that might seem to offer a useful approach to shallow crustal settings—the carbonate – water oxygen isotope thermometer (which rapidly equilibrates at most diagenetic and low-grade metamorphic conditions; Epstein et al. (1953)) is rarely useful because one generally lacks precise constraints on the δ^{18}O of crustal waters (Sheppard, 1986).

Carbonate clumped isotope thermometry offers a relatively new approach to determine the thermal histories of surface and shallow crustal processes (see review by John M Eiler (2011)). Because it is based on a homogeneous equilibrium recorded by the carbonate mineral lattice, and carbonates appear to often grow at or near isotopic equilibrium, it is potentially useful (as good as est. ±10 °C) as a recorder of crustal processes up to ~300 °C. While most uses of this technique have focused on paleoclimate problems using biogenic and soil carbonates, proof-of-concept studies have already demonstrated its usefulness for the study of early diagenesis (Huntington et al., 2011), dolomitization (J M Ferry et al., 2011), cementation (Dale et al., 2014), and hydrothermal alteration at temperatures relevant to the shallow crust (Bristow et al., 2011).

Carbonate clumped isotope thermometry in sub-surface environments is complicated because apparent temperatures may be modified by solid state diffusion, which re-orders bonds between rare isotopes on geologic timescales (Dennis and Schrag, 2010). Studies of C–O bond reordering kinetics in calcite predict that measurable resetting should occur at temperatures as low as ~115 °C on timescales of hundreds

of millions of years (Passey and Henkes, 2012; Henkes et al., 2014; Stolper and J M Eiler, 2015). Moreover, the exact clumped isotope composition preserved in a crystal, and the degree to which it is reset from an initial value, can depend on the specific T-t path through the window where C–O reordering can occur. This phenomenon presents a problem for the interpretation of paleoclimate records in deeply buried samples, but also presents an opportunity for a new tool to study the thermal histories of rocks—a 'clumped isotope geospeedometry'—i.e., the constraint of cooling rate (or other features of a cooling history) based on the preservation of apparent temperatures. This concept has been successfully employed in some initial studies to predict the cooling rate of a metamorphic core complex (Passey and Henkes, 2012), the maximum burial depths of carbonate fossils in depositional basins (Henkes et al., 2014; Shenton et al., 2015), and the geotherm traversed by buried and exhumed soils (Stolper and J M Eiler, 2015).

Here we examine the clumped isotope systematics of calcite and dolomite in a contact metamorphic environment, compare these results with the heterogeneous C and O isotope exchange equilibria between these two minerals, and interpret these findings with respect to experimental determinations of the kinetics of clumped isotope re-ordering and intermineral exchange of stable isotopes. To the best of our knowledge, this is the first study to integrate constraints from multiple simultaneous clumped isotope equilibria with each other and with more conventional stable isotope geothermometers. Our purpose is both to illuminate the thermal history surrounding a shallow crustal intrusion, including locations and times that are poorly constrained by other techniques, and to illustrate a general methodology that may be helpful in studying thermal histories of other metamorphic settings.

2.2 Background

The formation of bonds between the rare, heavy isotopes of C and O in carbonates (i.e., ^{13}C–^{18}O bearing carbonate ion groups) is governed by the thermodynamic balance between minimization of vibrational energy (lowest when heavy isotopes are bonded to each other), and maximization of configurational entropy (highest when all carbon and oxygen isotopes are randomly distributed among all isotopologues of CO3-2—a state referred to as the stochastic distribution). This balance can be expressed by the isotope exchange reaction (for calcite):

$$Ca^{13}C^{16}O_3 + Ca^{12}C^{18}O^{16}O_2 = Ca^{12}C^{16}O_3 + Ca^{13}C^{18}O^{16}O_2. \qquad (2.1)$$

The equilibrium constant for this reaction, $K_{eq}1$, is measured by digestion of a carbonate phase in phosphoric acid and analysis of the isotopic composition of the evolved CO_2 by sector mass spectrometry (or potentially other methods, such as absorption spectroscopy); the essential point here is that the proportion of ^{13}C–^{18}O bonds in the evolved CO_2 is fractionated by acid digestion but (apparently) not re-equilibrated by exchange. Thus, just as for an acid-digestion measurement of the $\delta^{18}O$ of carbonates, one can indirectly observe the state of isotopic ordering in reactant CO_3 groups by observing that in the product CO_2 molecules. The degree to which multiple isotopic substitution—or isotopic 'clumping'—is present in a sample of CO_2 is expressed as:

$$\Delta_{47} = \left[\left(\frac{R^{47}}{R^{47*}} - 1\right) - \left(\frac{R^{46}}{R^{46*}} - 1\right) - \left(\frac{R^{45}}{R^{45*}} - 1\right)\right] \times 1000, \tag{2.2}$$

where R^{47}, R^{46}, and R^{45} are the measured intensity ratios of masses 47, 46, and 45 over mass 44, respectively, of the evolved CO_2, and the * denotes the expected value for a ratio given a stochastic distribution of isotopes among all isotopologues (Ghosh et al., 2006; John M Eiler and E. Schauble, 2004; Wang, E. A. Schauble, and John M Eiler, 2004). Because $K_{eq}1$ in carbonate is temperature-dependent, the measured Δ_{47} value of CO_2 evolved from that carbonate depends on the growth temperature (assuming the carbonate grew at or near equilibrium with respect to reaction 2.2).

The kinetics of clumped isotope reordering in carbonate

If a crystal is not in clumped isotopic equilibrium with its ambient temperature, the clumped isotope composition can evolve toward equilibrium by C–O bond reordering, provided atomic mobility allows migration of isotopes among nearby crystal sites (Passey and Henkes, 2012). The exact mechanism for this reordering is unclear, but likely involves the breakage of C-O bonds and subsequent reformation using C and O from neighboring carbonate groups or interstitial positions within the crystal lattice (Henkes et al., 2014). Calcite Δ_{47} reordering exhibits non-first order behavior in laboratory heating experiments (Passey and Henkes, 2012; Henkes et al., 2014; Stolper and J M Eiler, 2015). Specifically, when heating a relatively high-Δ_{47} calcite crystal, C–O bonds reorder toward a stochastic distribution rapidly but incompletely during the first few hours, after which the rate of re-equilibration slows. Henkes et al. (2014) attribute the rapid reordering to diffusion along crystallographic defects that can be annealed at high temperature. Once these 'transient' structural or point defects are eliminated, reordering occurs solely using unannealable defects,

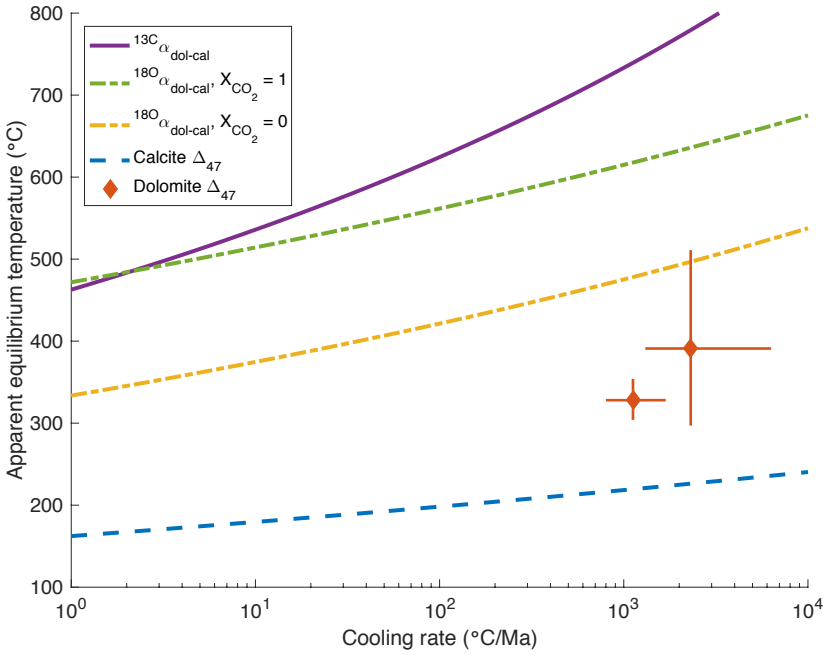

Figure 2.1: Apparent equilibrium blocking temperatures of single isotope and bulk isotope thermometers in calcite and dolomite. Carbon-13, and dry ($X_{CO_2} = 1$) oxygen-18 lines are derived from the calcite diffusion experiments of Labotka et al. (2011). Wet oxygen-18 parameters are from the calcite data of Farver (1994). Following the convention of Labotka et al. (2011), all three single isotope exchange apparent equilibrium blocking temperature relations are calculated using the Dodson-style equation of Lasaga (1998), assuming linear cooling rates and a grain size of 100 μm: $T_c = \frac{E_a/R}{\ln?[2K_0T_c^2/(a^2SE_a/R)]}$, where E_a, R, K_0, T_c, a, and S are the activation energy, gas constant, frequency factor, apparent equilibrium blocking temperature, grain radius, and cooling rate, respectively. These curves implicitly assume that self-diffusion in calcite is the rate-limiting step to re-equilibration, which is consistent with results from limited measurements of dolomite single-isotope diffusion (Anderson, 1972). The calcite Δ_{47} curve is calculated using the optical calcite data and eqn. (14) of Passey and Henkes (2012). No dolomite Δ_{47}reordering parameters are yet published, but clumped isotope measurements of dolomite from the Predazzo contact aureole (Ferry et al., 2011) and the Notch Peak aureole (this study) suggest that it should preserve apparent equilibrium temperatures ~100 °C above calcite. Cooling rates for these data are estimated from a thermal model of the Notch Peak aureole developed in section 2.6, and a similar model reflecting the geometry, depth, and sample location in the Predazzo aureole, and uncertainties therein (Ferry et al., 2002).

such as intrinsic defects or ionic impurities (Henkes et al., 2014). Stolper and J M Eiler (2015) hypothesize that the similarity in reordering behavior among

different calcite samples, and the observation of the same behavior in a second phase (apatite), suggests that it reflects something intrinsic and universal to the kinetics of clumped isotope reordering rather than an idiosyncrasy of deformational or other defects. These authors fit the experimental data by simultaneously solving two first order linear differential equations for two reaction rate constants. The physical justification for this model is that C–O bond reordering occurs in two steps: (1) isotopic exchange between neighboring carbonate groups, and (2) diffusion of carbonate groups through the crystal lattice. When a relatively high-Δ_{47} carbonate is heated, such that it has an excess of ^{13}C–^{18}O bonds compared to equilibrium at its new condition, rapid initial reordering occurs through division of the clumped isotopologues to form two neighboring carbonate groups that each possess one rare isotope. However, these adjacent species effectively create a population of domains within the crystal that are enriched in both ^{13}C and ^{18}O, which readily re-exchange with each other to maintain a high overall abundance of clumped species. This can be thought of as a special case of well known 'mixing' effects, where mixing two populations that differ in bulk isotopic composition but share a state of isotopic ordering results in a mixture with an excess of 'clumps' (John M Eiler and E. Schauble, 2004; John M Eiler, 2007; John M Eiler, 2013). Further decline in the abundance of clumped species depends on the migration of ^{13}C and ^{18}O away from each other by the slower process of diffusion through the crystal lattice.

Although the models of Henkes et al. (2014) and Stolper and J M Eiler (2015) are calibrated to describe statistically indistinguishable data, their distinct theoretical groundings lead to discrepancies in how they should be applied to the case of a high-grade marble undergoing slow cooling. Since the calcite crystals in this marble are formed above the temperature where Henkes et al. (2014) suggest transient defects anneal, only the slower, 'post-annealing' reordering kinetics should be considered when modeling the change in Δ_{47} with cooling. According to the Stolper and J M Eiler (2015) model, however, the rapid reordering phase is an intrinsic property of the crystal lattice, and should not be annealed even when a sample is crystallized at high temperatures. This difference is subtle for all natural carbonates measured so far, but could be significant for a material with exceptionally large capacity for reordering via the rapid mechanism (i.e., a high concentration of pairs or transient defects, depending on the model). It is not yet known whether one, both, or neither of these models accurately describe clumped isotope re-ordering kinetics in natural materials. Both models predict apparent equilibrium blocking temperatures in calcite of 150 – 200 °C, which are consistent with measurements of slowly cooled

marbles (John M Eiler, 2011; Passey and Henkes, 2012). The apparent equilibrium blocking temperature should be dependent on the cooling rate near this temperature; initial measurements suggest that this dependence has been observed (Stolper and J M Eiler, 2015). Apparent equilibrium blocking temperatures in dolomitic marbles are 300 – 350 °C (J M Ferry et al. (2011); Table 2.8), which suggest that the carbonate clumped isotope reordering kinetics in dolomite are slower than in calcite (Fig. 2.1).

Dolomite – calcite stable isotope exchange reactions

Although the focus of this study is the clumped isotope geochemistry of co-existing calcite and dolomite in metamorphic rocks, these measurements are complemented by simultaneously considering fractionations of carbon and oxygen isotopes between co-existing calcite and dolomite. These fractionations are temperature-dependent when controlled by equilibrium thermodynamics, and have been demonstrated to be effective thermometers (Sheppard and Schwarcz, 1970). At thermodynamic equilibrium, dolomite is higher in δ^{13}C and δ^{18}O than co-existing calcite, by amounts that vary from ~0.5 to 1.5‰ (δ^{13}C) and from ~0.5 to 2.5‰ (δ^{18}O) at temperatures from ~700 to 200 °C, respectively. Theoretical predictions of these fractionations (Chacko and Deines, 2008; Deines, 2004; E. A. Schauble, Ghosh, and John M Eiler, 2006) are in general agreement with both laboratory experiments (Horita, 2014; Matthews and Katz, 1977), and observations of a suite of natural meta-limestones from the Chester dome area, Vermont, USA (Sheppard and Schwarcz, 1970). It is worth noting, however, that natural dolomite – calcite isotope fractionations are highly scattered when a wide diversity of rocks are considered, likely due to the failure to attain and/or preserve local equilibrium at the scale of analysis (John M Ferry, Ushikubo, et al., 2010). In addition, in environments where H_2O-rich fluids react with carbonate rocks, variable amounts of water – mineral exchange and isotopic fractionations due to decarbonation reactions may disturb originally equilibrated intermineral fractionations (T C Labotka et al., 2011).

The solid-state diffusion rates of oxygen and carbon in calcite and dolomite suggest that stable isotope exchange equilibria between these minerals should have higher apparent equilibrium blocking temperatures than the clumped isotope thermometers (Anderson (1972), Farver (1994), and T C Labotka et al. (2011); Fig. 2.1). At geologically rapid cooling rates in dry environments, calcite grains hundreds of microns across are effectively closed to diffusion-limited changes in bulk isotopic composition at temperatures below 600 °C (T C Labotka et al., 2011). Water

fugacity has a strong effect on oxygen diffusivity, lowering the apparent equilibrium blocking temperature by as much as 150 °C in pure H_2O (Farver, 1994; T C Labotka et al., 2011). (It is interesting to note that despite the effect of f_{H_2O} on oxygen and carbon diffusivity, to date no effect of f_{H_2O} on clumped isotope reordering rate has been observed; (Passey and Henkes, 2012)) The experimentally determined self-diffusion rates of C and O in calcite (in the case of O, assuming a value of f_{H_2O}) can be used to estimate the blocking temperatures of C and O exchange between coexisting calcite and dolomite (Lasaga, 1998; Fig. 2.1). The rates of C and O self-diffusion in dolomite are poorly understood, but one published study suggests that they are more rapid than in calcite at comparable conditions (Anderson, 1972). Therefore, our calculations assume that diffusion through calcite is the rate-limiting step to dolomite – calcite isotopic re-equilibration (note that this assumption may be invalid in rocks containing much more calcite than dolomite, or in which calcite is far finer grained than dolomite; Eiler et al., 1992). These calculations show that in contact metamorphic environments with relatively high X_{CO_2} values (>0.5, consistent with the unit of interest in this study), low f_{H_2O} (tens of MPa, appropriate for the unit), and relatively rapid cooling rate (>100 °C/Ma), the dolomite – calcite oxygen and carbon isotope exchange thermometers are expected to have apparent equilibrium blocking temperatures on the order of 550 – 700 °C (Fig. 2.1). It should be noted, however, that if isotopic self-diffusion in dolomite is faster than in calcite, dolomite could continue to equilibrate with a pore fluid (or other co-existing phase) to a lower temperature.

The stable isotope systematics of contact metamorphism of carbonates

Here we examine the expected stable isotope systematics (including both clumped isotope and heterogeneous isotope exchange equilibria) for carbonates that undergo a metamorphic event broadly resembling that experienced in shallow crustal contact metamorphic settings. A key question for models of stable isotope systematics associated with metamorphism of carbonates is whether the rate-limiting step for setting the isotopic composition of a mineral grain is atomic mobility through a pre-existing mineral lattice (i.e., inter- or intra-crystalline diffusion), or any of the several processes of mineral growth (recrystallization by grain coarsening or dissolution/reprecipitation; new mineral growth associated with a metamorphic reaction, for example calcite formed by the talc-in reaction, dolomite+quartz+water = calcite+talc+CO_2). Diffusion-controlled processes only permit rapid and complete changes in isotopic composition when ambient temperatures exceed the blocking

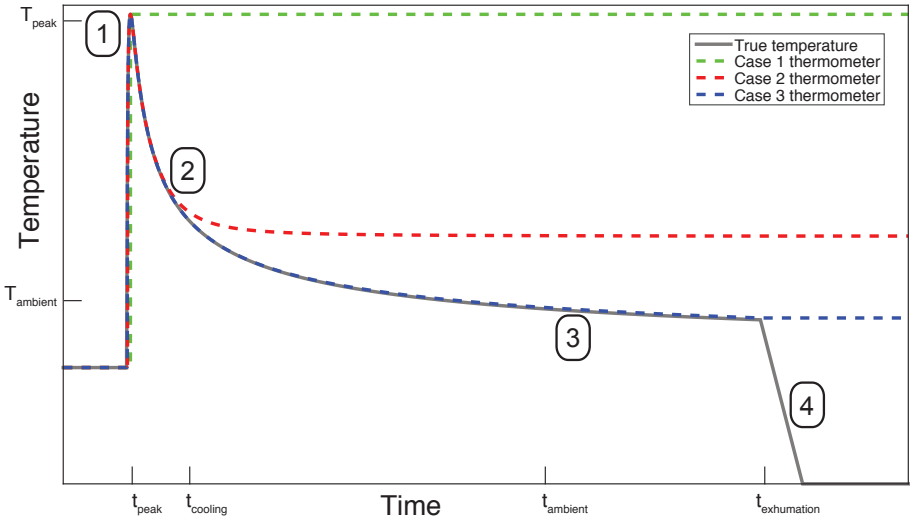

Figure 2.2: Schematic diagram of the behavior of case-1, 2, and 3 exchange thermometers in a representative thermal metamorphic event. The four key events are 1) peak crystallization, 2) cooling down from peak temperature to the ambient/burial temperature, 3) incubation at ambient temperature, and 4) exhumation to surface. A case-1 thermometer ($T_{peak} < T_c$) records the temperature of peak metamorphism. A case-2 thermometer ($T_{ambient} < T_c < T_{peak}$) records an apparent equilibrium blocking temperature dependent on the cooling rate near this value (T_c). The case-3 ($T_c \leq T_{ambient}$) thermometer fully re-equilibrates with the ambient temperature of the system, and records this value, provided exhumation is rapid enough to quench the system to further exchange.

temperature, whereas processes of mineral growth should be expected to equilibrate the new mineral with grain boundary fluid and other newly forming minerals essentially instantaneously (i.e., because the kinetics of isotopic exchange of dissolved inorganic carbonate in aqueous or carbonic fluid is rapid at all temperatures and time scales of interest). Partial recrystallization during multiple pre-peak homogeneous or heterogeneous metamorphic reactions can result in cumulative clumped or bulk isotope compositions that are mixtures of all the relict generations of a single phase. Because we focus on contact metamorphic marbles that exhibit coarse, equilibrated fabrics, we examine simplified models in which carbonates thermometers always achieve their equilibrium values when they first reach their peak metamorphic temperatures. Instances where this condition is not met may be identifiable in some cases, as discussed below. However, note that these predictions differ from expectations for unmetamorphosed or weakly metamorphosed rocks in the outermost parts of contact metamorphic aureoles. Our examination of the stable isotope systematics

of carbonates from the Notch Peak aureole will assume a default model consisting of four stages in the thermal history: 1) crystallization at peak conditions in response to a local thermal disturbance, driving all carbonates to internal equilibrium Δ_{47} values and heterogeneous equilibrium with respect to calcite – dolomite fractionations of O and C isotopes; 2) cooling from peak conditions to the ambient temperature of the country rock; 3) incubation at this ambient temperature; and 4) exhumation and cooling to surface temperatures (Fig. 2.2).

The behavior of the various stable isotope homogeneous and heterogeneous equilibria will be determined by the kinetics controlling intracrystalline stable isotope distributions and intercrystalline exchange, as well as the peak temperature of recrystallization, the background ambient temperature in the crust at the depth of interest, and the rates of initial cooling and subsequent exhumation. We examine three end-member scenarios that could apply to any one of the isotopic proxies of interest:

- Case-1: The peak temperature is below the intrinsic (diffusion-limited) apparent equilibrium blocking temperature. Following crystallization at the peak temperature, isotopic redistribution in response to cooling cannot occur, and the peak temperature is faithfully recorded. In the case of heterogeneous equilibrium, it is unlikely that both minerals recrystallized at the same temperature. However, the rocks we examine, the product phase (dolomite) is low in overall abundance and produced at the expense of some of a large reservoir of the reactant phase; as long as the product equilibrates with the reactant at the peak temperature, then this temperature should still be preserved.

- Case-2: The apparent equilibrium blocking temperature falls between the peak temperature and the ambient temperature. As the rock cools from peak conditions, isotopic redistribution freely and continuously re-equilibrates until the partial reordering zone (i.e., the region where reordering is sluggish enough that the actual Δ_{47} value will lag behind the equilibrium Δ_{47} value) is reached. The exact apparent equilibrium blocking temperature that is preserved depends on the cooling rate through this temperature window and how close the ambient temperature is to the nominal apparent equilibrium blocking temperature.

- Case-3: The apparent equilibrium blocking temperature falls below both the peak and ambient temperatures. All features of the peak temperature and

initial cooling path are lost due to re-equilibration at the ambient temperature. The final recorded temperature will depend on the exhumation rate; e.g., in the limiting case of exhumation that is rapid enough to effectively quench early in the exhumation path, the ambient temperature of the crust at the depth of initial contact metamorphism will be preserved.

Thus, the final recorded temperature (based on Δ_{47} values of calcite or dolomite, or calcite – dolomite fractionations) may be interpreted as a constraint on one or more elements of the thermal history, depending on the relationship between the apparent equilibrium blocking temperature and the temperatures and rates of various key processes.

An essential point that guides our further development of these principles below is that many carbonate rocks possess several independent isotope equilibria: i.e., a calcite – dolomite marble records a Δ_{47} value of calcite, a Δ_{47} value of dolomite, and two calcite – dolomite heterogeneous equilibria (one for carbon isotopes and one for oxygen isotopes). Since the apparent equilibrium blocking temperatures for two or more of these isotope exchange thermometers are different, analysis of one rock should permit reconstruction of several features of the thermal history. For instance, given what is understood about the reordering kinetics of these thermometers, for a metamorphic event with a peak temperature in excess of 300 °C and an ambient temperature near or below 200 °C, a single rock containing calcite and dolomite could quantitatively constrain the peak conditions, cooling path, and incubation temperature (i.e., ambient temperature at the relevant depth in the crust) of the event (Fig. 2.2).

Finally, it is important to note that the diffusion-controlled processes considered in our idealized model outlined above may be altered by recrystallization and/or fluid – rock reaction at temperatures other than the peak temperature. Such processes often can be recognized and characterized through texturally resolved isotopic measurements.

2.3 Geologic overview of the Notch Peak aureole: A natural laboratory for clumped isotope reordering processes

We examine the stable isotope systematics, including clumped isotope compositions, of marbles from the Notch Peak contact metamorphic aureole in western Utah. The Notch peak pluton (Jg in Fig. 2.3) is a Late Jurassic-aged (Rb-Sr isochron age = 145 ± 1.9 Ma; Nabelek et al., 1988) quartz monzonite that discordantly intrudes

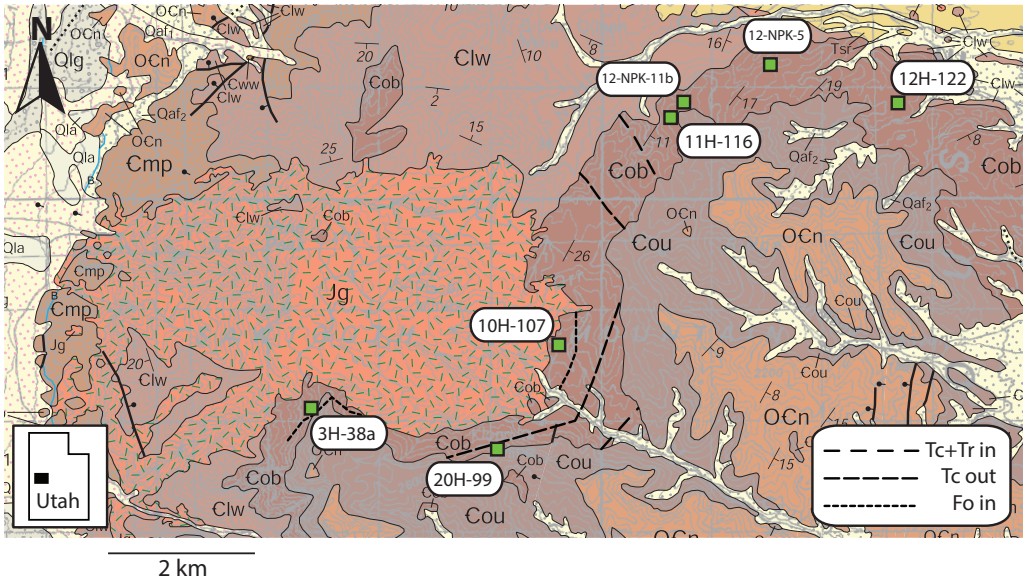

Figure 2.3: Sample locations in the Notch Peak aureole, Utah, USA (modified after Hintze and Davis, 2002)

into middle and upper Cambrian limestones, flat-lying at the time of intrusion, in the central portion the House Range, Utah (Hover-Granath et al., 1983). The surface exposure of the pluton is approximately 7x4 km in area, although the body is believed to have a laccolithic shape (i.e., it is wider in the subsurface; Hover-Granath et al., 1983). Exhumation by block faulting in the Miocene Epoch has created exceptional exposure of the intrusion and host rocks surrounding it: the pluton can be observed in contact with as much as 800 m of vertical sedimentary section, and individual beds of the relevant units can be traced up to 6 km away from the contact with the pluton (Hover-Granath et al., 1983). The regional dip of the host limestones and dolostones is roughly 10° to the southeast, although proximal to the intrusion the strata are domed away from it. The metamorphic aureole surrounding the pluton has a regular, simple geometry; highest-grade marbles are found closest to the contact, with progressively lower grades found by moving directly away from it.

Among the units that are intruded by the Notch Peak Stock are the Weeks (Clw in Fig. 2.3) and Orr Formations: Cambrian limestones with subequal and minor silty/siliciclastic components, respectively. Additional intruded formations below the Weeks, including the Marjum Formation (Cmp in Fig. 2.3), are not considered in this study. Based on reconstruction of the regional sedimentary strata, the section overlying the Orr Formation was 6.2 – 6.5 km thick at the time of intrusion (Hover-

Granath et al., 1983). The Big Horse Limestone Member (Cob in Fig. 2.3) of the Orr Fm. is a ~220 m-thick cliff-forming unit and the focus of this study (Hintze and Davis, 2002; Powell, 1959). The unit is composed of six cycles of argillite and limestone, each tens of meters thick. Each argillite grades gradually into limestone, consistent with a shallowing-upward shelf platform sequence (Hover-Granath et al., 1983). The boundary between the top of each limestone and overlying argillite, however, is sharp (Hover-Granath et al., 1983). Many beds contain peloids, the upper cycles of the member are fossiliferous, and the top of each cycle is capped by an algal-rich or oolitic layer (Hover-Granath et al., 1983).

Nominally unmetamorphosed limestones in the Big Horse Member are primarily skeletal grainstones, with partial replacement by rhombohedral dolomite, and detrital silicate phases. Millimeter-sized cracks infilled with secondary calcite are common. The first identifiable metamorphic reaction in Big Horse limestones produces talc and tremolite, at a map distance of ~1.8 km from the contact with the pluton (Hover-Granath et al., 1983). At 0.8 km from the contact, the next isograd marks the first appearance of talc-free assemblages with tremolite or diopside as the primary medium-grade metamorphic phase. The highest-grade marbles, less than 0.25 km from the contact, are forsterite-bearing. Throughout the metamorphic suite, calcite and dolomite coarsen and change fabric, from skeletal and cement to hornfelsic or granoblastic grains 300 – 600 μm across. Temperatures of all metalimestones from calcite – dolomite Mg-solvus thermometry are between 400 and 525 °C (Hover-Granath et al., 1983). Apparent temperatures measured with this technique in unmetamorphosed samples >5 km from the pluton are highly variable between 180 and 290 °C, and have been previously interpreted to represent relict diagenetic or primary sedimentary compositions, which likely never attained calcite – dolomite heterogeneous equilibrium, and therefore cannot be used to constrain the peak temperatures of these rocks (Hover-Granath et al., 1983). Although not the focus of this study, the argillite layers contain a complementary trend in metamorphic grade, albeit with different index minerals (Hover-Granath et al., 1983).

Fluid flow in the Notch Peak aureole

Because the metamorphic and thermal history of the Notch Peak contact metamorphic aureole is relatively well understood, considerable efforts have been undertaken to study its history of fluid flow and reaction sequence. Bulk δ^{18}O values for metalimestones are approximately constant throughout the aureole ($\delta^{18}O_{VSMOW} \approx$~20‰), while those of meta-argillite layers decrease from ~18‰ in unmetamorphosed sam-

ples towards values as low as 8‰ in high-grade samples (Nabelek et al., 1984). This observation has been cited as strong evidence for higher time-integrated water fluxes in argillite than in limestone layers, possibly facilitated by reaction-enhanced permeability due to the increased capacity of this lithology for reaction of carbonate with co-existing silicate (Cui et al., 2002; Nabelek, 2009; Nabelek et al., 1984). The highest-grade argillite layers (wollastonite-bearing assemblages) are highly variable in δ^{18}O, even at similar distances from the contact with the pluton, suggesting channelized fluid flow, and/or variations in mixing ratios of isotopically distinct magmatic and/or meteoric fluids. These findings, and the results from 2-D numerical models of thermal and fluid evolution in the aureole, have been cited as evidence for down-temperature fluid flow with a dominantly vertical component (i.e., up and away from the laccolith, perpendicular to bedding) (Nabelek, 2007; 2002; Nabelek et al., 1992). Although it has been argued that the distribution of whole-rock δ^{18}O within 500 m of the contact and the observed location of the diopside-in isograd are better explained by a model of up-temperature, horizontal fluid flow (Ferry and Dipple, 1992), such conclusions are inconsistent with the results of hydrodynamic models of fluid flux in metamorphic terranes (Ferry et al., 2013).

We focus on limestones and meta-limestones from a single cycle at the top of the Big Horse Limestone Member; here, uniform bulk δ^{18}O values are strong evidence that, regardless of direction, fluid flow was minimal, being concentrated into adjacent argillite beds and limestone horizons in immediate contact with them. We narrow our focus onto these rocks in order isolate the effects of lateral temperature variations on the clumped isotope systematics of contact metamorphic rocks, anticipating that in a subsequent study we will apply these insights to understanding the more complex meta-argillite layers, and differences in thermal history with depth in the vertical section.

2.4 Samples and methods

Samples

We examine the stable isotope, including clumped isotope, systematics of 60 aliquots (representing various phases and textures) from seven rock samples (Tables 2.2, 2.3). All but one (10H-107) are from the same limestone bed near the top of the Big Horse Limestone Member. The bed commonly outcrops as the top layer of a ~20 m cliff, and a distinctive ooid-rich layer marks its top. The mineral assemblages, textures, whole-rock stable isotope values, and Mg concentration in calcite for five of the seven samples were previously studied in (Hover-Granath et al., 1983; Hover, 1981;

Nabelek et al., 1984), and are representative of the unit at all metamorphic grades (from 0.01 to 5.36 km from the pluton contact). Two additional samples were collected by us in October 2012 to extend sampling below the talc-in isograd.

All seven samples contain minor dolomite. Dolomite/calcite ratios were measured by powder X-ray diffraction. Specifically, the relative heights of the strongest calcite and dolomite peaks (at 2-theta positions of 29.5 and 30.9, respectively) were compared to those of physical mixtures of calcite and dolomite standards, mixed in known proportions. Dolomite contents were all between 1.8 and 9.7% by weight.

Stepped phosphoric acid digestion

Clumped isotope analysis of carbonate is commonly performed by evolving CO_2 from bulk carbonate powder reacted with 104% phosphoric acid, either overnight at 25 °C in McCrea-style reaction vessels, or for less than an hour at 90 °C in a common acid bath (e.g., see methods of Passey et al., 2010). When these methods are applied to powdered samples containing both calcite and dolomite, the evolved CO_2 is a mixture from each of these components (though the room temperature extraction may leave some dolomite unreacted). To separately determine the $\delta^{13}C$, $\delta^{18}O$) and Δ_{47} of coexisting calcite and dolomite, we used a stepped reaction procedure, modified from the methods of Al-Aasm et al. (1990) and Guo (2009). First, all samples were ground to a fine powder and sifted to <106 μm to ensure a uniform grain size distribution. To obtain an isolated calcite-derived CO_2 fraction, ~15 mg of powder was reacted with 10 mL of 104% phosphoric acid in a glass vacuum reaction vessel immersed in a water bath equilibrated at 25 °C. For two hours, CO_2 evolved from the reaction was continuously frozen in liquid N_2 (LN2 hereafter) on an adjacent glass U-trap. This continuous freezing prevented a buildup of pressure in the reaction vessel headspace, which was observed to slow the reaction rate and keep evolved CO_2 in the acid solution. This CO_2 fraction was separated from co-condensing H_2O by cryogenic procedures, and was sealed in a Pyrex™ break-seal. Any CO_2 evolved after the two-hour mark was discarded. To obtain an isolated dolomite-derived CO_2 fraction, a mass of powder containing the equivalent of ~20 mg of dolomite (150 – 500 mg total powder for our samples) was reacted in a McCrea-style vessel with 10 mL of acid (McCrea, 1950). For the first 24 hours, the reaction, conducted at 25 °C, was left open to a vacuum line backed by a liquid N2 trap and a rough pump so that all CO_2 evolved during this step was removed and effectively none remained dissolved in the acid. At the end of 24 hours, the tube was evacuated using a mercury diffusion pump to baseline ($\sim 1 \times 10^{-2}$ Pa),

closed off, immersed in a water bath at 50 °C and allowed to continue reaction, evolving CO_2 for an additional 24 hours. All CO_2 produced during this second step was cryogenically purified and sealed in a Pyrex™ tube. Tests on standard powders demonstrated that no isotopic exchange between CO_2 and other oxygen reservoirs occurs when CO_2 is allowed to remain in the reaction vessel headspace for 24 hours at 50 °C.

It is well-established that the reaction of solid carbonate with anhydrous phosphoric acid to release CO_2, imparts an oxygen isotope fractionation between reacting carbonate and produced CO_2 that is phase-specific and temperature-dependent (Kim and O'Neil, 1997; Rosenbaum and Sheppard, 1986; Sharma and Clayton, 1965; Pn K Swart, Burns, and Leder, 1991). Raw $\delta^{18}O$ values of CO_2 evolved from calcite (at 25 °C) and dolomite (at 50 °C) were corrected using previously determined fractionation factors ($\alpha^{^{18}O}_{CO_2-\text{mineral}}$, where $\alpha^{^{18}O}_{a-b} = {}^{18}R_a/{}^{18}R_b$, and ${}^{18}R_a = [^{18}O]/[^{16}O]$ in phase a) of 1.01025 (Pn K Swart, Burns, and Leder, 1991) and 1.01038 (Rosenbaum and Sheppard, 1986), respectively. For digestion at 90 °C in an automated common acid bath system, we used fractionation factors of 1.00821 for calcite (Pn K Swart, Burns, and Leder, 1991) and 1.00922 for dolomite (based on a 2nd-order polynomial interpolation of 25, 50, and 100 °C data of Rosenbaum and Sheppard (1986)).

Based on the yields of tests on pure end-member standards, it was determined that 90% of calcite is digested in the first two hours at 25 °C and 10% in the following twenty-two. No calcite remains undigested after 24 hours at 25 °C, provided one continuously removes the headspace CO_2. Less than 1% of dolomite reacts in the first two hours, 30% over the first 24 hours at 25 °C, and 70% in the following 24 hours at 50 °C. Because nearly all samples in this study have less than 5% dolomite, any potential contribution of dolomite to the CO_2 evolved from calcite during the first two hours is negligible. Nevertheless, the small but measurable rate of dolomite reaction at 25 °C may be important for any future studies of rocks containing greater proportions of dolomite. The most significant source of potential experimental error introduced by this method is that each fraction we collect (i.e., nominally calcite or dolomite) contains only a portion of the CO_2 from that phase (the first ~90 % of the CO_2 from calcite and the last ~70 % of the CO_2 from dolomite).

The efficacy and accuracy of our stepped phosphoric acid digestion method was tested by applying it to known mixtures of calcite and dolomite standards with distinct, known $\delta^{13}C$, $\delta^{18}O$, and Δ_{47} values. After the appropriate oxygen isotope reaction fractionation corrections were applied (as described above), we observed

Mineral	$\alpha^{13}_{\text{fraction-complete}}$	α^{13} error	$\alpha^{18}_{\text{fraction-complete}}$	α^{18} error
Calcite	0.99999	0.00002	1.00036	0.00003
Dolomite	1.00019	0.00002	1.00026	0.00005

Table 2.1: Average ($n = 2 - 3$) fractionation factors for partial recovery of CO_2 from calcite and dolomite during stepped acid digestion procedure. Errors are 1σ standard errors of the fractionations, derived by propagating the standard errors of the replicate measurements of the partial recovery, and complete recovery methods. These measurements are in Table 2.9. Δ_{47} values of calcite and dolomite standards obtained using the stepped digestion procedure were indistinguishable from their unfractionated values outside of uncertainty, so no corrections were applied.

small but significant (<0.4‰ for $\delta^{18}O$, <0.2‰ for $\delta^{13}C$) discrepancies between the bulk isotope values of CO_2 from calcite and dolomite obtained using the stepped digestion method and those obtained by conventional online and offline reactions of the pure phases in the same analytical session (Table 2.9). We believe that these discrepancies are caused by kinetic fractionations during the phosphoric acid reaction that are expressed due to the incomplete retrieval of digested CO_2 in any one step. We corrected for this artifact, (i.e., to better reflect the values we would have observed if phosphoric acid digestion had been complete), based on the average $\delta^{13}C$ and $\delta^{18}O$ values of replicate measurements of mixtures of dolomite and calcite standards, using our stepped digestion procedure (Tables 2.1, 2.9). Δ_{47} values from mixed calcite and dolomite standards subject to offline stepped digestion procedure were indistinguishable within error from values for complete offline digestion of pure samples; therefore, no correction was applied to Δ_{47} values of calcite and dolomite measured using the stepped digestion procedure.

Stable isotope analysis of product CO_2

$\delta^{13}C$, $\delta^{18}O$, and Δ_{47} values for CO_2 produced from both offline stepped digestion in phosphoric acid and online bulk digestion in a common acid bath held at 90 °C were obtained using a Thermo 253 IRMS at Caltech following the methods outlined in Huntington et al. (2009), Passey, Levin, et al. (2010) and Dennis, Affek, et al. (2011). In brief, CO_2 was purified from contaminants using automated ethanol – CO_2 ice (~ -67 °C) and LN2 baths, and an online prep-GC system with a Porapak-Q 120/80 mesh column held at −20 °C. CO_2 voltages were measured at masses 44, 45, 46, 47, 48, and 49 and compared to a reference tank from Oztech in automatic dual inlet mode. Mass spectrometric nonlinearities were corrected for by observation of the dependence of Δ_{47} on bulk 47 for pure CO_2 equilibrated at 1000 °C. At least one

secondary carbonate standard was measured daily.

Carbonate Δ_{47} values were projected into the interlaboratory absolute reference frame (ARF) using a secondary transfer function determined by routine measurement of gases equilibrated at 1000 °C and 25 °C (Dennis, Affek, et al., 2011). Samples reacted online at 90 °C were corrected to the 25 °C-Δ_{47} scale using the acid fractionation factor of 0.092‰ (in the ARF). The Δ_{47} acid fractionation factor for dolomite reacted at 50 °C was determined by comparing the values obtained by offline digestion of an in-house pure dolomite standard to the average value of that standard when reacted on-line at 90 °C (for the same measurement sessions) and with the 0.092‰ correction applied. Based on the average of 5 offline standard dolomite digestions, a 50 °C acid fractionation factor of 0.040‰ was used to correct all dolomite samples to the 25 °C scale (Table 2.10). This value is nearly identical to that that predicted for calcite analyzed at 50 °C (Ghosh et al., 2006), and is in agreement, within uncertainty, with the 50 °C fractionation factor experimentally determined for a variety of carbonate phases, including dolomite, by Defliese, Hren, and Lohmann (2015). Our correction is 0.030‰ smaller than that determined for a variety of dolomites, including the same reference standard used by Defliese, Hren, and Lohmann (2015), by Murray, Arienzo, and Peter K Swart (2016). Given the agreement between the Δ_{47}– T relationships of dolomite and calcite measured in our lab using both the common acid bath technique at 90 °C and sealed vessels at 25 °C (c.f., Fig. 3 in Stolper and J M Eiler (2015)), it seems clear to us that the large discrepancy in phosphoric acid fractionation factor between calcite and dolomite observed by Murray, Arienzo, and Peter K Swart (2016) must not apply to our analytical setup.

The relationship between Δ_{47} and temperature has been the subject of several studies, with some disagreement (e.g., Ghosh et al. (2006), Grauel et al. (2013), Kluge et al. (2015), and Zaarur, Affek, and Brandon (2013)). The calibration is particularly poorly understood at high temperature, where calibration datasets are few, and small differences in Δ_{47} can amount to predicted temperature differences of many tens of degrees (Bonifacie et al., 2011; Kluge et al., 2015; Passey and Henkes, 2012; Stolper and J M Eiler, 2015). Much of the disagreement appears to result from interlaboratory methodological differences, possibly due to different acid digestion techniques or correction schemes for mass spectrometric artifacts (i.e., calibrations are generally coherent within labs but differ in temperature sensitivity between some labs). To minimize potential errors that interlaboratory discrepancies may introduce,

we used a high-temperature calibration based on a dataset of synthetic calcites and dolomites grown at known temperatures and measured at Caltech on the same instrument as the data of this study: $\Delta_{47,\mathrm{ARF}} = 0.001083 \times (10^6/\mathrm{T}^2)^2 + 0.02854 \times (10^6/\mathrm{T}^2) + 0.25865$, where T is in Kelvin. This is a second-order polynomial fit in Δ_{47} vs. 1/T2-space to the data of Ghosh et al. (2006), Guo et al. (2009), Bonifacie et al. (2011), and Stolper and J M Eiler (2015). Most of these data were generated before 25°C-equilibrated gases were routinely measured for correction to the absolute reference frame. Therefore, these data were projected into the absolute reference frame using a 1st-order linear least-squares fit ($r^2 = 1.00$) of accepted values of carbonate standards and 1000°C-equilibrated gases in the internal laboratory and absolute reference frames (i.e., the average secondary transfer function for this specific instrument; Dennis, Affek, et al. (2011)). We note that much of our interpretation of the following results rely on differences in Δ_{47} values (or lack thereof) among metamorphic grades and between phases, rather than the exact temperatures these values suggest.

2.5 Results

Sample	Dist (km)	X_{dol}	n (Bulk, Cal, Dol)	Cal (tot) $\delta^{13}C$ (‰)	Cal (tot) $\delta^{13}C$ error (‰)	Cal (tot) $\delta^{18}O$ (‰)	Cal (tot) $\delta^{18}O$ error (‰)	Dol $\delta^{13}C$ (‰)	Dol $\delta^{13}C$ error (‰)	Dol $\delta^{18}O$ (‰)	Dol $\delta^{18}O$ error (‰)	$T_{13\alpha}$ (°C)	$T_{18\alpha}$ (°C)	T_{model} (°C)	$T_{X_{Mg}}$ (°C)	$T_{X_{Mg}}$ error (°C)
10H-107	0.09	0.018	3, 4, 2	-0.211	0.013	-10.428	0.048	0.215	0.003	-9.926	0.037	566	408	575		
3H-38a	0.15	0.033	9, 3, 3	0.737	0.009	-10.24	0.033	1.116	0.011	-9.958	0.025	657	537	550	495	17
20H-99	0.58*	0.097	2, 3, 2	0.748	0.009	-9.811	0.049	1.482	0.006	-8.998	0.014	292	299	420	445	11
11H-116	1.88	0.057	6, 1, 4	0.937	0.042	-9.982	0.088	1.662	0.021	-9.443	0.029	297	392	300	248	32
12-NPK-11b	2.63	0.032	2, 1, 2	0.597	0.006	-9.945	0.046	1.46	0.003	-8.962	0.015	237	258	220		
12-NPK-5	4.01	0.03	2, 3, 2	0.692	0.016	-9.755	0.027	1.855	0.008	-8.522	0.02	153	211	170		
12H-122	5.36	0.033	4, 1, 1	0.738	0.043	-10.14	0.131	2.38	0.05	-8.588	0.1	45	166	160		

Table 2.2: Average values of $\delta^{13}C$ and $\delta^{18}O$ in calcite and dolomite. Reported calcite values (calcite, total) are the unweighted mean of all individual offline calcite digestions and online bulk digestions with the dolomite $\delta^{13}C$ and $\delta^{18}O$ contributions removed (see Methods section for details). Errors are 1σ standard errors of the mean of multiple analyses, or the 1σ typical external reproducibility for offline digestion where only one replicate was used (0.05‰ and 0.1‰ for $\delta^{13}C$ and $\delta^{18}O$, respectively; individual measurements available in the electronic annex). Oxygen-18 and carbon-13 equilibrium fractionation temperatures are calculated using the equations of Horita (2014) and Sheppard and Schwarcz (1970), respectively. Model peak temperatures are from the distance–T relation of John M Ferry and Dipple (1992), except for sample 12H-122, which is beyond 4 km, where the 4th-order equation is no longer valid. Here, peak temperature was estimated based on the burial depth of the unit and a reasonable upper crustal geotherm (see section 2.6). Actual distance of sample 20H-99 (*) is 0.23 km, however this rock is from a different set of outcrops (in Contact Canyon) than the rest of the sample suite, where isograds are compressed. To more accurately compare sample 20H-99 to the others, it was projected to the distance it would lie at along the main transect in North Canyon

Sample	Distance (km)	n (Bulk, Cal, Dol)	Bulk Δ_{47} (‰)	Bulk Δ_{47} error (‰)	Cal Δ_{47} (‰)	Cal Δ_{47} error (‰)	Cal Δ_{47} (total) (‰)	Cal Δ_{47} error (‰)	Dol Δ_{47} (‰)	Dol Δ_{47} error (‰)	$T_{\Delta_{47},cal}$ (°C)($\pm 1\sigma$)	$T_{\Delta_{47},dol}$ (°C)($\pm 1\sigma$)
10H-107	0.09	3, 4, 2	0.453	0.009	0.451	0.027	0.452	0.015	0.351	0.005	150^{+15}_{-13}	313^{+15}_{-14}
3H-38a	0.15	9, 3, 3	0.443	0.005	0.444	0.02	0.446	0.006	0.34	0.006	156^{+6}_{-6}	348^{+22}_{-20}
20H-99	0.58*	2, 3, 2	0.426	0.005	0.42	0.02	0.426	0.012	0.341	0.01	177^{+15}_{-13}	344^{+38}_{-31}
11H-116	1.88	6, 1, 4	0.453	0.011	0.43	0.014	0.456	0.011	0.359	0.013	146^{+10}_{-10}	291^{+37}_{-30}
12-NPK-11b	2.63	2, 1, 2	0.469	0.007	0.465	0.013	0.467	0.005	0.458	0.007	137^{+4}_{-4}	144^{+6}_{-6}
12-NPK-5	4.01	2, 3, 2	0.44	0.011	0.434	0.013	0.435	0.009	0.402	0.004	167^{+10}_{-9}	208^{+6}_{-6}
12H-122	5.36	4, 1, 1	0.475	0.013	0.445	0.01	0.467	0.011	0.439	0.016	137^{+10}_{-9}	163^{+18}_{-16}

Table 2.3: Average Δ_{47} values of online bulk powder measurements, and offline calcite, dolomite digestions. Total calcite values were obtained by averaging all offline measurements of calcite fractions and online bulk measurements with the dolomite contribution removed (see Methods section for details). Errors in bulk, calcite, total calcite, and dolomite Δ_{47} values are 1σ standard errors of the mean of multiple analyses, or 1σ measurement errors where only one replicate was used. The Δ_{47}–temperature calibration is based on a second-order polynomial fit in Δ_{47} vs. $1/T^2$-space to the data of Ghosh et al. (2006), Guo et al. (2009), Bonifacie et al. (2011), and Stolper and J M Eiler (2015) (see Methods for details). Actual distance of sample 20H-99 (*) is 0.23 km, however this rock is from a different set of outcrops (in Contact Canyon) than the rest of the sample suite, where isograds are compressed. To more accurately compare sample 20H-99 to the others, it was projected to the distance it would lie at along the main transect in North Canyon.

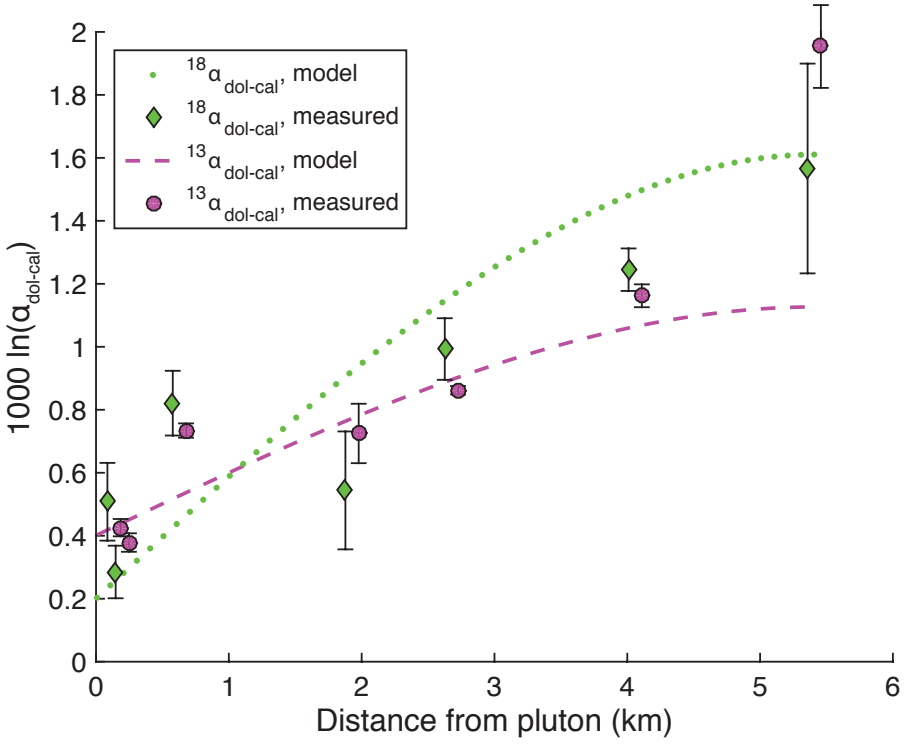

Figure 2.4: Assessment of the accuracy of the bulk δ^{13}C and δ^{18}O exchange thermometers. Measured dolomite – calcite fractionations are compared to those predicted from equilibrium crystallization at the temperatures predicted by published thermal models of the Big Horse Ls Member (Table 2.2). Errors are 2σ standard errors, generated by propagation of mean dolomite and calcite δ^{13}C or δ^{18}O errors, assuming dolomite and calcite measurements are uncorrelated (not strictly true, see Methods section). Equilibrium temperature-bulk isotope relationships for carbon-13 and oxygen-18 are derived from Sheppard and Schwarcz (1970) and Horita (2014), respectively.

We made a total of 32 measurements of calcite or dolomite extractions from seven samples using the offline stepped digestion technique. We also made 28 measurements of mixed samples of calcite and dolomite using the online common acid bath technique. The exact proportion of each carbonate phase was determined in each sample using the yields of calcite and dolomite from offline extractions, assuming that only 90% of all calcite present is reacted in the first step and 70% of all dolomite in the second (see Section 2.4 for details on how these yields, and associated corrections for the resulting fractionation, were determined). Calcite δ^{13}C, δ^{18}O, and Δ_{47} values for each online, common acid bath analysis were then determined by subtracting out the contribution of each of these values from the offline dolomite measurements of that sample, assuming calcite and dolomite contribute to the on-

line common acid bath measurement in their measured proportions. Obviously this method could potentially introduce further errors because of some variability in the yields of carbonate phases during the partial digestions and uncertainty in the bulk isotope correction factors associated with these reactions. Moreover, errors in the calcite composition from each online measurement would be slightly correlated with errors in dolomite δ^{13}C, δ^{18}O, and Δ_{47} because the dolomite composition must be subtracted out. However, because dolomite is less than 10% (modal) of all samples, and in most cases less than 5%, these corrections were small (< 0.01‰ for Δ_{47}, which is less than the 1σ error of measurement), and any correlation would be undetectable. Because stable isotope indices have non-linear dependence on proportions of end members in mixtures, these mixing calculations were made using concentrations of individual isotopologues and then converted to δ or Δ_{47} values. All 60 raw analyses are shown in Tables 2.5, 2.6, and 2.7. Mean Δ_{47} values for each phase in each sample were obtained by calculating an error-weighted average of all replicates ($n = 2 - 9$) using the equation $\Sigma_{i=1}^{n} \frac{1}{\sigma_i^2} \Delta_{47,i} / \Sigma_{i=1}^{n} \frac{1}{\sigma_i^2}$, where σ_i is the analytical standard error of each measurement. Reported uncertainty of each weighted mean is the standard deviation of all replicates divided by $\sqrt{n}$, where n is the number or replicates. The mean δ^{13}C, δ^{18}O, and weighted mean Δ_{47} values for each phase in each sample are reported in Tables 2.2 and 2.3.

Bulk δ^{13}C and δ^{18}O values from this study agree with published isotopic measurements of the same samples to within 0.27‰ (Nabelek et al., 1984; Table 2.2). Values of δ^{13}C and δ^{18}O for calcite are relatively constant at all distances in the aureole (Table 2.2). Calcite δ^{18}O (VPDB) ranges between –10.5 and –9.7‰, with no relation between oxygen isotopic composition and metamorphic grade. Except for sample 10H-107, which was taken from a different bed in the Big Horse Limestone Member than the other seven, all calcite δ^{13}C (VPDB) values fall between 0.6 and 1.0‰, again with no apparent trend with metamorphic grade. The slight variation in bulk δ^{13}C and δ^{18}O between beds in the unit is consistent with previous studies of the unit (Nabelek et al., 1984). Dolomite δ^{13}C and δ^{18}O values are heavier than the respective values for calcite at the same location, by between 0.4 and 2‰ (Fig. 2.4). In general, dolomite δ^{13}C and δ^{18}O decrease with increasing metamorphic grade (Table 2.2).

Dolomite Δ_{47} values are roughly bimodal (Table 2.3). All samples within 2 km of the contact between limestone and pluton have Δ_{47} values between 0.340 and 0.360‰ (statistically indistinguishable from one another, within error). In contrast,

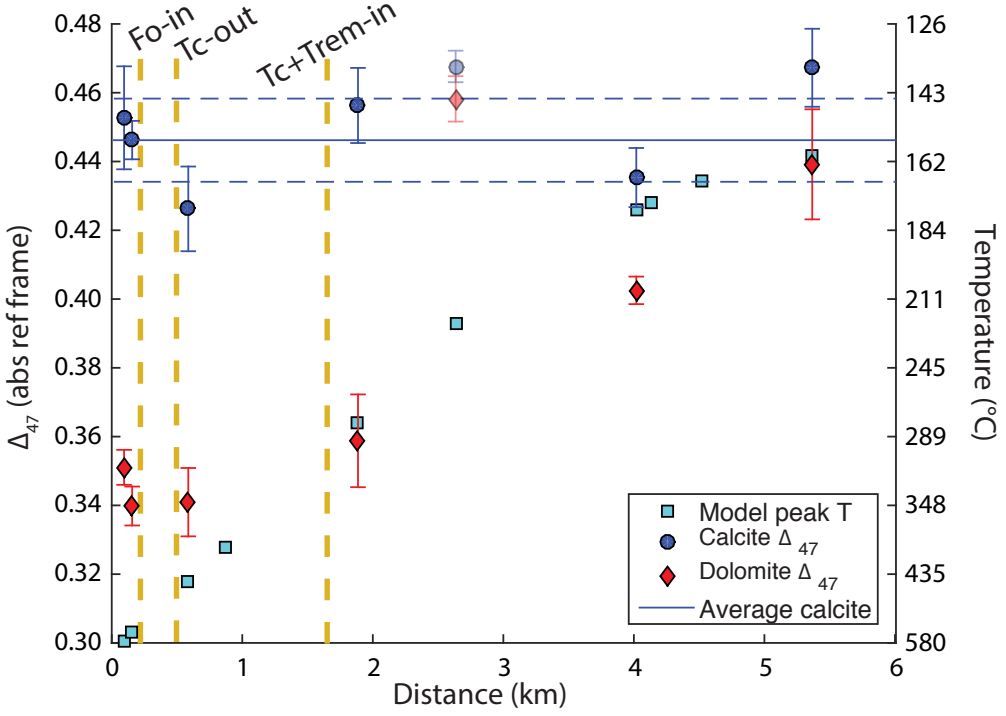

Figure 2.5: Δ_{47} values for calcite and dolomite in the Notch Peak aureole. Errors on individual points are 1σ standard errors of the weighted average of replicates. Blue line is the weighted average of all calcite Δ_{47} measurements in the aureole, with dashed lines denoting the 2σ error envelope on this value. Model peak T values are derived from the equations in John M Ferry and Dipple (1992) and Theodore C Labotka, Peter I Nabelek, and Papike (1988). Dashed gold lines denote the approximate locations of the main metamorphic isograds in the unit. Semitransparent points at 2.63 km are for sample 12–NPK–11b, where abundant secondary cross-cutting carbonate veining has overprinted the primary dolomite and calcite temperature signals (See section 2.6 for details).

dolomite in the three samples further than 2 km from the contact have Δ_{47} values ranging between 0.402 and 0.458. Calcite Δ_{47} values are all between 0.426 and 0.467‰, with no apparent trend vs. distance from the contact. All calcite Δ_{47} values are statistically indistinguishable from each other, within the errors on each set of replicate measurements (Fig. 2.5).

2.6 Discussion

δ^{13}C and δ^{18}O thermometry of the Notch Peak Aureole

Values of δ^{13}C and δ^{18}O in calcite generally vary little (<0.9‰) between individual hand samples, with no systematic changes with distance from the pluton. The one

exception, sample 10H-107, is from a different bed than the other seven samples, ~100 m lower in the Big Horse Limestone Member, and prior study of the formation suggests that this is likely just a reflection of original stratigraphic variations (P I Nabelek et al., 1984). Dolomite δ^{13}C and δ^{18}O values, on the other hand, decrease by as much as much as 2.1 and 1.4‰, respectively, from unmetamorphosed limestones to Fo-bearing marbles. Because whole-rock isotopic composition can vary subtly among rocks from the same stratigraphic unit, we focus on the carbon-13 and oxygen-18 fractionation between coexisting calcite and dolomite in order to study the isotopic effects due solely to metamorphic reactions. We find a positive correlation between $\alpha^{^{13}\mathrm{C}}_{\mathrm{dol-cal}}$ ($\alpha^{^{13}\mathrm{C}}_{\mathrm{dol-cal}} = {}^{13}R_{\mathrm{dolomite}}/{}^{13}R_{\mathrm{calcite}}$, where ${}^{13}R_{\mathrm{mineral}} = [{}^{13}\mathrm{C}]/[{}^{12}\mathrm{C}]$ in a given mineral) and distance to the pluton (Fig. 2.4). Similar behavior is suggested in oxygen isotope partitioning, but cannot be resolved in the high-grade samples outside of uncertainty (Fig. 2.4). All samples are rock-buffered, have no evidence of metasomatism, and have small dolomite/calcite ratios. As a result, the observed fractionations are largely controlled by the isotopic composition of dolomite in each sample. At least three processes can alter dolomite δ^{13}C and δ^{18}O values: decarbonation reactions, new dolomite growth during prograde metamorphism, and low temperature exchange with a hydrothermal fluid, either before metamorphism (i.e., diagenesis) or after. Dolomite recrystallization by grain coarsening also occurs during metamorphic events; this process modifies Δ_{47}. but should not alter δ^{13}C and δ^{18}O values unless it occurs in the presence of another phase that is exchangeable at the conditions of grain coarsening. It is likely that all three of these processes affected the studied samples to some extent, so the observed signal should not be attributed to exclusively one cause. Nevertheless, it is worth considering which is the primary control on the isotopic composition of dolomite across a metamorphic gradient, as this constrains the source and timing of dolomite formation in these samples.

Low-temperature alteration: one possible explanation of our findings is that dolomite in all samples was produced by infiltration of an Mg-bearing fluid during epigenesis prior to, or low-temperature recrystallization subsequent to, contact metamorphism. Indeed, this process must have occurred to produce dolomite in sample 12H-122, which was >5 km from the pluton contact and fully insulated from the metamorphic event. If this were true for all samples, the δ^{13}C and δ^{18}O values of dolomite in this case might be expected to be influenced both by host calcite and the dolomitizing fluid, and likely out of equilibrium with calcite. Given that calcite δ^{13}C does not correlate with distance or metamorphic grade, the trend between dolomite – calcite

δ^{13}C fractionation and grade would thus be entirely coincidental.

This interpretation also is not supported by the textures of these samples. Diagenetic dolomite in sample 12H-122 (unmetamorphosed) occurs as fine-grained (~50 – 400 μm) rhombs replacing calcite in echinoids and peloids (Hover, 1981). In Fo-bearing high-grade marbles, however, coarse-grained (300 – 600 μm) dolomite has a granoblastic texture (Hover, 1981). Dolomite is a minor, scattered phase in the Big Horse Limestone Member, so the textural contrast between these rocks cannot be explained by grain coarsening alone. Rather, it suggests that while diagenetic dolomite was initially present in the bed, this was lost in contact metamorphosed samples, probably due to both dolomite-consuming reactions and high-temperature growth and grain coarsening. Thus, it seems reasonable to expect that δ^{13}C values were set during metamorphism, and there is no obvious evidence for retrograde or diagenetic modification of dolomite subsequent to metamorphism.

Calcite – dolomite stable isotope equilibrium: A second possibility is that trends in the δ^{13}C and δ^{18}O values of dolomite represent equilibrium inter-mineral fractionations between dolomite and calcite, which are established during dolomite growth at or near peak metamorphic conditions. Because the peak temperatures at all grades in the Notch Peak aureole are at or below the apparent equilibrium blocking temperatures for intercrystalline oxygen and carbon isotope diffusion in a quickly-cooled contact aureole (~600 – 800 °C, dependent on grain size, cooling rate, and f_{H_2O}, Fig. 2.1), we expect the intermineral isotope thermometers to behave as case-1, above; i.e., they should faithfully record the temperature of equilibrium mineral crystallization (Sec. 2.2). We tested this prediction by comparing the temperatures given by these fractionations to peak temperatures in the unit at different distances, as calculated by published thermal models of the Notch Peak aureole (which are themselves made to be consistent with the phase equilibria determinations from the contact aureole). For this analysis, the empirical calibration of carbon-13 dolomite-calcite partitioning of Sheppard and Schwarcz (1970) and the experimentally-derived oxygen-18 calibration of Horita (2014) were used. The temperature profiles of John M Ferry and Dipple (1992) and Theodore C Labotka, Peter I Nabelek, and Papike (1988) were used to estimate peak temperatures at all distances in the aureole. Following the convention of previous workers, reported distances are map distances to the pluton contact; true distances are smaller because the contact with the laccolithic pluton dips below the carbonate sequence (Theodore C Labotka, Peter I Nabelek, and Papike, 1988). Even so, given its position in the

exposed, intruded section (>0.5 km above the base, Fig. 2.3), this discrepancy is likely insignificant.

With the exception of low-grade sample 20H-99, carbon-13-based temperatures largely agree with modeled peak temperatures within 3 km of the contact (Fig. 2.4). There is good reason to question the robustness of this finding: this temperature proxy is insensitive in this temperature range, and thus has particularly large errors in the highest-grade samples. Even so, the positive trend between dolomite – calcite carbon-13 fractionation and distance to the contact (i.e., smallest fractionations closest to the pluton) agrees with expectations, suggesting a dependence on peak temperature has been resolved. If this is the case, the anomalously large fractionation in sample 20H-99 may indicate that dolomite last crystallized from calcite during metamorphism somewhat below peak conditions in the sample. Large uncertainties in δ^{18}O fractionations obscure any trends within the metamorphosed samples. Even so, all metamorphosed samples have lower calcite – dolomite fractionations of δ^{18}O values than the most distal unmetamorphosed samples.

We consider it possible that some of the variation in C and O isotope distributions among carbonate phases reflects not only analytical errors but also disturbance of high temperature equilibrium by post-metamorphic isotopic redistributions. For instance, retrograde exsolution of dolomite from high-Mg calcite during cooling is a well-documented phenomenon; this can affect the accuracy of both bulk isotope fractionations (Wada and Suzuki, 1983), and the calcite – dolomite Mg-solvus thermometer (Müller et al., 2008). Indeed, fine exsolution lamellae of dolomite within calcite have been observed in the highest-grade sample in this study (10H-107; Hover Granath, Papike, and T C Labotka (1983)), which may explain some scatter—assuming our offline stepped digestion measurements succeeded at separating dolomite lamellae from host calcite. We also have not characterized the degree of grain-scale heterogeneity in stable isotope ratios of our samples, although it likely exists at some level (John M Ferry, Ushikubo, et al., 2010). Nevertheless, calcite – dolomite oxygen and carbon isotope fractionations are generally consistent with dolomite growth at or near peak temperatures in these samples. In the forsterite-bearing samples, the likely cause of this growth is the quartz-absent, tremolite-forming reaction: talc + calcite = tremolite + dolomite + H_2O + CO_2 (Hover Granath, Papike, and T C Labotka, 1983).

Outside the talc + tremolite-in isograd, the correlations between calcite – dolomite stable isotope fractionations and distance are more robust. This is somewhat surpris-

ing given that the rhombohedral dolomite replacing carbonate clasts was previously interpreted to have a uniformly diagenetic origin in samples 12H-122 and 11H-116 (Hover, 1981). If these decreasing fractionations do represent dolomite crystallization at increasing temperatures, it would suggest that prograde dolomite growth from reaction of calcite occurred at anchimetamorphic conditions (i.e., below ~350 °C but above the ambient burial temperature of the unit) by a reaction that did not involve silicate phases.

Decarbonation reactions: At 150 MPa and moderate X_{CO_2} values, talc, tremolite, diopside, and forsterite are produced by decarbonation reactions involving dolomite and a silicate phase (c.f. Fig. 7 in Müller et al. (2008) and P I Nabelek (2002)). The presence of these Mg-bearing silicate phases in the metamorphosed samples of the present study indicates that some amount of decarbonation must have occurred. The CO_2 – dolomite equilibrium oxygen isotope fractionation varies between ~5 and 7‰ at the temperatures of metamorphism in the Notch Peak aureole (O'Neil and Epstein, 1966), so it is conceivable that decarbonation could drive residual dolomite to lower $\delta^{18}O$ (Bottinga, 1968; Shieh and Taylor Jr, 1969; Taylor and O'Neil, 1977; Wada and Suzuki, 1983). For example, the observed $\delta^{18}O$ of dolomite in the highest grade Notch Peak marbles can be explained by a model that assumes a starting $\delta^{18}O_{VPDB}$ of –8.6‰ (equivalent to the dolomite in unmetamorphosed sample 12H-122), a CO_2 – dolomite fractionation (α^{18O}) given by: $1000\ln(\alpha^{18O}) = 5$ (the approximate equilibrium CO_2 – dolomite fractionation at 600 °C ((Chacko and Deines, 2008; O'Neil and Epstein, 1966) it is less clear what should happen if the fractionation is kinetically controlled), and ~25% progress of dolomite decarbonation following the Rayleigh fractionation law ($^{18}R = {}^{18}R_0 \times F^{\alpha-1}$, where F is the fraction of material remaining, ^{18}R is the oxygen isotope ratio of the remaining material, and $^{18}R_0$ is the initial ratio). This calculation assumes that the oxygen-bearing products of dolomite decarbonation do not exchange with the residue once generated, which is valid because temperatures throughout the aureole are too low for C or O-isotope exchange between dolomite and coexisting phases unless exchange is facilitated by recrystallization (e.g., Bergfeld et al., 2003). The carbon isotope effect of dolomite decarbonation has not been measured directly, but it can be estimated by dividing the CO_2 – calcite carbon-13 fractionation by the equilibrium dolomite – calcite carbon-13 fractionation: $1000\ln(\alpha^{13C}_{CO_2-dol}) \approx 3$ at 400 – 600 °C (Bottinga, 1968; Bottinga, 1969; Sheppard and Schwarcz, 1970; Peter I Nabelek, 1991; Chacko, Mayeda, et al., 1991). Again, using this fractionation and an initial $\delta^{13}C$ of 2.4‰ (the carbon isotopic composition of dolomite in sample 12H-122), the $\delta^{13}C$ of dolomite in the

highest-grade samples can be generated with ~35% decarbonation.

The question is, are the effects of decarbonation recorded by dolomite, or were those effects erased by equilibration of dolomite with co-existing phases through grain coarsening or other mechanisms? Decarbonation seems likely to be the primary control of stable isotope variations only in samples that preserve textures consistent with dolomite-consuming reactions. Dolomite in the highly metamorphosed samples we examined is generally coarse-grained and granoblastic, suggesting grain growth rather than loss by decarbonation. We conclude that some dolomite decarbonation must have occurred near peak metamorphic conditions in order to produce forsterite, but that dolomite fabrics suggest any resulting stable isotope effects of this reaction are unlikely to have been preserved. It is also worth noting that this reaction is inferred to have consumed only a minor amount of the dolomite present (Hover Granath, Papike, and T C Labotka, 1983).

Low-grade sample 20H-99, on the other hand, has strong textural evidence for dolomite decarbonation by the reaction: dolomite + quartz + $H_2O \rightarrow$ calcite + talc + CO_2 (Hover Granath, Papike, and T C Labotka, 1983). The sample contains talc and 2nd-generation, coarse-grained, hornfelsic calcite. Dolomite has a sub- to anhedral habit, unlike in more distal samples where it is rhombohedral (Hover, 1981). Despite the availability of bulk rock chemistry for the sample (Hover, 1981), the extent of dolomite decarbonation cannot be calculated directly without knowledge of the initial molar amounts of dolomite, quartz, feldspars, and clay minerals. However, using the isotopic composition of dolomite in sample 12H-122 as an initial value, Rayleigh models for $\delta^{13}C$ and $\delta^{18}O$ predict reaction progress of ~25% and ~10%, respectively (see above for calculation details). The disagreement between the two isotope systems could have many causes, including incorrect starting compositions due to natural bulk rock variation (Table 2.2), inaccurate isotope fractionation factors for the decarbonation process, and isotopic zoning at the grain reaction front that was not measured in this study. Given these uncertainties, we simply conclude that the observed isotopic variation is consistent with such a mechanism.

All samples more than 1.6 km from the pluton contact are nominally unmetamorphosed (i.e., not talc-bearing), yet have resolvable differences in their dolomite – calcite isotopic fractionations that increase with distance. These samples cannot have undergone the lowest-temperature metamorphic decarbonation reaction observed in sample 20H-99, and we are not aware of any other decarbonation reaction that plausibly could have influenced their dolomite stable isotope compositions.

In summary, isotopic fractionations and textures in high-grade samples are most consistent with prograde dolomite growth in apparent equilibrium with calcite, even though some decarbonation and retrograde exsolution must have occurred. Dolomite in nominally unmetamorphosed samples was previously determined to be of diagenetic origin, but the trend in isotopic fractionations requires that dolomite growth occurred under anchimetamorphic conditions, when the local temperature was elevated due to the presence of the pluton (though no other metamorphic minerals were produced). The texture and isotopic composition of dolomite in the low-grade talc-bearing sample are consistent with decarbonation of an originally-diagenetic endmember, although if dolomite in more distal samples has a metamorphic origin, it is possible that it does in sample 20H-99 as well.

Dolomite Δ_{47} values

Much of the uncertainty in the preceding section regarding the origin of dolomite in the Notch Peak aureole can be addressed by considering the constraint imposed by dolomite Δ_{47} measurements. Unlike δ^{13}C and δ^{18}O values, dolomite Δ_{47} values can be reset by several mechanisms (solid state diffusion, heterogeneous reaction, and grain coarsening recrystallization), they are independent of bulk rock isotopic composition, and can be measured at a precision that is useful for comparison with independent determinations of peak metamorphic temperatures.

Apparent equilibrium blocking temperatures in high-grade marbles: Based on the arguments and data presented in section 2.2, we expect that the Δ_{47} value of dolomite in and near the Notch Peak aureole will have an apparent equilibrium blocking temperature above the ambient temperature (i.e., the crustal temperature far from the pluton) but below the peak temperature in the metamorphic aureole, and thus that it will behave as our case-2 geothermometer. We observe that the Δ_{47} values of dolomites are indistinguishable in all samples inside the talc + tremolite-in isograd, with a weighted mean value that implies an apparent temperature of 328^{+13}_{-12} °C (1σ std error) (Fig. 2.5). This result closely resembles other measurements of dolomite marbles, which have been interpreted as apparent equilibrium blocking temperatures limited by intracrystalline atomic mobility (J M Ferry et al. (2011); Table 2.8). Therefore, we interpret the Δ_{47} values of dolomite inside the talc + tremolite-in isograd as the apparent equilibrium blocking temperatures of atomic re-arrangements during cooling from peak metamorphic temperatures. We cannot assess the effects of dolomite decarbonation or exsolution from calcite on Δ_{47} values because any such effect that occurred above the apparent equilibrium blocking

temperature would have been obscured by solid state reordering during cooling. In fact, the uniform temperature of ~330 °C from dolomite Δ_{47} in all metamorphosed samples confirms that no retrograde dolomite modification occurred below this temperature.

This result is unsurprising given other studies of exsolution and retrograde isotopic exchange in calc-silicate contact metamorphic rocks. Metamorphism of such rocks is generally brief and drives off volatiles, lowering reaction rates; therefore, pervasive retrograde recrystallization long after peak conditions is rare (Cathles, Erendi, and Barrie, 1997; S J Cook, J R Bowman, and Forster, 1997). For instance, in the Alta aureole in northern Utah, homogeneous calcite δ^{18}O and low calcite – dolomite X_{Mg} temperatures have been argued to indicate that carbonate recrystallization occurred, but only down to the temperature range of 500 – 550 °C, which is ~50 °C below peak conditions (John R Bowman, Valley, and Kita, 2008; S J Cook, J R Bowman, and Forster, 1997; Stephen J Cook and John R Bowman, 1994). When late-stage recrystallization, exsolution, or isotopic exchange does occur, it is often because of exceptional conditions, such as multiple intrusive events, that produce polymetamorphism or a prolonged elevated temperature (e.g., John R Bowman, Valley, and Kita (2008) and Lackey and Valley (2004). For these reasons, we think that the conditions of metamorphism in marbles in the Big Horse Limestone member (dry, short-lived), and the preservation of near-equilibrium calcite – dolomite isotopic fractionations, support our interpretation that dolomite Δ_{47} values were set by intracrystalline isotopic redistribution rather than exsolution or some other heterogeneous reaction.

Peak temperatures in the outer aureole: The John M Ferry and Dipple (1992) and P I Nabelek et al. (1984) thermal models of the Notch Peak aureole suggest that a peak temperature of 330 °C occurs at a map distance of ~1.7 km from the contact with the pluton. In samples beyond this distance, dolomite should behave as a normal case-1 geothermometer and faithfully record the temperature of dolomite crystallization—i.e., either a diagenetic or burial metamorphic temperature, or perhaps a temperature corresponding to the peak reached by the cool, outer portions of the aureole (if that thermal pulse was associated with dolomite crystallization). Beginning with sample 11H-116 at a distance from the pluton of 1.9 km, we observe a trend of decreasing dolomite $T_{\Delta 47}$ with increasing distance from the pluton that is largely consistent with thermal models of peak temperatures in the outer parts of the Notch Peak aureole (excluding sample 12-NPK-11b, see below), terminating with a value

indistinguishable from the estimated background temperature (i.e., outside of any influence from the pluton) at 5.4 km map distance to the contact. This is strong evidence for dolomite crystallization in response to heating from the intrusion. Moreover, the complementary lowering of dolomite $\delta^{13}C$ and $\delta^{18}O$ values suggests that this was not just recrystallization of diagenetic dolomite. Instead, it is likely that some dolomite crystallized through exchange with a local, rock-buffered fluid, such that the higher-temperature anchimetamorphic sample (11H-116) inherited a $\delta^{13}C$ and $\delta^{18}O$ composition closer to coexisting calcite than a lower-temperature sample (12-NPK-5) further from the intrusion. To our knowledge, this is the first time the thermal structure of a sub-greenschist grade metamorphic belt has been mapped with clumped isotopes. The variations in peak temperature recorded by Δ_{47} values of dolomite in this part of the aureole are otherwise cryptic; i.e., they are not documented by evidence preserved by mineral phase assemblages or textures.

Sample 12-NPK-11b is an exception to the pattern of dolomite Δ_{47} values described above. In this rock, abundant cm-scale cross-cutting secondary carbonate veining, and agreement between dolomite and calcite Δ_{47} thermometers, suggest that dolomite (along with calcite, see below) grew or recrystallized long after cooling from the peak temperatures reached in response to nearby intrusion, and prior to exhumation in the Miocene Epoch. We have omitted this sample from our discussion of peak metamorphism and cooling, as it seems obvious to us that it has been subject to a secondary process that disturbed the clumped isotope systematics. Curiously, the $\delta^{13}C$ and $\delta^{18}O$ fractionations between dolomite and calcite are still consistent with the predicted peak temperature reached by the sample, implying that recrystallization of dolomite occurred in a rock-buffered system.

Calcite Δ_{47} temperatures

Calcite Δ_{47} values are indistinguishable from each other, with an error-weighted mean of 0.446 ± 0.012 (2σ std. errors), which corresponds to an apparent temperature of 156 ± 12 °C. This temperature is generally consistent with the expected ambient temperature in the system far from the intrusion, given 6.2 – 6.5 km of overburden at the time of intrusion and a typical continental upper-crustal geotherm. However, two observations make this result unexpected: the apparent equilibrium temperature everywhere in the aureole, including its strongly metamorphosed inner regions, is modestly but significantly less than the apparent equilibrium blocking temperatures expected for slowly cooled calcite or observed apparent temperatures in common regional metamorphic marbles (John M Eiler, 2011; Henkes et al., 2014;

Passey and Henkes, 2012; Stolper and J M Eiler, 2015). Also, calcite was expected to exhibit a case-2 thermometer behavior, like dolomite (Fig. 2.1). However, calcite apparent temperatures are statistically uniform across our sample suite, with no gradient with increasing distance from the pluton contact. We show below that these two observations place significant new constraints on the geotherm and exhumation history of the crustal section intruded by the Notch Peak pluton.

Before we develop a thermal model based on these data, it is worth considering whether uniform calcite Δ_{47} values simply represent the temperature of some broad recrystallization event rather than a diffusion-limited, intracrystalline reordering process. The petrographic evidence does not support the former interpretation. Calcite grain size coarsens with metamorphic grade, and the ~300 – 600 μm, granoblastic textures in the highest-grade marble are unmistakably distinct from the finer-grained carbonate clasts with relict sedimentary textures in samples below but near the talc + tremolite-in isograd (Hover Granath, Papike, and T C Labotka, 1983). If all samples were partially or completely recrystallized, these textural distinctions would be obscured. For this reason, we suggest that the uniform calcite Δ_{47} temperature of 156 ± 12 °C reflects intracrystalline atomic mobility during the temperature – time history of the aureole after intrusion and metamorphism.

A thermal model for calcite Δ_{47} reordering in a contact aureole

Parameter	Value	Units	Description	Source
T_0	1173	K	initial monzonite temperature	Nabelek (2009)
dT/dz	0.025	K/m	geothermal gradient in limestones	Nabelek (2009)
ρ_l	2700	kg/m^3	density of limestone	Ahrens (1995)
ρ_m	2700	kg/m^3	density of monzonite	Ahrens (1995)
A_l	0.3	μW/m^3	radiogenic heat production of limestone	Wollenberg (1987)
A_m	0.7	μW/m^3	radiogenic heat production of monzonite	Wollenberg (1987)
Thermal diffusivity equation $\kappa = 0.534 + 5.017 \times e^{-T/222.1}$				

Table 2.4: Description of the values used to numerically solve the thermal diffusion equation in the model Notch Peak aureole.

We explore this possibility using a 2-D thermal model of the Notch Peak pluton and surrounding country rock. The geometry and numerical grid spacing of the model replicate that of P I Nabelek (2009) for the same pluton: the model was 20 km wide by 8 km deep, with grid spacing at 50 m. It was initialized with a

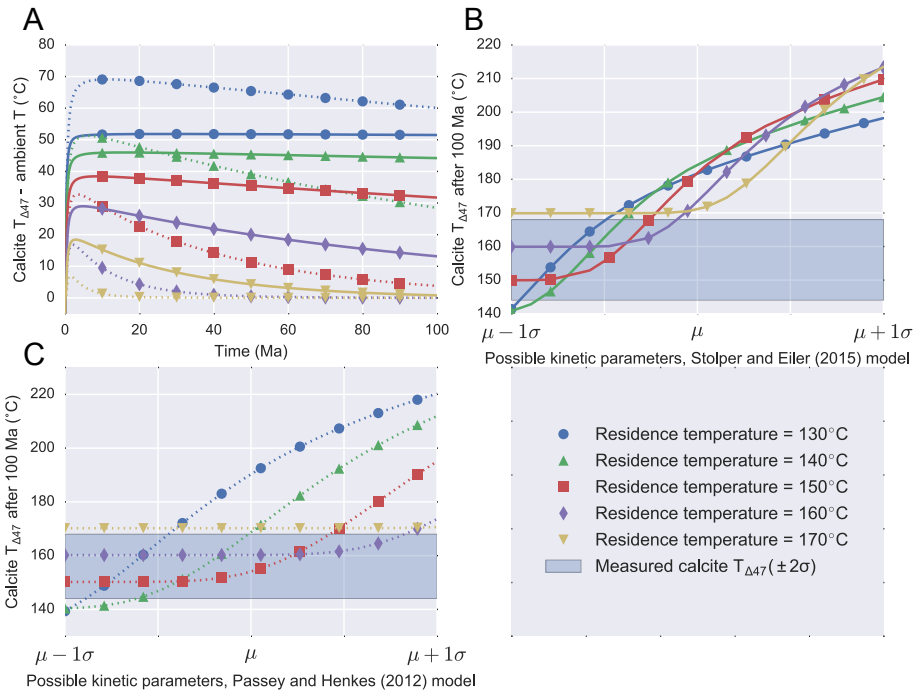

Figure 2.6: Models for calcite Δ_{47} reordering during cooling in the aureole of the Notch Peak pluton. Calcite apparent equilibrium temperatures approach the ambient temperature of the system during the 100 Ma after intrusion, but whether full re-equilibration occurs depends on the residence temperature and the reordering model used (A). Solid lines were generated using the exchange-diffusion model of Stolper and J M Eiler (2015), and dotted lines using the first-order approximation model for optical calcite from Passey and Henkes (2012). Arrhenian parameters were varied by up to 1σ of their reported values and uncertainties to examine the sensitivity of final calcite Δ_{47} temperature to the exact rate constants used (B, C). Symbols are included for clarity, and do not necessarily represent locations where calculations were performed.

laccolithic pluton 6 km wide and up to 2 km tall at the center, with a uniform initial temperature of 900 °C. Initial conditions in the host rock were determined by a geothermal gradient of 25 °C/km, beginning at 75 °C at 3 km depth. Values for densities and radiogenic heat production terms in the monzonite and limestone are given in Table 2.4. Because of the significant dependence of thermal diffusivity and heat capacity on temperature (Whittington, Hofmeister, and Peter I Nabelek, 2009), these parameters were recalculated at every node for every time step. A finite-difference scheme was used to solve the thermal diffusion equation, plus the radiogenic heat production, in each 50m x 50m square, in one-year steps. Initial tests on a simple 1-D heat pulse of a similar scale demonstrated that this finite difference

model accurately reproduced the analytical solution to this system. We accounted for the latent heat of crystallization using an apparent heat capacity term for the cooling pluton: $c^*_{\text{app}} = c_{\text{mag}} + \Delta H/\Delta\text{T}$, where the latent heat of fusion (ΔH = 246.5 J/g) is added over the temperature interval of crystallization (900 – 600 °C), and the magmatic heat capacity (c_{mag}) is the average of the crystalline and liquid granitic heat capacities (at the appropriate temperature), weighted by the fraction of melt remaining, assuming a linear increase in the amount of crystallization with drop in temperature (Peter I Nabelek, Hofmeister, and Whittington, 2012). This results in an apparent thermal diffusivity term, $\kappa^* = \kappa/(\rho c^*)$, which increases the rate at which heat diffuses out of the pluton and into the limestone until the monzonite is fully crystallized at 600 °C (Peter I Nabelek, Hofmeister, and Whittington, 2012).

Our model makes several simplifying assumptions: the latent heat is released evenly over the prescribed temperature range; we do not account for heat transport by advective/convective fluid flow; and we do not consider the dependence of density on temperature, the contrasting fluid histories of interbedded limestone and argillite layers, or the state changes accompanying metamorphism in the inner aureole. We argue, however, that this model is sufficient for our purposes because 1) the metalimestone layers of the Big Horse Limestone Member demonstrably experienced relatively little magmatic fluid infiltration, and 2) calcite clumped isotope apparent equilibrium blocking temperatures are only sensitive to the T – t path in the realm of approximately 125 – 300 °C. It is not necessary to accurately capture the fluid-controlled and reaction-controlled heat distribution in the early stages of metamorphism because these mechanisms do not significantly affect the bulk heat content of the system, especially in the limestones during late-stage cooling, when these mechanisms are no longer active.

The thermal model was run for 10 Ma. The T – t paths (in 1 year increments) at the positions of the studied samples were recorded. To explore the conditions under which the metamorphic apparent equilibrium blocking temperature signal can be completely lost to post-metamorphic, diffusion-limited reordering, we predicted the change in calcite Δ_{47} throughout the Notch Peak cooling history using both the calcite clumped isotope exchange – diffusion reordering model of Stolper and J M Eiler (2015) and the first order reordering model of Passey and Henkes (2012). Because the former model requires a functional form of T(t) to simultaneously solve the ordinary differential equations for the exchange and diffusion kinetic parameters, we fit our model T – t paths to a version of the asymptotic cooling function of Ghose

and Ganguly (1982): $T = a/((1 + \frac{t+b}{c})) + d$, where a represents the theoretical peak temperature at $t + b = 0$, b is the temporal offset term used to obtain the actual peak temperature at $t = 0$, c is the cooling timescale, and d is the ambient temperature of the system. We initialized the models such that at time $t = 0$, calcite Δ_{47} was in equilibrium with the peak temperature of the system. This could be achieved either by crystallization of calcite at peak conditions, or rapid diffusion-limited reordering to peak (or near-peak) conditions during the first few thousands of years. In every sample within 3 km of the contact, calcite clumped isotope reordering is rapid enough at $t = 0$ that this condition is easily met. The peak temperature in this zone is also well above that at which Henkes et al. (2014) observed the decay of a rapid reordering component, which they attribute to the annealing of transient defects in the calcite crystal lattice. Therefore, it is sufficient to use their first-order approximation model, which considers only equilibrium, intrinsic defects. Following the convention of these workers, we use the kinetic parameters for optical calcite, as this material is most similar to the marbles in our system (i.e., we used the model of Passey and Henkes (2012)). Preliminary runs of both reordering models demonstrated that calcite clumped isotopes remain in equilibrium with cooling temperatures until ~350 °C. Since samples within the metamorphic aureole have similar cooling paths at and below 350 °C, a uniform T-t function can be used to model calcite Δ_{47} reordering in all samples within the mineralogically-defined metamorphic aureole.

Calcite Δ_{47} apparent equilibrium temperatures at the end of these runs were independent of peak temperature, and insensitive to late-stage cooling timescale (within the constraints on this parameter suggested by our 2-D thermal model), so the only realistically modifiable parameter is the long-term incubation temperature of the limestone bed (i.e., the ambient temperature at this depth, far from the influence of the pluton). To examine the sensitivity of the calcite Δ_{47} reordering process to residence temperature, we varied the ambient temperature of the system between 130 and 170 °C, while keeping all other T(t) fit parameters constant (specifically, $a = 1079$ °C, $b = 2.05 \times 10^4$ years, $c = 1.84 \times 10^4$ years in above equation). Calcite Δ_{47} reordering models were run for 100 Ma. Based on the overlying stratigraphic section, it is suggested that the depth of the studied bed (and, as a result, the ambient temperature of it) remained constant from the time of intrusion (~145 Ma; P. Nabelek et al. (1988)) until exhumation in the Miocene Epoch, allowing for at least 100 Ma of residence at the ambient temperature of the system for Δ_{47} reordering prior to quenching during exhumation (Hintze and Davis, 2002; Hover Granath,

Papike, and T C Labotka, 1983). Calcite Δ_{47} reordering models for a similar Paleozoic Era sedimentary section in southeastern Nevada by Shenton et al. (2015) demonstrate that Basin and Range exhumation does quench this thermometer.

The essential criterion for evaluating these models is: under which conditions does calcite Δ_{47} fully equilibrate with the long term residence temperature, thereby erasing the difference in Δ_{47} between high grade metamorphic calcite close to the pluton and diagenetic calcite far from it? The difference between calcite Δ_{47} temperature and ambient (i.e., equilibrium) temperature as a function time was considered for a range of residence temperatures (Fig. 2.6). With the Stolper and J M Eiler (2015) model, calcite Δ_{47} fully equilibrates with a residence temperature of 170 °C, but only if given a full 100 Ma to do so. At residence temperatures of 160 °C and below, calcite Δ_{47} approaches but does not reach equilibrium, whereby a difference between high grade and unmetamorphosed calcite Δ_{47} is preserved. These models suggest that the observation of uniform calcite Δ_{47} temperatures of 156 ± 12 °C (2σ std. errors) is only possible if the true residence temperature was at the upper end of this range. In the Passey and Henkes (2012) model, full re-equilibration occurs for all residence temperatures above 150 °C (Fig. 2.6). Thus, using the kinetic parameters for optical calcite from Passey and Henkes (2012), our measurements are compatible with a large range of acceptable residence temperatures.

Both sets of kinetic parameters are derived from linear regressions of Arrhenius plots with considerable uncertainty, especially when extrapolated to the temperatures of interest for this study. To explore the sensitivity of these models to the exact rate constants used, we varied the activation energies and natural log of the frequency factors by adding or subtracting up to 1σ uncertainty from their mean values. It is not immediately apparent how to generate families of likely kinetic parameters by perturbing these values within their reported uncertainties because their covariance matrices are not reported. For the Passey and Henkes (2012) model, we assumed that the populations of possible values for the activation energy and natural log of the frequency factor are perfectly anti-correlated, so$E_a$and lnK_0 were varied in conjunction by the same proportion of their 1σ uncertainty. This approach minimizes the change in the rate constants at the temperatures of interest, and is the most conservative estimate of the actual uncertainty on the linear regression; the true 1σ uncertainty envelope of the rate constants is likely larger. For the Stolper and J M Eiler (2015) model, we varied the Arrhenian parameters for the diffusion of singles in this same way, while leaving the rate constants for isotopic exchange

among pairs unmodified. Because diffusion of singles is the rate-limiting step at the temperatures of interest, we observed that reasonable modifications of the Arrhenian parameters for isotope exchange among pairs had no effect on the model results.

The calcite Δ_{47} temperatures at the end of our 100 Ma T-t path are extremely sensitive to the kinetic parameters chosen (Fig. 2.6). For the same residence temperature, final calcite Δ_{47} can range from fully equilibrated in the $\mu - 1\sigma$ models (i.e., lower activation energy and frequency factor, and a higher rate constant at the temperature of interest), to as much as 65 °C above thermal equilibrium in the $\mu + 1\sigma$ models (i.e., extrapolation of higher activation energy and frequency factor leading to slower reordering below ~300 °C). These results hold for both models (Figs. 2.6). Comparison with the measured calcite Δ_{47} temperature of the bed indicates that while most sets of likely kinetic parameters for the Passey and Henkes (2012) model are compatible with our measurements over a wide range of residence temperatures, only iterations of the Stolper and J M Eiler (2015) model at the lower end of the 1σ uncertainty envelopes on the activation energy and natural log of the frequency factor for diffusion of singles can reproduce the observed result. In addition, the final difference between calcite apparent equilibrium temperature and residence temperature is sensitive to the exact residence temperature of the system. Using our temperature calibration and the most likely calcite reordering models, a marble incubated at 150 °C should fully re-equilibrate on the measured timescale (i.e., behave as a case-3 thermometer), while a marble held at 140 °C will retain an apparent equilibrium temperature of 170 °C (case-2 behavior). This has the intriguing implication that along a vertical transect of high-grade marbles in a contact aureole one would expect to observe an inverted temperature profile: hottest apparent equilibrium temperatures at the shallowest depth due to incomplete re-equilibration, and colder apparent equilibrium temperatures with increasing structural depth (Figs. 2.6). Our dataset does not have the geometry to speak to the existence of this peculiar feature, but perhaps future studies will.

Our model fit to the observed distribution of calcite Δ_{47} values offers new constraints on the geologic history of the region surrounding the Notch Peak aureole. Barring heating by additional burial under a late-Mesozoic or Cenozoic unit that has since been completely eroded at a previously-unrecognized unconformity, our models indicate that the Big Horse Limestone Member can't have been exhumed much before the Miocene Epoch, else the difference in Δ_{47} values that must have existed between high-grade and unmetamorphosed calcites at the peak of metamorphism would have

been preserved. Moreover, assuming the estimate of overlying sediment thickness of 6.2 – 6.5 km from Hover Granath, Papike, and T C Labotka (1983) is correct, this result provides a tight constraint on the local geotherm; even when expanding the range of acceptable ambient temperatures to 145 – 170 °C (to allow for some error on the Δ_{47}– temperature calibration), the Cenozoic upper crustal geotherm must have been between 22.3 and 27.4 °C/km. This range is typical for the shallow crust in passive continental interiors (Nathenson and Guffanti, 1988), but significantly lower than the modern borehole-derived thermal gradients in the area surrounding Notch Peak (greater than 30 °C/km, often much greater; Blackett (2004)). This observation is consistent with the transition to the Basin and Range extensional regime in the Miocene Epoch, where crustal thinning increased local heat flow and steepened thermal gradients. Accurate slopes and, especially, shapes of paleo-geothermal gradients, are essential in order to properly estimate denudation/erosion rates in low-temperature thermochronometric studies (e.g., Dempster and Persano (2006)). Although our 1-D study cannot constrain the shape of the paleo-geotherm, it demonstrates the potential of multiple-phase clumped isotope techniques to address such problems.

2.7 Conclusions

Even in rocks as simple as two-phase dolomite-bearing limestones, four stable isotope geothermometers are available to determine the thermal histories of metamorphic events. Because these four thermometers have different re-equilibration behaviors in response to changing conditions, they record distinct aspects of the cooling history of a sample, and collectively impose surprisingly nuanced constraints on temperature – time history. In the Notch Peak aureole, UT, $\alpha^{^{13}\mathrm{C}}_{\mathrm{dol-cal}}$ and $\alpha^{^{18}\mathrm{O}}_{\mathrm{dol-cal}}$ fractionations from coexisting calcite and dolomite correlate with distance to the intruded pluton, indicating relatively rapid cooling and minimal modification subsequent to peak conditions. Within 4 km to the contact, temperatures in equilibrium with the $\alpha^{^{13}\mathrm{C}}_{\mathrm{dol-cal}}$ fractionations largely agree with those expected from thermal models of the aureole, but large uncertainties on the measurements preclude their use as precise indicators of crystallization temperature. At greater distances, the disagreement between $\alpha^{^{13}\mathrm{C}}_{\mathrm{dol-cal}}$ and $\alpha^{^{18}\mathrm{O}}_{\mathrm{dol-cal}}$ fractionation temperatures is an indication of diagenetic dolomite growth out of isotopic equilibrium with coexisting calcite. Notably, this result implies that metamorphic recrystallization in response to the thermal pulse occurred in rocks beyond, but near, the talc + tremolite-in isograd and the nominal onset of metamorphism. Dolomite Δ_{47} values record ap-

parent equilibrium blocking temperatures in the inner metamorphic aureole and peak temperatures in the outer aureole. The interface between the two maps the location of the ~330 °C isograd, and thus metamorphic grades below the onset of easily recognized greenschist-facies metamorphism can be distinguished. Calcite Δ_{47} values are constant across the entire range of studied samples, which requires complete reordering down to the ambient temperature of the system following the metamorphic event. We use multiple calcite Δ_{47} reordering models to show that not only is this behavior consistent with cooling history of the aureole, it constrains the exact incubation temperature of the unit throughout the late Mesozoic and Cenozoic Eras. Together, the two clumped isotope thermometers suggest that the unit was held at 145 – 170 °C for at least ~100 Ma until exhumation in the Miocene Epoch.

2.8 Supplementary data tables

Sample	Dist. to contact (km)	$\delta^{13}C$ (VPDB) (‰)	$\delta^{13}C$ (error) (‰)	$\delta^{18}O$ (VPDB) (‰)	$\delta^{18}O$ (error) (‰)	Δ_{47} (‰)	Δ_{47} error (‰)	T (Δ_{47}, °C)	X_{dol}	Mineral assemblage (+Cc-Do)
10H-107	0.09	-0.273	0.003	-10.341	0.005	0.52	0.01	99.7	0.018	Tr-Di-Phl-Gr
10H-107	0.09	-0.188	0.004	-10.417	0.005	0.392	0.011	223.8	0.018	Tr-Di-Phl-Gr
10H-107	0.09	-0.187	0.003	-10.373	0.006	0.438	0.012	163.6	0.018	Tr-Di-Phl-Gr
10H-107	0.09	-0.194	0.004	-10.62	0.006	0.428	0.013	174.6	0.018	Tr-Di-Phl-Gr
3H-38A	0.15	0.698	0.004	-10.023	0.006	0.489	0.01	119.7	0.033	Qz-Tr-Fo-Chl-Pl-(Tc)-Gr
3H-38A	0.15	0.705	0.004	-10.328	0.009	0.437	0.011	164.7	0.033	Qz-Tr-Fo-Chl-Pl-(Tc)-Gr
3H-38A	0.15	0.695	0.003	-10.402	0.003	0.425	0.007	178	0.033	Qz-Tr-Fo-Chl-Pl-(Tc)-Gr
20H-99	0.23	0.784	0.003	-9.669	0.002	0.452	0.009	149.8	0.097	Qz-Tc-Tr-Pl-Gr
20H-99	0.23	0.75	0.003	-9.922	0.007	0.394	0.015	220.5	0.097	Qz-Tc-Tr-Pl-Gr
20H-99	0.23	0.731	0.004	-9.92	0.004	0.391	0.011	225.4	0.097	Qz-Tc-Tr-Pl-Gr
11H-116	1.88	1.184	0.002	-9.545	0.003	0.43	0.014	172.3	0.057	Qz-Chl-Phl-Pl-Gr
12-NPK-11b	2.63	0.609	0.003	-10.037	0.01	0.465	0.013	138.3	0.032	Qz-Chl-Gr
12-NPK-5	4.01	0.704	0.003	-9.722	0.009	0.406	0.01	202.4	0.03	Qz-Chl-Gr
12-NPK-5	4.01	0.719	0.003	-9.678	0.006	0.433	0.005	169	0.03	Qz-Chl-Gr
12-NPK-5	4.01	0.722	0.001	-9.778	0.003	0.451	0.007	150.8	0.03	Qz-Chl-Gr
12H-122	5.36	0.773	0.002	-9.825	0.003	0.445	0.01	156.5	0.033	Qz-Chl-Pl-Kfs-Gr

Table 2.5: Individual measurements of calcite clumped isotopes using the offline stepped acid digestion procedure.

Sample	δ^{13}C (VPDB) (‰)	δ^{13}C (error) (‰)	δ^{18}O (VPDB) (‰)	δ^{18}O (error) (‰)	Δ_{47} (‰)	Δ_{47} error (‰)	T (Δ_{47}, °C)
10H-107	0.218	0.002	-9.963	0.004	0.356	0.009	298.8
10H-107	0.212	0.002	-9.889	0.004	0.346	0.009	327.7
3H-38A	1.096	0.005	-9.996	0.01	0.328	0.011	395.1
3H-38A	1.135	0.005	-9.911	0.02	0.345	0.009	330.9
3H-38A	1.116	0.005	-9.968	0.014	0.346	0.015	327.7
20H-99	1.476	0.003	-9.012	0.004	0.326	0.011	404.2
20H-99	1.489	0.002	-8.983	0.004	0.346	0.007	327.7
11H-116	1.6	0.003	-9.408	0.007	0.386	0.008	234
11H-116	1.688	0.002	-9.504	0.004	0.323	0.009	418.7
11H-116	1.674	0.003	-9.478	0.004	0.363	0.008	281.2
11H-116	1.687	0.003	-9.383	0.003	0.342	0.012	340.8
12-NPK-11b	1.463	0.005	-8.977	0.008	0.467	0.014	136.7
12-NPK-11b	1.457	0.005	-8.947	0.009	0.453	0.01	148.9
12-NPK-5	1.846	0.003	-8.542	0.003	0.4	0.009	211.2
12-NPK-5	1.863	0.005	-8.502	0.006	0.408	0.016	199.6
12H-122	2.695	0.003	-8.588	0.008	0.439	0.016	162.6

Table 2.6: Individual measurements of dolomite clumped isotopes using the offline stepped acid digestion procedure.

Sample	δ^{13}C (VPDB) (‰)	δ^{13}C (error) (‰)	δ^{18}O (VPDB) (‰)	δ^{18}O (error) (‰)	Δ_{47} (‰)	Δ_{47} error (‰)	T (Δ_{47}, °C)
10H-107	-0.167	0.002	-10.228	0.003	0.447	0.011	154.6
10H-107	-0.234	0.004	-10.504	0.01	0.47	0.014	134.2
10H-107	-0.208	0.004	-10.49	0.01	0.442	0.016	159.5
3H-38A	0.778	0.008	-10.225	0.012	0.459	0.012	143.5
3H-38A	0.772	0.007	-10.209	0.008	0.443	0.008	158.5
3H-38A	0.763	0.007	-10.223	0.011	0.445	0.01	156.5
3H-38A	0.749	0.005	-10.349	0.01	0.431	0.011	171.2
3H-38A	0.787	0.012	-10.263	0.004	0.456	0.012	146.2
3H-38A	0.791	0.003	-10.153	0.002	0.434	0.011	167.9
3H-38A	0.764	0.002	-10.067	0.009	0.428	0.013	174.6
3H-38A	0.751	0.006	-10.225	0.02	0.417	0.016	187.8
3H-38A	0.705	0.003	-10.33	0.008	0.452	0.007	149.8
20H-99	0.808	0.002	-9.699	0.002	0.421	0.012	182.8
20H-99	0.811	0.002	-9.693	0.003	0.43	0.01	172.3
11H-116	0.921	0.008	-10.173	0.008	0.493	0.012	116.9
11H-116	0.903	0.009	-10.203	0.01	0.476	0.014	129.4
11H-116	0.936	0.005	-9.967	0.006	0.431	0.01	171.2
11H-116	0.936	0.002	-9.987	0.006	0.475	0.014	130.2
11H-116	0.968	0.002	-9.908	0.006	0.446	0.016	155.6
11H-116	0.97	0.001	-9.882	0.003	0.428	0.011	174.6
12-NPK-11b	0.619	0.006	-9.875	0.006	0.464	0.015	139.2
12-NPK-11b	0.619	0.005	-9.864	0.011	0.477	0.018	128.6
12-NPK-5	0.714	0.002	-9.725	0.007	0.429	0.011	173.4
12-NPK-5	0.671	0.003	-9.798	0.008	0.452	0.012	149.8
12H-122	0.849	0.009	-10.009	0.016	0.491	0.009	118.3
12H-122	0.848	0.009	-10.038	0.016	0.472	0.012	132.6
12H-122	0.636	0.002	-10.557	0.004	0.473	0.013	131.8
12H-122	0.842	0.004	-10.057	0.021	0.43	0.016	172.3

Table 2.7: Individual clumped isotope measurements of bulk powders using an online common acid bath (mixed calcite and dolomite).

Sample	δ^{13}C (VPDB) (‰)	δ^{13}C (error) (‰)	δ^{18}O (VPDB) (‰)	δ^{18}O (error) (‰)	Δ_{47} (‰)	Δ_{47} error (‰)	T (Δ_{47}, °C)
Gabbs-17	-5.893	0.011	-15.514	0.011	0.346	0.009	327.7
Gabbs-17	-5.931	0.011	-15.522	0.01	0.332	0.007	377.9
ML-INYO	-0.558	0.007	-7.522	0.006	0.33	0.011	386.3
ML-INYO	-0.576	0.003	-7.508	0.006	0.316	0.005	457

Table 2.8: Individual clumped isotope measurements of two high-grade dolomite marbles from the Western US. Gabbs-17 is a massive, buff, crystalline dolomite marble from Gabbs, NV, that was regionally metamorphosed as part of Tertiary fold and thrust belt, with additional contact metamorphism due to intrusion of granitic plutons (Humphrey and Wyatt, 1958; Cathles, Erendi, and Barrie, 1997). ML-INYO is a white, crystalline dolomite marble from Inyo Range, CA regionally metamorphosed due to burial beneath ∼10 km of section Cambrian and younger (Nelson, 1962). Gabbs-17 is part of the Caltech Working Mineral Collection, sampler unknown. ML-INYO was collected by G.R. Rossman.

Method	Sample	δ^{13}C (‰)	δ^{13}C (error) (‰)	δ^{18}O (‰)	δ^{18}O (error) (‰)	Δ_{47} (‰)	Δ_{47} error (‰)
Calcite, online	Carrara marble	2.114	0.005	-2.152	0.01	0.411	0.014
		2.06	0.005	-2.261	0.026	0.404	0.01
		2.108	0.003	-2.155	0.013	0.42	0.01
		2.101	0.006	-2.167	0.023	0.405	0.009
		2.095	0.004	-2.196	0.013	0.446	0.01
		2.033	0.004	-2.301	0.01	0.433	0.009
		2.098	0.005	-2.174	0.012	0.436	0.017
		2.108	0.005	-2.155	0.01	0.423	0.015
Calcite offline: 0-2 hrs at 25 °C	Carrara mable + SS07 dolomite	2.064	0.002	-1.863	0.005	0.446	0.01
		2.097	0.004	-1.814	0.008	0.417	0.015
Dolomite online	SS07 dolomite	7.525	0.003	-2.31	0.014	0.598	0.013
		7.535	0.004	-2.27	0.011	0.597	0.012
		7.539	0.002	-2.247	0.024	0.6	0.012
Dolomite offline: 24-48 hrs at 50 °C	Carrara mable + SS07 dolomite	7.722	0.003	-2.025	0.016	0.6	0.015
		7.729	0.004	-2.065	0.01	0.602	0.012
		7.737	0.006	-1.972	0.012	0.622	0.014

Table 2.9: Individual measurements of the calcite standard Carrara marble, an in-house dolomite standard (SS-07), and mixtures of the two subjected to the stepped extraction procedure described in section 2.4 of the main text. Offline extractions of calcite or dolomite from mixtures of the standards were only compared to online (i.e., common acid bath) measurements of pure phases from the same analytical session in order to minimize the effect of instrumental drift on δ^{13}C and δ^{18}O values. For these offline extractions, the two standards were mixed in proportions comparable to those observed in the natural samples(i.e., X_{dolomite} values of $0.02 - 0.1$ by moles).

References

Anderson, T F (1972). "Self-diffusion of carbon and oxygen in dolomite". In: *Journal of Geophysical Research* 77, pp. 857–862.

Blackett, R E (2004). "Geothermal gradient data for Utah". In: *Geothermal Resources Council Transactions*.

Bonifacie, Magali et al. (2011). "Calibration and applications of the dolomite clumped isotope thermometer to high temperatures". In: *Mineralogical Magazine* 75.3, p. 551.

Bottinga, Yan (1968). "Calculation of fractionation factors for carbon and oxygen isotopic exchange in the system calcite-carbon dioxide-water". In: *The Journal of Physical Chemistry* 72.3, pp. 800–808.

– (1969). "Calculated fractionation factors for carbon and hydrogen isotope exchange in the system calcite-carbon dioxide-graphite-methane-hydrogen-water vapor". In: 33.1, pp. 49–64.

Rxn T (°C)	Measurement session	δ^{13}C (‰)	δ^{13}C (error) (‰)	δ^{18}O (‰)	δ^{18}O (error) (‰)	Δ_{47} (‰), no acid corr	Δ_{47} (‰), acid corr	Δ_{47} error (‰)
90	Apr-13	7.286	0.006	-1.696	0.014	0.506	0.598	0.012
90	Apr-13	7.376	0.013	-1.566	0.011	0.54	0.632	0.009
90	Apr-13	7.29	0.009	-1.685	0.016	0.519	0.611	0.014
90	Apr-13	7.351	0.009	-1.671	0.018	0.514	0.606	0.011
90	Apr-13	7.365	0.007	-1.632	0.011	0.53	0.622	0.018
90	Apr-13	7.266	0.007	-1.881	0.018	0.506	0.598	0.008
90	Apr-13	7.264	0.004	-1.831	0.007	0.511	0.603	0.006
90	May-13	7.28	0.005	-1.794	0.007	0.534	0.626	0.009
90	May-13	7.208	0.004	-1.938	0.007	0.521	0.613	0.008
90	Jul-13	7.525	0.002	-2.31	0.005	0.506	0.598	0.01
90	Jul-13	7.535	0.003	-2.27	0.004	0.505	0.597	0.009
90	Jul-13	7.539	0.003	-2.247	0.003	0.508	0.6	0.01
50	Jul-13	7.613	0.003	-2.065	0.007	0.577	0.617	0.016
50	Jul-13	7.612	0.004	-2.004	0.005	0.572	0.612	0.015
50	Oct-13	8.167	0.002	-1.327	0.004	0.562	0.602	0.011
50	Oct-13	8.182	0.003	-1.306	0.002	0.563	0.603	0.011

Table 2.10: Individual measurements used to determine the Δ_{47} acid digestion fractionation of dolomite when reacted at 50 °C in McCrea (1950)-style vessels, by comparison with the mean Δ_{47} value of the same standard (SS07) when reacted by the common acid bath technique at 90 °C. With an acid digestion fractionation correction of 0.040‰, the mean of the offline 50 °C measurements agrees with the mean of the online 90 °C measurements (with the accepted fractionation correction of 0.092‰).

Bowman, John R, John W Valley, and Noriko T Kita (2008). "Mechanisms of oxygen isotopic exchange and isotopic evolution of 18O/16O-depleted periclase zone marbles in the Alta aureole, Utah: insights from ion microprobe analysis of calcite". In: *Contributions to Mineralogy and Petrology* 157.1, pp. 77–93.

Bristow, Thomas F et al. (2011). "A hydrothermal origin for isotopically anomalous cap dolostone cements from south China". In: *Nature* 474.7349, pp. 68–71.

Cathles, Larry M, A H J Erendi, and T Barrie (1997). "How long can a hydrothermal system be sustained by a single intrusive event?" In: *Economic Geology* 92.7-8, pp. 766–771.

Chacko, Thomas and Peter Deines (2008). "Theoretical calculation of oxygen isotope fractionation factors in carbonate systems". In: 72.15, pp. 3642–3660.

Chacko, Thomas, Toshiko K Mayeda, et al. (1991). "Oxygen and carbon isotope fractionations between CO 2 and calcite". In: 55.10, pp. 2867–2882.

Cook, S J, J R Bowman, and C B Forster (1997). "Contact metamorphism surrounding the Alta stock: Finite element model simulation of heat- and 18O/16O mass-transport during prograde metamorphism". In: *American Journal of Science* 297.1.

Cook, Stephen J and John R Bowman (1994). "Contact metamorphism surrounding the Alta stock; thermal constraints and evidence of advective heat transport from calcite+ dolomite geothermometry". In: *American Mineralogist* 79.5-6, pp. 513–525.

Dale, Annabel et al. (2014). "Time-capsure concretions: Unlocking burial diagaenetic processes in the Mancos Shale using carbonate clumped isotopes". In: *Earth and Planetary Science Letters* 394.C, pp. 30–37.

Defliese, William F, Michael T Hren, and Kyger C Lohmann (2015). "Compositional and temperature effects of phosphoric acid fractionation on Δ47 analysis and implications for discrepant calibrations". In: *Chemical Geology* 396, pp. 51–60.

Deines, Peter (2004). "Carbon isotope effects in carbonate systems". In: 68.12, pp. 2659–2679.

Dempster, T J and C Persano (2006). "Low-temperature thermochronology: Resolving geotherm shapes or denudation histories?" In: *Geology* 34.2, pp. 73–76.

Dennis, Kate J, Hagit P Affek, et al. (2011). "Defining an absolute reference frame for 'clumped' isotope studies of CO2". In: *Geochimica et Cosmochimica Acta VL - IS - SP - EP - PY - T2* - 75.22, pp. 7117–7131.

Dennis, Kate J and Daniel P Schrag (2010). "Clumped isotope thermometry of carbonatites as an indicator of diagenetic alteration". In: *Geochimica et Cosmochimica Acta VL - IS - SP - EP - PY - T2* - 74.14, pp. 4110–4122.

Eiler, John M (2007). ""Clumped-isotope" geochemistry—The study of naturally-occurring, multiply-substituted isotopologues". In: *Earth and Planetary Science Letters* 262.3–4, pp. 309–327.

– (2011). "Paleoclimate reconstruction using carbonate clumped isotope thermometry". In: *Quaternary Science Reviews* 30.25-26, pp. 3575–3588.

– (2013). "The Isotopic Anatomies of Molecules and Minerals". In: *Annual Review of Earth and Planetary Sciences* 41.1, pp. 411–441.

Eiler, John M and Edwin Schauble (2004). "18O13C16O in Earth's atmosphere". In: *Geochimica et Cosmochimica Acta* 68.23, pp. 4767–4777.

Epstein, Samuel et al. (1953). "Revised carbonate-water isotopic temperature scale". In: *Geological Society of America Bulletin* 64.11, p. 1315.

Farver, John R (1994). "Oxygen self-diffusion in calcite: Dependence on temperature and water fugacity". In: *Earth and Planetary Science Letters* 121.3–4, pp. 575–587.

Ferry, J M et al. (2011). "Formation of dolomite at 40-80 C in the Latemar carbonate buildup, Dolomites, Italy, from clumped isotope thermometry". In: *Geology* 39.6, pp. 571–574.

Ferry, John M and Gregory M Dipple (1992). "Models for coupled fluid flow, mineral reaction, and isotopic alteration during contact metamorphism: the Notch Peak aureole, Utah". In: *American Mineralogist* 77, pp. 577–591.

Ferry, John M, Takayuki Ushikubo, et al. (2010). "Assessment of grain-scale homogeneity and equilibration of carbon and oxygen isotope compositions of minerals in carbonate-bearing metamorphic rocks by ion microprobe". In: 74.22, pp. 6517–6540.

Frey, Martin (1987). "Very low-grade metamorphism of clastic sedimentary rocks". In: *Low temperature metamorphism*. Blackie Glasgow, pp. 9–58.

Ghose, S and J Ganguly (1982). "Mg-Fe Order-Disorder in Ferromagnesian Silicates". In: *Advances in Physical Geochemistry*. Ed. by SurendraK Saxena. New York, NY: Springer New York, pp. 3–99–99.

Ghosh, Prosenjit et al. (2006). "13C-18O bonds in carbonate minerals: A new kind of paleothermometer". In: *Geochimica et Cosmochimica Acta* 70.6, pp. 1439–1456.

Grauel, Anna-Lena et al. (2013). "Calibration and application of the 'clumped isotope' thermometer to foraminifera for high-resolution climatereconstructions". In: 108.C, pp. 125–140.

Guo, Weifu et al. (2009). "Isotopic fractionations associated with phosphoric acid digestion of carbonate minerals: Insights from first-principles theoretical modeling and clumped isotope measurements". In: 73.24, pp. 7203–7225.

Henkes, Gregory A et al. (2014). "Temperature limits for preservation of primary calcite clumped isotope paleotemperatures". In: 139.C, pp. 362–382.

Hintze, Lehi F and F D Davis (2002). "Geologic map of the Tule Valley 30'x 60' Quadrangle and parts of the Ely, Fish Springs, and Kern Mountains 30' x 60' Quadrangles, northwest Millard County, Utah". In: *Utah Geological Survey Map* 30, p. 60.

Horita, Juske (2014). "Oxygen and carbon isotope fractionation in the system dolomite–water–CO2 to elevated temperatures". In: *Geochimica et Cosmochimica Acta VL - IS - SP - EP - PY - T2* - 129 IS -.C, pp. 111–124.

Hover Granath, V C, J J Papike, and T C Labotka (1983). "The Notch Peak contact metamorphic aureole, Utah: Petrology of the Big Horse limestone member of the Orr Formation". In: *Geological Society of America Bulletin* 94.7, pp. 889–906.

Hover, V C (1981). "The Notch Peak Metamorphic Aureole, Utah: Mineralogy, petrology, and geochemistry of the Big Horse Canyon member of the Orr formation". MA thesis. State University of New York at Stony Brook.

Humphrey, F L and M Wyatt (1958). "Scheelite in feldspathized granodiorite at the Victory Mine, Gabbs, Nevada". In: *Economic geology and the bulletin of the Society of Economic Geologists* 53.1, pp. 38–64.

Huntington, K W et al. (2009). "Methods and limitations of 'clumped' CO2 isotope (Δ47) analysis by gas-source isotope ratio mass spectrometry". In: *Journal of Mass Spectrometry* 44.9, pp. 1318–1329.

Kim, Sang-Tae and James R O'Neil (1997). "Equilibrium and nonequilibrium oxygen isotope effects in synthetic carbonates". In: 61.16, pp. 3461–3475.

Kirschner, David L, Zachary D Sharp, and Henri Masson (1995). "Oxygen isotope thermometry of quartz-calcite veins: Unraveling the thermal-tectonic history of the subgreenschist facies Morcles nappe (Swiss Alps)". In: *Geological Society of America Bulletin* 107.10, pp. 1145–1156.

Kluge, Tobias et al. (2015). "Laboratory calibration of the calcium carbonate clumped isotope thermometer in the 25–250°C temperature range". In: 157, pp. 213–227.

Labotka, T C et al. (2011). "An experimental study of the diffusion of C and O in calcite in mixed CO2-H2O fluid". In: *American Mineralogist* 96.8-9, pp. 1262–1269.

Labotka, Theodore C, Peter I Nabelek, and J J Papike (1988). "Fluid infiltration through the Big Horse Limestone Member in the Notch Peak contact-metamorphic aureole, Utah". In: *American Mineralogist* 73, pp. 1302–1324.

Lackey, Jade Star and John W Valley (2004). "Complex patterns of fluid flow during wollastonite formation in calcareous sandstones at Laurel Mountain, Mt. Morrison Pendant, California". In: *Geological Society of America Bulletin* 116.1, p. 76.

Müller, T et al. (2008). "Forward modeling of the effects of mixed volatile reaction, volume diffusion, and formation of submicroscopic exsolution lamellae on calcite-dolomite thermometry". In: *American Mineralogist* 93.8-9, pp. 1245–1259.

Mullis, Josef et al. (1994). "Fluid regimes during late stages of a continental collision: Physical, chemical, and stable isotope measurements of fluid inclusions in fissure quartz from a geotraverse through the Central Alps, Switzerland". In: 58.10, pp. 2239–2267.

Murray, Sean T, Monica M Arienzo, and Peter K Swart (2016). "Determining the". In: 174.C, pp. 42–53.

Nabelek, P I (2002). "Calc-silicate reactions and bedding-controlled isotopic exchange in the Notch Peak aureole, Utah: implications for differential fluid fluxes with metamorphic grade". In: *Journal of Metamorphic Geology* 20.4, pp. 429–440.

– (2009). "Numerical Simulation of Kinetically-controlled calc-silicate reactions and fluid flow with fransie". In: *American Journal of Science* 309.7, pp. 517–548.

Nabelek, P I et al. (1984). "Contrasting fluid/rock interaction between the Notch Peak granitic intrusion and argillites and limestones in western Utah: Evidence from stable isotopes and phase assemblages". In: *Contributions to Mineralogy and Petrology* 86.1, pp. 25–34.

Nabelek, Peter I (1991). “Stable isotope monitors”. In: *Reviews in Mineralogy and Geochemistry* 26.1, pp. 395–435.

Nabelek, Peter I, Anne M Hofmeister, and Alan G Whittington (2012). “The influence of temperature-dependent thermal diffusivity on the conductive cooling rates of plutons and temperature-time paths in contact aureoles”. In: *Earth and Planetary Science Letters* 317–318 IS -, pp. 157–164.

Nabelek, PeterI et al. (1988). “Effects of fluids on the interaction of granites with limestones: The Notch Peak stock, Utah”. In: *Contributions to Mineralogy and Petrology* 99.1, pp. 49–61–61.

Nathenson, Manuel and Marianne Guffanti (1988). “Geothermal gradients in the conterminous United States”. In: *Journal of Geophysical Research: Solid Earth* 93.B6, pp. 6437–6450.

Nelson, C A (1962). “Lower Cambrian-Precambrian Succession, White-Inyo Mountains, California”. In: *Geological Society of America Bulletin* 73.1, pp. 139–144.

O’Neil, James R and Samuel Epstein (1966). “Oxygen Isotope Fractionation in the System Dolomite-Calcite-Carbon Dioxide”. In: *Science* 152.3719, pp. 198–201.

Passey, Benjamin H and Gregory A Henkes (2012). “Carbonate clumped isotope bond reordering and geospeedometry”. In: *Earth and Planetary Science Letters* 351–352.0, pp. 223–236.

Passey, Benjamin H, Naomi E Levin, et al. (2010). “High-temperature environments of human evolution in East Africa based on bond ordering in paleosol carbonates”. In: *Proceedings of the National Academy of Sciences* 107.25, pp. 11245–11249.

Rosenbaum, J and Simon M F Sheppard (1986). “An isotopic study of siderites, dolomites and ankerites at high temperatures”. In: 50.6, pp. 1147–1150.

Schauble, Edwin A, Prosenjit Ghosh, and John M Eiler (2006). “Preferential formation of 13C–18O bonds in carbonate minerals, estimated using first-principles lattice dynamics”. In: 70.10, pp. 2510–2529.

Sharma, Taleshwar and Robert N Clayton (1965). “Measurement of O18O16 ratios of total oxygen of carbonates”. In: 29.12, pp. 1347–1353.

Shenton, Brock J et al. (2015). “Clumped isotope thermometry in deeply buried sedimentary carbonates: The effects of bond reordering and recrystallization”. In: *Geological Society of America Bulletin*.

Sheppard, Simon M F (1986). “Characterization and isotopic variations in natural waters”. In: *Reviews in Mineralogy and Geochemistry* 16.1, pp. 165–183.

Sheppard, Simon M F and Henry P Schwarcz (1970). “Fractionation of carbon and oxygen isotopes and magnesium between coexisting metamorphic calcite and dolomite”. In: *Contributions to Mineralogy and Petrology* 26.3, pp. 161–198.

Shieh, Y N and H P Taylor Jr (1969). "Oxygen and hydrogen isotope studies of contact metamorphism in the Santa Rosa Range, Nevada and other areas". In: *Contributions to Mineralogy and Petrology* 20.4, pp. 306–356.

Stolper, D A and J M Eiler (2015). "The kinetics of solid-state isotope-exchange reactions for clumped isotopes: A study of inorganic calcites and apatites from natural and experimental samples". In: *American Journal of Science* 315.5, pp. 363–411.

Swart, Pn K, S J Burns, and J J Leder (1991). "Fractionation of the stable isotopes of oxygen and carbon in carbon dioxide during the reaction of calcite with phosphoric acid as a function of temperature and technique". In: *Chemical Geology: Isotope Geoscience section* 86.2, pp. 89–96.

Taylor, Bruce E and James R O'Neil (1977). "Stable isotope studies of metasomatic Ca-Fe-Al-Si skarns and associated metamorphic and igneous rocks, Osgood Mountains, Nevada". In: *Contributions to Mineralogy and Petrology* 63.1, pp. 1–49.

Wada, H and Katsuhiko Suzuki (1983). "Carbon Isotopic Thermometry Calibrated by Dolomite-Calcite Solvus Temperatures". In: 47.4, pp. 697–706.

Wang, Zhengrong, Edwin A Schauble, and John M Eiler (2004). "Equilibrium thermodynamics of multiply substituted isotopologues of molecular gases". In: *Geochimica et Cosmochimica Acta* 68.23, pp. 4779–4797.

Whittington, Alan G, Anne M Hofmeister, and Peter I Nabelek (2009). "Temperature-dependent thermal diffusivity of the Earth's crust and implications for magmatism". In: *Nature* 458.7236, pp. 319–321.

Zaarur, Shikma, Hagit P Affek, and Mark T Brandon (2013). "A revised calibration of the clumped isotope thermometer". In: *Earth and Planetary Science Letters* 382, pp. 47–57.

Chapter 3

EXPERIMENTAL DETERMINATION OF THE PRESERVATION POTENTIAL OF THE DOLOMITE CLUMPED ISOTOPE THERMOMETER

3.1 Abstract

Dolomite clumped isotope compositions are indispensable for determining the temperatures and fluid sources of dolomitizing environments, but only if they have not been modified since formation. Carbonate Δ_{47} values are susceptible to resetting by recrystallization during diagenesis, and, even in the absence of dissolution and reprecipitation reactions, alteration by solid-state reordering during prolonged residences at elevated temperatures. In order to understand the potential of dolomite Δ_{47} values to preserve the conditions of dolomitization in ancient sections, the kinetic parameters of solid-state reordering in this phase must be determined. We heated mm-sized crystals of near-stochiometric dolomite in a René-type cold seal apparatus at temperatures between 409 and 717 °C for 0.1 to 450 hours. In order to prevent the decarbonation of dolomite to calcite, periclase, and CO_2 at these conditions, the system was pressurized with CO_2 to 0.45–0.8 kbar. Over the course of 31 temperature-time points and 128 individual Δ_{47} measurements of powdered dolomite crystals from these points, we observed the evolution of dolomite Δ_{47} values from the initial (unheated) composition of the crystals (0.452 ± 0.004‰, corresponding to a formation temperature of ~143 °C) towards high-temperature equilibrium distributions. Complete re-equilbration occurred in the longest time points of the 563 to 717 °C experiments. As with previous heating experiments using calcite and apatite, dolomite Δ_{47} exhibited complex reordering behavior inadequately described by first-order Arrhenian-style models. Instead, we fit the data using two published models for clumped isotope reordering: the transient defect/equilibrium defect model of Henkes et al. (2014), and the exchange-diffusion model of D. A. Stolper and J M Eiler (2015). For both models, we found optimal reordering parameters by using global least-squares minimization algorithms and estimated uncertainties on these fits with a Monte Carlo scheme that resampled individual Δ_{47} measurements and re-fit the dataset of these new mean values. Dolomite Δ_{47} rate constants determined using both models are resolvably slower than those of calcite and apatite. Both models predict that high-grade dolomite crystals should

preserve apparent equilibrium blocking temperatures of between ~240 and 300 °C during cooling on geologic timescales, which are consistent with clumped isotope measurements of slowly-cooled dolomite marbles. In simple heating scenarios, on the other hand, the two models disagree. The transient defect/equilibrium defect model suggests that early epigenetic dolomite fabrics resist detectable reordering at ambient temperatures as high as 180 °C for tens of millions of years, while the exchange-diffusion model predicts incipient partial reordering as low as 150 °C. In either case, barring later recrystallization, dolomite Δ_{47} values should be faithful recorders of the conditions of dolomitization in sedimentary sections buried no hotter than ~150 °C for tens of millions of years.

3.2 Introduction

Dolomite is pervasive in the rock record, yet largely absent from sites of active carbonate precipitation. Although modern seawater is supersaturated with respect to dolomite, it appears that that sluggish crystallization kinetics inhibit dolomite precipitation at surface conditions, i.e., dolomite is out-competed by other carbonate phases unless fluid compositions are uniquely favorable to precipitation of this high-Mg carbonate (Arvidson and Mackenzie, 1999; Machel, 2004; Warren, 2000). On the other hand, models of precipitation rate suggest that even small temperature increases will preferentially raise dolomite crystallization rates with respect to calcite, which may contribute to the often-observed pseudomorphic replacement of calcite by dolomite during early diagenesis (Arvidson and Mackenzie, 1999). Temperature is by no means the only parameter regulating dolomite formation; fluid chemistry, rock porosity, water/rock ratio, and the interplay between dissolution, diffusion, and precipitation all have roles in determining when and where dolomite forms (Gregg et al., 2015; Jonas et al., 2015; Machel, 2004; Warren, 2000; Blättler, Miller, and Higgins, 2015). Nevertheless, constraining the temperatures of dolomitization is critical for evaluating competing models for this process (e.g., Murray and Swart (2017)).

Carbonate clumped isotope thermometry is a relatively new technique based on the homogeneous exchange of heavy isotopes of carbon and oxygen in aqueous carbonate groups, which are precipitated and preserved as carbonate minerals (Ghosh et al. (2006); also see reviews by John M Eiler (2011) and John M Eiler (2007)). The net equation describing the distribution of these isotopes in dolomite is:

$$CaMg(^{13}C^{16}O_3)_2 + CaMg(^{12}C^{18}O^{16}O_2)_2 = CaMg(^{13}C^{18}O^{16}O_2)_2 + CaMg(^{12}C^{16}O_3)_2. \quad (3.1)$$

The equilibrium constant for this reaction is determined by measuring the Δ_{47} value of CO_2 produced through the digestion of carbonate in phosphoric acid by dual-inlet isotope ratio mass spectrometry. The Δ_{47} value (reported in ‰) is defined as:

$$\Delta_{47} = R^{47}/R^{47*} - 1, \quad (3.2)$$

where R47 is the measured abundance ratio of CO_2 isotopologues of mass 47 Da (primarily $^{13}C^{18}O^{16}O$) to the unsubstituted species ($^{12}C^{16}O_2$ at 44 Da), and R47* is the expected ratio for a stochastic distribution of these isotopologues (Wang, E. A. Schauble, and John M Eiler, 2004). Δ_{47} values of lab-grown dolomites are dependent on precipitation temperature, and thus Δ_{47} values in natural materials can be used to estimate the temperature of (re)crystallization (Bonifacie, Calmels, et al., 2017; Ghosh et al., 2006).

Using this technique, recent dolomitization in extant carbonate platforms has been observed at a range of subsurface temperatures, from soon after deposition to later recrystallization in Mg-rich brines at 15–70 °C (Murray and Swart, 2017; Winkelstern and Lohmann, 2016). Estimates of $\delta^{18}O$ values of the fluids in equilibrium with these phases, a useful consequence of Δ_{47}-derived temperature determinations, can further constrain the conditions of dolomite formation (Murray and Swart, 2017). This approach may be especially useful for interrogating the conditions of dolomite formation in ancient sections, where far less is known about the chemistry of seawater and seawater-derived brines (Bergmann, 2013; J M Ferry et al., 2011). However, most ancient carbonate platforms have been subjected to protracted burial diagenesis and low-grade metamorphism, which could overprint Δ_{47} measurements. Interpretation of dolomite Δ_{47}–derived temperatures and fluid $\delta^{18}O$ contents in these sections requires knowledge of the conditions under which they can be modified.

Solid-state reordering in carbonate minerals

Fine-grained carbonate fabrics are susceptible to recrystallization during diagenesis (Shenton et al., 2015; Winkelstern and Lohmann, 2016). During deep burial and low-grade metamorphism, cryptic dissolution and reprecipitation can even reset Δ_{47} values while preserving early diagenetic textures (Lloyd, John M Eiler, and Nabelek,

2017; Shenton et al., 2015). Even in the absence of recrystallization, primary carbonate clumped isotope temperatures can be obscured by solid-state reordering, defined as the diffusion and exchange of heavy isotopes of carbon and oxygen in intact crystals in order to re-equilibrate with new ambient temperatures (Dennis and Schrag, 2010; Passey and Henkes, 2012). The kinetics of carbonate clumped isotope reordering have been determined in a variety of calcites by observing the time-dependent changes in Δ_{47} values as low-temperature configurations approach high-temperature equilibrium while held in furnaces at fixed temperatures between 385 and 692 °C (Henkes et al., 2014; Passey and Henkes, 2012; D. A. Stolper and J M Eiler, 2015). Extrapolation of the Arrhenian parameters derived from these experiments suggests that calcite crystals are susceptible to detectable amounts of reordering, and therefore the formation temperatures within are compromised, when heated to ambient temperatures as low as 100 °C for tens of millions of years (D. A. Stolper and J M Eiler, 2015).

Apparent equilibrium blocking temperatures in slowly-cooled dolomite marbles—i.e., the diffusion-limited concentration of ^{13}C–^{18}O bonds preserved when a high-temperature phase internally re-equilibrates with progressively lower temperatures during cooling—are ~100 °C higher than those in coexisting calcite marbles (250–300 °C vs. 150–200 °C), which suggests that the rates of solid-state clumped isotope reordering in dolomite are slower than in calcite (Bonifacie, John M Ferry, et al., 2011; John M Eiler, 2011; J M Ferry et al., 2011; Lloyd, John M Eiler, and Nabelek, 2017; Ryb et al., 2017). If so, dolomite Δ_{47} records should be more resistant to alteration during burial and heating, and could be accurate archives of the conditions of dolomitization in ancient sections. Here, we report a series of heating experiments using fragments of a dolomite megacryst in order to determine the rate constants for dolomite Δ_{47} solid-state reordering. We use these parameters to predict to the susceptibility of the dolomite Δ_{47} thermometer to alteration during deep burial and metamorphism.

Contrasting models for solid state reordering

An additional motivation for this study is to address outstanding questions regarding the mechanism for such re-equilibration and the primary controls on its rate. Time–Δ_{47} trends in all published lab-based heating experiments are inadequately described by first-order rate equations. Instead, models to fit the calcite and apatite Δ_{47} reordering data require a transient mechanism for initial, rapid re-equilibration superimposed upon a persistent, 'background' reordering rate (Henkes et al., 2014;

Passey and Henkes, 2012; D. A. Stolper and J M Eiler, 2015). Although calibrated to results that are statistically indistinguishable, the two existing models have distinct physical groundings that lead to contrasting interpretations of the behavior of the clumped isotope thermometer in natural settings.

Based on the widely-held view that atomic diffusion in minerals is facilitated by structural defects (Y. Zhang, 2010), Henkes et al. (2014) attribute initial, non-first order reordering to a high concentration of crystallographic defects in low-temperature crystals. In their model, many of these defects are annealed during prolonged heating, which reduces the mobility of carbonate components and progressively slows the reordering rate. The time-invariant reordering rate observed during later stages of these heating experiments thus reflects the concentration of un-annealable defects (e.g., cation substitutions, vacancies). This interpretation suggests that every carbonate grain should have a unique susceptibility to solid-state reordering that is emblematic of its specific defect concentration, and that for high-temperature materials, only equilibrium defects need be considered. Nonetheless, all calcite minerals considered so far have similar equilibrium reordering rates that appear to be independent of Mn concentration, crystallization environment, and other external constraints on possible contributors to the 'equilibrium' defect concentration.

The model proposed by D. A. Stolper and J M Eiler (2015) attributes non-first order Δ_{47} reordering behavior to physical limits on reordering rate imposed by the geometry of the calcite crystal lattice. Specifically, they hypothesize that changes in clumped isotope composition occur through exchange of heavy C and O isotopes only among neighboring carbonate groups. Thus although initial, rapid partial re-equilibration readily occurs in unit cells where both ^{13}C and ^{18}O are present in neighboring carbonate groups (defined by the authors as 'pairs'), complete re-equilibriation is rate-limited by the diffusion of ^{13}C or ^{18}O-bearing groups (defined as 'singles') through the crystal lattice. Unlike the Henkes et al. (2014) model, this construction implies that the capacity of carbonate minerals to partially re-equilibrate Δ_{47} by the non-first order mechanism is an intrinsic feature of the system. Thus, rapid initial changes in Δ_{47} in response to changing conditions should occur during both the heating of cold carbonates and the cooling of hot ones, provided some excess of pairs persists.

Estimates of calcite Δ_{47} compositions from both models are consistent with measurements of reordered natural materials, but those of apatite Δ_{47} compositions are not (D. A. Stolper and J M Eiler, 2015). In carbonatites, apatite apparent equilib-

rium blocking temperatures are 40–60 °C colder than those of coexisting calcite (D. A. Stolper and J M Eiler, 2015). Parallel heating experiments, however, predict that apatite Δ_{47} values should preserve apparent temperatures 30–50 °C above calcite Δ_{47} values during the cooling of high-temperature igneous or metamorphic rocks (D. A. Stolper and J M Eiler, 2015). The cause of the disagreement between measured and modeled apatite Δ_{47} values is not established, but may be due to accelerated reordering through the accumulation of radiation damage (D. A. Stolper and J M Eiler, 2015), or could reflect an incomplete understanding of the spatial distribution or bonding environment of carbonate groups in this mineral (Kolodny and Kaplan, 1970). On the other hand, the apparent agreement between natural and experimental reordered calcite Δ_{47} rates could be fortuitous, and the mechanisms for Δ_{47} reordering could be broadly misunderstood. Testing the agreement between modeled and observed apparent equilibrium Δ_{47} values in a new mineral phase may indicate which of the above statements is more likely, and could resolve outstanding questions regarding the controls on clumped isotope reordering rate.

3.3 Materials and methods

In order to directly compare dolomite and calcite Δ_{47} reordering rates, we replicated the experimental design and measurement conditions of D. A. Stolper and J M Eiler (2015) as closely as possible. The following methods description emphasizes conditions unique to these dolomite experiments

Sample selection

Because Δ_{47} signals of fine-grained carbonate fabrics are vulnerable to overprinting during dissolution-reprecipitation reactions at grain boundaries, large, homogeneous crystals are preferable for high-temperature reordering experiments. However, the precipitation of coarse dolomite crystals is kinetically limited at near-surface temperatures. Large (>10 cm), high-temperature crystals, on the other hand, are resolved in Δ_{47} value from the equilibrium infinite-temperature limit by only a small multiple of the typical uncertainty on replicate Δ_{47} measurements and are thus inadequate for measuring rate constants with useful precision. As a compromise between these competing needs, we used an aggregate of cm-sized, translucent, rhombohedral dolomite crystals that formed in an open fissure from hydrothermal fluids at somewhat elevated temperatures in Eugui, Spain. Eugui dolomite is the type locality for optical-quality dolomite (Lugli et al., 2000), compositionally homogeneous, near-perfectly stoichiometric, well-ordered, and largely free of structural defects (Barber,

H C Heard, and Wenk, 1981; Navrotsky and Capobianco, 1987; R J Reeder and Nakajima, 1982; R J Reeder and Wenk, 1983). It has been the starting material for a large number of investigations of dolomite crystallinity, thermal stability, deformation and dissolution rates (Barber, H C Heard, and Wenk, 1981; Chai and Navrotsky, 1996; Martinez, J. Zhang, and R J Reeder, 1996; Richard J Reeder and Markgraf, 1986; Urosevic et al., 2012), and a reference standard against which the physical and chemical properties of sedimentary and saddle dolomites are compared (Barber, R J Reeder, and Smith, 1985; Jones, Luth, and MacNeil, 2001). Given the paucity of ordered, stochiometric, megacrystic dolomite in nature, and the utility of direct comparison of Δ_{47} reordering rates to other properties of this well-characterized sample, the Eugui dolomite is an ideal material for these experiments, provided its initial Δ_{47} composition is sufficiently uniform and resolved from the equilibrium high-temperature limit.

Our sample of Eugui dolomite was acquired from Susan M. Ulrich Fine Minerals. The sample is a ~900 g, ~8 x 8 x 5 cm aggregate of transluscent, rhombohedral crystals 1–3 cm across, protruding from a base of massive, white crystalline dolomite (Supplementary Fig. 3.8). The mineralogy and crystallinity of this material was confirmed by powder X-ray diffractometry (XRD). Briefly, a single crystal from the aggregate was broken off, powdered, and analyzed using a Bruker Phaser D2 XRD with a 20 KeV beam, 20–60 2-theta scan range, 0.05 step size, and 0.5 s integration time. The locations and widths of scan peaks are consistent with well-ordered dolomite.

Elemental and isotopic composition and homogeneity

The elemental abundances of one colorless, mm-sized fragment the primary aggregate and one fragment from the white crystalline base were measured on a JEOL JXA-8200 electron probe micro-analyzer. Using a 15 KeV beam, with a 20 nA beam current, and a 10 μm spot size, the concentrations of the oxides of CaO, MgO, FeO, and MnO were determined for ten spots on each fragment, and standardized against analyses of dolomite, siderite, and rhodochrosite from the same analytical session. Averages and standard deviations of these measurements for each crystal are reported in Table 3.4. Using the measured oxide abundances and an assumed CO_2 content, we derive a formula for the colorless crystal that is nearly stoichiometric dolomite: $Ca_{0.500}Mg_{0.493}Fe_{0.006}Mn_{0.001}(CO_3)_{1.0}$. The white dolomite material from the base has a comparable stoichiometry, with a lower Fe content (0.294 ± 0.056 mol. %) and a similar Mn content (0.126 ± 0.018 mol. %).

In order to determine the isotopic composition of the acquired sample and test its homogeneity, we cleaved translucent, faceted, crystal fragments from three distal locations on the crystal aggregate. We additionally extracted material from a large, white crystal at the base of the aggregate and from two locations on the white-gray, massive, polycrystalline dolomite matrix below it in order to compare the colorless, faceted crystals (which are the experimental material of our study) to their host carbonate (Supplementary Fig. 3.8). Care was taken to avoid, or physically abrade, a soft, red-tan powder found at base of the crystal aggregate. Fragments from each of these six sites were powdered, dry, in an agate mortar and pestle to < 106 μm, and analyzed for δ^{13}C, δ^{18}O, and Δ_{47} content using standard procedures for automated digestion, purification, and measurement by dual-inlet isotope ratio mass spectrometry, outlined below (Section 2.3) and described in detail elsewhere (e.g., Passey, Levin, et al. (2010)). Mean carbonate Δ_{47} values from each site agree within 2σ standard errors of replicate measurements, suggesting that the entire sample, including the massive crystalline base, formed at approximately uniform conditions, with a Δ_{47} value of 0.452 ± 0.003 ‰ (1σ std. error, n = 31, reported in the absolute reference frame (ARF; Dennis, Affek, et al. (2011)). The bulk ^{13}C and ^{18}O contents vary among sample sites: δ^{13}C values are confined to a relatively narrow range of +2.19 to +2.78 ‰ (vs. VPDB); δ^{18}O values of the translucent crystal aggregate are similarly uniform ($\delta^{18}O_{VPDB}$ of –13.66 to –13.34 ‰), but significantly higher than those of the massive dolomite base (as low as –16.47 ± 0.95 ‰). Heterogeneity in bulk isotope composition is potentially problematic because materials with distinct carbon-13 and oxygen-18 contents, but similar Δ_{47} values, do not mix linearly (John M Eiler and E. Schauble, 2004). Such non-linear mixing effects, however, are insignificant for the compositional variations reported here: physical mixtures of dolomite domains with identical Δ_{47} compositions, nearly identical δ^{13}C values, but ~3 ‰ differences in δ^{18}O will generate apparent enrichments in Δ_{47} of at most 0.0003 ‰; such discrepancies are a small percentage of typical analytical uncertainty and thus functionally undetectable. Even so, due to the differences in mineral habit, coloration, and Fe content between the colorless crystal aggregate and the fine white dolomite at its base, and the uncertainty regarding how such differences might affect reordering rate, we used only fragments of the colorless aggregate for our heating experiments. This habit appears to be nearly homogeneous with respect to all three measured isotopic parameters, and thus is an appropriate material for the present study.

Heating experiments

Because dolomite is thermodynamically unstable at atmospheric pressure at the temperatures of the reordering experiments, all experiments were performed at elevated pressures in a rapid-quench, metal René-type cold seal apparatus (Blank, E. M. Stolper, and Carroll, 1993), the exact same apparatus used for the calcite heating experiments of D. A. Stolper and J M Eiler (2015). For each run, two to eight mm-sized fragments from the colorless aggregate of dolomite crystals (total mass: 47–91 mg) were placed in an unsealed platinum capsule, affixed to the end to an iridium rod using platinum wire, and sealed into the water-cooled chamber of the cold seal apparatus. The system was pressurized, placed in a resistance furnace set to the target temperature for each run, and allowed to thermally equilibrate for at least two hours. Each reordering experiment began by raising the iridium rod and platinum capsule into the heated end of the cold-seal tube using a magnetic collar. Each experiment was terminated by removing the collar, which dropped the Pt capsule into the water-cooled jacket and quenched the samples to ~20 °C in 1–2 seconds. Following each experiment, the system was depressurized, the crystals were retrieved, and the reusable Pt capsule was sonicated in 5 N HCl for 10 minutes to remove any residual carbonate.

In an initial run pressurized with Ar to 67.6 MPa at 717 °C for 5 minutes, dolomite decarbonation occurred: at the end of the experiment, crystals were coated in a fine, white powder, and had undergone a mass loss of 3.8 %. Previous experiments have demonstrated that at these conditions, dolomite dissociates to periclase and calcite by the (simplified) reaction (Goldsmith and Hugh C Heard, 1961; Graf and Goldsmith, 1955):

$$\mathrm{CaMg(CO_3)_2} \rightarrow \mathrm{CaCO_3 + MgO + CO_2}. \tag{3.3}$$

Note that the empirical reaction is more complicated because the impure product calcite lies on a solid solution with $MgCO_3$, and its exact stoichiometry is dependent on temperature and the partial pressure of CO_2 (p_{CO_2}) (Graf and Goldsmith, 1955). At 717 °C, dolomite is stable at p_{CO_2} values above ~15 MPa but below ~3 GPa, where it dissociates into aragonite and magnesite (Goldsmith and Hugh C Heard, 1961; Graf and Goldsmith, 1955; Shirasaka, Takahashi, and Nishihara, 2002). So, in subsequent runs, we pressurized the cold seal apparatus with 43.5–78.4 MPa of CO_2 instead of Ar. We monitored for decarbonation in these experiments with high-magnification imagery and mass measurements before and after each run. When

using CO_2 as headspace gas, no visible decarbonation occurred and mass loss was limited to at most 1.6% but typically ~0.6%, which we attribute to incomplete recovery of small crystal fragments.

During the first heating experiment pressurized with CO_2 (at 717 °C, 64.2 MPa, 5 minutes), the Pt capsule, wire, Ir rod, and dolomite crystals were coated with a lustrous grey-black patina, presumably a graphitic residue resulting from the oxidation of the inner metal surfaces of the cold seal pipe. A reaction between the cold seal surfaces and CO_2 is further implicated because the patina was restricted to the hot end of the Ir rod, and was thicker on the outer surfaces of the Pt capsule than the inner surfaces. During subsequent runs progressively less deposition occurred, and after ten heating experiments graphitic coatings were no longer observed. To preclude contamination of carbonate samples by a deposited carbon source, we removed the graphitic coating by sonicating crystals in acetone for 15 minutes, and then evaporating the acetone overnight in a fume hood. Control tests using unheated crystals demonstrated no change in mass or isotopic composition as a result of this cleaning procedure.

In total, we conducted thirty-one heating experiments with CO_2 pressures of 43.5–78.4 MPa at temperatures between 409 and 717 °C for times between 0.125 and 455 hours. Temperature accuracy was tested by measuring the temperature inside the heated end of the cold seal pipe while the apparatus was equilibrated in the resistance furnace using a calibrated type-K thermocouple inserted through the open, cold, bottom of the pipe. A steep thermal gradient was observed between the hot, top of the pipe and the water-cooled midpoint 20 cm below. We calibrated this gradient by measuring the temperature in the pipe in 1 cm increments over a 4 cm section enveloping the location where the samples reside in the pipe at the furnace setpoints of all experiments. The average temperature over the closest (to the sample site) 2 cm section is slightly higher than but well defined by the furnace setpoint: $T_{measured} = 1.0275 * T_{furnace} - 2.3929$ ($r^2 = 0.9998$). We use this calibration to estimate the temperature in the Pt capsule during each run, but note that these measurements do not exactly replicate conditions in the cold seal apparatus during heating experiments because the apparatus does not permit measurement of temperatures inside the tube when it is sealed and pressurized.

A potential concern of heating dolomite in the presence of high p_{CO_2} is the exchange of carbonate ions in the crystals with headspace gas. To test for this, we recovered and measured the bulk isotopic composition of tank CO_2 used in run #11 (at 511 °C,

64.6 MPa, 12.8 hours): $\delta^{13}C_{VPDB}$ = –41.2 ‰, $\delta^{18}O_{VPDB}$ = –32.3 ‰. Dolomite in equilibrium with this CO_2 at this temperature would have $\delta^{13}C_{VPDB}$ and $\delta^{18}O_{VSMOW}$ compositions of –44.1 and –37.1 ‰, respectively (O'Neil and Epstein, 1966; E. A. Schauble, Ghosh, and John M Eiler, 2006). Since these values are ~47 ‰ (for $\delta^{13}C$) and 23 ‰ (for $\delta^{18}O$)) lower than the mean composition of the unheated dolomite crystal, we'd expect even partial gas-mineral isotope exchange to dramatically shift the compositions of heated samples to lower values, and for the size of such shifts to increase with time at a given temperature. The lack of variations in $\delta^{13}C$ or $\delta^{18}O$ greater than 1 ‰ and further lack of correlations with time among all heating experiments indicate that exchange with headspace gas does not significantly contribute to the single (or presumably, clumped) isotope compositions in these runs.

Analytical methods

Cleaned, heated dolomite crystals and their unheated counterparts were analyzed by standard carbonate clumped isotope techniques (e.g., (Passey, Levin, et al., 2010)). Briefly, crystals were ground, dry, with an agate mortar and pestle until entire samples passed through a 106 μm sieve. Powders were loaded into silver capsules, and digested for 20 minutes in a common acid bath of 104 % phosphoric acid held at 90 °C. We note that this powdering is necessary in order to completely react dolomite in the allotted time. Evolved CO_2 was continually separated from H_2O on a dry ice + ethanol trap held at –67 °C and frozen in liquid N_2 at –196 °C. Organic contaminants were removed by passing CO_2 through a Porapaq Q 50/80 packed mesh column held at –20 °C in a He stream at a flow rate of 15 cm^3/min. Cleaned CO_2 was analyzed at masses 44–49 on a Thermo MAT 253 dual-inlet isotope ratio mass spectrometer at Caltech against a calibrated reference CO_2 tank acquired from Oztech®.

Voltages on masses 44–48 were extracted from binary measurement files and reduced to $\delta^{13}C_{VPDB}$, $\delta^{18}O_{VPDB}$, and raw Δ_{47} values using a Python script that is publicly available and regularly updated (www.github.com/maxmansaxman/clumpy). $\delta^{13}C$ and $\delta^{18}O$ values (and by extension, raw Δ_{47} values) were calculated using the Brand, Assonov, and Coplen (2010) reference parameters recommended by Daëron et al. (2016) and Schauer et al. (2016) and the Taylor polynomial method described by Daëron et al. (2016). In each 1–3 week session, raw Δ_{47} values were corrected for nonlinearities and source scrambling, and projected into the absolute reference frame (ARF) using contemporaneous 1000 °C-equilibrated CO_2 gases that were measured daily and 25 °C-equilibrated gases that were measured 4x per week (Dennis, Affek,

et al., 2011). Two intralaboratory carbonate standards were measured daily to independently monitor the stability and accuracy of the reference frame.

Dolomite $\delta^{18}O_{VPDB}$ values were calculated from $\delta^{18}O_{VPDB}$ values of measured CO_2 using the predicted dolomite–CO_2 ^{18}O phosphoric acid fractionation interpolated to 90 °C from a 2nd-order polynomial fit to the 25 °C, 50 °C, and 100 °C fractionations from Rosenbaum and Sheppard (1986). Δ_{47} values of these 90 °C reactions were corrected to the canonical 25 °C scale by adding a 90 °C phosphoric acid fractionation factor of 0.092 ‰ (Passey and Henkes, 2012). This value is significantly lower than the dolomite Δ_{47} acid fractionation suggested by Murray, Arienzo, and Swart (2016); however, as demonstrated by Bonifacie, Calmels, et al. (2017), discussed in Lloyd, John M Eiler, and Nabelek (2017), and further supported by the high-temperature equilibration experiments of the present study (see below), it appears that dolomite and calcite have indistinguishable Δ_{47} acid fractionations on the carbonate clumped isotope systems at Caltech.

We report Δ_{47}-derived temperatures, and calculate equilibrium Δ_{47} values for heating experiments, using two separate Δ_{47}–T calibrations. First, we fit all data using eqn. 2 from Bonifacie, Calmels, et al. (2017), which is a 2nd-order polynomial fit to natural and experimental dolomites and calcites equilibrated at 25–1600 °C, most of which were measured at Caltech on the same instrument of the present study. Although this equation is not recommended for low-temperature studies, calculating Δ_{47} reordering rate constants requires a continuous Δ_{47}–T function spanning the entire range over which Δ_{47} values are measured. We note that although we report Δ_{47} values adjusted to the legacy 25 °C acid scale, the employed Δ_{47}–T equation is explicitly calibrated for carbonates reacted at 90 °C, as these are here.

Although eqn. 2 from Bonifacie, Calmels, et al. (2017) fits Δ_{47} data measured in multiple laboratories over a wide range of temperatures, there is significant disagreement between experimental data and the polynomial at the temperatures most critical for our dolomite reordering: by forcing the regression to consider the anomalously enriched Δ_{47} values of the calcite re-equilibration experiments of Passey and Henkes (2012), it misses the study's own high temperature dolomite precipitation experiments by as much as 0.02‰ (Fig. 4 in Bonifacie, Calmels, et al. (2017)). However, as discussed in Bonifacie, Calmels, et al. (2017), the ab initio equilibrium dolomite and calcite Δ_{63}–T relationships predicted by E. A. Schauble, Ghosh, and John M Eiler (2006) agree remarkably well with the Δ_{47} values of all reported dolomite precipitation experiments when a carbonate–CO_2

90 °C acid fractionation factor of 0.176‰ is added. So, we also fit our reordering data with Δ_{47} values calculated using this equation, in order to test whether it more accurately represents the Δ_{47}–T relationship in the realm of 300–800 °C. Specifically, all equilibrium Δ_{47} values, reaction progress variables, and predicted reordering capacities we re-calculated using the equation:

$$\Delta_{(47,ARF90)} = (-3.4075e^9)/T^4 + (2.3655e^7)/T^3 - (2.6317e^3)/T^2 - 5.8537/T + 0.176, \quad (3.4)$$

where T is in kelvin, and $\Delta_{47,\mathrm{ARF90}}$ is in ‰ (E. A. Schauble, Ghosh, and John M Eiler, 2006; Bonifacie, Calmels, et al., 2017). Because the inverse equation (T in terms of Δ_{47}) has no analytical solution, it is estimated using 5 iterations of the Newton-Raphson method. Note that although this equation is specifically calibrated for calcite, predicted calcite and dolomite Δ_{63}–T relationships agree within 0.004‰ above 30 °C, and within 0.001‰ above 150 °C. So, given typical analytical uncertainties, the choice of calcite or dolomite Δ_{47}–T ab initio calibration makes no difference at the temperatures of interest here. Conversely, because the E. A. Schauble, Ghosh, and John M Eiler (2006) predictions are consistently lower in Δ_{47} than the Bonifacie, Calmels, et al. (2017) calibration by 0.010–0.015 ‰ between 300 and 500 °C, but in adequate three-way agreement (all within 0.005 ‰) between 40 and 240 °C, the choice of Δ_{47}–T calibration matters greatly for fitting our dolomite reordering data, but not significantly for forward-modeling Δ_{47} reordering in sedimentary basins.

In Section 5, we find that fits generated using the ab initio Δ_{47}–T calibration are in better agreement with natural observations of reordered dolomite. So, in the following description of the results of fitting routines, Eqn. 3.4 is implicitly used for all calculations unless otherwise noted. Nonetheless, fitting parameters using both calibrations are reported in the data tables below.

3.4 Results of dolomite reordering experiments

Thirty-one heating experiments were performed on fragments of translucent Eugui dolomite crystals at temperatures between 409 °C and 717 °C, under CO_2 pressures of 43.5 to 78.4 MPa, for times between 0.125 and 455 hours. Powders from these experiments and the unheated starting material were measured during nine analytical sessions over the course of two years. Thirty-five measurements of unheated powders from these nine sessions tightly constrain the initial Δ_{47} composition to 0.452 ±

Heating T °C	Heating time (hrs)	PCO_2 (MPa)	n	$\delta^{13}C$ (VPDB)	$\delta^{13}C$ 1σ std (‰)	$\delta^{18}O_{mineral}$ (VPDB)	$\delta^{18}O$ 1σ std (‰)	Δ_{47} (‰)	Δ_{47} 1σ s.e. (‰)
N/A	0	N/A	35	2.6	0.22	-14.61	1.02	0.452	0.002
409	42	70.0	4	2.37	0.02	-14.63	0.09	0.433	0.004
	311	67.9	5	2.26	0.07	-15.05	1.42	0.395	0.021
460	86	50.5	5	2.5	0.06	-13.85	0.3	0.376	0.01
	314	72.0	7	2.59	0.28	-14.19	0.7	0.39	0.007
486	2.4	67.1	3	2.51	0.1	-13.7	0.52	0.412	0.012
	24	69.4	7	2.71	0.04	-13.89	0.14	0.401	0.006
	68.8	53.0	4	2.68	0.04	-14.01	0.09	0.349	0.018
	169.4	43.5	3	2.8	0.04	-13.98	0.09	0.348	0.004
	238.2	57.4	3	2.49	0.05	-14.14	0.1	0.335	0.006
	455.28	66.3	5	2.41	0.04	-14.08	0.12	0.333	0.008
511	1	62.8	3	2.27	0.01	-14.9	0.05	0.401	0.005
	2.5	63.2	5	2.4	0.04	-14.27	0.11	0.411	0.003
	12.83	63.1	4	2.14	0.03	-14.53	0.08	0.348	0.008
	48.2	53.4	3	2.39	0.03	-14.92	0.1	0.342	0.007
	65	61.4	4	2.49	0.1	-14.39	0.28	0.346	0.009
	160	61.9	4	1.97	0.16	-14.4	0.69	0.326	0.012
563	1	70.6	4	2.7	0.12	-14.19	0.11	0.359	0.008
	17	61.2	5	2.17	0.28	-14.35	0.06	0.318	0.008
	67.75	71.0	5	2.55	0.03	-14.48	0.11	0.311	0.011
	160.5	61.9	3	2.66	0.19	-14.35	0.57	0.3	0.026
614	0.08	59.0	4	2.14	0.02	-14.87	0.03	0.396	0.005
	0.13	69.4	3	2.64	0.04	-14.19	0.06	0.388	0.003
	0.25	71.0	3	2.09	0.03	-14.25	0.08	0.344	0.012
	0.42	78.4	4	1.99	0.12	-14.7	0.36	0.331	0.004
	1	55.8	3	2.84	0.03	-14.4	0.1	0.326	0.007
	3	73.0	3	2.32	0.01	-14.88	0.06	0.311	0.003
	4.07*	70.3	7	1.85	0.1	-15.13	0.31	0.338	0.005
	64	74.6	7	2.07	0.13	-14.79	0.25	0.323	0.01
717	0.08	64.2	1	2.48	0.15	-14.24	0.15	0.302	0.017
	0.75	60.5	3	2.53	0.03	-14.54	0.07	0.29	0.007
	15.25	55.8	4	2.24	0.14	-14.66	0.37	0.322	0.01

Table 3.1: Mean $\delta^{13}C$, $\delta^{18}O$, and Δ_{47} values of dolomite from all heating experiments and the unheated starting material. Reported uncertainties on $\delta^{13}C$ and $\delta^{18}O$ are 1σ standard deviations of individual measurements. Uncertainties on Δ_{47} values are 1σ standard errors. ^{18}O compositions of dolomite fragments are calculated from $\delta^{18}O$ values of CO_2 using a 90 °C dolomite–CO_2 common acid bath fractionation of: $\alpha^{18} = 1.009218$ (see Section 2.3). Δ_{47} are reported in the CO_2-equilibrated absolute reference frame, and corrected to the 25 °C acid scale by adding a fractionation factor of 0.092 ‰. Asterix denotes an experiment where aberrant $\delta^{13}C$, $\delta^{18}O$, and Δ_{47} values all suggest minor contamination by a secondary carbonate, so this sample is omitted from analyses and model fits.

0.002 ‰, corresponding to a formation temperature of 143 ± 2 °C (Table 3.5). The standard deviation of these measurements (0.014 ‰) is in excellent agreement with the shot-noise limit of a single analysis, which suggests that the crystal aggregate used for the heating experiments is homogeneous in Δ_{47}. Because this starting value is only ~0.150 ‰ above equilibrated compositions at the temperatures of the heating experiments, 3–7 replicate analyses of each experimental product were typically run in order to determine their Δ_{47} values with useful precision. In total, 128 individual analyses of dolomite powders from heating experiments were made (Table 3.6). Mean values and 1σ standard errors of replicate analyses are reported in Table 3.1. Mean Δ_{47} values of carbonate standards Carrara Marble and TV03 across all measurement sessions were 0.414 ± 0.023‰ (1σ s.d., n = 60) and 0.729 ± 0.021‰ (1σ s.d., n = 58), respectively. No significant variations of Δ_{47} values of these

standards between different measurement sessions were observed, so no secondary corrections were applied.

Within every temperature series, Δ_{47} values decrease with time and asymptotically approach the equilibrium values predicted by the Bonifacie, Calmels, et al. (2017) 2nd-order Δ_{47}–T equation. The time required to reach equilibrium is inversely proportional to the temperature of the experiment: at 717 °C, dolomite Δ_{47} compositions are indistinguishable from equilibrium within five minutes, whereas at 511 °C, apparent equilibration is not observed until 160 hours. The terminal Δ_{47} value in the 486 °C series is barely resolved from equilibrium after 455 hours. Although significant change in Δ_{47} values occur in the two coldest series (409 and 460 °C), equilibrium is not reached over the timescales of the experiments. Qualitatively similar behavior is observed when equilibrium Δ_{47} values are predicted using the (E. A. Schauble, Ghosh, and John M Eiler, 2006) Δ_{47}–T equation.

Dolomite Δ_{47} values for every temperature–time point are lower than or indistinguishable (within 2σ standard errors) from the preceding time point, with one exception: the mean Δ_{47} value of the penultimate time point in the 614 °C series (t = 4.067 hrs, n = 7) is ~0.027 ‰ above the mean value after 3 hrs (n = 3) of heating at the same temperature. Due to the small 1σ standard errors on these two points (0.005 and 0.003 ‰), the 4 hr time point appears to be resolvably higher in Δ_{47} than the three hr time point. A likely cause is minor contamination by foreign carbonate with a high Δ_{47} value. Indeed, this aberrant sample has the lowest δ^{13}C and δ^{18}O values among all heating experiments, both of which are beyond two standard deviations from the means of the δ^{13}C and δ^{18}O values of all other heating experiments. Because these three independent lines of evidence suggest that the dolomite from the 4 hr, 614 °C experiment is contaminated (anomalously high Δ_{47} value, anomalously low δ^{13}C and δ^{18}O values), we omit this time point from all subsequent analyses.

3.5 Extracting dolomite Δ_{47} reordering rate constants from experimental data

Here we describe our approach to fitting these dolomite Δ_{47} reordering data with a variety of kinetic models. We first demonstrate that as with calcite and apatite, dolomite clumped isotopic re-equilibration is inadequately described by a single first-order (Arrhenian) rate equation. Then, given no a priori reasons for preferring either model, we fit our data using two published non-first order clumped isotope reordering models, describing minor modifications to the models as necessary. In

the following section, we use the results of these models in the context of external constraints to argue for the preference of one of the two.

A strategy for fitting noisy dolomite Δ_{47} reordering data

The typical procedure for deriving Arrhenian parameters from experimental data is as follows: 1) observe the progress of a reaction at a single temperature in order to derive a reaction rate constant (k) for that temperature; 2) repeat 1) at a handful of temperatures, ideally over the largest possible range where substantial reaction progress can be observed on laboratory timescales; and 3) fit a linear line to the derived rate constants in a plot of ln(k) vs. 1/T (i.e., an Arrhenius plot). For a reaction that obeys a first order Arrhenian equation, the rate constant at a given temperature is:

$$k = K_0 e^{-E_a/(RT}, \tag{3.5}$$

where E_a is the activation energy (usually reported in kJ/mol), K_0 is the pre-exponential factor (in s^{-1}), R is the universal gas constant (= 8.314 J mol–1 K^{-1}), and T is temperature (in K). Thus for a linear fit on an Arrhenius plot, the slope of the line is equivalent to E_a/R, and the intercept is the natural log of K_0. Even when reaction progress does not conform to a single first-order rate law, this general approach can still be employed. For example, in the exchange-diffusion model of D. A. Stolper and J M Eiler (2015), calcite Δ_{47} reordering is described by the interplay of two reaction mechanisms, one for the exchange of neighboring carbonate groups, and another for the diffusion of carbonate groups through the crystal lattice. Although the differential equations describing the relationship between the two mechanisms that are used to fit any single temperature–time series are relatively complex, the output of this model is two independent rate constants, one for exchange and one for diffusion, at the temperature of the experiments. By repeating this exercise at other temperatures, the rates of the exchange and diffusion reactions can be described by separate Arrhenius parameters derived from linear fits to separate lines.

Our dataset is poorly suited for extraction of Arrhenian parameters by the above procedure for two reasons: 1) the initial Δ_{47} value of our 'optical' quality dolomite is ~0.150 ‰ lower than those of optical calcites used in previous studies (Passey and Henkes, 2012; D. A. Stolper and J M Eiler, 2015); this low starting Δ_{47} value halves the Δ_{47} range over which reordering can be observed, so the analytical uncertainties of individual Δ_{47} measurements have outsized importance and must be explicitly

considered in the fits. And, 2) the full range of reaction progress is observed over a relatively limited range of temperatures (486–614 °C) on laboratory timescales (i.e., tens of minutes to hundreds of hours), because outside this range the reaction proceeds too rapidly to observe or too slowly for substantial change to occur. In order to incorporate 'incomplete' reaction progress curves from data generated outside this range into the fits, we departed from the data processing strategies used in previous calcite and apatite reordering studies and instead developed custom global least-squares minimization routines to fit all available Δ_{47} data simultaneously. To observe the sensitivities of these fits to the underlying data, we ran iterative Monte Carlo simulations whereby individual Δ_{47} measurements were randomly resampled from normal distributions defined by their measured Δ_{47} values and analytical uncertainties. We used the distributions of families of parameters from these iterations to calculate true ideal reordering parameters, the uncertainties on them, and observe correlations among them. We describe our models and evaluate their success below.

A first-order reordering model

Although neither calcite nor apatite Δ_{47} reordering could be adequately fit with a first-order Arrhenian reaction model, it is worth considering whether dolomite can. We thus attempted to fit our data using the first-order model derived in Passey and Henkes (2012). Here, the reaction progress variable is defined as:

$$F = (\Delta_{47,\text{init}} - \Delta_{47,t})/(\Delta_{47,\text{init}} - \Delta_{47,\text{equil}}), \tag{3.6}$$

where $\Delta_{47,t}$ is the mean measured Δ_{47} value of a given heating experiment at a given time, $\Delta_{47,\text{equil}}$ is the clumped isotope composition in equilibrium with the temperature of that experiment, and $\Delta_{47,\text{init}}$ is the mean initial (unheated) composition of the material, 0.452 ‰ (Eqn. A12, Passey and Henkes (2012)). Note that for this model and all subsequent ones, we do not consider the effect of varying $\Delta_{47,\text{init}}$ within its uncertainty envelope on resulting fits because this uncertainty is small (1σ s.e. = 0.002‰) and does not significantly contribute to the value of F. Over the limited range of clumped and bulk compositions measured here, the rate law for Eqn. 1 can be approximated as (c.f. Appendix A, Passey and Henkes (2012)):

$$\frac{\Delta_{47,t} - \Delta_{47,equil}}{\Delta_{47,init} - \Delta_{47,equil}} = e^{-kt}. \tag{3.7}$$

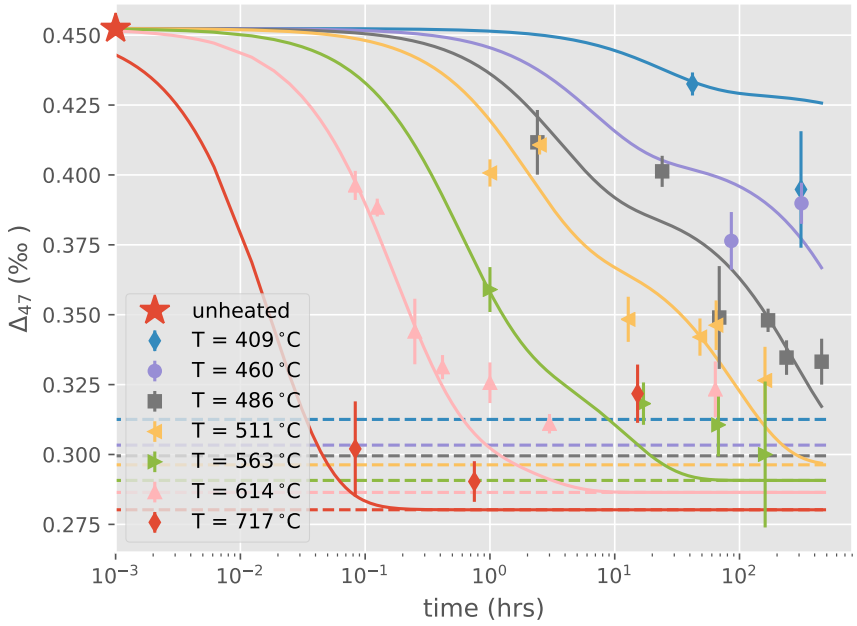

Figure 3.1: Error-weighted global least squares fit to dolomite heating experiments using the transient defect/equilibrium defect model of Henkes et al. (2014) (Eqn. 10). Red star is the mean unheated initial composition. Other symbols are mean of replicate measurements of heating experiments, with 1σ standard errors. Solid lines are the global fit to the data. Dashed lines are equilibrium Δ_{47} values for every temperature.

So, by combining Eqns. 4, 5, and 6, we can derive a simple relationship between a measurable reaction progress variable (F) and the fundamental Arrhenian parameters governing its rate:

$$\ln[1 - F] = -tK_0 e^{-E_a/RT}, \tag{3.8}$$

which can be expanded using the definition of F to:

$$\Delta_{47,t} = e^{-E_a/RT} \times (\Delta_{47,\text{init}} - \Delta_{47,\text{equil}}) + \Delta_{47,\text{equil}}. \tag{3.9}$$

With two unknowns (K_0 and E_a), Eqn. 8 makes an explicit prediction for the Δ_{47} value resulting from heating our dolomite fragment at a single temperature for a prescribed length of time. Thus, we can use a least-squares algorithm to find the ideal K_0 and E_a values that minimize the cumulative differences between predicted and mean measured Δ_{47} values for all thirty heating experiments simultaneously.

Note that although one could instead minimize the differences between measured and predicted ln[1–F] values using Eqn. 7, as Passey and Henkes (2012) and Henkes et al. (2014) do, we choose not to because such an approach severely overweights small discrepancies between data and model at large values of F. This is especially problematic because, as clumped isotope compositions closely approach equilibrium, ln[1–F] values are particularly sensitive to external factors, such as the choice of Δ_{47}–T calibration used to predict $\Delta_{47,\mathrm{equil}}$ values. Although these biases can be somewhat compensated for by propagating analytical uncertainties into ln[1–F]-space and employing an error-weighted least-squares algorithm, we find that it is more intuitive and accurate (with respect to internal and external uncertainties) to fit our data in the same reference frame that they were acquired.

We implemented this approach using the *leastsq* algorithm from the *scipy.optimize* module in Python 2.7 to minimize differences between measured and predicted $\Delta_{47,t}$ values according to Eqn. (8). Optimal values for K_0 and E_a were $7.85 * 10^{10}\ s^{-1}$ and 233 kJ/mol. Repeating the exercise while weighting residuals by the inverse squares of the 1σ standard errors of mean Δ_{47} measurements yielded similar results: $1.44 * 10^{9}\ s^{-1}$ and 205 kJ/mol. No attempt was made to estimate the uncertainties on these values because it is clear from comparison of experimental Δ_{47} data and predicted Δ_{47} reordering curves using these values that the fits are poor (Fig. 3.9). Although this simple model adequately agrees with data for high-temperature experiments (at 563 °C, 614 °C, and 717 °C), it is incapable of capturing the more complex reordering behavior evident in the experiments run at lower temperatures. For the 511 °C series, the model severely underestimates the amount of early Δ_{47} reordering that occurs within 1 hr (by about 0.04 ‰) and predicts complete re-equilibration within 65 hours, despite the fact that the datum at this time is resolved from equilibrium by ~0.033 ‰ (Fig. 3.1). The failure of the first-order model is especially obvious at 460 °C: in order to accommodate a net decrease in Δ_{47} of 0.075 ‰ after 86 hours, the first-order model is forced to fully equilibrate, and lower in Δ_{47} by another 0.058 ‰, within ~300 hours. However, the agreement (within uncertainty) of the Δ_{47} values of 460 °C experiments at 86 and 314 hours suggests that no detectable reordering occurred over this time interval. It is clear that as with calcite and apatite, dolomite Δ_{47} reordering is inadequately described by first-order kinetics. Instead, a more complex, non-first order model is required to fit these data.

	$\ln K_c$	E_c	$\ln K_d$	E_d	$\ln K_2$	E_2
Best fit to measured data	20.2	213.8	15.3	161.2	5.8	96.9
Mean of acceptable fits	20.6	217.2	15.1	160.3	6.3	100.6
1σ standard deviation	5.2	32.8	3.3	23.5	5	33.4

Table 3.2: Dolomite Δ_{47} reordering parameters for the Henkes et al. (2014) transient defect/equilibrium defect model. 'Best fit' parameters were generated using an error-weighted least squares global fit to the mean measured data reported in Table 1. Mean and 1σ s.d. of acceptable fits are the averages and standard deviations for each parameter based on fits to ~10,000 Monte Carlo simulations of the underlying Δ_{47} measurements. Activation energies are all reported in kJ/mol. Pre-exponential factors are reported in s^{-1}.

The transient defect/equilibrium defect model

To account for the initially-rapid Δ_{47} reordering that is observed in their experiments, Henkes et al. (2014) invoke an additional, transient reordering mechanism with the rate constant k_d, whose contribution to the net reordering rate declines by a temperature-dependent exponential decay rate k_2. The physical grounding for this model is described in Section 4.3. Mathematically, this approach amounts to adding an additional term to Eqn. 6 whose relative size decays with time (Henkes et al., 2014):

$$ln\left(\frac{\Delta_{47,t}-\Delta_{47,equil}}{\Delta_{47,init}-\Delta_{47,equil}}\right) = -k_c t + \frac{k_d}{k_2}(e^{-k_2 t}-1). \tag{3.10}$$

Note that here, k_c is equivalent to the k term in the previous section, and represents the rate constant for invariant reordering governed by the equilibrium defect concentration. Each of these three rate constants is described by an independent Arrhenius equation, so the full, ten-parameter equation describing Δ_{47} as a function of time becomes:

$$\Delta_{47,t} = e^{-tK_c e^{-E_c/RT}} \times e^{\frac{K_d e^{E_d/RT}}{K_2 e^{E_2/RT}} \times [e^{-tK_2 e^{E_2/RT}} - 1]} \times (\Delta_{47,\mathrm{init}} - \Delta_{47,\mathrm{equil}}) + \Delta_{47,\mathrm{equil}}. \tag{3.11}$$

This equation has six unknowns, i.e., pre-exponential factors and activation energies for each of the three rate constants: the equilibrium defect component (k_c), the transient defect component (k_d), and the annealing rate of the transient defect component (k_2). Analogous to the procedure described in Section 4.2, we use the

scipy.optimize leastsq global least squares minimization algorithm to fit Eqn. 10 for all thirty data points and derive optimal Arrhenius parameters for the three rate constants.

This procedure finds reasonable values for all six parameters, which can be used to generate reordering curves that adequately describe the data (Fig. 3.1, Table 3.2). Initial attempts to fit these data while weighting each Δ_{47} value by the inverse square of its 1σ standard error produced unreasonable, negative values for the activation energies of k_d and k_2. This occurred because small residuals on a few data points with unusually small standard errors (e.g., 1σ std. errors of three points are 0.003 ‰) were greatly over-weighted by the fit penalty function at the expense of all other points. To compensate for this, while still weighting data points proportional to their uncertainties, we imposed an upper limit on the weight of any data point determined by the reciprocal of the shot-noise limited variance given by the expected standard error of a single measurement (0.017‰) and the number of replicates. We estimated the true uncertainties on these 'best fit' Arrhenius parameters using an iterative Monte Carlo scheme. For each iteration the following sequence was performed: 1) each of the 121 individual Δ_{47} measurements were resampled from normal distributions defined by their mean Δ_{47} values and standard measurement errors using 121 independent, true random number generators; 2) mean Δ_{47} values for all thirty experiments were re-computed from the new measurements generated in step 1); and, 3) new optimal Arrhenius parameters were generated by fitting Eqn. 10 to this iteration's mean Δ_{47} values using the same least-squares algorithm described above.

We repeated this procedure for 10,000 iterations, recording the set of six Arrhenius parameters generated in each one. Of this collection of fits, 0.21 % were discarded because one or more parameters were negative. Histograms of each parameter, and covariances among them, for the remaining 9,979 evaluations are shown in Fig. 3.10. Distributions are approximately Gaussian. Minor secondary aberrations in the histograms of $\ln K_d$, E_d, $\ln K_2$, and E_2, however, suggest that a small minority of the iterations produced families of parameters with distributions that are offset from, but largely overlap with, the dominant Gaussian populations. Given no a priori reason for preferring one population of fits to another, we report the mean values and standard deviations of the entire data set as conservative estimates of the most likely Arrhenius parameters and the uncertainties on them (Table 3.2).

It is well established but rarely acknowledged that uncertainties on paired Arrhenius

parameters are highly correlated (Héberger and Kemény, 1987; Nagy and Turányi, 2011). Since such correlations have direct bearing on the application of carbonate Δ_{47} reordering models (e.g., Lloyd, John M Eiler, and Nabelek (2017)), it is worth considering how the families of dolomite Δ_{47} reordering parameters covary here. It is evident from cross-plots of the Monte Carlo evaluations of the six parameters that they fall into two groups (Fig. 3.10). Pearson correlation coefficient matrices of these families of parameters bear this out as well (Table 3.7). $\ln K_c$ and E_c are strongly correlated (r^2 = 0.991), but not remotely correlated with any other parameters. Arrhenius parameter pairs $\ln K_d$ and E_d, and $\ln K_2$ and E_2 are similarly well-correlated (r^2 of 0.992 and 0.987, respectively), and in addition, all four parameters have significant correlations between them (r^2 of 0.507 to 0.614). These correlations provide useful guidelines for how to apply the uncertainties listed in Table 3.2 to reordering models. For the first-order approximation model (i.e., solely considering Δ_{47} reordering due to unannealable defects), reasonable estimates of 1σ confidence intervals can be found by jointly varying mean values of $\ln K_c$ and E_c by their 1σ standard deviations (Table 3.2). The lack of an analytical solution to Eqn. 10 precludes application of the full transient defect/equilibrium defect model to anything other than isothermal temperature-time paths (Henkes et al., 2014). Nonetheless, uncertainties on rate constants for such scenarios should be propagated by perturbing $\ln K_d$, E_d, $\ln K_2$, and E_2 jointly by equal proportions of the standard deviations on their mean values. The effects of Arrhenius parameter uncertainties on predictions for the susceptibility of dolomite Δ_{47} to reordering are evaluated in a later section.

A dolomite exchange–diffusion reordering model

A second model that successfully accounts for the non-first order Δ_{47} reordering behavior observed during heating experiments was developed by D. A. Stolper and J M Eiler (2015). Rather than relying on the annealment of defects to account for decreasing reordering rate with time, they use a model that explicitly accounts for the formation and destruction of multiply-substituted carbonate groups through isotope exchange among adjacent, singly-substituted groups ('pairs'). Here, the two-stage reordering occurs because complete re-equilibration is initially buffered against by a high concentration of pairs that persist adjacent to previous clumped carbonate groups until further heating causes these pairs to be diffused away as singles. The reaction progress parameter, ξ, here tracks the concentration of clumped isotopologues with time, from an initial concentration ($[^{13}C^{18}O^{16}O_2{}^{2-}]_0$) to a final

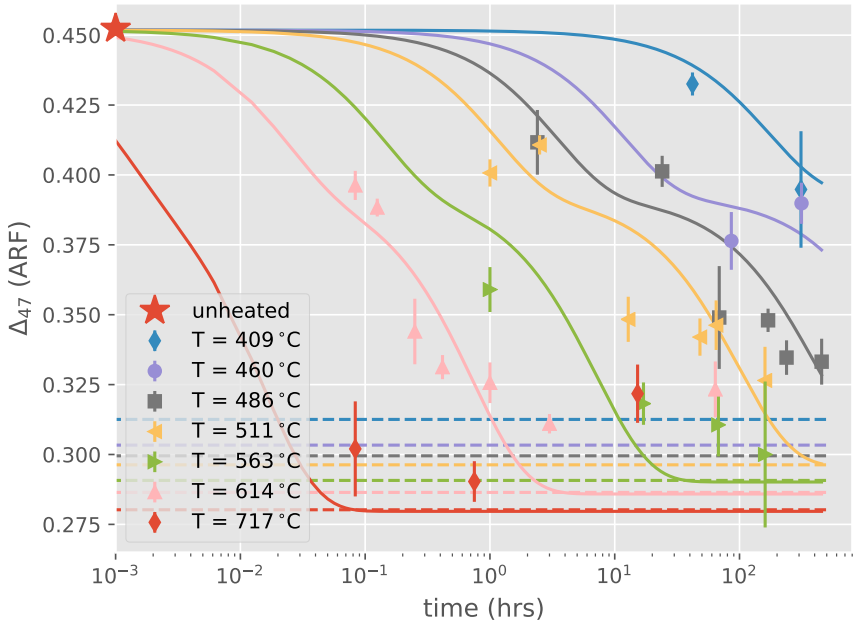

Figure 3.2: Error-weighted global least squares fit to dolomite heating experiments using the exchange-diffusion model of D. A. Stolper and J M Eiler (2015) (Eqns. 12–14). Red star is the mean unheated initial composition. Other symbols are mean of replicate measurements of heating experiments, with 1σ standard errors. Solid lines are the global fit to the data. Dashed lines are equilibrium Δ_{47} values for every temperature.

concentration in equilibrium with the reaction temperature ($[^{13}C^{18}O^{16}O_2^{2-}]_{eq}$). This reaction progress parameter is related to the Δ_{47} value by:

$$\Delta_{47} = \left(\frac{[^{13}C^{18}O^{16}O_2^{2-}]_0 - \xi}{[^{13}C^{18}O^{16}O_2^{2-}]^*} - 1 \right) + \Delta_{47,T=\infty}, \tag{3.12}$$

where $[^{13}C^{18}O^{16}O_2^{2-}]^*$ is the concentration of the primary multiply-substituted species given a stochastic distribution of ^{13}C and ^{18}O, and $\Delta_{47,T=\infty}$ is the theoretical Δ_{47} value at infinite temperature (0.2665 ‰ for the T–Δ_{47} calibration employed in this study; Bonifacie et al., 2016; note that in Eqn. 11 the actual value of $\Delta_{47,T=\infty}$, not reported permil notation, is used). This approximation ignores the contribution of other isotopologues at cardinal mass 47, which is reasonable for typical carbonate compositions given the analytical uncertainty on Δ_{47} measurements (Wang et al. 2004). With a few simplifications described in D. A. Stolper and J M Eiler (2015), the derivative of reaction progress at a given time, t, can be defined as:

$$\frac{d\xi}{dt} = k_f \times [{}^{12}C^{16}O_3{}^{2-}] \times \left([{}^{13}C^{18}O^{16}O_2{}^{2-}]_0 - \xi\right) - k_f \times \frac{[{}^{12}C^{16}O_3{}^{2-}] \times [{}^{13}C^{18}O^{16}O_2{}^{2-}]_{eq}}{[pair]_{eq}} \times [pair]_t, \tag{3.13}$$

where the corresponding time-dependent pair concentration is governed by:

$$\frac{d[pair]_t}{dt} = k_f \times [{}^{12}C^{16}O_3{}^{2-}] \times \left([{}^{13}C^{18}O^{16}O_2{}^{2-}]_0 - \xi\right) - k_f \times \frac{[{}^{12}C^{16}O_3{}^{2-}] \times [{}^{13}C^{18}O^{16}O_2{}^{2-}]_{eq}}{[pair]_{eq}} \times [pair]_t. \tag{3.14}$$

In this set of differential equations, the three unknowns are k_f, $k_{\text{diff,single}}$, and $[\text{pair}]_{\text{eq}}$, representing the rate constant for exchange between neighboring singles, the rate constant for diffusion of singles through the crystal lattice, and the concentration of pairs at equilibrium. z is the number of adjacent carbonate groups in the unit cell (6 for dolomite as well as calcite). Concentrations of singly-substituted species are treated as constants and calculated directly from the mean $\delta^{13}C$ and $\delta^{18}O$ values of the crystal. As D. A. Stolper and J M Eiler (2015) did, we initially assumed that the pair concentration at high-temperature equilibrium was indistinguishable from a stochastic configuration of singly-substituted species distributed throughout the crystal lattice, calculated as:

$$[pair]_{rand} = \frac{[{}^{13}C^{16}O_3{}^{2-}] \times \left(1 - \left(1 - \left[{}^{12}C^{18}O^{16}O_2{}^{2-}\right]\right)^z\right) + [{}^{12}C^{18}O^{16}O_2{}^{2-}] \times \left(1 - \left(1 - \left[{}^{13}C^{16}O_2{}^{2-}\right]\right)^z\right)}{2}. \tag{3.15}$$

We additionally assumed that the rate constants k_f and $k_{\text{diff,single}}$ conform to the Arrhenius equation, so at any temperature their values can be derived from independent pairs of E_a and K_0 (Eqn. 4). We can thus solve the system of Eqns. 12 and 13 using the scipy.integrate.odeint wrapper for the lsoda ODE solver to predict ξ and [pair] at every experimental temperature-time point, given global values for these four Arrhenius parameters: $\ln K_{0,f}$, $E_{a,f}$, $\ln K_{0,\text{diff,single}}$, $E_{a,\text{diff,single}}$. Residuals between measured Δ_{47} values and those predicted by ξ and Eqn. 11 can thus be fed to the error-weighted scipy.optimize leastsq global least squares minimization algorithm in order to find optimal values for $\ln K_{0,f}$, $E_{a,f}$, $\ln K_{0,\text{diff,single}}$, $E_{a,\text{diff,single}}$.

Integrating Eqns. 12 and 13 to any time point requires initial values for ξ and [pair]. Initial reaction progress is 0 by definition, but the proper initial concentration of pairs is less intuitive. As with the D. A. Stolper and J M Eiler (2015) model and the reaction-diffusion model for OH and H_2O in silicates model upon which the former is based (Zhang et al., 1995), we find that initializing this dolomite Δ_{47} reordering model with a random distribution of pairs results in a poor fit to the data. D. A. Stolper and J M Eiler (2015) find the best fit to their calcite Δ_{47} data when $[\text{pair}]_0$ is 0.030 ‰ larger than $[\text{pair}]_{\text{rand}}$. They hypothesize that this pair excess is the result of an equilibrium pseudo-secondary isotope effect that preferentially pairs singly-substituted carbonate groups when the calcite crystal is precipitated at 55 °C. Using this optimal $[\text{pair}]_0$, the pair concentration at the end of the 430 °C run, and the assumption that no preference exists at the high temperature limit, they propose the equation:

$$ln\left(\frac{[\text{pair}]_{\text{eq}}}{[\text{pair}]_{\text{rand}}}\right) = \frac{m_p}{\text{T}}, \tag{3.16}$$

where m_p = 0.0992, to calculate the equilibrium pair concentration as a function of calcite bulk composition (from Eqn. 14) and temperature (in Kelvin). Model fits of our dolomite Δ_{47} data using this value for m_p in Eqn. 15 and the formation temperature of our material (142.5 °C) fail to capture the 'kinks' in the reordering dataset. This failure is due to an overabundance of initial pairs that increases the rate of the clump-forming back reaction, which obscures the 'rapid' reordering stage that must initially occur. A new m_p must be found for dolomite, but the optimal initial and equilibrium pair concentrations, which depend on mp, are codependent on the optimal rate constants for exchange and diffusion for any solutions to Eqns. 12 and 13. To account for this possibility, we introduced m_p as another free parameter for our fits, and used this parameter along with Eqn. 15 to calculate $[\text{pair}]_{\text{eq}}$ for every experimental temperature and the initial pair concentration for the formation temperature. We then used our global least squares algorithm to minimize the difference between mean measured and predicted Δ_{47} values for five independent parameters: $\ln K_{0,\text{f}}$, $E_{a,\text{f}}$, $\ln K_{0,\text{diff,single}}$, $E_{a,\text{diff,single}}$, and mp.

Results of the error-weighted least squares fit are reported in Table 3.3, and shown in Fig. 3.2. The optimal value for m_p is markedly different from that of calcite: 0.0668 vs. 0.0992, which results in approximately two thirds of the predicted equilibrium pair excess at the same temperature. This discrepancy is not inherently problematic. Calcite and dolomite have different temperature sensitivities to a

T–Δ_{47} calibration		ln $K_{0,\text{exchange}}$	$E_{a,\text{exchange}}$	ln $K_{0,\text{diffusion}}$	$E_{a,\text{diffusion}}$	m_p
Eqn. 2, Bonifacie, Calmels, et al. (2017)	Best fit to measured data	21.5	194.5	31.8	273.6	0.0668
	Mean of acceptable fits	21.2	192.8	32.3	276.5	0.0663
	1σ standard deviation	1.2	7.6	1.8	11.9	0.0063
Table 6, E. A. Schauble, Ghosh, and John M Eiler (2006) + 0.176‰	Best fit to measured data	25.3	220.1	31.5	275.3	0.0766
	Mean of acceptable fits	24.2	214	31.9	278.8	0.072
	1σ standard deviation	2.1	13.5	2.5	16.3	0.015

Table 3.3: Dolomite Δ_{47} reordering parameters for the D. A. Stolper and J M Eiler (2015) exchange–diffusion model. Sources of fits, and units, are summarized in Table 3.2.

variety of equilibrium isotope effects; indeed, such discrepancies are the foundation for a variety of thermometers, including the dolomite–calcite ^{18}O and ^{13}C intermineral thermometers (Sheppard and Schwarcz, 1970). Since this apparent pair excess is hypothesized to represent a pseudo-secondary isotope effect by which the net free energy of a crystal lattice is lowered when heavy isotope-bearing carbonate groups are preferentially paired, it is reasonable to expect that the different lattice dimensions of different minerals would result in different temperature sensitivities to this hypothesized effect. As with the transient defect/equilibrium defect model, we used a Monte Carlo scheme to observe the dependence of the fitted parameters (ln $K_{0,\text{f}}$, $E_{a,\text{f}}$, ln $K_{0,\text{diff,single}}$, $E_{a,\text{diff,single}}$, and m_p) on the analytical uncertainties on the measurements underlying the mean Δ_{47} data. As in Section 4.3, we independently varied the raw Δ_{47} measurements by their uncertainties and re-fit the resulting data for 10,000 iterations. We then used the distributions of acceptable fits to observe the uncertainties on and correlations among the five parameters.

Mean Arrhenius parameters (and mp) for the Monte Carlo simulations are extremely similar to those of the best fit to the actual mean data (Table 3.3). Distributions of individual parameters are approximately Gaussian, suggesting that the standard deviations of these distributions are appropriate estimates of the totals uncertainties on these parameters (Fig. 3.11). As with the transient defect/equilibrium defect parameters, corresponding pairs of Arrhenius parameters for exchange and diffusion

rates are strongly correlated (Pearson r^2 values for exchange and diffusion components are 0.874 and 0.987, respectively), but only moderately correlated between mechanisms (r^2 of, at most, 0.227). Accordingly, we suggest covarying pairs of E_a and $\ln K_0$ for each rate constant when applying these parameters to forward reordering models, and only covarying paramaters across components in accordance with the correlations reported in Table 3.7. m_p values are apparently independent of all four Arrhenius parameters (max r^2 = 0.059), which suggests that fits are not sensitive to the exact m_p value chosen. If so, it is reasonable to fix m_p to its mean value (0.0663) in forward models.

Re-fitting calcite reordering data

In order to directly compare Arrhenius parameters for calcite and dolomite Δ_{47} reordering, these values must be reported in the same reference frame, and (ideally) be produced by the same data fitting routine. Although D. A. Stolper and J M Eiler (2015) report Δ_{47} data for their calcite heating experiments in the ARF, lacking a published Δ_{47}–T relation at the time, they are restricted to running reordering models in the intralaboratory Caltech Reference Frame (CRF). In addition to precluding direct comparison between our reordering parameters and theirs, this disconnect complicates the use of the calcite exchange–diffusion model to fit any data generated outside of Caltech, as such data must be artificially compressed into the CRF before modeling. To assist both our own comparisons and ongoing work of the community at large, we re-fit the original calcite heating experiments of D. A. Stolper and J M Eiler (2015) using the E. A. Schauble, Ghosh, and John M Eiler (2006)-derived Δ_{47}–T calibration and our own fitting algorithms described in Section 4.4. To better understand the sensitivity of the fits to the choice of m_p, as above, we treated this pairs slope as a true free parameter in all fits. To more accurately estimate the true uncertainties on the calcite reordering parameters, we ran analogous Monte Carlo simulations where individual calcite Δ_{47} measurements (provided by D. Stolper, pers. comm.) were randomly perturbed according to their analytical uncertainties and re-fit for 10,000 iterations. The resulting Arrhenius parameters and uncertainties are reported in Table 3.9.

3.6 Discussion

Here we compare our dolomite Δ_{47} reordering parameters to previously published parameters for calcite. We use trends among these parameters and external constraints to suggest that the exchange-diffusion model more closely approximates the

mechanism for the non-first order reordering behavior observed in all carbonates. We then use forward models and these favored Arrhenius parameters to predict Δ_{47} values of dolomites in a variety of geologically-relevant scenarios, and discuss the implications for preserving original dolomite Δ_{47} compositions and constraining the thermal histories of deeply-buried sediments.

Assessing the agreement with dolomite marbles

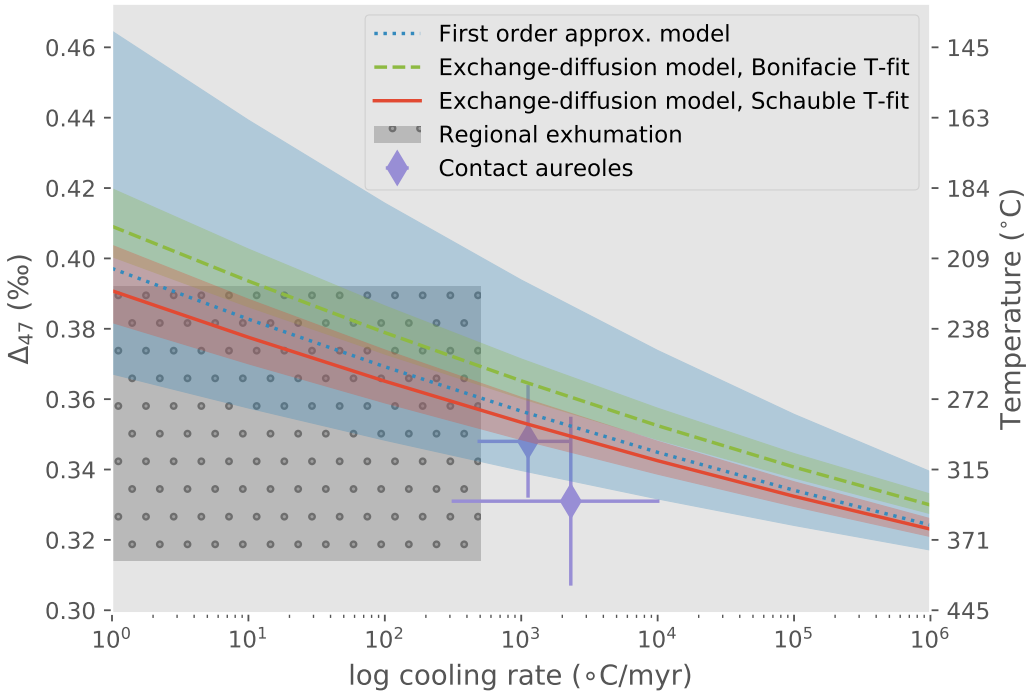

Figure 3.3: Predicted dependence of dolomite Δ_{47} apparent equilibrium blocking temperature on cooling rate, and the measured apparent equilibrium blocking temperatures of natural dolomite marbles. Blue, red, and green shaded regions denote 2σ uncertainties on predictions of the first order approximation to the transient defect/equilibrium defect model, and the exchange-diffusion model using two different T–D47 calibrations. Cooling rates with uncertainties for the Notch Peak and Predazzo contact aureoles were estimated from conductive cooling models described in Lloyd et al. (2017). Low temperature cooling rates from regionally exhumed terranes are rarely known with useful precision, and the range of apparent equilibrium temperatures measured in such systems is larger than would be expected if regional exhumation was the sole determining variable (c.f., Ryb et al. 2017). Thus, we plot only the rough region over which these processes are likely to operate.

Any reasonable model for dolomite Δ_{47} reordering must be able to reproduce the apparent equilibrium blocking temperatures measured in cooled metamorphic ter-

ranes. Dolomite Δ_{47} temperatures in high-grade marbles range from 250 to 450 °C, and broadly correlate with cooling rate: colder clumped isotope temperatures are found in slowly-cooled dolomite marbles from orogenic belts (e.g., del Real et al., 2016), while the hottest dolomite Δ_{47} temperatures are found in the contact aureoles from shallow plutonic intrusions (Ferry et al., 2011; (Lloyd, John M Eiler, and Nabelek, 2017)). We compared these values to those predicted by dolomite Δ_{47} reordering models during linear cooling from high temperature (Fig. 3.3). Briefly, we initialized reordering models with dolomite Δ_{47} values and pair concentrations in equilibrium at 600 °C, and held them at this temperature for 105 years. Then, we cooled the system from 600 to 0 °C at fixed rates between 100 and 106 °C/Ma. For both Δ_{47}–T calibrations, we modeled the changes in Δ_{47} values on these temperature-time paths using the exchange-diffusion model and the unannealable (equilibrium) component of the transient defect/equilibrium defect model, and the corresponding parameters for these models determined above. We estimated the uncertainties on the predictions of the first-order equilibrium defect model by co-varying pairs of $\ln K_c$ and E_c by the same proportion of their standard deviations and repeating the modeling exercise. The final predicted Δ_{47} values from the exchange-diffusion model were comparably sensitive to uncertainties on the rate constants for the exchange and diffusion components, but the uncertainties on the rate constants for these two components are largely uncorrelated with each other (r^2 =0.27). So, we sequentially perturbed the Arrhenius parameters for the two components and report the values most different from the mean value at every time point, for the most conservative estimate of the net effect of uncertainties on the predicted apparent equilibrium blocking temperatures for dolomite marbles.

Modeled apparent equilibrium blocking temperatures increase with increasing cooling rate (Fig. 3.3). Temperatures predicted by the two models agree within uncertainty, which suggests that the first-order approximation model may be sufficient for estimating the apparent equilibrium blocking temperatures in simple monotonic cooling systems. With the Bonifacie et al. (2016)-derived parameters, predicted Δ_{47}-derived temperatures from both models are moderately but notably colder than those measured in slowly-cooled dolomite marbles (Fig. 3.3). For instance, the exchange-diffusion model predicts apparent equilibrium temperatures of between 190 and 260 °C (2σ) for exhumation/cooling rates between 10 and 100 °C/Ma. And, apparent equilibrium blocking temperatures at or above 300 °C require exhumation rates in excess of ~5 x 103 °C/Ma. Directly comparing these predictions to observed Δ_{47} values from exhumed metamorphic terranes is challenging because

precise constraints on the cooling rates at these relatively low temperatures are uncommon, and processes related to exhumation such as strain-induced recrystallization tend to disperse Δ_{47} values and obscure primary reordering signals (Ryb et al., 2017). Comparisons with dolomite marbles from contact aureoles are more straightforward, although not necessarily more accurate, because their T-t paths can be estimated with conductive cooling models built for the geometry of specific intrusions (Lloyd, John M Eiler, and Nabelek, 2017). Nonetheless, we note that while both dolomite Δ_{47} reordering models agree with measured values from the Notch Peak aureole within 2σ uncertainty (Lloyd, John M Eiler, and Nabelek, 2017), only the first order approximation model is capable of reproducing the exceptionally low Δ_{47} value of the Predazzo aureole ($\Delta_{47,\mathrm{ARF}} = 0.327 \pm 0.023$‰; Ferry et al. (2011), but projected into the ARF using the transfer function of Ryb et al. (2017)), and even then only at the slowest reordering rates permitted by our 2σ uncertainty envelope.

On the other hand, with the E. A. Schauble, Ghosh, and John M Eiler (2006) calibration, acceptable agreement between natural dolomites and forward-modeled predictions is observed for both regionally-metamorphosed and contact-metamorphosed settings (Fig. 3.3). These discrepancies occur because Δ_{47}-derived temperature estimates in the realm of 250–450 °C are especially sensitive to the choice of calibration curve and minor (< 0.01‰) analytical artifacts, a persistent challenge of the technique (e.g., Huntington et al. (2009), Dennis, Affek, et al. (2011), and Daëron et al. (2016)). In fact, this temperature range is also where equilibrium dolomite Δ_{47} values are least well constrained: Δ_{47} values of synthetic dolomites grown at 302 and 351 °C disagree with predictions from the T–Δ_{47} calibration used in this study by 0.014 and 0.033 ‰, respectively (Bonifacie, Calmels, et al., 2017). Thus, these significant discrepancies indicate that dolomite clumping in the range of 250–450 °C is still incompletely understood, and could explain the apparent disagreement between our models and others' measurements. Because the Schauble-derived parameters agree better, we recommend using these values, and exclusively consider models built on these values for the remainder of this study. On the other hand, given the variations in the structural characteristics of natural dolomites, it is possible that the reordering parameters determined for the Eugui dolomite formed from hydrothermal fluid in an open fissure are not applicable to coarse, granoblastic dolomite fabrics formed under stress in regionally-metamorphosed sections. New heating experiments, with a different starting material, would be needed to address this possibility.

Comparisons with calcite reordering parameters

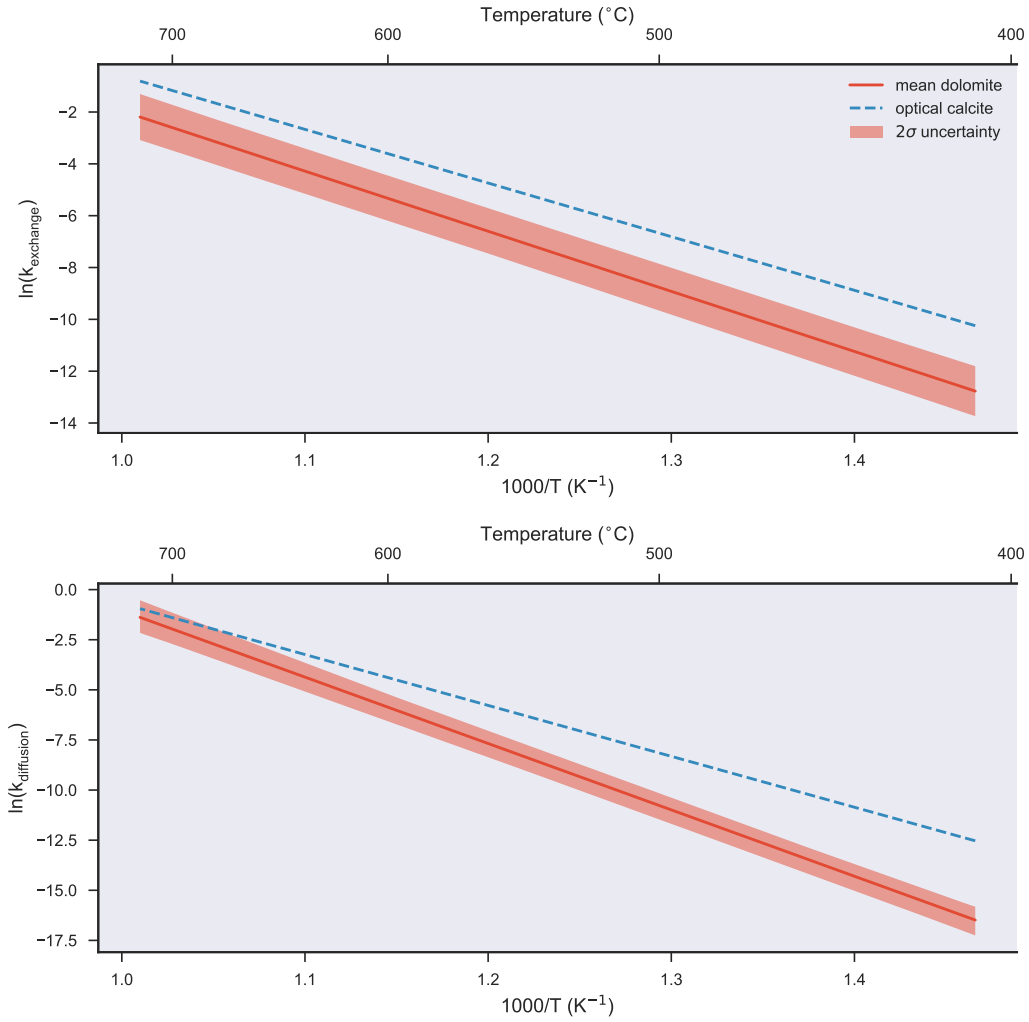

Figure 3.4: Arrhenius plots for the rate constants for the exchange and diffusion components of the D. A. Stolper and J M Eiler (2015) model. Dolomite rate constants (and uncertainties) from this study are compared with optical calcite rate constants from this publication.

Arrhenius plots of derived dolomite Δ_{47} reordering parameters can be used to directly compare these values with those of calcite, and consider whether trends in these parameters are consistent with expectations for the hypothesized mechanisms behind the two reordering models (Figs. 3.4, 3.5). We first consider the parameters of the exchange-diffusion model because their interpretation is more straightforward. Arrhenius parameters for dolomite are larger than calcite for both components, but more dissimilar from calcite with respect to the diffusion of singles. At temperatures below ~700 °C, dolomite reordering is generally slower than calcite, and this behav-

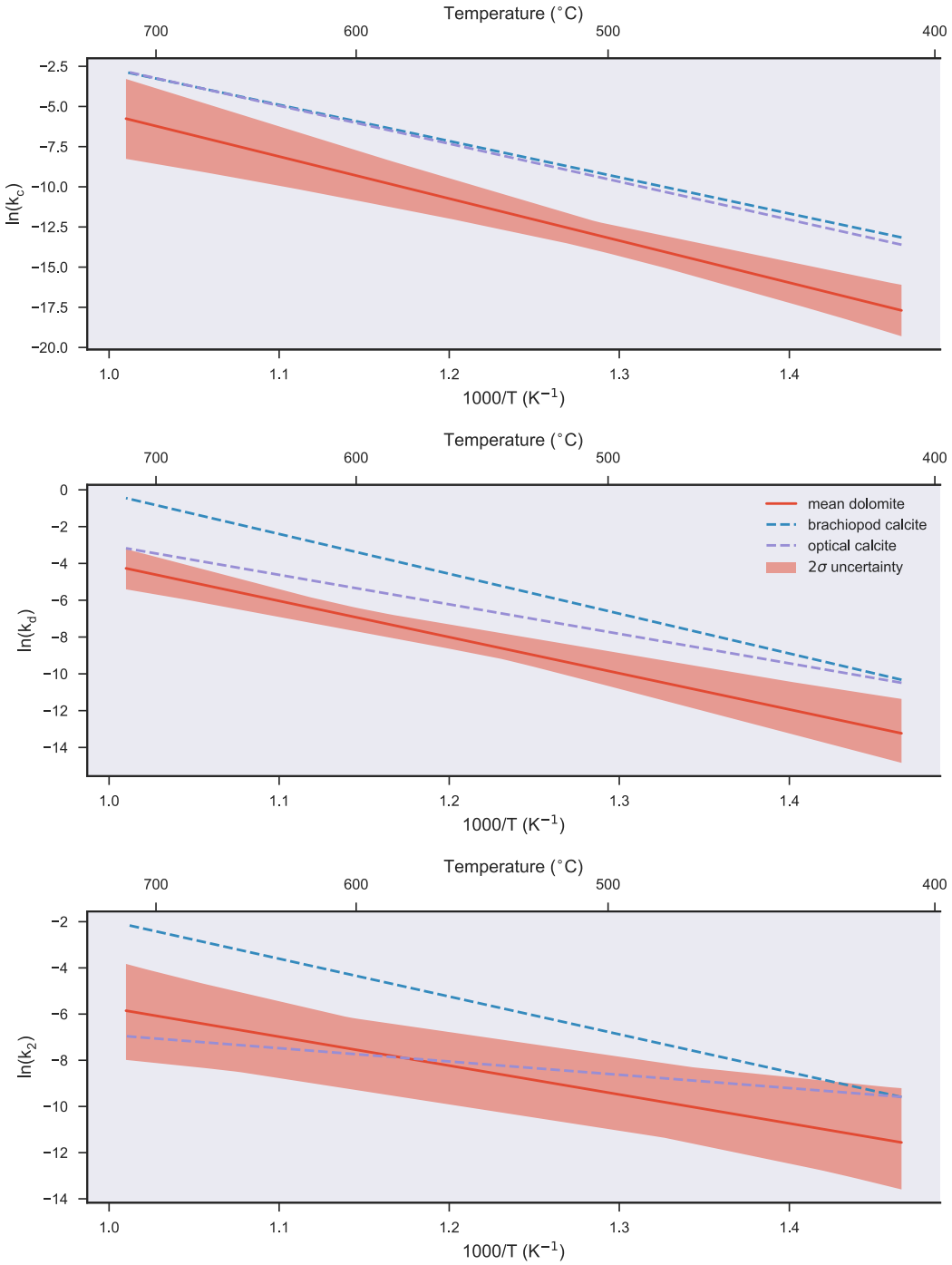

Figure 3.5: Arrhenius plots for the rate constants for the equilibrium component, transient component, and annealing rate on the transient component, for the Δ_{47} reordering model of Henkes et al. (2014)Henkes et al. (2014). These are compared to the parameters for optical calcite and brachiopod calcite reported therein.

ior is present in both components (Fig. 3.4). At 700 °C and above, the rate of isotopic exchange between pairs in dolomite continues to be somewhat slower than in cal-

cite (although perhaps not outside the uncertainty of the calcite parameters), while singles diffusion rates are indistinguishable between the phases. In extrapolations to temperatures below 400 °C, the rates of both mechanisms in calcite and dolomite diverge. This behavior is consistent with the compensation (Meyer-Neldel) rule, i.e., the empirical phenomenon that activation energies and pre-exponential factors of related chemical processes are typically correlated (e.g., Yelon, Movaghar, and Branz (1992)). A consequence of this effect is that the rates of chemical processes with a shared mechanism, such as the diffusion of species through similar crystal structures, tend to diverge at low temperatures and converge at a high temperature (Brady and Cherniak, 2010; J R Farver, 2010). The diffusivities of different elements in carbonates have an unusually strong adherence to the compensation rule (r^2 = 0.97; Brady and Cherniak (2010)), perhaps due to their simple stoichiometry and similar crystal structures. Experimental data for carbonates other than calcite are limited, but suggest that diffusivities of the same species are systematically slower in dolomite (Anderson, 1972). This ordering is consistent with the predictions of the anion porosity model of Zheng and Fu (1998), wherein the tighter packing of anions in dolomite unit cells results in increases in the activation energy and pre-exponential factor for oxygen self-diffusion in this phase. Of course, oxygen-self diffusion in carbonates and the singles diffusion component of clumped isotope reordering are not equivalent processes; indeed, the rates of these two processes are different in natural systems (Lloyd, John M Eiler, and Nabelek, 2017) ((Lloyd, John M Eiler, and Nabelek, 2017)), and the former is strongly dependent on f_{H_2O} while the latter apparently is not (Passey and Henkes, 2012). Instead, we merely note that the order of Δ_{47} reordering rates in calcite, dolomite, and magnesite suggested by the apparent equilibrium blocking temperatures in natural carbonates ((Real et al., 2016)Real et al., 2016; (Lloyd, John M Eiler, and Nabelek, 2017)), and corroborated by this study, is consistent with the ranking of ion porosities in these three related phases (Fortier and Giletti, 1989; Zheng and Fu, 1998). Moreover, it is noteworthy that the isokinetic temperature for elemental diffusion in carbonates—i.e., the temperature at which diffusivities of all species converge—is 690 °C (Brady and Cherniak, 2010), which is in good agreement with the temperature at which $k_{\text{diff,single}}$ in calcite and dolomite are indistinguishable (~700°C; Fig. 3.4). This is further, albeit circumstantial, evidence that the physical process represented by $k_{\text{diff,single}}$ may be comparable to atomic-scale diffusion through the crystal lattice. By the same logic, it is perhaps unsurprising that the rates of pair exchange in calcite and dolomite are so similar. If k_f represents the rate of exchange of ^{18}O atoms between neighboring

carbonate groups, its primary control should be the strength of the C–O bond. This C–O bond strength should be similar in all carbonates, and relatively insensitive to second-order effects such as the spacing of carbonate groups and the ionic strength of the local cations (Cole and Chakraborty, 2001).

The adherence of Arrhenius parameters for the exchange-diffusion model to expected trends for chemical processes such as diffusion and isotopic exchange is contrasted by the departure of parameters for the transient defect/equilibrium defect model from similar expectations. Although the activation energy for the equilibrium defect component in dolomite is most likely 20–30 kJ/mol larger than that of either optical calcite or brachiopod calcite, the dolomite pre-exponential factor is intermediate between the two (Henkes et al., 2014) ((Henkes et al., 2014)). Unusual trends are also apparent from the Arrhenius plots of the other two components (Fig. 3.5): rate constants for transient defect reordering and the annealing rate of these defects diverge at high temperatures, and converge, if at all, at temperatures less than 400 °C. It is reasonable to expect that defect concentration, and perhaps defect style, would be idiosyncratic to each carbonate grain and its formation environment (Passey and Henkes, 2012). It is more surprising that the concentration-normalized annealing rate is not an intrinsic property of a mineral. The progressive annealing of defects in carbonates has been invoked previously to explain the anomalously-rapid, time-dependent self-diffusion rate of oxygen in calcite at 550–600 °C (Kronenberg, Yund, and Giletti, 1984; John R Farver, 1994). Although the data from these experiments are too sparse to explicitly calculate Arrhenius parameters for this process, it is evident that the annealing rate operates on timescales of hours to days at 550 °C (John R Farver, 1994). Δ_{47} reordering experiments, however, suggest that calcites are fully annealed with respect to defects at 475 °C in a matter of minutes, and presumably in far less time at 550 °C (Henkes et al., 2014). Although these annealing rates are merely inferred from observations of the time-dependence of distinct processes that are not directly comparable (see above), the vast differences in rate are still difficult to reconcile. How can calcite be fully annealed with respect to Δ_{47} reordering after an hour at 475 °C, yet completely 'open' to transient defect-assisted ^{18}O diffusion after the same treatment? What physical change occurs in carbonates on hours-to-days timescales at 550 °C, and how does it affect Δ_{47} reordering kinetics? It is not possible to address the latter question with existing clumped isotope reordering datasets because all studied samples are fully or nearly equilibrated with respect to Δ_{47} at this temperature after an hour, but perhaps it will be possible by studying carbonates with slower reordering kinetics (such as, apparently, magnesite (Real

et al., 2016)). In general, the inconsistencies of Arrhenius parameters from this model with expectations for Arrhenian processes are by no means unassailable evidence that non-first order Δ_{47} reordering behavior is not defect-controlled. Still, due to the broad agreement of parameters from the exchange-diffusion model with expected trends in calcite and dolomite, we suggest that this formulation more closely approximates the behavior of carbonate groups in a crystal lattice.

Implications for recovery of dolomite formation temperatures and peak burial conditions

Dolomite reordering parameters can be used to predict the time-temperature treatments under which dolomite formation conditions can be recovered from ancient buried sections. We first explored the susceptibility of dolomite to reordering using simple 'box car' heating models (Fig. 3.6). In these scenarios, dolomite formed at 25 °C was instantaneously heated to a specified peak temperature, held there for 60 Ma, and then quenched back to 25 °C. Peak temperatures ranged between 120 and 240 °C. Predicted Δ_{47} values from the transient defect/equilibrium defect model and the first-order approximation model are indistinguishable over this range. Both models predict no measureable Δ_{47} reordering when dolomite is held at 150 °C or below. At 180 °C, dolomite Δ_{47}-derived temperatures are partially reordered from 25 °C to ~35 °C after 60 Ma. Full re-equilibration occurs at 210 °C and above, but the timescale for re-equilibration is sensitive to the exact peak temperature used: dolomite Δ_{47} values require 60 Ma to fully reorder at 210 °C, but less than 5 Ma to fully reorder at 240 °C. Error envelopes are omitted from Fig. 3.6 for clarity, but note that propagating uncertainties on the Arrhenius parameters for the equilibrium defect component dramatically shifts the window where dolomite Δ_{47} values are sensitive to specific temperatures. Over a conservative 1σ window of likely pairs of E_c and $\ln K_c$, dolomite Δ_{47} values held at 210 °C for 5 Ma may be fully re-equilibrated or not reordered at all. Likewise, the highest temperature that epigenetic dolomite can be held at for 60 Ma without measurably altering its Δ_{47} value may be as high as 190 °C or as low as 140 °C (within 1σ). Since laboratory experiments at or near these conditions would be impractical, observations of naturally reordered dolomite fabrics in well-constrained sections may be needed to more precisely calibrate these reordering kinetics.

In contrast to cooling systems where the first-order approximation and exchange-diffusion models give similar predictions, in box car heating scenarios significant differences in the style of predicted dolomite Δ_{47} reordering behavior are apparent.

Henkes et al. (2014)-style models predict a single temperature window over which the complete transition from unperturbed to fully-equilibrated Δ_{47} values occur, even if the exact location of this window is uncertain. In D. A. Stolper and J M Eiler (2015)-style models, dolomite Δ_{47} reordering during burial occurs in two distinct steps (Fig. 3.6). Partial re-equilibration occurs on various timescales between 150 and 210 °C. Once this partially reordered state is reached, Δ_{47} values are effectively invariant for the remainder of the heat treatment. Full Δ_{47} equilibrium is only approached at higher temperatures, likely ~240 °C and above. This two-phase behavior is a natural consequence of the model construction (D. A. Stolper and J M Eiler, 2015); rapid partial reordering occurs by destruction of $^{13}C^{18}O^{16}O_2{}^{2-}$ groups through exchange with neighboring carbonate groups containing no rare isotopes. In the temperature realm where singles are effectively closed to diffusion, this process builds up an excess of pairs that buffer the system against further reordering through the clump-forming back-reaction. Only at higher temperatures is the singles diffusion rate fast enough to deplete this pair excess and allow complete re-equilibration of the crystal. This same two-phase reordering style is observed in calcite, but at lower temperatures. Because the rates of exchange and diffusion are more disparate in dolomite than calcite, the temperature window in which Δ_{47} values are partially open to reordering is relatively large (~100 °C). Because partially reordered dolomite Δ_{47} values increase monotonically but with alternating concavity, large changes in apparent equilibrium Δ_{47} value can accompany small changes in ambient temperature around an inflection point.

To understand the implications of these nonlinear sensitivities of dolomite and calcite Δ_{47} reordering rates to certain temperature windows, we jointly modeled these two systems in a simple burial-residence-exhumation scenario (Fig. 3.7). Here, calcite Δ_{47} was initialized in equilibrium at 25 °C and dolomite Δ_{47} at 50 °C. We heated both of these by burying the system at a rate of 1 mm/yr along a geotherm of 25 °C/km to a depth and peak temperature of 9 km at 225 °C. Calcite and dolomite were held at this depth for 5 Ma, and subsequently exhumed to surface conditions at the same rate as burial. Initial calcite and dolomite Δ_{47} compositions are scrambled at temperatures similar to those suggested from binary box-car models: calcite Δ_{47} values begin to reorder at ambient temperatures as low as 120 °C, while dolomite Δ_{47} values resist reordering until at least 160 °C. Due to the offset two-stage reordering required by the exchange-diffusion models, three switches in the relative ordering of dolomite and calcite apparent equilibrium temperatures are predicted over the course of a typical burial path (Fig. 3.7). Below

120°C, the differences between calcite and dolomite Δ_{47} values should equate to their true differences because neither has reordered. When calcite Δ_{47} values are open to partial reordering through exchange with neighbors but dolomite Δ_{47} are not (~135–160 °C), the former should have a higher apparent equilibrium temperature, largely independent of the actual formation temperatures of the two phases. Dolomite is only partially open to re-equilibration where calcite can fully equilibrate, so in this window (~170–200 °C) calcite apparent temperatures should rapidly shift from similar to, to dramatically hotter than, dolomite apparent temperatures. Given reasonably rapid exhumation rates, the relative ordering of calcite and dolomite Δ_{47} apparent equilibrium temperatures should be preserved. Importantly, this finding suggests that measurements of Δ_{47} values from coexisting calcite and dolomite fabrics should provide tighter constraints on burial histories of deeply buried sections than measurements of a single phase alone. For instance, an infinitude of non-unique T-t paths can generate partially reordered calcite with an apparent equilibrium temperature of 125 °C, including a rapid quench of a section that barely reached 200 °C, or a slow exhumation of a section buried considerably deeper. Based on whether they are below or above calcite, apparent equilibrium temperatures in dolomite would easily distinguish between these two end-members. Conversely, if no calcite Δ_{47} values are in apparent equilibrium above ~75 °C, then peak conditions were insufficient to even partially reorder dolomite, and dolomite Δ_{47} values can be interpreted as faithful records of dolomitization conditions in the section.

3.7 Conclusions

Dolomite Δ_{47} values have great potential for comparing the conditions of dolomitization in ancient carbonate sections to those of the modern, but only if these clumped isotope compositions were unmodified by prolonged burial heating in the intervening times. We subjected fragments of a stoichiometric, well-ordered dolomite crystal aggregate to isothermal heating experiments in a cold seal apparatus held at 409 to 717 °C for between 5 minutes and 455 hours to observe the dependence of dolomite Δ_{47} reordering rate on temperature and time. We fit these data to two existing models for carbonate clumped isotope reordering, generating Arrhenius parameters that can be used to predict dolomite Δ_{47} values for any reasonable temperature-time path. Although we prefer the exchange-diffusion model of D. A. Stolper and J M Eiler (2015) to the transient defect/equilibrium defect model of Henkes et al. (2014) because derived parameters for the latter model are less consistent with expected trends among diffusivities in carbonates, both models are capable of reproducing the ap-

parent equilibrium blocking temperatures observed in cooled high-grade dolomites from contact aureoles and regionally metamorphosed terranes (~250–300 °C). The reordering style in simple burial heating scenarios differs markedly between the models, but the models agree that dolomite is likely resistant to reordering of diagenetic Δ_{47} values at ambient temperatures at least as high as 120 °C, and possibly up to 160 °C, for geologic timescales. Due to their distinct reordering kinetics, we suggest that Δ_{47} measurements from coexisting calcite and dolomite fabrics can be used to distinguish among burial histories that would be otherwise ambiguous.

3.8 Supplementary Materials

	CaO (wt. %)	MgO (wt. %)	FeO (wt. %)	MnO (wt. %)	CO_2 (wt. %)	Total (wt. %)	
Colorless crystal	29.93	21.21	0.48	0.08	47.37	99.07	Mean
	0.13	0.25	0.07	0.02	N/A	0.21	1 Std. Dev. (n = 10)
White crystal	30.14	21.27	0.23	0.1	47.37	99.1	Mean
	0.19	0.24	0.04	0.01	N/A	0.28	1 Std. Dev. (n = 10)

Table 3.4: Major and minor element contents of two crystal fragments of the starting material of this study, determined on a JEOL JXA-8200 electron probe micro-analyzer with a KeV beam, 20 nA beam current, and a 10 μm spot size. CO_2 content was not measured; reported CO_2 values assume material has perfect carbonate stoichiometry.

Meas. date	Run num.	Run T (°C)	Run time (hrs)	$\delta^{13}C$ (VPDB)	$\delta^{13}C$ 1σ std (‰)	$\delta^{18}O_{mineral}$ (VPDB)	$\delta^{18}O$ 1σ std (‰)	Δ_{47} (‰)	Δ_{47} 1σ s.e. (‰)
4/29/14	9	400	42	2.374	0.003	-14.66	0.006	0.436	0.013
4/29/14	9	400	42	2.406	0.004	-14.563	0.01	0.421	0.012
4/30/14	9	400	42	2.359	0.003	-14.734	0.005	0.433	0.014
5/5/14	9	400	42	2.352	0.004	-14.547	0.011	0.44	0.007
9/21/14	15	400	311	2.179	0.002	-14.901	0.004	0.408	0.005
5/2/15	15	400	311	2.189	0.002	-17.547	0.006	0.459	0.008
9/21/15	15	400	311	2.328	0.002	-14.26	0.007	0.336	0.01
9/23/15	15	400	311	2.289	0.002	-14.336	0.004	0.405	0.021
9/27/15	15	400	311	2.327	0.003	-14.226	0.006	0.366	0.013
9/17/14	13	450	314	2.789	0.002	-14.287	0.002	0.384	0.007
9/18/14	13	450	314	1.956	0.001	-12.627	0.004	0.349	0.014
9/19/14	13	450	314	2.685	0.004	-14.499	0.004	0.395	0.011
10/22/14	13	450	314	2.649	0.003	-14.598	0.005	0.405	0.008
10/22/14	13	450	314	2.649	0.003	-14.603	0.004	0.405	0.014
10/23/14	13	450	314	2.626	0.003	-14.417	0.003	0.392	0.013
10/25/14	13	450	314	2.757	0.001	-14.286	0.004	0.399	0.013
10/26/14	14	450	86	2.521	0.002	-14.136	0.007	0.384	0.016
10/27/14	14	450	86	2.398	0.003	-13.358	0.004	0.373	0.012
11/16/14	14	450	86	2.532	0.001	-14.012	0.005	0.41	0.01
9/21/15	14	450	86	2.516	0.003	-13.913	0.009	0.368	0.013
9/26/15	14	450	86	2.55	0.002	-13.822	0.003	0.347	0.015
4/17/15	27	475	24	2.692	0.003	-13.905	0.007	0.399	0.012
4/18/15	27	475	24	2.697	0.003	-13.99	0.008	0.412	0.011
4/20/15	27	475	24	2.631	0.003	-14.096	0.005	0.413	0.009
9/19/15	27	475	24	2.745	0.005	-13.843	0.005	0.379	0.019
9/21/15	27	475	24	2.704	0.003	-13.971	0.004	0.421	0.015
9/25/15	27	475	24	2.734	0.004	-13.685	0.005	0.393	0.011
9/28/15	27	475	24	2.768	0.003	-13.741	0.002	0.392	0.01

Table 3.6 continued from previous page

Meas. date	Run num.	Run T (°C)	Run time (hrs)	$\delta^{13}C$ (VPDB)	$\delta^{13}C$ 1σ std (‰)	$\delta^{18}O_{mineral}$ (VPDB)	$\delta^{18}O$ 1σ std (‰)	Δ_{47} (‰)	Δ_{47} 1σ s.e. (‰)
4/18/15	28	475	455.28	2.38	0.002	-14.14	0.007	0.358	0.008
4/18/15	28	475	455.28	2.374	0.002	-14.217	0.004	0.314	0.011
9/19/15	28	475	455.28	2.422	0.002	-13.946	0.005	0.346	0.006
9/21/15	28	475	455.28	2.423	0.005	-14.121	0.006	0.328	0.011
9/25/15	28	475	455.28	2.461	0.003	-13.967	0.003	0.32	0.013
9/19/15	29	475	68.8	2.665	0.004	-13.997	0.013	0.304	0.013
9/22/15	29	475	68.8	2.633	0.003	-14.146	0.004	0.381	0.009
9/25/15	29	475	68.8	2.727	0.003	-13.968	0.005	0.377	0.017
9/26/15	29	475	68.8	2.692	0.003	-13.941	0.006	0.334	0.021
9/20/15	30	475	2.4	2.545	0.003	-14.083	0.005	0.427	0.02
9/24/15	30	475	2.4	2.401	0.005	-13.112	0.005	0.389	0.021
9/24/15	30	475	2.4	2.59	0.002	-13.904	0.002	0.419	0.009
9/19/15	31	475	169.4	2.755	0.004	-14.086	0.004	0.35	0.014
9/24/15	31	475	169.4	2.82	0.004	-13.951	0.005	0.354	0.017
9/26/15	31	475	169.4	2.818	0.004	-13.911	0.004	0.34	0.017
9/19/15	32	475	238.2	2.455	0.003	-14.216	0.005	0.347	0.006
9/22/15	32	475	238.2	2.467	0.003	-14.185	0.012	0.328	0.014
9/25/15	32	475	238.2	2.546	0.002	-14.03	0.007	0.329	0.019
4/24/14	6	500	48.2	2.35	0.005	-15.016	0.012	0.33	0.014
4/25/14	6	500	48.2	2.391	0.002	-14.926	0.005	0.343	0.009
4/26/14	6	500	48.2	2.415	0.005	-14.808	0.014	0.353	0.018
5/1/14	10	500	1	2.26	0.003	-14.92	0.01	0.404	0.012
5/2/14	10	500	1	2.283	0.004	-14.934	0.007	0.407	0.008
5/2/14	10	500	1	2.275	0.005	-14.833	0.014	0.391	0.007
5/3/14	11	500	12.83	2.117	0.003	-14.576	0.01	0.332	0.008
5/3/14	11	500	12.83	2.165	0.005	-14.451	0.02	0.359	0.008
5/4/14	11	500	12.83	2.151	0.005	-14.479	0.014	0.337	0.014
5/4/14	11	500	12.83	2.111	0.003	-14.629	0.008	0.365	0.012
5/4/14	12	500	2.5	2.404	0.003	-14.265	0.02	0.412	0.009
5/4/14	12	500	2.5	2.393	0.004	-14.326	0.019	0.405	0.008
5/4/14	12	500	2.5	2.381	0.004	-14.309	0.015	0.412	0.011
5/5/14	12	500	2.5	2.37	0.003	-14.363	0.031	0.422	0.01
11/15/14	12	500	2.5	2.466	0.004	-14.091	0.007	0.402	0.01
10/24/14	16	500	65	2.335	0.001	-14.812	0.004	0.371	0.006
10/25/14	16	500	65	2.539	0.004	-14.27	0.007	0.329	0.009
10/26/14	16	500	65	2.539	0.003	-14.251	0.007	0.344	0.009
10/26/14	16	500	65	2.547	0.003	-14.234	0.007	0.341	0.011
10/26/14	17	500	160	2.053	0.003	-14.748	0.003	0.347	0.01
10/26/14	17	500	160	2.064	0.002	-14.678	0.006	0.33	0.009

Table 3.6 continued from previous page

Meas. date	Run num.	Run T (°C)	Run time (hrs)	$\delta^{13}C$ (VPDB)	$\delta^{13}C$ 1σ std (‰)	$\delta^{18}O_{mineral}$ (VPDB)	$\delta^{18}O$ 1σ std (‰)	Δ_{47} (‰)	Δ_{47} 1σ s.e. (‰)
10/27/14	17	500	160	2.031	0.004	-14.801	0.005	0.337	0.007
10/27/14	17	500	160	1.735	0.005	-13.372	0.013	0.292	0.012
10/31/14	21	550	160.5	2.442	0.002	-15.007	0.005	0.352	0.016
11/14/14	21	550	160.5	2.786	0.004	-14.077	0.008	0.278	0.011
9/22/15	21	550	160.5	2.756	0.003	-13.974	0.008	0.27	0.012
11/13/14	22	550	17	2.652	0.005	-14.401	0.008	0.32	0.012
11/13/14	22	550	17	2.177	0.003	-14.239	0.003	0.325	0.009
9/27/15	22	550	17	1.998	0.004	-14.387	0.008	0.294	0.016
9/27/15	22	550	17	2.003	0.004	-14.368	0.005	0.34	0.022
9/27/15	22	550	17	2	0.002	-14.339	0.004	0.312	0.018
11/13/14	23	550	67.75	2.528	0.003	-14.52	0.005	0.337	0.009
11/13/14	23	550	67.75	2.573	0.005	-14.528	0.005	0.32	0.007
11/17/14	23	550	67.75	2.574	0.003	-14.533	0.004	0.303	0.006
9/20/15	23	550	67.75	2.506	0.004	-14.518	0.005	0.322	0.011
9/24/15	23	550	67.75	2.582	0.002	-14.28	0.01	0.271	0.012
11/14/14	24	550	1	2.782	0.004	-14.337	0.006	0.363	0.005
11/15/14	24	550	1	2.515	0.003	-14.06	0.003	0.348	0.011
9/20/15	24	550	1	2.747	0.003	-14.19	0.008	0.345	0.006
9/26/15	24	550	1	2.74	0.003	-14.184	0.005	0.38	0.016
4/27/14	1	600	0.08	2.148	0.005	-14.857	0.018	0.402	0.011
4/27/14	1	600	0.08	2.151	0.004	-14.847	0.013	0.388	0.012
4/28/14	1	600	0.08	2.107	0.003	-14.874	0.01	0.387	0.012
4/29/14	1	600	0.08	2.142	0.003	-14.922	0.011	0.408	0.011
4/24/14	4	600	1	2.861	0.002	-14.345	0.012	0.324	0.013
4/26/14	4	600	1	2.847	0.005	-14.351	0.014	0.339	0.014
4/27/14	4	600	1	2.81	0.003	-14.516	0.006	0.314	0.006
4/29/14	7	600	3	2.308	0.003	-14.952	0.007	0.317	0.008
4/30/14	7	600	3	2.33	0.003	-14.855	0.002	0.305	0.011
4/30/14	7	600	3	2.323	0.004	-14.831	0.007	0.311	0.012
9/17/14	18	600	64	2.141	0.002	-14.686	0.004	0.322	0.013
9/18/14	18	600	64	2.035	0.001	-14.954	0.005	0.345	0.011
9/20/14	18	600	64	2.038	0.001	-14.92	0.003	0.34	0.01
10/21/14	18	600	64	1.887	0.002	-14.827	0.005	0.321	0.007
10/23/14	18	600	64	1.936	0.002	-15.175	0.005	0.356	0.008
10/25/14	18	600	64	2.233	0.005	-14.475	0.006	0.283	0.01
10/27/14	18	600	64	2.198	0.004	-14.525	0.005	0.296	0.006
9/17/14	19	600	4.07	1.922	0.002	-15.001	0.003	0.328	0.015
9/18/14	19	600	4.07	1.934	0.003	-14.953	0.005	0.333	0.01
9/20/14	19	600	4.07	1.867	0.003	-15.073	0.007	0.351	0.005

Table 3.6 continued from previous page

Meas. date	Run num.	Run T (°C)	Run time (hrs)	δ^{13}C (VPDB)	δ^{13}C 1σ std (‰)	$\delta^{18}O_{mineral}$ (VPDB)	δ^{18}O 1σ std (‰)	Δ_{47} (‰)	Δ_{47} 1σ s.e. (‰)
10/22/14	19	600	4.07	1.725	0.001	-15.451	0.003	0.356	0.007
10/22/14	19	600	4.07	1.798	0.003	-15.302	0.006	0.326	0.009
10/23/14	19	600	4.07	1.716	0.002	-15.474	0.005	0.35	0.005
10/25/14	19	600	4.07	1.965	0.002	-14.624	0.006	0.323	0.008
9/17/14	20	600	0.42	1.872	0.002	-15.049	0.004	0.337	0.012
9/19/14	20	600	0.42	1.902	0.002	-14.958	0.004	0.322	0.012
10/25/14	20	600	0.42	2.096	0.002	-14.372	0.006	0.34	0.012
10/27/14	20	600	0.42	2.094	0.002	-14.411	0.01	0.326	0.008
11/14/14	25	600	0.25	2.065	0.003	-14.341	0.006	0.348	0.008
11/16/14	25	600	0.25	2.116	0.004	-14.205	0.013	0.362	0.01
9/20/15	25	600	0.25	2.084	0.003	-14.192	0.011	0.322	0.025
11/15/14	26	600	0.125	2.6	0.004	-14.218	0.005	0.382	0.006
11/16/14	26	600	0.125	2.67	0.004	-14.121	0.006	0.392	0.012
11/17/14	26	600	0.125	2.658	0.003	-14.224	0.005	0.391	0.008
4/24/14	3	700	0.08	2.477	0.003	-14.236	0.008	0.302	0.012
4/23/14	5	700	0.75	2.538	0.004	-14.507	0.008	0.302	0.01
4/25/14	5	700	0.75	2.494	0.003	-14.623	0.005	0.292	0.015
4/26/14	5	700	0.75	2.563	0.004	-14.485	0.01	0.277	0.014
10/22/14	8	700	15.25	2.124	0.003	-14.962	0.004	0.327	0.009
10/23/14	8	700	15.25	2.117	0.002	-14.992	0.003	0.349	0.007
10/25/14	8	700	15.25	2.352	0.002	-14.38	0.004	0.307	0.017
11/15/14	8	700	15.25	2.359	0.002	-14.293	0.005	0.304	0.008

Table 3.6: Individual single and clumped isotope measurements of dolomite samples from each heating experiment. Uncertainties on δ^{13}C and δ^{18}O values are 1σ standard deviations of replicate measurements. Uncertainties on Δ_{47} are 1σ standard errors of the mean. Note that here, reported temperatures are furnace setpoints, which were converted to actual temperatures in the sample chamber using the calibration described in Section 2.3

date	Crystal corner	$\delta^{13}C$ (VPDB)	$\delta^{13}C$ 1σ std (‰)	$\delta^{18}O_{mineral}$ (VPDB)	$\delta^{18}O$ 1σ std (‰)	Δ_{47} (‰)	Δ_{47} 1σ s.e. (‰)
11/15/13	BM	2.765	0.005	-14.325	0.011	0.47	0.008
11/16/13	BM	2.65	0.005	-14.701	0.008	0.456	0.019
11/17/13	BM	2.661	0.003	-14.717	0.008	0.435	0.011
11/17/13	BM	2.686	0.003	-14.621	0.008	0.446	0.012
4/27/14	BR	2.153	0.002	-14.778	0.005	0.451	0.014
4/28/14	BR	2.204	0.003	-14.658	0.007	0.44	0.012
4/29/14	BR	2.222	0.003	-14.655	0.009	0.448	0.012
11/17/13	FL	2.741	0.006	-14.21	0.009	0.484	0.021
5/2/14	FL	2.824	0.004	-13.944	0.02	0.474	0.017
5/3/14	FL	2.704	0.003	-14.193	0.009	0.442	0.016
5/4/14	FL	2.83	0.004	-13.866	0.019	0.461	0.009
9/18/14	FL	2.732	0.002	-14.213	0.004	0.46	0.009
9/19/14	FL	2.7	0.003	-14.223	0.006	0.487	0.012
10/24/14	FL	2.839	0.002	-13.86	0.004	0.432	0.013
10/26/14	FL	2.817	0.003	-13.988	0.002	0.45	0.013
10/27/14	FL	2.856	0.004	-13.853	0.006	0.472	0.01
9/19/15	FL	2.787	0.002	-13.687	0.005	0.444	0.018
9/20/15	FL	2.807	0.004	-13.776	0.009	0.457	0.02
9/23/15	FL	2.845	0.005	-13.672	0.005	0.451	0.016
12/18/13	FR	2.774	0.003	-13.655	0.005	0.44	0.012
12/19/13	FR	2.775	0.002	-13.748	0.005	0.443	0.016
4/27/14	FR	2.554	0.005	-14.07	0.024	0.455	0.01
4/28/14	FR	2.536	0.006	-14.104	0.02	0.439	0.012
11/15/13	GB	2.483	0.004	-14.945	0.008	0.425	0.015
11/16/13	GB	2.514	0.004	-14.867	0.003	0.445	0.005
11/17/13	GB	2.458	0.004	-14.996	0.009	0.459	0.018
11/19/13	MCW	2.368	0.005	-17.394	0.01	0.463	0.022
12/19/13	MCW	2.668	0.004	-16.852	0.009	0.44	0.018
11/13/14	MCW	2.314	0.003	-17.365	0.006	0.455	0.017
5/1/15	MCW	2.034	0.003	-14.944	0.004	0.461	0.017
5/2/15	MCW	2.347	0.003	-17.062	0.008	0.434	0.01
11/17/13	WCR	2.344	0.004	-14.856	0.008	0.46	0.014
12/18/13	WCR	2.612	0.005	-14.206	0.007	0.451	0.015
12/19/13	WCR	2.624	0.006	-14.136	0.026	0.447	0.015
12/19/13	WCR	2.628	0.003	-14.131	0.015	0.456	0.012

Table 3.5: Individual measurements of unheated fragments of the Eugui dolomite crystal aggregate, from disparate locations of the sample.

References

Anderson, T F (1972). "Self-diffusion of carbon and oxygen in dolomite". In: *Journal of Geophysical Research* 77, pp. 857–862.

Arvidson, R S and F T Mackenzie (1999). "The dolomite problem; control of precipitation kinetics by temperature and saturation state". In: *American Journal of Science* 299.4, pp. 257–288.

	$\ln K_c$	E_c	$\ln K_d$	E_d	$\ln K_2$	E_2
$\ln K_c$	1	0.996	-0.213	-0.202	0.143	0.127
E_c	0.996	1	-0.19	-0.179	0.155	0.143
$\ln K_d$	-0.213	-0.19	1	0.996	0.737	0.783
E_d	-0.202	-0.179	0.996	1	0.712	0.767
$\ln K_2$	0.143	0.155	0.737	0.712	1	0.994
E_2	0.127	0.143	0.783	0.767	0.994	1

Table 3.7: Pearson correlation coefficients for the families of Arrhenius parameters for the transient defect/equilibrium defect model generated using the Monte Carlo scheme described in Section 4.3

	$\ln K_{\text{exchange}}$	$E_{a\text{exchange}}$	$\ln K_{\text{diffusion}}$	$E_{a\text{diffusion}}$	m_p
$\ln K_{\text{exchange}}$	1	0.935	-0.477	-0.463	0.045
$E_{a\text{exchange}}$	0.935	1	-0.377	-0.357	-0.195
$\ln K_{\text{diffusion}}$	-0.477	-0.377	1	0.994	-0.187
$E_{a\text{diffusion}}$	-0.463	-0.357	0.994	1	-0.242
m_p	0.045	-0.195	-0.187	-0.242	1

Table 3.8: Pearson correlation coefficients for the families of Arrhenius parameters and m_p for the exchange-diffusion model, generated using the Monte Carlo scheme described in Section 4.4

Barber, D J, H C Heard, and H R Wenk (1981). "Deformation of dolomite single crystals from 20–800 C". In: *Physics and Chemistry of Minerals* 7, pp. 271–286.

Barber, D J, R J Reeder, and D J Smith (1985). "A TEM microstructural study of dolomite with curved faces (saddle dolomite)". In: *Contributions to Mineralogy and Petrology* 91, pp. 82–92.

Bergmann, Kristin Diane (2013). "Constraints on the carbon cycle and climate during the early evolution of animals". PhD thesis. California Institute of Technology.

Blank, J G, E M Stolper, and M R Carroll (1993). "Solubilities of carbon dioxide and water in rhyolitic melt at 850 C and 750 bars". In: *Earth and Planetary Science Letters*.

Blättler, Clara L, Nathaniel R Miller, and John A Higgins (2015). "Mg and Ca isotope signatures of authigenic dolomite in siliceous deep-sea sediments". In: *Earth and Planetary Science Letters* 419.C, pp. 32–42.

Bonifacie, Magali, Damien Calmels, et al. (2017). "Calibration of the dolomite clumped isotope thermometer from 25 to 350°C, and implications for a universal calibration for all (Ca, Mg, Fe)CO3 carbonates". In: *Geochimica et Cosmochimica Acta VL - IS - SP - EP - PY - T2 -* 200, pp. 255–279.

T–Δ_{47}calibration		$\ln K_{0,\text{exch}}$	$E_{a,\text{exch}}$	$\ln K_{0,\text{diff}}$	$E_{a,\text{diff}}$	m_p
Eqn. 2, Bonifacie, Calmels, et al. (2017)	Best fit to measured data	25.3	203.5	32.4	259.3	0.0856
	Mean of acceptable fits	25.9	204.2	37.4	290.1	0.0903
	1_ standard deviation	4.1	25.3	2.1	14	0.0033
Table 6, E. A. Schauble, Ghosh, and John M Eiler (2006) + 0.176‰	Best fit to measured data	32.2	243.9	33.4	265.5	0.0959
	Mean of acceptable fits	32.2	243.9	33.4	265.5	0.0959
	1_ standard deviation	4.7	27.2	1.1	6.6	0.007

Table 3.9: Calcite Δ_{47} reordering parameters for the data of D. A. Stolper and J M Eiler (2015) exchange–diffusion model. Sources of fits, and units, are summarized in Table 2.

Bonifacie, Magali, John M Ferry, et al. (2011). "Calibration and applications of the dolomite clumped isotope thermometer to high temperatures". In: *Mineralogical Magazine* 75.3, p. 551.

Brady, J B and D J Cherniak (2010). "Diffusion in Minerals: An Overview of Published Experimental Diffusion Data". In: *Reviews in Mineralogy and Geochemistry* 72.1, pp. 899–920.

Brand, Willi A, Sergey S Assonov, and Tyler B Coplen (2010). "Correction for the 17O interference in δ(13C) measurements when analyzing CO2 with stable isotope mass spectrometry (IUPAC Technical Report)". In: *Pure and Applied Chemistry* 82.8.

Chai, L and A Navrotsky (1996). "Synthesis, characterization, and energetics of solid solution along the dolomite-ankerite join, and implications for the stability of ordered CaFe (CO3) 2". In: *American Mineralogist* 81, pp. 1141–1147.

Cole, D R and S Chakraborty (2001). "Rates and mechanisms of isotopic exchange". In: *Reviews in Mineralogy and . . .*

Daëron, M et al. (2016). "Absolute isotopic abundance ratios and the accuracy of Δ47 measurements". In: *Chemical Geology* 442 IS -, pp. 83–96.

Dennis, Kate J, Hagit P Affek, et al. (2011). "Defining an absolute reference frame for 'clumped' isotope studies of CO2". In: *Geochimica et Cosmochimica Acta VL - IS - SP - EP - PY - T2 -* 75.22, pp. 7117–7131.

Dennis, Kate J and Daniel P Schrag (2010). “Clumped isotope thermometry of carbonatites as an indicator of diagenetic alteration”. In: *Geochimica et Cosmochimica Acta VL - IS - SP - EP - PY - T2* - 74.14, pp. 4110–4122.

Eiler, John M (2007). ““Clumped-isotope” geochemistry—The study of naturally-occurring, multiply-substituted isotopologues”. In: *Earth and Planetary Science Letters* 262.3–4, pp. 309–327.

– (2011). “Paleoclimate reconstruction using carbonate clumped isotope thermometry”. In: *Quaternary Science Reviews* 30.25-26, pp. 3575–3588.

Eiler, John M and Edwin Schauble (2004). “18O13C16O in Earth’s atmosphere”. In: *Geochimica et Cosmochimica Acta* 68.23, pp. 4767–4777.

Farver, J R (2010). “Oxygen and Hydrogen Diffusion in Minerals”. In: *Reviews in Mineralogy and Geochemistry* 72.1, pp. 447–507.

Farver, John R (1994). “Oxygen self-diffusion in calcite: Dependence on temperature and water fugacity”. In: *Earth and Planetary Science Letters* 121.3–4, pp. 575–587.

Ferry, J M et al. (2011). “Formation of dolomite at 40-80 C in the Latemar carbonate buildup, Dolomites, Italy, from clumped isotope thermometry”. In: *Geology* 39.6, pp. 571–574.

Fortier, S M and B J Giletti (1989). “An empirical model for predicting diffusion coefficients in silicate minerals”. In: *Science* 245, pp. 1481–1484.

Ghosh, Prosenjit et al. (2006). “13C-18O bonds in carbonate minerals: A new kind of paleothermometer”. In: *Geochimica et Cosmochimica Acta* 70.6, pp. 1439–1456.

Goldsmith, Julian R and Hugh C Heard (1961). “Subsolidus phase relations in the system CaCO3–MgCO3”. In: *The Journal of Geology*, pp. 45–74.

Graf, Donald L and Julian R Goldsmith (1955). “Dolomite—magnesian calcite relations at elevated temperatures and CO 2 pressures”. In: 7.3, pp. 109–128.

Gregg, Jay M et al. (2015). “Mineralogy, nucleation and growth of dolomite in the laboratory and sedimentary environment: A review”. In: *Sedimentology* 62.6, pp. 1749–1769.

Héberger, K and S Kemény (1987). “On the errors of Arrhenius parameters and estimated rate constant values”. In: *International Journal of Chemical Kinetics* 19, pp. 171–181.

Henkes, Gregory A et al. (2014). “Temperature limits for preservation of primary calcite clumped isotope paleotemperatures”. In: 139.C, pp. 362–382.

Huntington, K W et al. (2009). “Methods and limitations of ‘clumped’ CO2 isotope ($\Delta 47$) analysis by gas-source isotope ratio mass spectrometry”. In: *Journal of Mass Spectrometry* 44.9, pp. 1318–1329.

Jonas, Laura et al. (2015). “Transport-controlled hydrothermal replacement of calcite by Mg-carbonates”. In: *Geology* 43.9, pp. 779–782.

Jones, B, R W Luth, and A J MacNeil (2001). “Powder X-ray diffraction analysis of homogeneous and heterogeneous sedimentary dolostones”. In: *Journal of Sedimentary Research* 71, pp. 790–799.

Kolodny, Y and I R Kaplan (1970). “Carbon and oxygen isotopes in apatite CO2 and co-existing calcite from sedimentary phosphorite”. In: *Journal of Sedimentary Research* 40.3, pp. 954–959.

Kronenberg, A K, R A Yund, and B J Giletti (1984). “Carbon and oxygen diffusion in calcite: Effects of Mn content and p H 2 O”. In: *Physics and Chemistry of Minerals*.

Lloyd, Max K, John M Eiler, and Peter I Nabelek (2017). “Clumped isotope thermometry of calcite and dolomite in a contact metamorphic environment”. In: *Geochimica et Cosmochimica Acta* 197, pp. 323–344. DOI: 10.1016/j.gca.2016.10.037.

Lugli, Stefano et al. (2000). “Petrography and geochemistry of the Eugui magnesite deposit (Western Pyrenees, Spain): evidence for the development of a peculiar zebra banding by dolomite replacement”. In: *Economic geology and the bulletin of the Society of Economic Geologists* 95.8, pp. 1775–1791.

Machel, Hans G (2004). “Concepts and models of dolomitization: a critical reappraisal”. In: *Geological Society, London, Special Publications* 235.1, p. 7.

Martinez, I, J Zhang, and R J Reeder (1996). “In situ X-ray diffraction of aragonite and dolomite at high pressure and high temperature: Evidence for dolomite breakdown to aragonite and magnesite”. In: *American Mineralogist* 81, pp. 611–624.

Murray, Sean T, Monica M Arienzo, and Peter K Swart (2016). “Determining the”. In: 174.C, pp. 42–53.

Murray, Sean T and Peter K Swart (2017). “Evaluating formation fluid models and calibrations using clumped isotope paleothermometry on Bahamian dolomites”. In: *Geochimica et Cosmochimica Acta VL - IS - SP - EP - PY - T2* - 206, pp. 73–93.

Nagy, Tibor and Tamás Turányi (2011). “Uncertainty of Arrhenius parameters”. In: *International Journal of Chemical Kinetics* 43.7, pp. 359–378.

Navrotsky, A and C Capobianco (1987). “Enthalpies of formation of dolomite and of magnesian calcites”. In: *American Mineralogist* 72, pp. 782–787.

O’Neil, James R and Samuel Epstein (1966). “Oxygen Isotope Fractionation in the System Dolomite-Calcite-Carbon Dioxide”. In: *Science* 152.3719, pp. 198–201.

Passey, Benjamin H and Gregory A Henkes (2012). “Carbonate clumped isotope bond reordering and geospeedometry”. In: *Earth and Planetary Science Letters* 351–352.0, pp. 223–236.

Passey, Benjamin H, Naomi E Levin, et al. (2010). “High-temperature environments of human evolution in East Africa based on bond ordering in paleosol carbonates”. In: *Proceedings of the National Academy of Sciences* 107.25, pp. 11245–11249.

Real, Pablo GarcÃ a del et al. (2016). “Clumped-isotope thermometry of magnesium carbonates in ultramafic rocks”. In: *Geochimica et Cosmochimica Acta VL - IS - SP - EP - PY - T2* - 193.C, pp. 222–250.

Reeder, R J and Y Nakajima (1982). “The nature of ordering and ordering defects in dolomite”. In: *Physics and Chemistry of Minerals* 8, pp. 29–35.

Reeder, R J and H R Wenk (1983). “Structure refinements of some thermally disordered dolomites”. In: *American Mineralogist* 68, pp. 769–776.

Reeder, Richard J and Steven A Markgraf (1986). “High-temperature crystal chemistry of dolomite”. In: *American Mineralogist* 71.5-6, pp. 795–804.

Ryb, U et al. (2017). “The clumped-isotope geochemistry of exhumed marbles from Naxos, Greece ”. In: *Earth and Planetary Science Letters* 470, pp. 1–12.

Schauble, Edwin A, Prosenjit Ghosh, and John M Eiler (2006). “Preferential formation of 13C–18O bonds in carbonate minerals, estimated using first-principles lattice dynamics”. In: 70.10, pp. 2510–2529.

Schauer, Andrew J et al. (2016). “Choice of 17O correction affects clumped isotope (Δ47) values of CO2 measured with mass spectrometry”. In: *Rapid Communications in Mass Spectrometry* 30.24, pp. 2607–2616.

Shenton, Brock J et al. (2015). “Clumped isotope thermometry in deeply buried sedimentary carbonates: The effects of bond reordering and recrystallization”. In: *Geological Society of America Bulletin*.

Shirasaka, M, E Takahashi, and Y Nishihara (2002). “In situ X-ray observation of the reaction dolomite= aragonite+ magnesite at 900–1300 K”. In: *American Mineralogist* 87, pp. 922–930.

Stolper, D A and J M Eiler (2015). “The kinetics of solid-state isotope-exchange reactions for clumped isotopes: A study of inorganic calcites and apatites from natural and experimental samples”. In: *American Journal of Science* 315.5, pp. 363–411.

Urosevic, Maja et al. (2012). “In situ nanoscale observations of the dissolution of”. In: *Geochimica et Cosmochimica Acta VL - IS - SP - EP - PY - T2* - 80.C, pp. 1–13.

Wang, Zhengrong, Edwin A Schauble, and John M Eiler (2004). “Equilibrium thermodynamics of multiply substituted isotopologues of molecular gases”. In: *Geochimica et Cosmochimica Acta* 68.23, pp. 4779–4797.

Warren, John (2000). “Dolomite: occurrence, evolution and economically important associations”. In: *Earth-Science Reviews* 52.1, pp. 1–81.

Winkelstern, Ian Z and Kyger C Lohmann (2016). “Shallow burial alteration of dolomite and limestone clumped isotope geochemistry”. In: *Geology* 44.6, pp. 467–470.

Yelon, A, B Movaghar, and H M Branz (1992). “Origin and Consequences of the Compensation (Meyer-Neldel) Law”. In: *Physical Review B* 46.19, pp. 12244–12250.

Zhang, Y (2010). “Diffusion in Minerals and Melts: Theoretical Background”. In: *Reviews in Mineralogy and Geochemistry* 72.1, pp. 5–59.

Zheng, Y F and B Fu (1998). “Estimation of oxygen diffusivity from anion porosity in minerals”. In: *GEOCHEMICAL JOURNAL* 32, pp. 71–89.

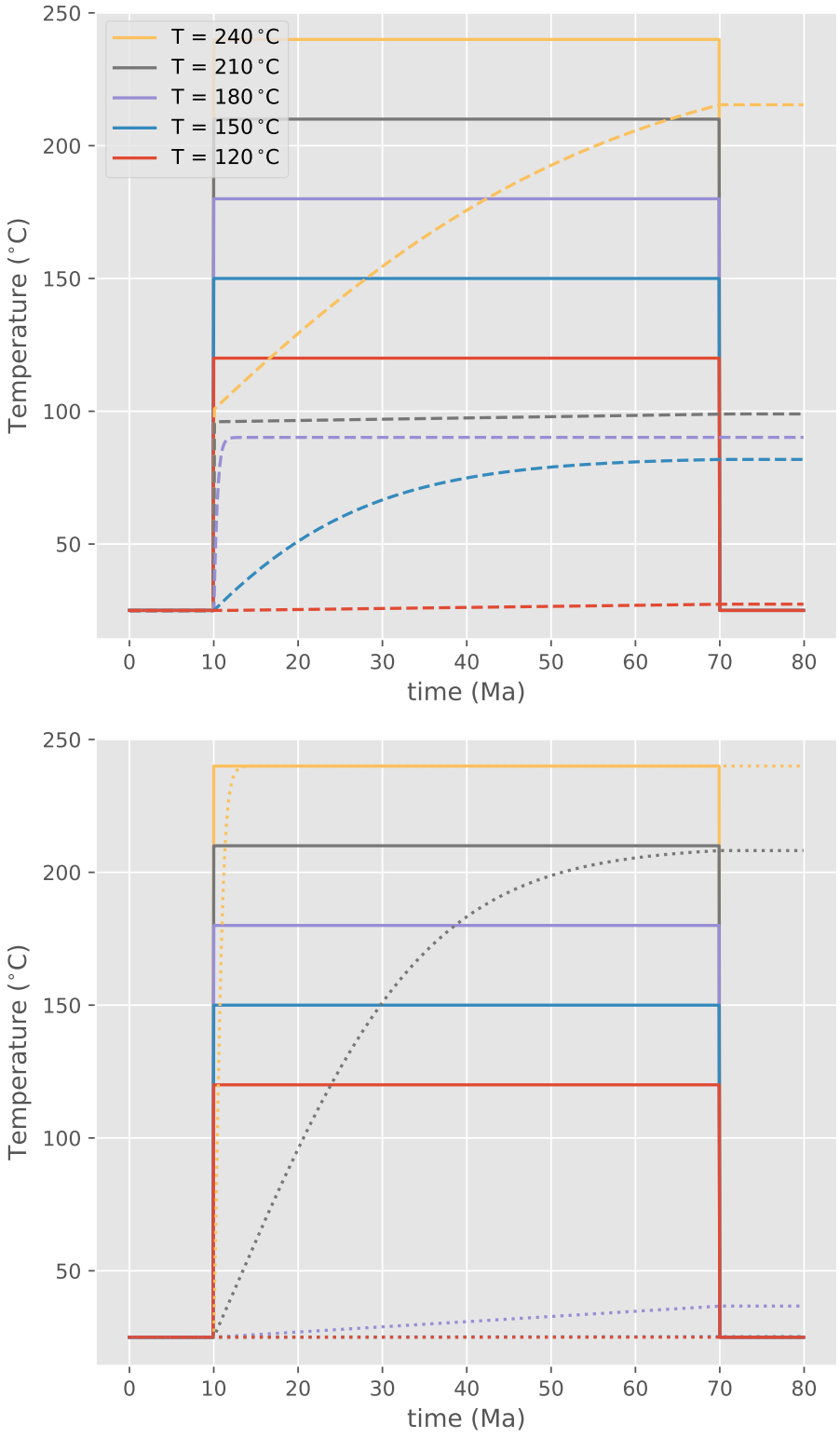

Figure 3.6: 'Box car' heating models of dolomite Δ_{47} reordering. Solid lines denote the true temperature-time path of each run. Dashed lines are dolomite Δ_{47} apparent equilibrium temperatures predicted using the exchange-diffusion model for each T-t path. Dotted lines are the dolomite Δ_{47} temperatures predicted using the transient defect/equilibrium defect model.

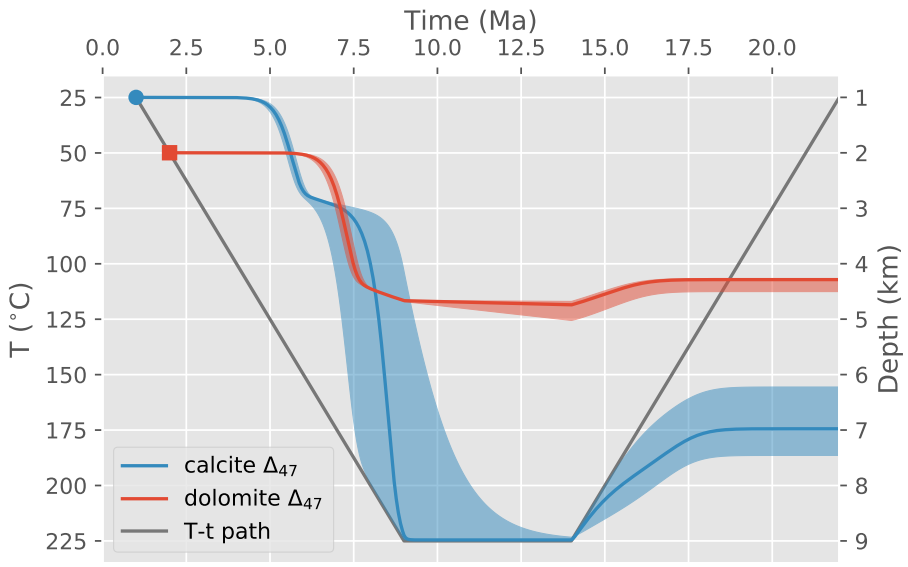

Figure 3.7: Expected reordering behaviors of the dolomite and calcite Δ_{47} thermometers using the exchange-diffusion model in a simple burial-exhumation scenario. Shaded areas denote 1σ confidence limits for the respective thermometer. Here, calcite is initially formed in equilibrium at 25 °C, and dolomite at 50 °C later on the burial path. This setup assumes no recrystallization after initial dolomite and calcite formation.

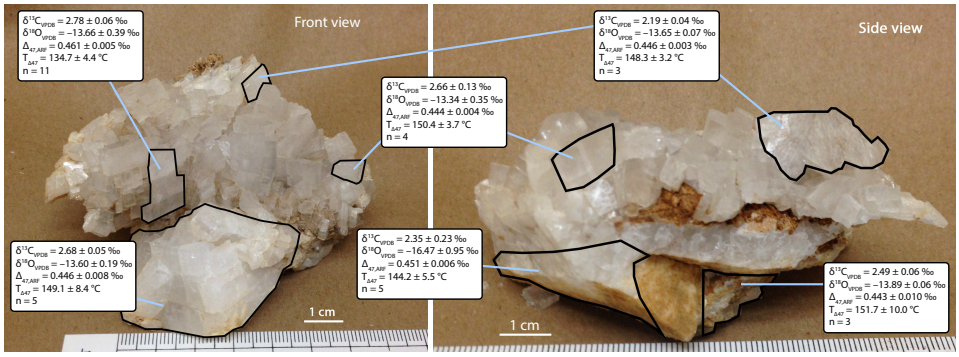

Figure 3.8: Photographs of the Eugui crystal aggregate used for this study. Prior to imaging, sample was bisected using a hammer and chisel to reveal internal structure and layering. Outlined portions denote approximate sections that were removed, powdered, and measured to test the cm-scale isotopic homogeneity of the sample. The entire sample is apparently homogeneous with respect to Δ_{47} and δ^{13}C, but the colorless crystal aggregate is ~3 ‰ heavier in δ^{18}O than the massive while base. All mm-sized fragments used for the heating experiments were taken from protruding, faceted crystals from the colorless crystal aggregate.

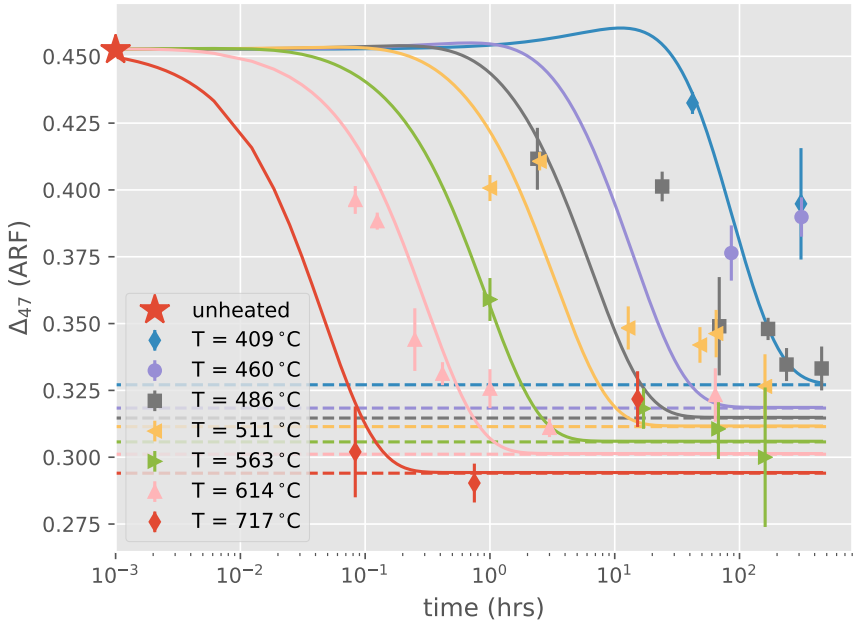

Figure 3.9: Weighted global least squares fit to dolomite heating experiments using the simple, first order reordering model (Eqn. 8, Main Text). Complex reordering behaviors evident in these data are not captured by the simple model.

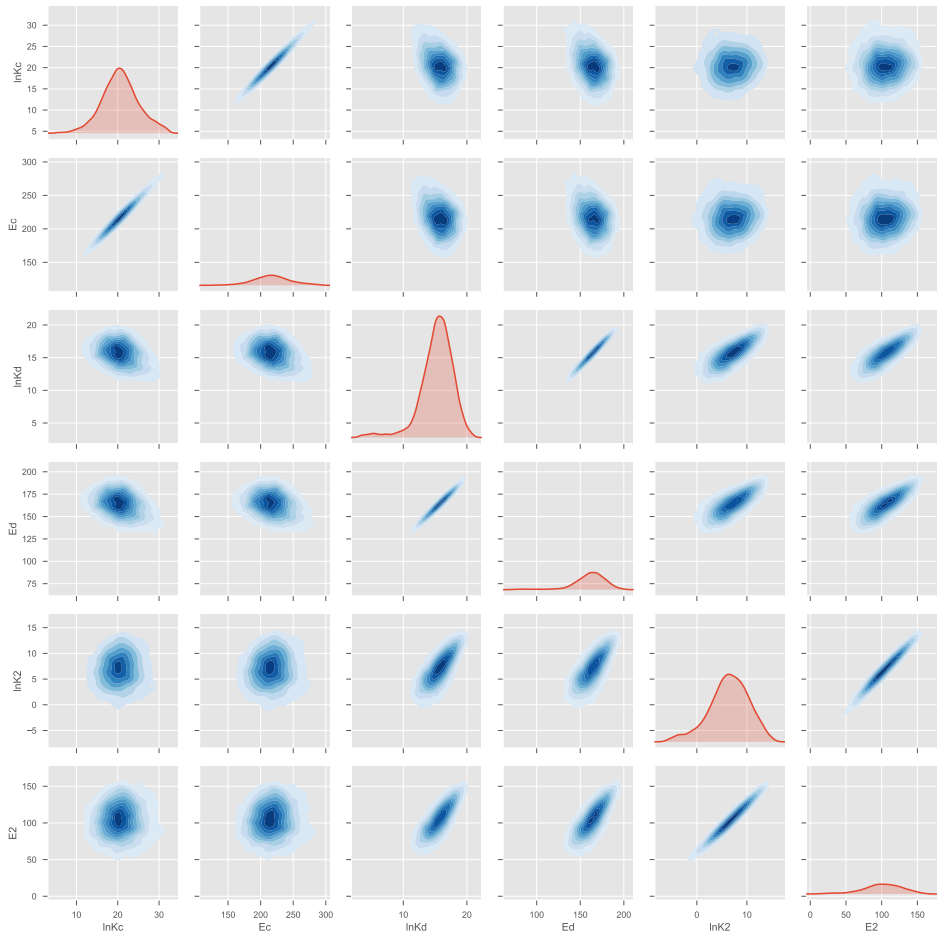

Figure 3.10: Univariate and bivaraite density plots for the Monte Carlo simulation of the six parameter transient defect/equilibrium defect model. Kernel density estimates were generated using the kdeplot function from the seaborn statistical data visualization package.

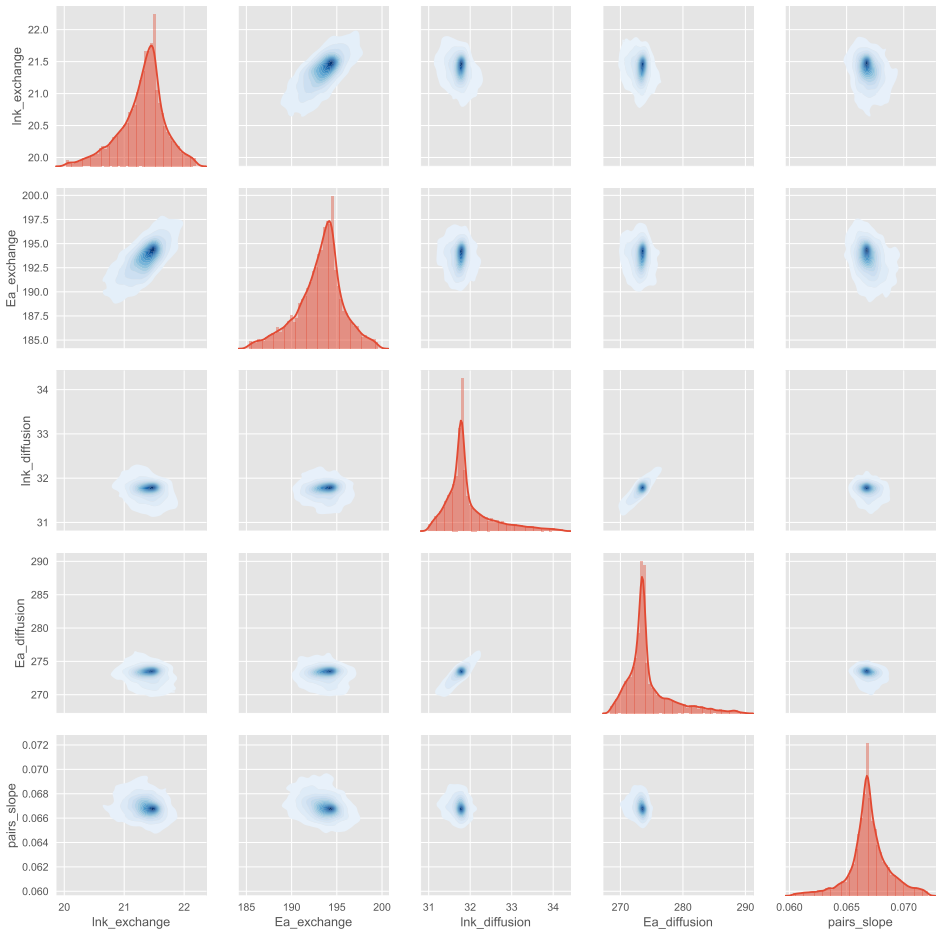

Figure 3.11: Univariate and bivaraite density plots for the Monte Carlo simulation of the five parameter exchange-diffusion model. Kernel density estimates were generated using the kdeplot function from the seaborn statistical data visualization package.

Chapter 4

A PRELIMINARY INVESTIGATION OF CARBONATE CLUMPED ISOTOPE COMPOSITIONS IN A MAJOR FOLD-AND-THRUST BELT

4.1 Introduction

Knowns and unknowns regarding application of carbonate clumped isotopes to metamorphic terranes

Carbonate clumped isotope thermometry is an established technique for recording the conditions (T, $\delta^{18}O_{fluid}$) of carbonate crystallization, but its use has been largely restricted to primary fabrics and surface processes. However because this thermometer maintains useful precision up to $\sim$ 300 °C, it can potentially be useful for probing the temperatures, (by extension) depths, and fluid-rock chemistry of diagenetic and tectonic processes in the shallow crust. In order to relate the temperatures recorded by carbonate clumped isotope compositions to discrete, geologically salient events, it is necessary to understand the conditions under which grains recrystallize. My initial work on the clumped isotope geochemistry of meta-carbonates in Notch Peak contact metamorphic aureole found that calcite Δ_{47} values can fully re-equilibrate in the solid state on million-year timescales at temperatures as low at 150 °C (Lloyd, John M Eiler, and Nabelek, 2017). Thus, excluding events where newly-crystallized fabrics are cooled somewhat rapidly, calcite clumped isotope compositions should only reliably record peak conditions below this temperature. In higher grade marbles from Naxos, we have shown that it's still possible to extract useful information regarding exhumation dynamics from calcite Δ_{47} blocking temperatures, but such inferences are less straightforward (Ryb et al., 2017).

Dolomite clumped isotope temperatures in the contact aureole agreed with expected peak temperatures in regions exposed to 300 to 150 °C (Lloyd, John M Eiler, and Nabelek, 2017). Importantly, these apparently-accurate monitors of peak temperature could be found even in samples where no obvious grain coarsening or heterogeneous metamorphic reactions had occurred. In essence, it appears possible to leverage this technique to distinguish between carbonates exposed to subtly different anchimetamorphic conditions in which no other textural or geochemical distinctions exist (Lloyd, John M Eiler, and Nabelek, 2017). On the other hand,

when multiple generations of obvious recrystallized carbonate textures are present (e.g., syntectonic vs. post-tectonic veins), it should be possible to reconstruct more complete histories of burial, exhumation, and deformation with single hand-samples or outcrops.

There are critical, outstanding questions about how these results replicate when 'scaled-up' to low-grade regional metamorphic terranes, namely:

1. What controls when carbonate grains recrystallize in accretionary wedges and major fold and thrust belts?
2. What aspects of the orogeny are recorded when strata experience protracted, variable histories of regional strain, fluid flow, burial, and exhumation during creation and emplacement of major nappe structures?
3. How do cm-scale, outcrop-scale, or strata-scale variations in fluid content, stress magnitude, mineralogy, and bulk rock lithology affect if and when such carbonate recrystallization occurs?
4. When peak metamorphic conditions are not preserved, can we reliably observe the temperatures of retrograde deformation, and constrain the timing of burial, deformation, and exhumation a nappe complex?

Why the Glarus Alps?

A classic study area of low-grade regional metamorphism, extensive work with thermal maturity indicators in the Helvetic nappes and Infrahelvetic complex have made explicit predictions for the km-scale trends in metamorphic grade, and which deformation features do and do not perturb metamorphic isograds (Fig. 4.1; Wang, FREY, and STERN (1996)). Although these thermal maturity indicators (e.g., vitrinite reflectance, illite crystallinity) cannot be directly related to temperature, they nonetheless inform general hypotheses for how carbonate clumped isotopes should behave in this region (Wang, FREY, and STERN, 1996). Specifically, based on past work with illite crystallinity and vitrinite reflectance, we predict that:

1. Carbonate clumped isotope temperatures will broadly increase from North to South, from diagenetic temperatures at the northern terminus of the Säntis Nappe to Greenschist-facies metamorphic conditions in the southernmost exposures of the Parautochthonous Infrahelvetic complex near Flims. Calcite Δ_{47}-derived temperatures will not exceed 200 °C once such conditions are

reached in this N-S gradient. Dolomite Δ_{47}-derived temperatures should continue to increase further south up to 300 °C.

2. Due to post-peak metamorphic faulting, we will observe discontinuous inverse metamorphic gradients when crossing the Glarus thrust, as long as such thrusting occurred at depths corresponding to temperatures below 300 °C. No temperature discontinuity will be observed across the Säntis thrust because no post-peak-metamorphic movement is believed to have occurred. Carbonate clumped isotope-derived isograds should cross all other structural features uninterrupted (e.g., the Säntis thrust, imbricate fold and thrusting in the Säntis nappe). Any deviation from this behavior will indicate post-peak-metamorphic deformation in the internal Helvetic nappe structure that was previously unrecognized because of limitations of available thermal maturity indicators.

In addition to these predictions for the behavior of carbonate Δ_{47} in adherence to regional metamorphic trends in the Glarus Alps, there remain open questions regarding the mechanisms by which deformation occurred along the Glarus thrust, and the details of the retrograde history of thrusting. Specifically:

1. *Contrasting models for the nature and evolution of deformation along the Glarus*: Recent arguments regarding the connection between rock textures produced by brittle deformation and paleo-seismic events have revived the debate over how the Glarus thrust (and similar 'megathrusts', for that matter) move (Dielforder, Vollstaedt, et al., 2015). This question can be reduced to two scenarios: did the primary deformation mechanism along the Glarus thrust evolve monotonically from ductile to brittle mechanisms due to gradual cooling and, thus, dynamic grain size constriction and strain localization (Ebert, Herwegh, and A. Pfiffner, 2007); or, did deformation style alternate multiple times between brittle and ductile mechanisms over the cooling history of the fault (N P Badertscher and Burkhard, 2000)?

   Evidence for cooling-induced strain localization: Maps of grain coarsening and twin density in the Lochsiten calc-tectonite argue for a secular transition from high-temperature deformation, dominated by dynamic recrystallization due to dislocation creep in a large (m-scale), coarse-grained shear zone, to low-temperature deformation, facilitated by granular flow and dissolution–reprecipitation reactions focused in a 10–20 cm band (Ebert, Herwegh, and

A. Pfiffner, 2007). In this model, only the final increments of motion at the coldest temperatures are recorded in brittle fractures, up to tens of meters long, containing 2–3 cm-sized polymict cataclastite (Marco Herwegh, Berger, and Ebert, 2005).

Evidence for ductile–brittle deformation cycles: On the other hand, N P Badertscher and Burkhard (2000) argue that the texture of the Lochsite calc-tectonite represents only the most recent phase among alternating cycles of cataclastic and viscous deformation throughout the strain history of the Glarus thrust. These cycles would have been triggered by the repeated buildup of high fluid pressure within the fault zone, which would have led to the release of pressure through periodic seismic events bearing high strain rates (N P Badertscher and Burkhard, 2000; Nicolas P Badertscher, Beaudoin, et al., 2002). In this model, observation of previous cycles of deformation is impeded because the texture observed in the Lochsite today is only representative of the the most recent event; previous brittle deformation features were overprinted by ductile shear and dynamic recrystallization during intervening background-levels of deformation at low strain rates. The idea of seismically-associated cataclastic deformation throughout the evolution of the Glarus thrust is not unreasonable; textural evidence for brittle fracturing, vein formation and dissolution–reprecipitation reactions is not restricted to the 'low-temperture' shear band described in Ebert, Herwegh, and A. Pfiffner (2007). In fact, there is ample geochemical and mechanical evidence linking earthquakes along the Glarus fault to individual brittle faulting textures and vein generations in the underlying Infrahelvetic flysch complex (Dielforder, Vollstaedt, et al., 2015). And, a recent model of the effect of diagenesis, illitization, and porosity loss in the flysch units found that both widely-distributed pressure solution (resulting in 'ductile-appearing' fabrics) and spatially-confined, brittle deformation could occur under the same thermomechanical conditions by varying only the strain rate (see Dielforder, Berger, and Marco Herwegh, 2016). Applying this reasoning to the Lochsite calc-tectonite, in conjunction with a chemo-mechanical model whereby shear heating during ductile creep deformation induces carbonate decomposition that generates highly overpressurized fluids capable of lubricating a principal slip zone and enabling brittle deformation during episodic stick-slip events (Poulet et al., 2014), it is conceivable that the textures of a cyclic process in the Lochsite calc-tectonite could erroneously appear monotonic in nature.

Tests of models through carbonate clumped isotope thermometry: Importantly, these two scenarios make contrasting predictions for the temperatures preserved in recrystallized carbonate fabrics across the observable shear zone (Fig. 4.2). Because the Ebert, Herwegh, and A. Pfiffner (2007) model requires that the zone of deformation (and thus, recrystallization) becomes spatially restricted with continued cooling during exhumation of the complex, dolomite clumped isotope temperatures should continuously decrease while moving from the footwall up into the brittle textures of latest, coldest shear zone. This assumes that dolomite recrystallization accompanied all phases of deformation, and that shear heating was short-lived and did not artificially elevate the ambient temperatures recorded by the recrystallized carbonates (see Swanson et al., 2012, for evidence that aligns with this notion). On the other hand, if large-scale cataclastic features were repeatedly erased by ductile shear and dissolution–reprecipitation reactions, then the apparently-ductile fabrics observed today should represent the last such cycle and have roughly uniform, low dolomite Δ_{47} temperatures. Both models agree that the very final stages of deformation are preserved in the late, cross-cutting catacalstic carbonate veins. Dolomite Δ_{47} temperatures of these terminal veins should indicate how far thrusting continued into the retrograde phase.

In principal, similar behaviors should be observed with calcite clumped isotope compositions. However, because peak temperatures are believed to have exceeded 200 °C even in the coldest, northernmost exposures of the Glarus thrust (M. Rahn et al., 1995; Ebert, Herwegh, and A. Pfiffner, 2007), we expect that solid-state reordering would overwrite any cooling-induced localization until the terminal stages of post-peak deformation, and even then only if these stages occurred below this blocking temperature.

2. *Mapping the extent of and along-strike variation in post-peak metamorphic thrusting along the fault*: Although the existence of continued motion on the Glarus thrust during retrograde metamorphism is well-documented in the discontinuous inverse anchimetamorphic isograds across the contact, key details regarding this retrograde motion remain enigmatic. We've identified two questions that detailed, accurate clumped isotope thermometry along the thrust fault can address.

   How much offset occurred during retrograde phase? Palinspastic reconstructions of the shelf sediments of the Helvetic nappes constrain displacement

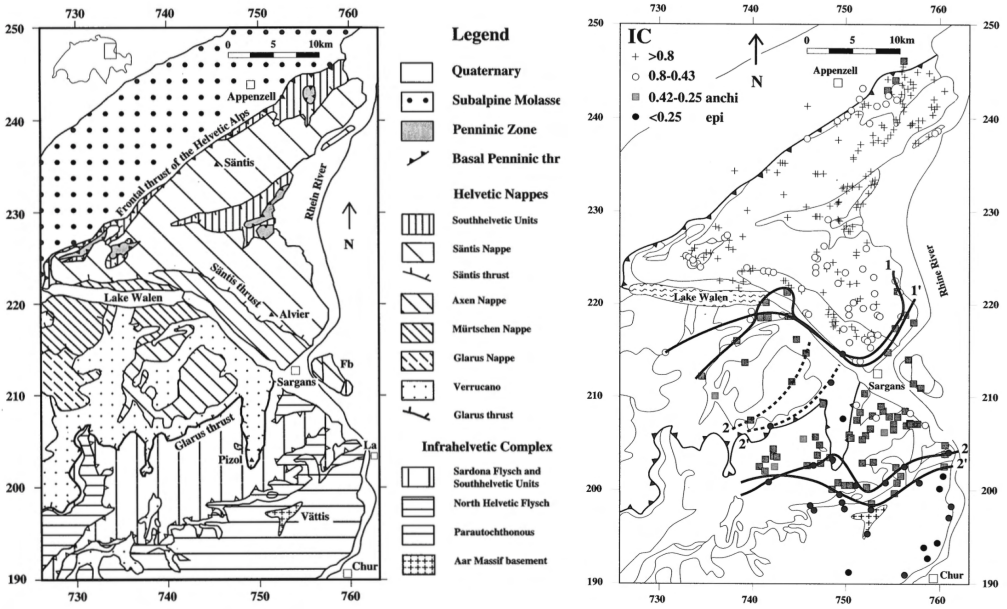

(a) Units and contacts in the Glarus alps (b) Illite crystallinity

Figure 4.1: Simplified map of the units, major faults, and trends in anchimetamorphic grade in the Glarus alps (Wang, FREY, and STERN, 1996).

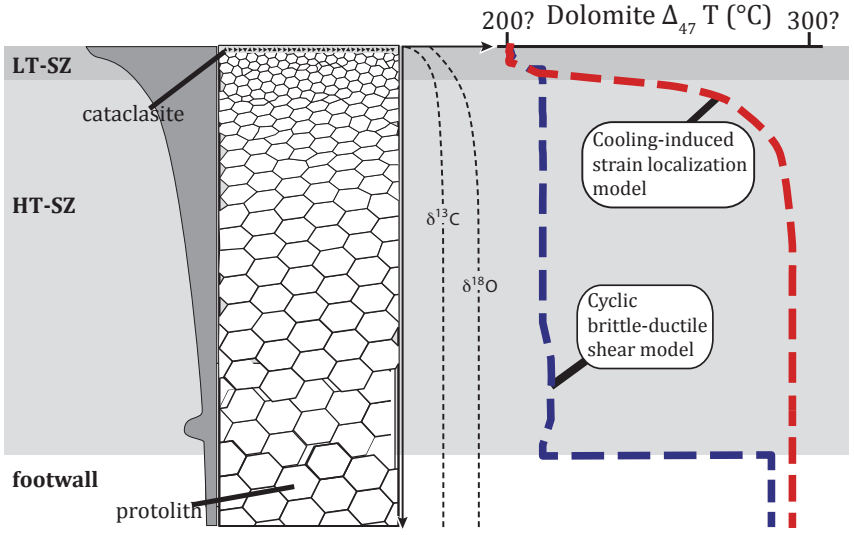

Figure 4.2: Contrasting predictions for temperature profiles across distinctive textures of a schematic of the Lochsite shear zone. Modified from Ebert, Herwegh, and A. Pfiffner (2007).

along the Glarus fault to at least 35 km (Schmid, 1975), and likely as much as 50 km (O A Pfiffner, 1985). Reconstructing the amount of this displacement that occurred after peak metamorphic conditions has implications for the relationship between deformation and exhumation in this system, but is challenging because typical thermal maturity indicators, which identify this offset, cannot be directly related to temperature. Using the offsets between peak temperatures from dolomite Δ_{47} values in the hanging wall and footwall of the thrust, along with coupled assumptions about the angle of the fault and the geothermal gradient at the time of deformation (constrained, to some extent, by the regional Δ_{47}-derived temperatures in the overlying Helvetic nappes), it will be possible to estimate the amount of post-peak metamorphic thrusting accommodated by this feature.

Was the Glarus thrust active during the doming and extrusion of the Aar massif? Today, the plane of the Glarus fault is domed, with the northern and southern limbs defining a combined angle of as much as 35° (Schmid, 1975). It remains an open question, however, whether deformation along the fault continued during this doming process, or exclusively preceded it. Linear, differential uplift rates recorded by apatite fission track cooling ages support a passive rotation of the fault surface during doming and exhumation (M. K. Rahn, Hurford, and FREY, 1997). On the other hand, kinematic linkages between the doming in the Aar massif, the compression in the Subalpine molasse, and the shortening of the Infrahelvetic complex suggest that up-doming of the active Glarus thrust occurred in response to this shortening (O A Pfiffner, 1986; Marco Herwegh, Hürzeler, et al., 2008). In the absence of shear heating, dolomite Δ_{47}-derived temperatures of the youngest generation of cataclastite veins should be a reliable proxy for depth at the time of rupture. If these final movements along the entire 25 km of exposed fault section (perpendicular to strike) were approximately contemporaneous, than the trend in temperatures, when divided by the estimated geothermal gradient (25–30 °C/km; M. K. Rahn, Hurford, and FREY, 1997), records the dip angle at the time of final thrusting (Fig: 4.3).

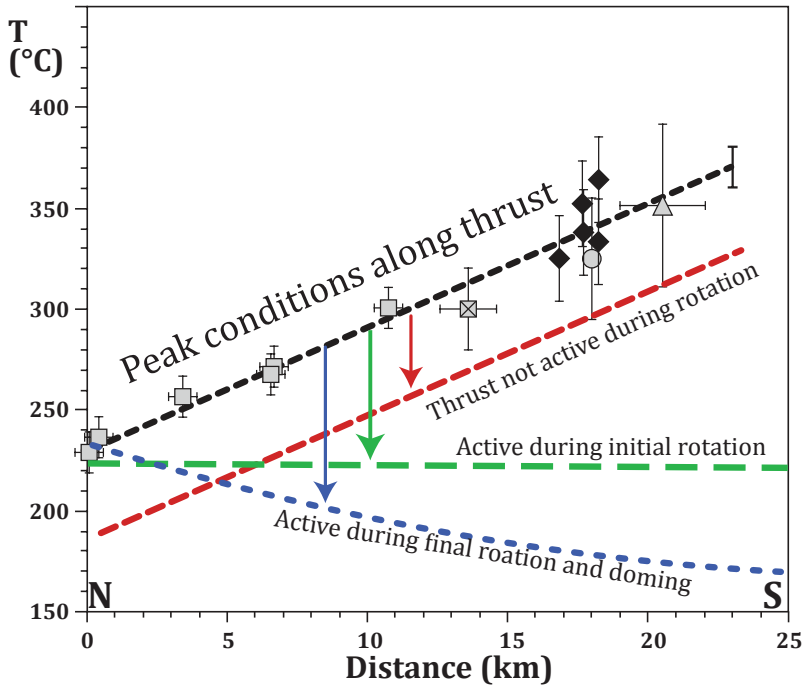

Figure 4.3: Cartoon demonstrating the procedure for the graphical determination of the relationship between terminal motion on the Glarus thrust and the doming/rotation of the fault plane using dolomite Δ_{47} temperatures. Estimates of peak conditions along N–S transect from Ebert, Herwegh, and A. Pfiffner (2007) and references therein. Red, green, and blue lines are hypothesized positions and orientations of measurements of final temperatures along the same transect. Coldest (blue) line assumes a dip angle of 8° (similar to the present-day orientation) and a geothermal gradient of 25 °C/km.

4.2 Methods

Sample collection

The primary sample collection was acquired over 10 days of fieldwork in September 2016. This sampling campaign had two foci:

1. *Regional metamorphic trends*: 138 hand samples of carbonates, marls, and flysch units, were obtained from a ~ 150 km^2 area covering the Helvetic nappes and the Infrahelvetic complex in and around the Glarus alps (Fig 4.4). Carbonate sample selection emphasized barren, texturally-simple grainstones, buff to gray in color, that were representative of the local lithology. With few exceptions, more northern samples of the Infrahelvetic complex were competent mudstones and argillites with high (suspected) carbonate contents. In more southern exposures of the comples, carbonates and siliceous carbonates

were more widely available.

2. *Glarus fault exposures*: To accurately constrain the fabric-specific temperatures of recrystallized and sheared carbonates on the Glarus thrust, vertical transects were performed at seven outcrops of the Lochsiten calc-tectonite, from localities covering the maximum possible range in original structural depth and along-strike variation (Fig. 4.4). In each transect, locally-representative samples were taken from ~5 m above to at least 10 m below the nominal fault surface. Sampling emphasized the 2 m of section below and closest to the fault surface, where oriented samples were taken to allow for resolution of cm-scale variations in the distance to the fault. Multiple generations of veins were retrieved where possible. In total, 80 such samples were obtained from the seven exposures (specifically, Chasserrug, Vorab Pign, Nagens, Pizol, Cassons, Piz Segans, and the Foostock).

To supplement this field campaign, critical additional samples were provided by the Herwegh group at University of Bern. These included:

- Texturally-complex hand samples from the two lowest-temperature exposures of the Glarus fault calc-tectonite (Lochsite and Risetenhoren), originally investigated for grain size, CPO, and twinning density, as part of Andreas Ebert's thesis (Ebert, 2006), and published in Ebert, Herwegh, and A. Pfiffner (2007).
- Quartz–calcite veins from three generations of deformation (G1, G2, G3) in the Infrahelvetic flysch, studied for $^{87}Sr/^{86}Sr$ composition and quartz–calcite $\delta^{18}O$ thermometry as part of Armin Dielforder's thesis (Dielforder, 2016), and published in Dielforder, Vollstaedt, et al. (2015).
- ~ 10 additional samples of the Infrahelvetic flysch, part of Venice Akker's ongoing PhD work, were also provided. These had been previously analyzed for modal mineralogy using powder X-ray diffraction (XRD).

Sample processing

For hand samples used in the regional study, weathered outer surfaces were removed, and texturally-simple billets were cut using a diamond-coated abrasion saw. Care was taken to produce cm-sized cubes of matrix carbonate with no visible secondary veins. These were crushed by mortar and pestle, and powdered by rotary mill

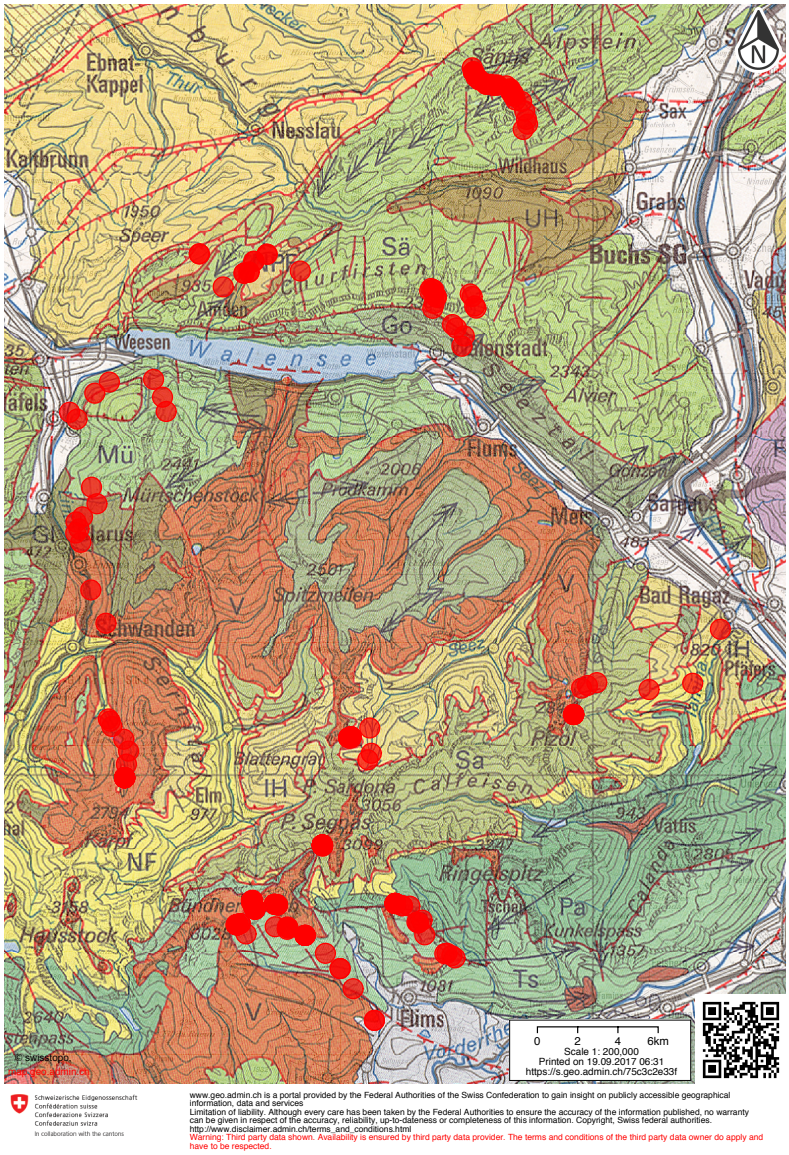

Figure 4.4: Tectonic map of the Glarus alps, showing approximate locations of all samples obtained in the September 2016 campaign. Generated using Tectonics 500 base map from `https://map.geo.admin.ch/`.

until all starting material passed through a < 104 μm sieve. Twenty-nine regional samples have been processed this way thus far.

Samples of the Lochsite calc-tectonite were treated in one of two ways. Texturally-simple hanging wall and footwall rocks were processed for bulk powders in the same manner as above (nineteen samples from three sites processed so far). Samples with complex textures, including the Lochisten calc-tectonites provided by the Bern group, were bisected and powders obtained from individual textures using a Dremel rotary drill (twelve samples so far). No additional processing was done for materials that arrived powdered or veins that were previously crushed.

XRD screening for dolomite

Samples for the regional metamorphic study were screened for semi-quantitative modal mineralogy using Bruker D2 Phaser powder X-ray diffractometer. Spectra were acquired using a 1.5 kV beam with 2 mA current, on a stage rotating at 15 revolutions/min, for angles of 20 to 50 2θ, with a step size of 0.010 2θ and a step time of 0.050 s. Relative contents of calcite and dolomite were estimated using the ratio of the integrated areas under the principal peak of each of these at 29.3, and 30.8 2θ, respectively. Phase-specific biases were accounted for by normalizing to the ratios from spectra of physical mixtures of known quantities of pure calcite and dolomite.

Isotopic methods and analyses

Samples containing a single carbonate phase were measured for $\delta^{13}C$, $\delta^{18}O$, and Δ_{47} compositions using typical methods for automated digestion, purification, and analysis by dual-inlet isotope ratio mass spectrometry (IRMS) at Caltech. Briefly, ~10 mg of carbonate powder (or a proportionally larger mass of siliceous samples) were reacted with 104% orthophosphoric acid in a common acid bath at 90 °C . Evolved CO_2 was continuously frozen, then separated from H_2O and other contaminants by cryogenic purification in an ethanol–dry ice slush (−77 °C), and elution through a packed Poropak Q 50/80 column held at −20 °C in an He stream flowing at ~20 mL/min. Isotopic composition of sample CO_2 was characterized by measuring intensities of masses 44–49 Da on a Thermo 253 dual-inlet IRMS against a reference CO_2 gas of known isotopic composition. Mass spectrometric non-linearities and drift were corrected for using analyses of 1000 °C– and 25 °C–equilibrated gases measured contemporaneously. Stability and reproducibility of the automated digestion apparatus were monitored using in-house carbonate standards measured

daily. Reported δ^{13}Cand δ^{18}O values were calculated using the ^{13C}R, ^{17O}R, and ^{18O}R values for the Vienna Pee-Dee Belemnite (VPDB) standard reported by Brand, Assonov, and Coplen (2010) and the Taylor polynomial solver routine described by Daëron et al. (2016). All Δ_{47} values are reported in the carbon dioxide equilibrium scale (CDES), corrected to the 25 °C phosphoric acid reference frame by the addition of a linear correction of 0.092 ‰.

Samples containing both dolomite and calcite were reacted using the stepped acid digestion procedure described in Lloyd, John M Eiler, and Nabelek (2017). With this method, CO_2 derived from intergrown calcite and dolomite can be isolated, purified, and analyzed separately, apparently without imparting an additional fractionation on their Δ_{47} values. Work with artificial mixtures of carbonate standards have shown that minor dolomite can be successfully purified from mixed carbonates in samples where dolomite is as little as 3 % of calcite by mass. In all mixed-phase samples reported here, dolomite is at least 8 % of calcite. After stepped digestion and isolation, calcite-derived and dolomite-derived CO_2 samples were further purified and analyzed on the cleaning apparatus and instrument described above. Here, calcite was reacted at 25 °C, so no Δ_{47} correction was applied. Dolomite reacted at 50 °C was corrected to the 25 °C reference frame by adding 0.040 ‰ to these Δ_{47} values (Lloyd, John M Eiler, and Nabelek, 2017).

4.3 Results and exploratory discussion

Regional metamorphism in the Helvetic nappes

Twenty-nine samples from the regional suite, plus eight flysch samples from Venice Akker, were powdered and characterized by XRD. Of these, five had sufficient dolomite for phase-specific clumped isotope determinations, and were subjected to the offline stepped acid digestion procedure. The rest of the sample set were measured for bulk Δ_{47} by the online method. In total, sixty-five Δ_{47} analyses of calcite in thirty-one samples from the Helvetic nappes and Infrahevetic complex have been made to date.

Bulk isotope data

Mean δ^{13}C values in the Helvetic nappes are relatively invariant, from ~1.0 to 3.5 ‰ (vs. VPDB) (Fig. 4.5). δ^{13}C values of the flysch are somewhat lighter, with the lowest values in the clay-rich, siliceous lithologies of the North Helvetic flysch (Figs. 4.5, 4.7). The same general trends also hold for the δ^{18}O values of the

calcite: most δ^{18}O values in the Helvetic carbonates are between –6 and –4 ‰ (vs. VPDB), with values ~5 and ~2 ‰ lower in the North and South Helvetic flysch, respectively (Fig. 4.6). Indeed, there appears to be a moderate correlation between δ^{13}C and δ^{18}O among all calcite samples in these units, although this is entirely due to covariation of these isotope systems within the Infrahelvetic complex. (r^2 = 0.46; Fig. 4.7). It is not immediately apparent why this covariance exists.

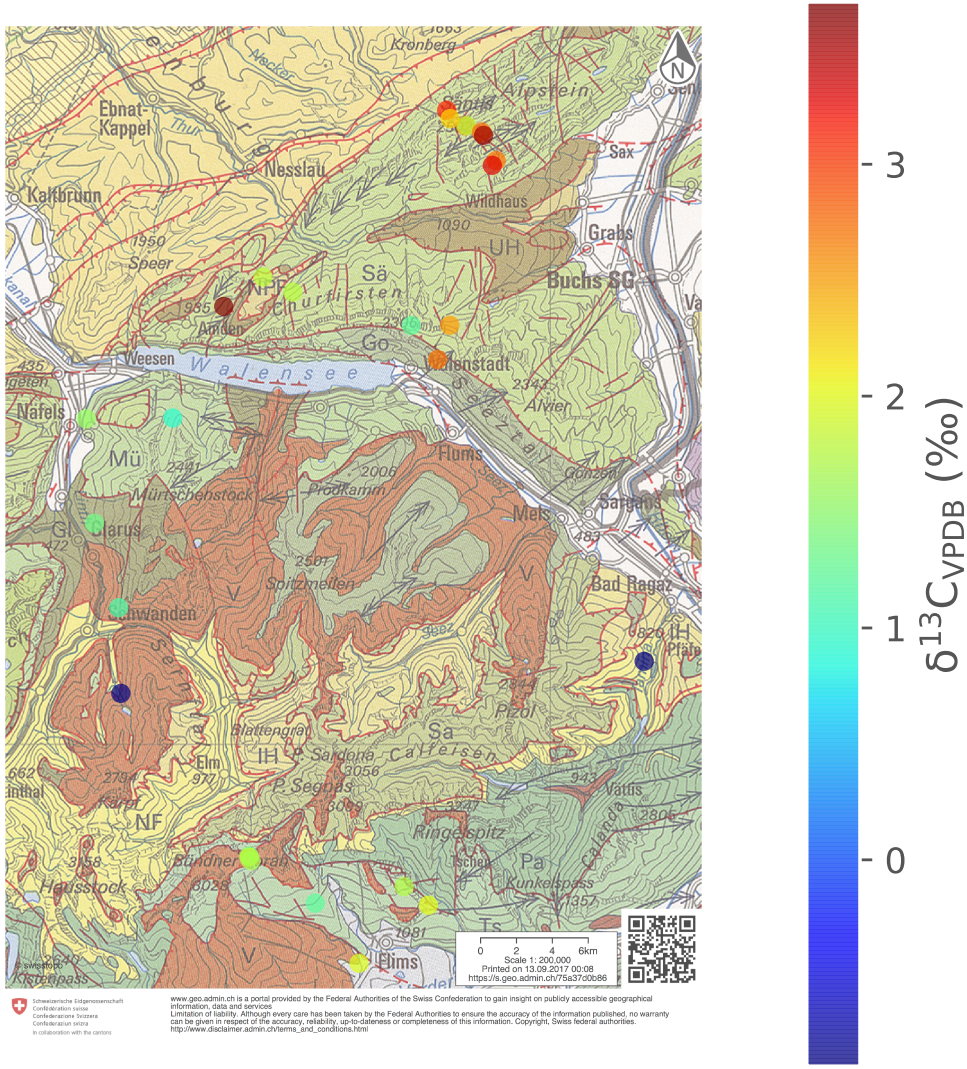

Figure 4.5: Calcite δ^{13}C values from the Helvetic nappes and Infrahelvetic flysch

Calcite Δ_{47} temperatures

In the Helvetic nappes north of the Walensee, calcite Δ_{47} temperatures generally increase to the south, from as low as ~40 °C in the northernmost outcrops of the

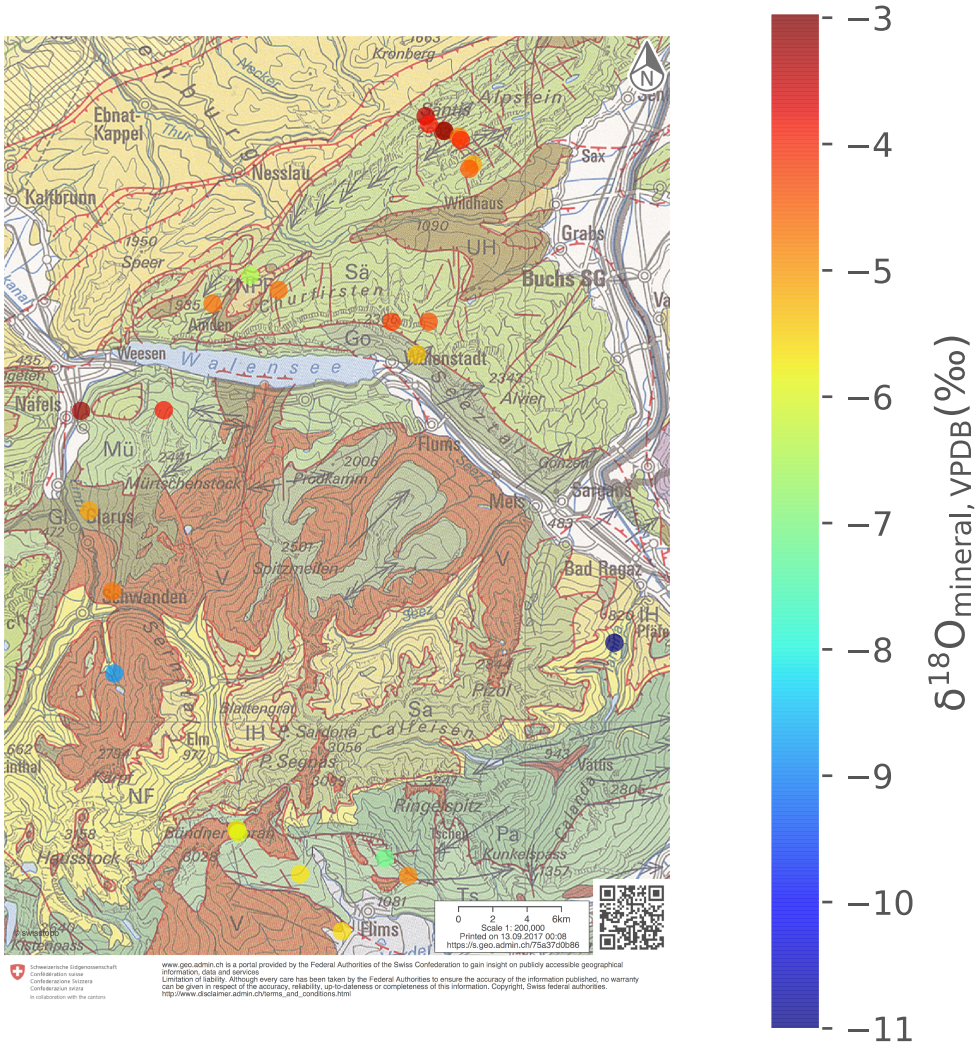

Figure 4.6: Calcite δ^{18}O values from the Helvetic nappes and Infrahelvetic flysch

Säntis nappe, to as high as 217 ± 16 °C in the units at the base of the southern face of the Chürfirsten (Figs. 4.8, 4.9). Within the colder sections calcite Δ_{47} temperatures are highly heterogeneous and vary by up to 50 °C across outcrop-scale lithological transitions (Figs. 4.8, 4.9). In the nappes south of the Walensee, we find largely uniform calcite Δ_{47} blocking temperatures (~ 200 °C), with the exception of one sample from the floor of the Linth valley ($T_{\Delta47}$ = 137 ± 7 °C; Fig. 4.8). It is not immediately apparent why this single low-lying sample, taken from a stream-side roadcut just north of Mollis, is anomalously cold. One possibility is that that the vector of maximum metamorphic gradient in this region does not exclusively trend north–south. That is, given the proximity of the Linth valley sample to the NE–SW-trending frontal thrust of the Helvetic alps, perhaps this sample underwent

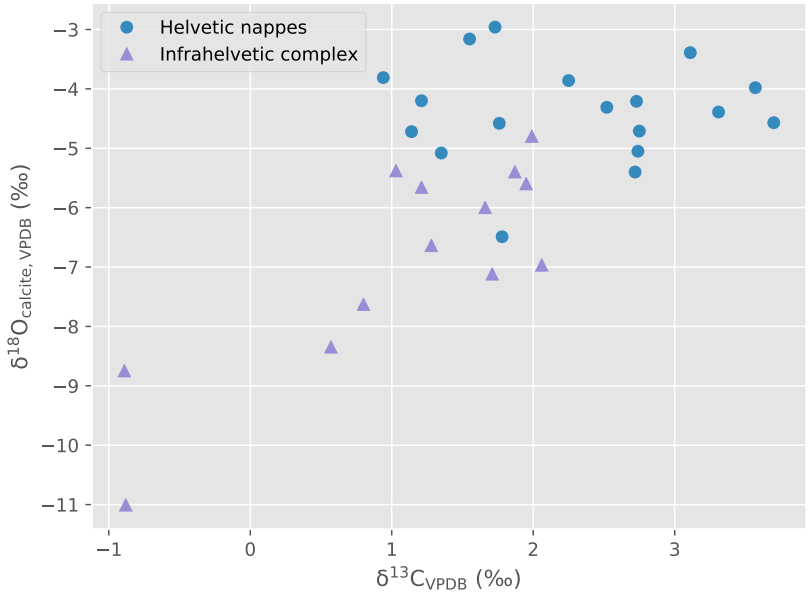

Figure 4.7: Cross-plot of calcite δ^{13}C and δ^{18}O values from the Helvetic nappes and Infrahelvetic flysch

relatively shallow burial compared to samples from units on the same northing, but further to the east. If the Helvetic nappes deepen to the east, some amount of previously-unrecognized doming or differential uplift/erosion would be required to produce in the topography and structure of the region today. It is also notable that this section belongs to the Mürtschenstock nappe, a separate tectonic block from the Säntis nappe, the primary focus of the anchimetamorphic regional metamorphism campaign. The apparent discontinuity between metamorphic trends in these two nappes could be the result of post-peak metamorphic thrusting or rotation along a fault internal to the Helvetic nappes, such at the Säntis thrust. Note that such a scenario disagrees with current models for the timing of nappe emplacement and exhumation, wherein only the out-of-sequence basal Glarus thrust was active subsequent to peak conditions in the nappe stack. Δ_{47} measurements of the ~15 unstudied Mürtschenstock nappe samples will allow more precise constraints of the thermal structure of this block, and enable assessment of whether these intra-nappe isograds are continuous across to the opposite shore of the Walensee.

Critically, even at this rough, regional scale, we observe a discontinuous inverse metamorphic gradient when crossing the Glarus thrust. Calcite Δ_{47} temperatures in the northernmost flysch samples are 110 – 145 °C, resolvably colder than the closest overlying nappe samples, and certainly colder than previous workers' es-

timates of peak conditions of the Verrucano greenschist ($T_{peak} \geq 350$ °C), which directly overlies these flysch samples (Figs. 4.8, 4.10). Note, however, that these temperatures are ~100 °C colder than the peak metamorphic temperatures in these flysch units predicted in previous studies (M. Rahn et al., 1995; Ebert, Herwegh, and A. Pfiffner, 2007). The possible causes of this discrepancy are further discussed in section 4.4. Further to the south, on the cliffs below the Vorab glacier, calcite $T_{\Delta 47}$ values from the parautochthonous Mesozoic cover sequence rise rapidly from ~110 to 175 °C over merely 300 m (Fig. 4.10). Such heterogeneity could simply be an example of inconsistent recrystallization behavior, similar to the scatter observed in the lowest grades of the Säntis nappe. Indeed, the close proximity to the Glarus fault in this section (the actual contact is eroded away, but the fault plane is less than 30 m overhead) could have induced localized recrystallization or reordering through localized strain or shear heating. On the other hand, vastly different fluid-rock ratios are not implicated, because bulk isotope data for these carbonates are largely homogeneous (both δ^{13}Cand δ^{18}O values agree within 1‰). Further study of the other ~8 unanalyzed samples from this section could eliminate some of these possibilties.

Correlation between $T_{\Delta 47}$ and $\delta^{18}O_{H2O}$: fortuitous coincidence or recrystallization/reordering at low water/rock ratios?

In both the Helvetic nappes and Infrahelvetic complex, a strong correlation is observed between calcite $T_{\Delta 47}$ and $\delta^{18}O_{H2O}$ (that is, the theoretical water ^{18}O content that would be in equilibrium with calcite of a measured ^{18}O content, at the apparent formation temperature) (Fig. 4.11). Such correlations are not necessarily useful nor significant; because theoretical $\delta^{18}O_{H2O}$ is dependent on $T_{\Delta 47}$, if calcite δ^{18}O values are invariant over a range of crystallization temperatures (i.e., calcites of similar origin recrystallized in the presence of vanishingly small amounts of fluid), then a perfect correlation will exist between these two parameters. Since unaltered Mesozoic shelf carbonates from the European margin should have broadly similar calcite δ^{18}O values, the strong covariation between $T_{\Delta 47}$ and $\delta^{18}O_{H2O}$ merely confirms that the Helvetic nappes experienced low fluid-rock ratios during burial and deformation. That the error-weighted regression to these data intersects a fluid δ^{18}O value of 0 ‰ at ~24 °C further confirms that these carbonates originally formed in a Mesozoic shallow marine setting, and that primary pore fluids remained closed to secondary sources. Note that recrystallization under low water/rock (W/R) conditions is not needed to generate such an array; varied extents of solid-state reordering of isotopically-similar calcite grains would produce the same apparent

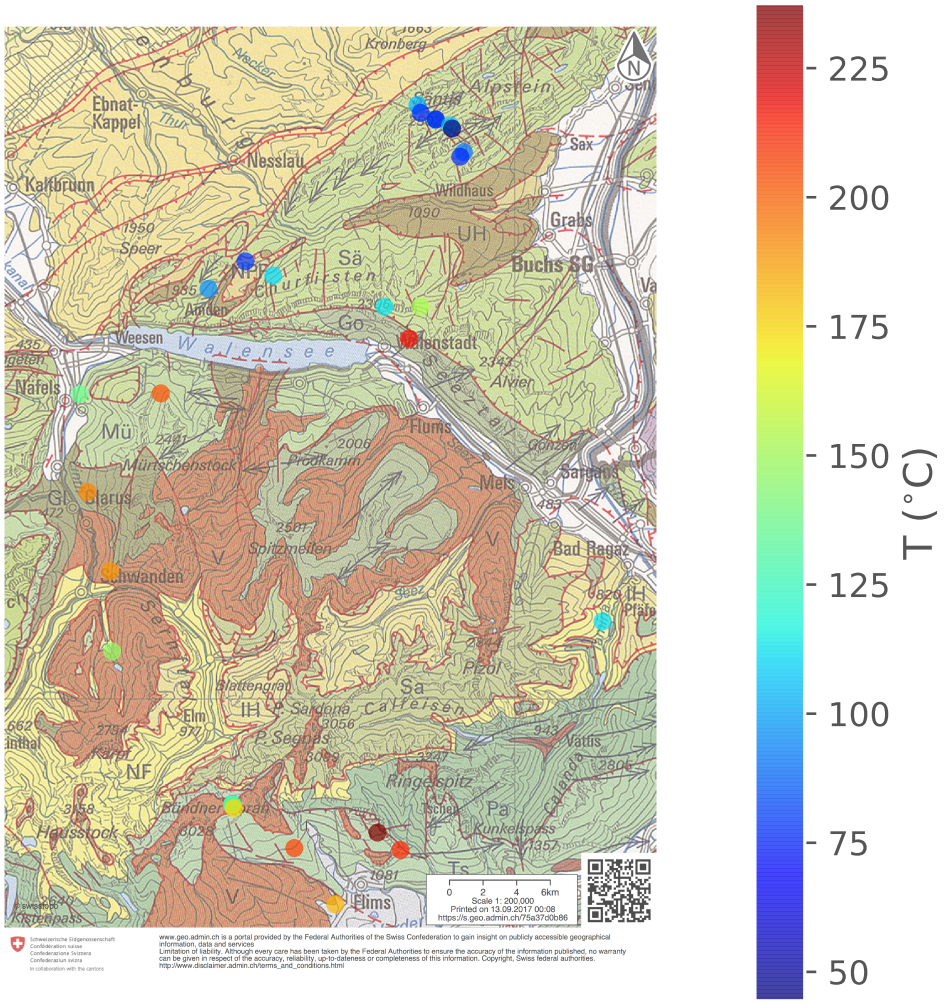

Figure 4.8: Calcite Δ_{47}-temperatures from the Helvetic nappes and Infrahelvetic flysch

correlation. However, since there is no known mechanism to generate vastly different Δ_{47} reordering susceptibilities in the same mineral, the strongest argument that these data are the result of dissolution–reprecipitation reactions with primary pore fluids of marine origin (as opposed to solid-state reordering) is the close spatial association of samples with matrix $T_{\Delta47}$ values that differ by 50 °C or more.

By the same logic, the parallel but offset correlation between $T_{\Delta47}$ and $\delta^{18}O_{H2O}$ values in calcites from the Infrahelvetic complex would seemingly suggest that they recrystallized under low W/R ratios in much the same manner as the nappes, albeit from a fluid source ~ 5 ‰ lighter in $\delta^{18}O$ than pristine ocean water (Fig. 4.11). Calcite $\delta^{18}O$ values, however, vary by ~ 6 ‰ in the complex, and independently

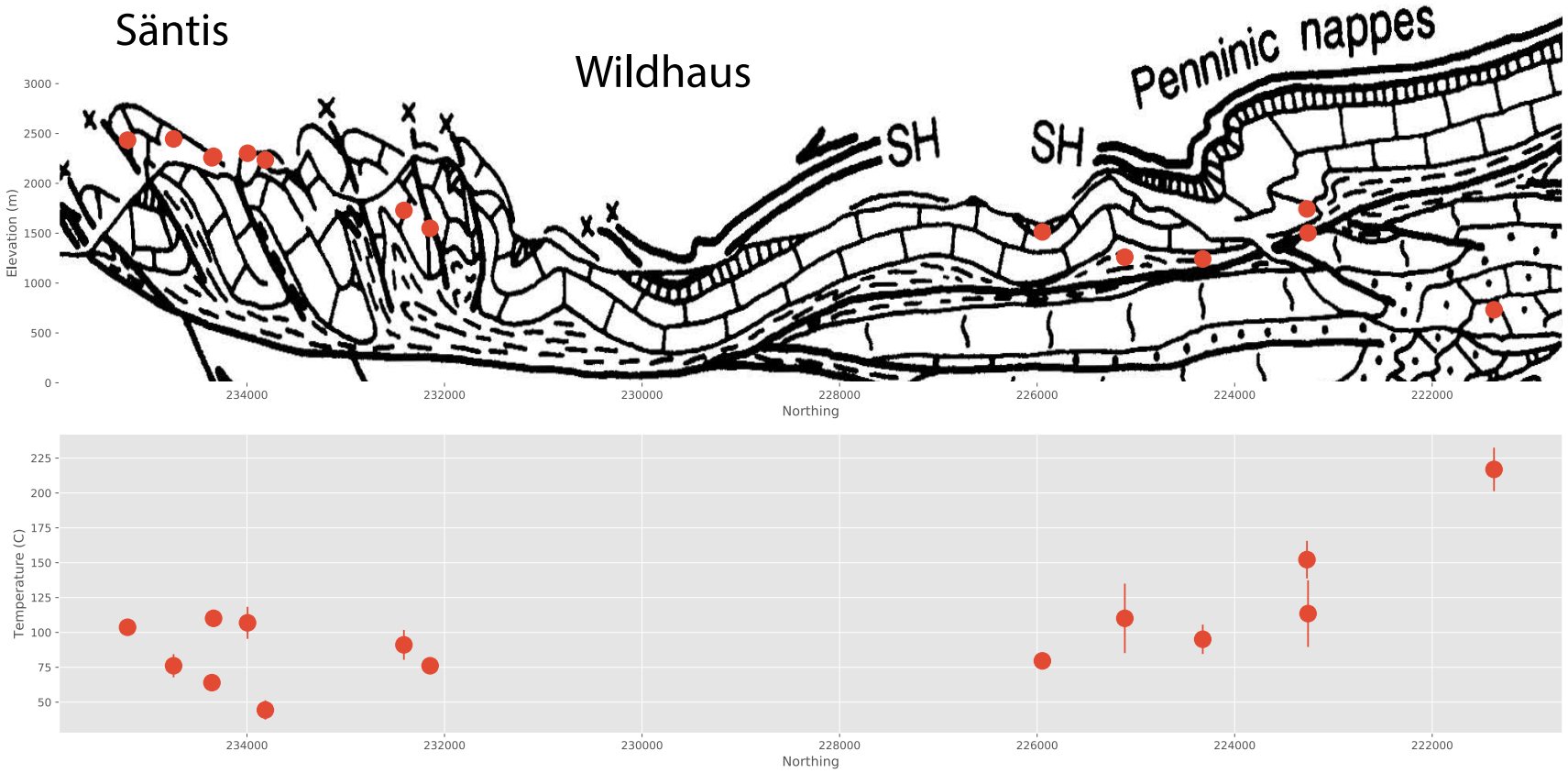

Figure 4.9: Calcite locations and Δ_{47}-temperatures in the northern Helvetic nappes. Approximate sample locations plotted on the regional cross section of O Adrian Pfiffner (1993).

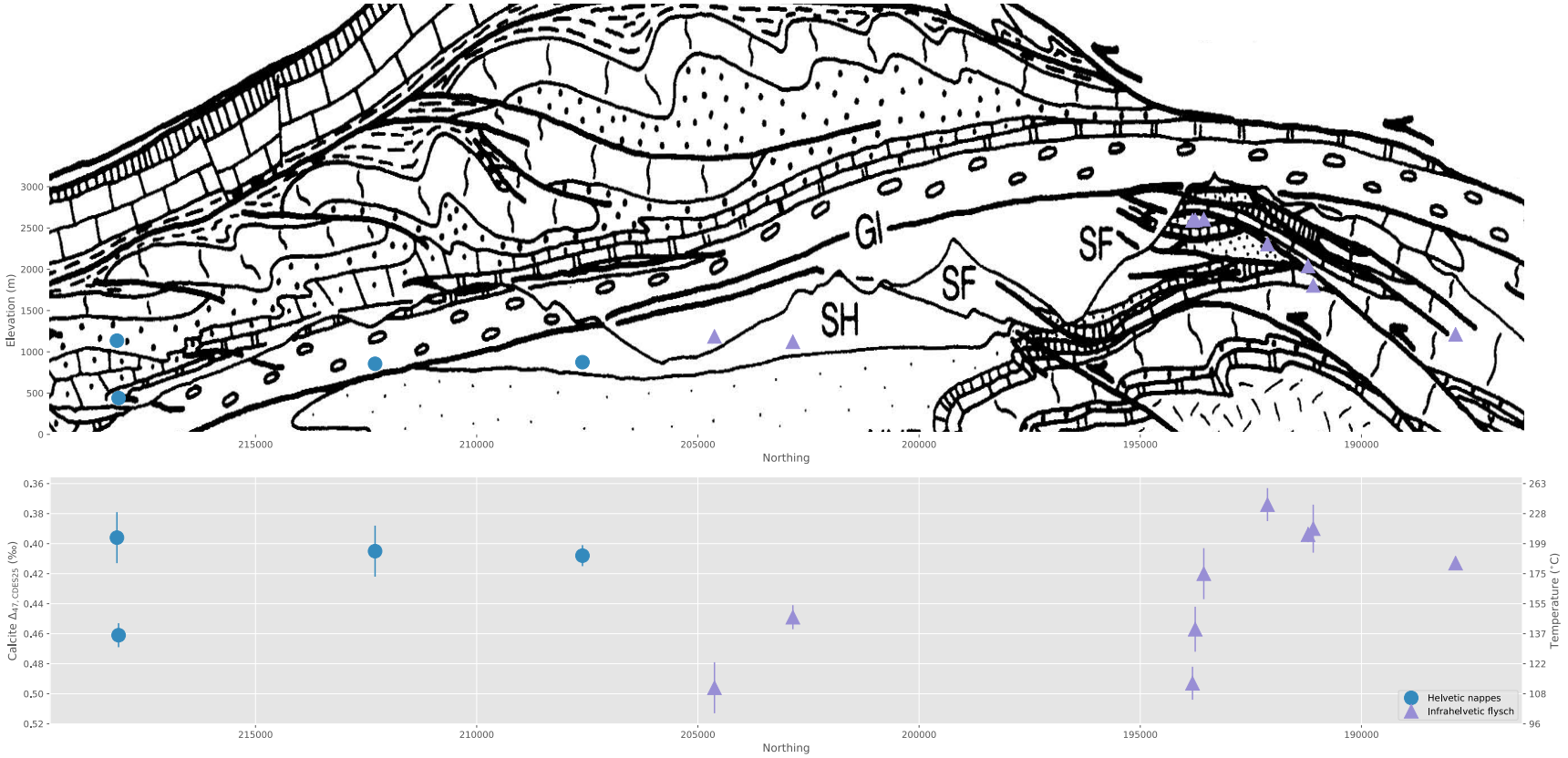

Figure 4.10: Calcite locations and Δ_{47}-temperatures in the southern Helvetic nappes and Infrahelvetic complex. Approximate sample locations plotted on the regional cross section of O Adrian Pfiffner (1993). Due to doming of the fault plane, some Helvetic nappe samples are inaccurately projected into this section.

correlate with $T_{\Delta 47}$ (Fig. 4.11). Such large range in calcite $\delta^{18}O$ requires either pervasive alteration by a secondary fluid (i.e., high W/R ratios), or that primary calcites are of mixed origin. The former explanation is incompatible with the data set because a W/R ratio large enough to so drastically shift bulk calcite ^{18}O contents would preclude substantial ^{18}O enrichment of the pore fluid. Instead, the apparent correlation between $T_{\Delta 47}$ and $\delta^{18}O_{H2O}$ is likely the result of the coincidental superposition of two independent processes: 1) lithologies in the Infrahelvetic complex transition from flysch sediments in the north to parautochthonous carbonate cover of the Aar massif in the south. This transition is accompanied by a secular shift in calcite $\delta^{18}O$ values, possibly due to an increased fluvial/meteoric component in the fluids responsible for the deposition of the flysch package (Fig. 4.6); 2) burial depths and peak temperatures in the Infrahelvetic complex also increase to the south due to the orientation and geometry of the wedge during burial and exhumation. Were peak temperatures invariant in the units, theoretical $\delta^{18}O_{H2O}$ values would nonetheless be expected to vary, albeit over a smaller range ($\sim$ 6 ‰) and with a shallower slope in $\delta^{18}O_{H2O}$ vs. $\delta^{18}O_{mineral}$-space ($m \approx 1$). On the other hand if calcite $\delta^{18}O$ values were constant, a range of $\delta^{18}O_{H2O}$ values would still be predicted due to the 100 °C variation in formation temperature. The combination of these effects results in a data set that appears unified in origin and recrystallization process, but in fact mixes sedimentary units of distinct provenance and thermal history.

Asymmetric dolomite recrystallization in the Infrahelvetic flysch

Because dolomite can be digested separately from calcite (see section 4.2), this phase can potentially preserve a different crystallization event not recorded in the pure calcium carbonates. Because its C – O bond reordering kinetics are substantially slower than those of calcite (Lloyd et al., *in prep*), dolomite Δ_{47} can faithfully retain such crystallization conditions up to 300 °C (Lloyd, John M Eiler, and Nabelek, 2017). Unfortunately, of the thirty-one samples analyzed for calcite Δ_{47} as part of the regional study, to-date only five samples from the Infrahelvetic complex have been found to contain sufficient dolomite for analysis. Further sample processing and screening by powder XRD will be required in order to find dolomite-bearing hand samples from the Helvetic nappes, and thus determine just how high above the calcite Δ_{47} blocking temperature were peak conditions in the the southernmost nappes. Still, even among the five dolomite-bearing samples studied so far, a story of contrasting origins and recrystallization in the flysch units and the parautochthonous cover sequence is observed, consistent with the one described in section 4.3.

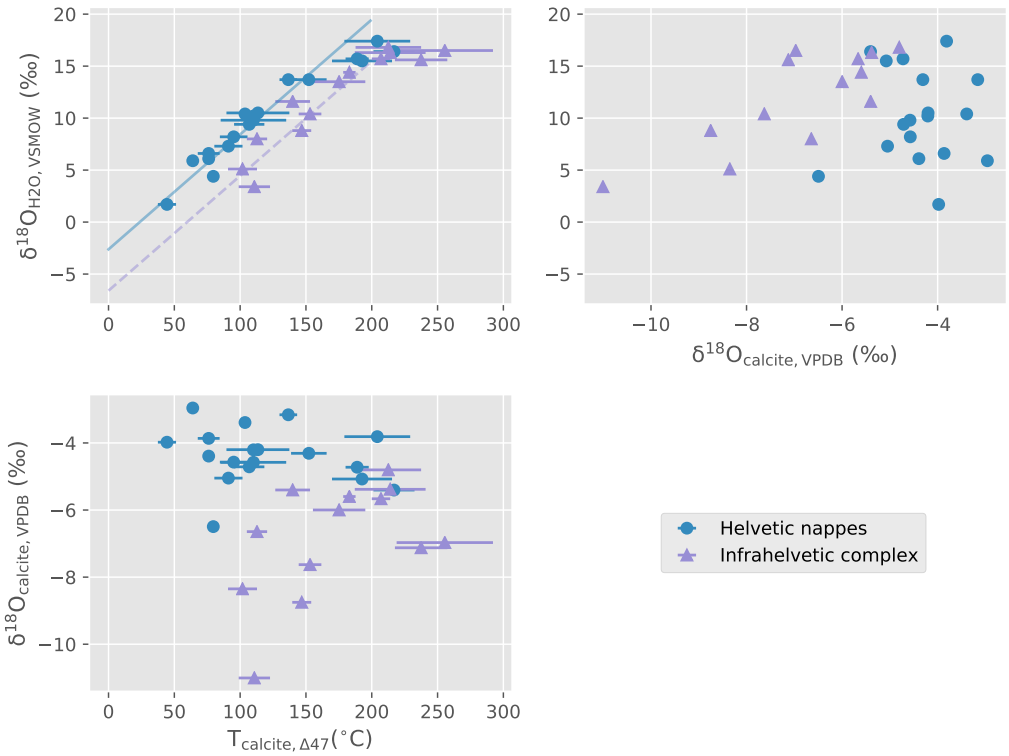

Figure 4.11: Triple-plot of calcite $\delta^{18}O$, $T_{\Delta47}$, and theoretical equilibrium water $\delta^{18}O$ in the Helvetic nappes and Infrahelvetic complex. $\delta^{18}O_{H2O}$ calculated from the empirical calibration of Friedman and O'neil (1977). Error-weighted linear regressions of temperature and fluid data were calculated using York, 1968 fits.

In marbles from the parautochthonous cover sequence (16–VP–11 and 16–VP–50), we observe dolomite and calcite Δ_{47} blocking temperatures broadly consistent with crystallization of both phases at or above 300 °C (Fig. 4.12). With only one stepped digestion of each sample to date, dolomite Δ_{47} values are highly uncertain and should not be confidently interpreted as accurate temperatures (due to the extreme sensitivity at low Δ_{47} values, the remarkably high apparent dolomite temperatures in these marbles are likely to regress to typical blocking temperatures ($\sim$ 300 °C) with further replication). Nonetheless, the relative ordering of co-existing dolomite and calcite Δ_{47} values in these two samples ($\Delta_{47,dolomite} < \Delta_{47,calcite}$) is consistent with metamorphism at moderately high grades, followed by solid-state reordering during cooling and exhumation. Notably, sample 16–VP–11 is from the section at the base of the Vorab glacier where highly heterogeneous calcite Δ_{47} values are observed (see section 4.3). If its dolomite blocking temperature is a constraint on the minimum peak temperature of the outcrop, it is difficult to understand how

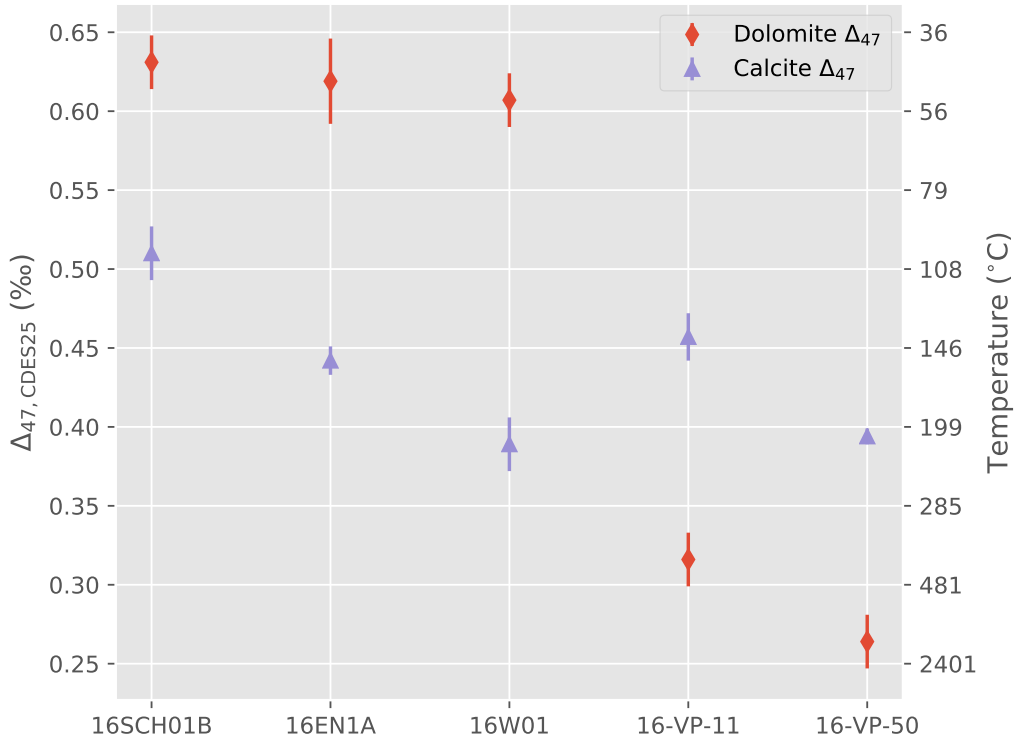

Figure 4.12: Paired dolomite and calcite Δ_{47} values and temperatures from the Infrahelvetic flysch (16SCH01B, 16EN1A, and 16W01) and parautochthonous cover of the Aar massif (16–VP–11,–50). With one exception, stepped dolomite extractions have not been replicated, so dolomite Δ_{47} values are highly uncertain. Locations of three flysch samples are unknown, so here all samples are simply ordered by their dolomite $T_{\Delta 47}$ value.

nearby matrix calcite Δ_{47} temperatures could remain as low as 113 ± 8 °C (sample 16–VP–10, n = 2) while being exposed to at least 300 °C. Did calcite grains in the parautochthonous sequence continue to dynamically recrystallize far into the retrograde exhumation pathway, possibly in response to strain related to deformation on the Glarus thrust? If so, why was such recrystallization locally focused in some units and not others? Are these specific samples closer to the fault plane than my 'dead reckoning' extrapolation would predict, but still far enough that bulk calcite $\delta^{18}O$ values were not modified? Further analyses of other samples from the section could help address these questions.

Exact locations of the dolomite-bearing flysch samples from are not yet known. Although not yet replicated, a wide range of calcite Δ_{47} temperatures are observed in these samples, from 100 to ~200 °C. If these calcite temperatures end up increasing to the south, it will be encouraging evidence of our ability to recover peak

temperatures in anchimetamorphosed samples of the Infrahelvetic flysch. Notably, dolomite Δ_{47}-temperatures are uniform in all flysch samples measured so far, and far colder than co-existing calcites: $T_{\Delta47,\text{dolomite}} = 43 - 53$ °C (Fig. 4.12). Due to its relatively sluggish reordering kinetics, it is unlikely that dolomite Δ_{47}-temperatures would end up below those of calcite crystallized if both phases crystallized at peak conditions. Thus, such 'inverse' Δ_{47} ordering requires that dolomite and calcite (re)crystallization were separated in both ambient temperature conditions and time. This can be reconciled in one of two ways: 1) long after peak burial conditions and partial exhumation, a late Mg-bearing fluid partially dolomitized these samples; Or, 2) diagenetic dolomite formed early on the prograde path, and resisted reordering and recrystallization for the duration of the burial–exhumation cycle, even as intermingled calcite did not. A late dolomitizing fluid is unlikely because such a brine may be expected to have an evolved, high ^{18}O content, but the Horita (2014) dolomite–water empirical $\alpha^{18}O$ calibration indicates that these dolomites formed from a fluid with a *lower* $\delta^{18}O$ value than pristine ocean water (Fig. 4.13). In fact, the theoretical dolomite $\delta^{18}O_{H2O}$ values lie directly on the trend defined by a York (1968) regression through the co-existing calcite $\delta^{18}O_{H2O}$ vs. $T_{\Delta47}$ data in the flysch units (Fig. 4.13). This agreement is most consistent with a unified model where all carbonate phases formed and recrystallized under rock-buffed conditions in the flysch.

Encouragingly, the temperatures of this early dolomite are consistent with those of carbonate diagenesis in the model of Dielforder (2016) for the Infrahelvetic flysch units (40–70 °C). Note, however, that preservation of such early dolomite has two requirements: 1) dolomite must have resisted substational solid-state reordering at peak temperatures in the flysch, which are at least as high as the calcite Δ_{47}-temperatures in each sample (100–200 °C); And, 2) dolomite must have resisted secondary rock-buffered recrystallization even as co-exisiting calcite grains may not have. The recently-determined solid-state reordering kinetics for dolomite suggest that this phase can likely resist even partial C – O bond reordering up to temperatures of about 140 °C. Preserving diagenetic Δ_{47} values at higher ambient temperatures is conceivable, but only if subjected to these conditions for (geologically) short durations of time, and only then if dolomite's capacity to partially reorder by exchange between neighboring carbonate groups is somewhat reduced. It is perhaps even more surprising that dolomites resisted modification by dissolution–reprecipitaiton reactions even as nearby calcites did not. This would appear to suggest that, once formed, dolomite is universally more stable than calcite in anchimetamorphic en-

vironments. Such a notion contrasts with the results of the Notch Peak contact aureole, where dolomite was found to reliably record peak metamorphic conditions between 150 and 300 °C. These contrasting crystallization behaviors may be due to differences in heating time, because the entire Notch Peak member was incubated at $\geq$ 150 °C for ~100 million years, whereas peak conditions in the flysch were fleeting by comparison. Or, perhaps the discrepancy could have a lithologic cause? Could dolomite in a clay and silica-rich flysch sample have less kinetic drive to recrystallize than a pure dolomite-bearing marble? Could differences in strain magnitude or rate induce differences in recrystallization behavior? The critical test for these questions will be observing dolomite recrystallization and reordering behavior in the overlying nappe sequence. This will elucidate whether this peculiar resistance to Δ_{47} modification is idiosyncratic to dolomite in the Infrahelvetic flysch units or a feature of the entire fold-and-thrust belt. To accomplish this, further sample processing and XRD screening are required to find dolomite-bearing segments of the Helvetic nappes across a range of metamorphic grades.

Discontinuous inverse temperature gradients along the Glarus fault

To directly constrain the amount of post-peak metamorphic offset on the Glarus thrust and attempt to distinguish between styles of deformation, we have measured Δ_{47} values across vertical sections of the thrust plane. To-date, twenty-four measurements have been made on nineteen powders from four outcrops of the Lochsiten calc-tectonite, hanging wall Verrucano, and footwall Infrahelvetic complex. Bulk powders have not yet been characterized for modal mineralogy by XRD. It is likely that the carbonate in these samples is predominantly calcite, but possible that measurements of minor dolomitic components will be viable in some samples through stepped acid extractions during a subsequent analytical session. Three of these outcrops are from southern exposures of the thrust exposed to relatively high temperatures (> 300°C; Piz Segans, Vorab Pign, and a previously-unreported outcrop near Berggasthaus Nagens (SCS: 735706/192097; Fig: 4.14)).

In all three of these outcrops, calcite Δ_{47} temperatures are indistinguishable from typical blocking temperatures in high grade marbles, with no resolvable differences between hanging wall, footwall, and calc-tectonite fabrics (cumulative mean $T_{\Delta 47}$ = 180 ± 14 °C; Figs. 4.15, 4.16, 4.17). This is not simply because the transitions between hanging wall and footwall units were not captured in our sampling; large shifts in calcite $\delta^{13}C$ and $\delta^{18}O$ are recovered from the contacts, which are consistent with previous studies of the stable isotope systematics of the Lochsite

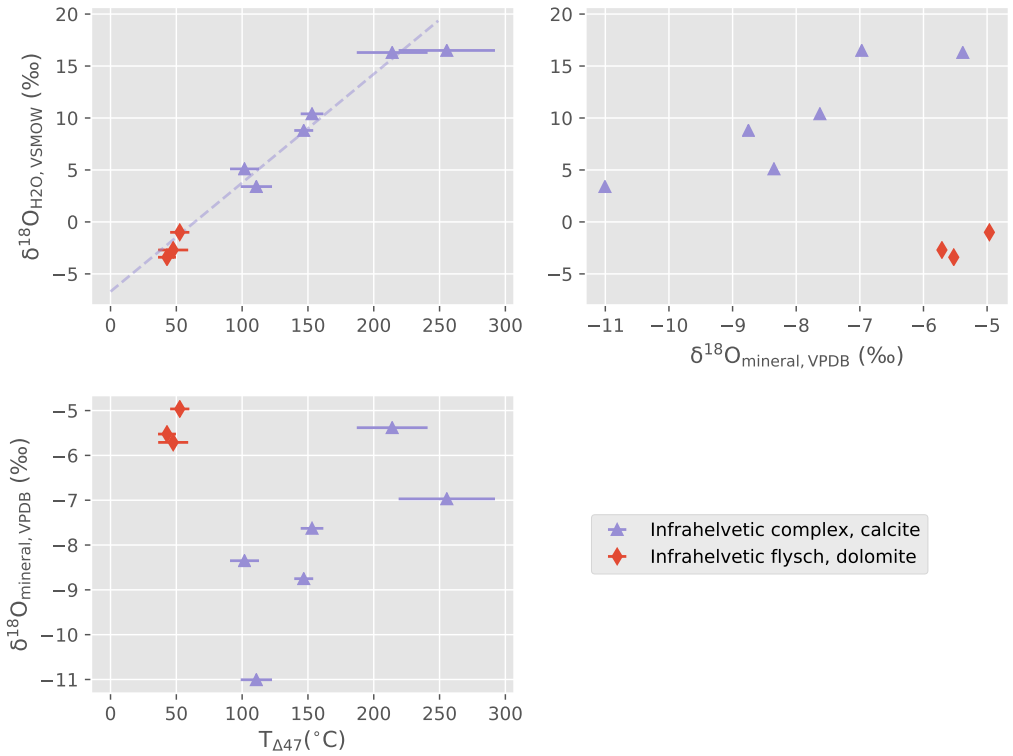

Figure 4.13: Triple-plot of calcite and dolomite $\delta^{18}O$, $T_{\Delta 47}$, and theoretical equilibrium water $\delta^{18}O$ in the North- and South-helvetic flysch. $\delta^{18}O_{H2O}$ values calculated from the empirical calibrations of Friedman and O'neil (1977) and Horita (2014) for calcite and dolomite, respectively. Error-weighted linear regression of calcite temperature and fluid data was calculated using a York, 1968 fit.

calc-tectonite (Nicolas P Badertscher, Beaudoin, et al., 2002; Nicolas P Badertscher, Abart, et al., 2002). Instead, this merely indicates that, here, the Lochsite crystallized at temperatures at or above ~180 °C, consistent with previous constraints on peak conditions at these outcrops (Ebert, Herwegh, and A. Pfiffner, 2007). Thus even resolvable textures, such as the gray and buff-colored mm-scale banding in calc-teconites from the new Vorab outcrop, which preserve large (~ 2 ‰) differences in calcite $\delta^{18}O$, have statistically identical, fully-reordered Δ_{47} values (Fig: 4.17). Importantly, the lack of any textures with calcite Δ_{47}-temperatures significantly below 180 °C may suggest that post-peak metamorphic thrusting was suspended at or above this temperature. Such arguments are inherently problematic because they are based on the absence of an observation of colder $T_{\Delta 47}$ textures. Still, if these results hold up to further investigation for these three outcrops, they would place new constraints on the ambient temperatures (and thus depths) at which the Glarus thrust was no longer active during the exhumation of the Helvetic nappes.

(a) Piz Segans (736563/196585)

(b) Close-up Piz Segans

(c) Vorab Pign (732335/192622)

(d) Unreported outcrop (735706/192097)

Figure 4.14: Pictures of high-grade outcrops of the Lochsiten calc-tectonite and enveloping units in the southernmost exposures of the Glarus fault plane.

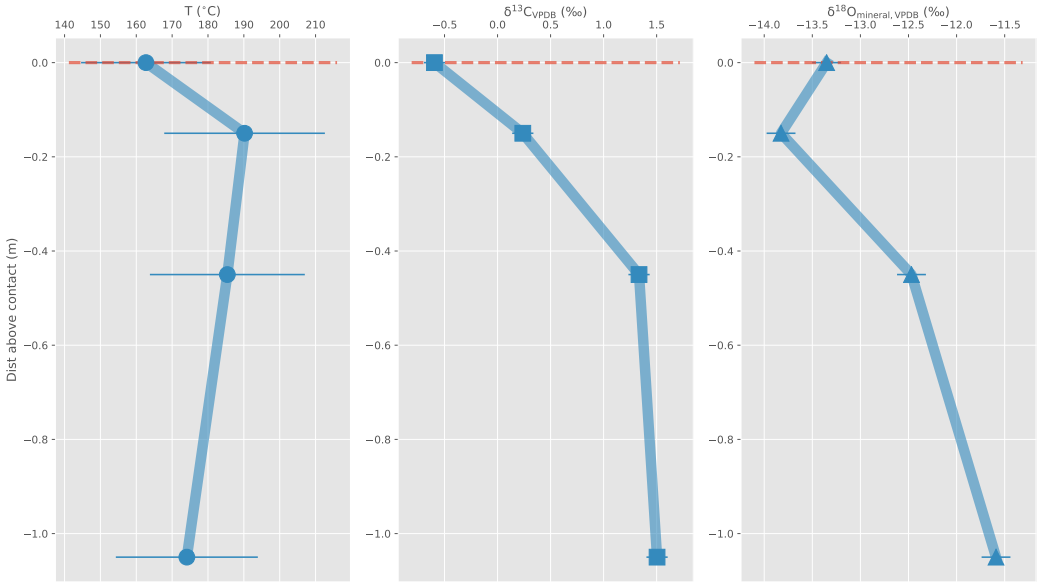

Figure 4.15: Calcite $T_{\Delta 47}$, $\delta^{13}C$, and $\delta^{18}O$ in the Piz Segans section.

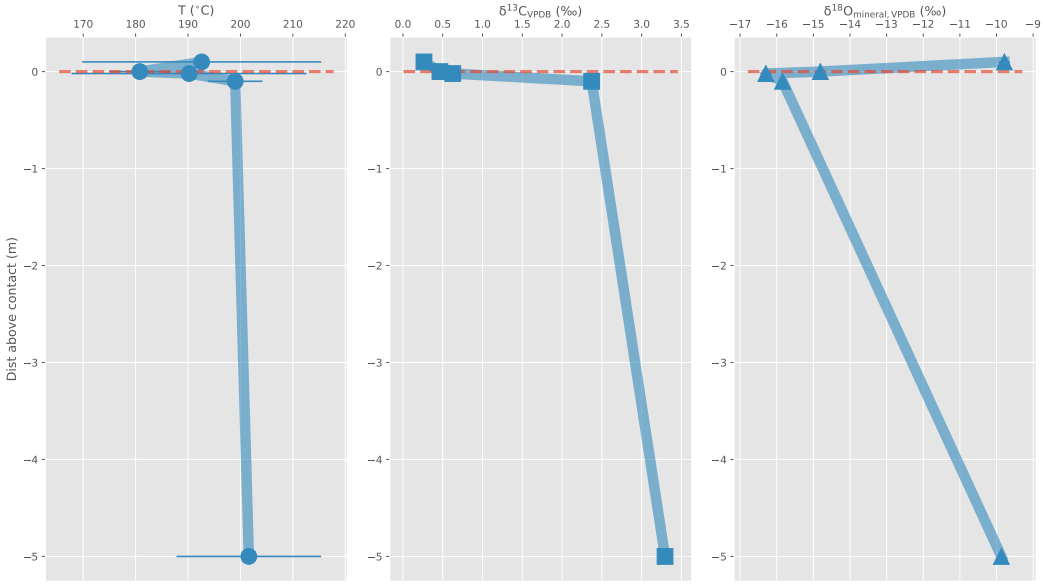

Figure 4.16: Calcite $T_{\Delta 47}$, $\delta^{13}C$, and $\delta^{18}O$ at the Vorab Pign outcrop.

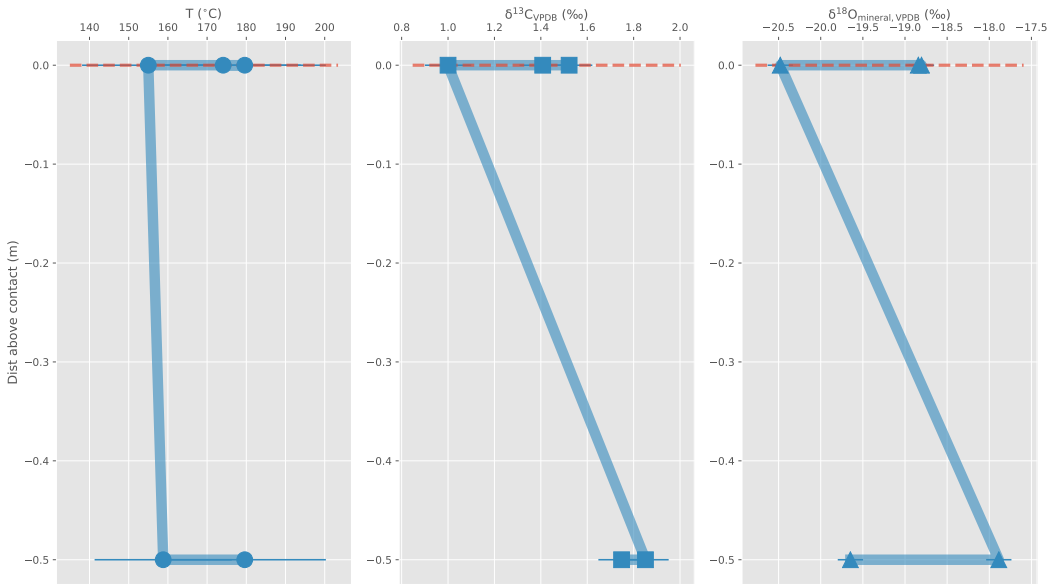

Figure 4.17: Calcite $T_{\Delta 47}$, $\delta^{13}C$, and $\delta^{18}O$ at the new Vorab contact. Individual data points at the same distance are texture-specific powders subsampled by micro-drilling.

The norhernmost section of the fault sampled in detail is from the Niderenbach valley on the north flank of Kärpf (SCS: 726740/199933). Here, the Niderenbach river has bored a cave through the fault plane at a juxtaposition of a carbonaceous slice of the hanging wall with flysch in the footwall, allowing for detailed three-dimmensional sampling of carbonate-rich lithologies on both sides of the fault (Fig 4.18). Footwall peak temperatures in a nearby outcrop at the same latitude have been previously estimated at ~270 °C based on illite crystallinity, vitrinite reflectance, and fluid inclusion data (M. Rahn et al., 1995; Ebert, Herwegh, and A. Pfiffner, 2007). Here, in addition to retaining bulk isotopic heterogeneity, a discontinuous inverse metamorphic gradient in calcite $T_{\Delta 47}$ is observed (Fig: 4.19): although the hanging wall slice contains typical calcite clumped isotope blocking temperatures (mean $T_{\Delta 47}$ = 217 ± 19 °C), footwall Δ_{47}-temperatures drop precipitously to 137 ± 3 °C 10 cm below the contact, and as low as 89 ± 10 °C another two meters below that. If peak temperatures were truly in excess of 200 °C at this locality, as suggested by all current models of the thermal structure of this section of the Glarus alps (Wang, FREY, and STERN, 1996; M. Rahn et al., 1995; M. K. Rahn, Hurford, and FREY, 1997; M. K. Rahn and Grasemann, 1999; Ebert, Herwegh, and A. Pfiffner, 2007; Dielforder, Berger, and Marco Herwegh, 2016), it is difficult to imagine how any early prograde calcite Δ_{47}-temperatures as low as 90 °C could have been preserved.

Instead, these data likely reflect ambient conditions of dynamic recrystallization during post-peak metamorphic offset along the fault, and suggest that here the Glarus thrust was active long into the retrograde phase, at depths corresponding to ambient temperatures as least as cold as the coldest Δ_{47}-temperatures measured so far.

Figure 4.18: The Glarus thrust contact exposed on the north flank of Kärpf (SCS: 726740/199933).

Fabric-specific deformation temperatures in the Lochsiten calc-tectonite

To probe the conditions of retrograde fault motion at a finer scale, we also measured Δ_{47} values from micro-drilled mm-scale fabrics from four Lochsite samples studied in detail in Andreas Ebert's thesis and subsequent publications (Ebert, 2006; Ebert, Herwegh, and A. Pfiffner, 2007; Andreas Ebert et al., 2008). These four samples span a large range in metamorphic conditions, from high-grade sheared marbles at the Nagens site, to a moderately-cool calc-tectonite from the Risentenhoren outcrop (peak conditions approximately similar to Kärpf), to the Lochsite UNESCO World Heritage outcrop at Schwanden, which is the lowest-temperature exposure of the fault plane that exists. All samples are pure or nearly pure carbonate, but phases have not been identified by XRD.

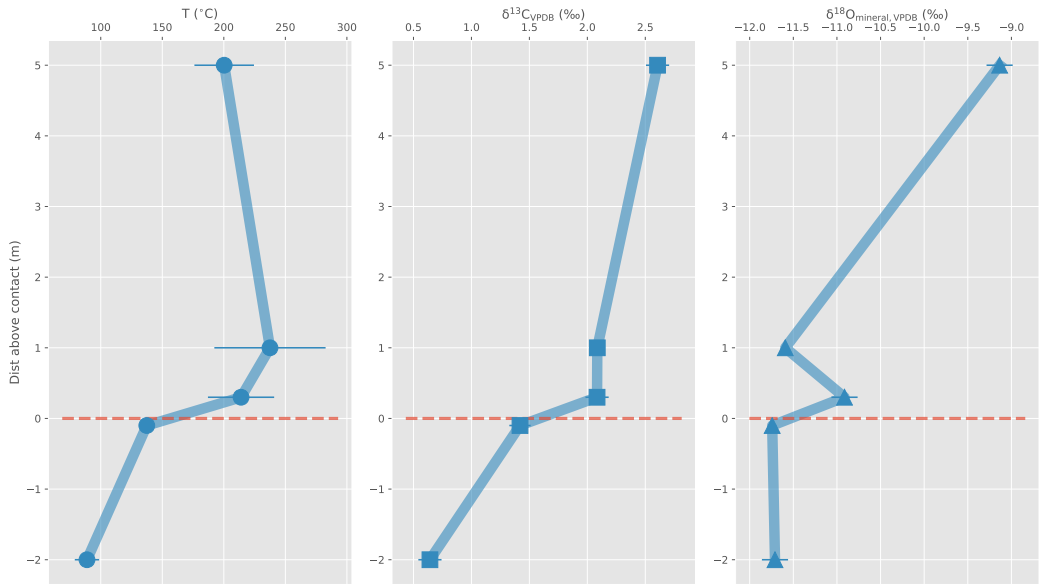

Figure 4.19: Calcite $T_{\Delta 47}$, $\delta^{13}C$, and $\delta^{18}O$ at the Kärpf outcrop.

At Nagens, a large gradient in carbonate $\delta^{18}O$ is observed with distance to the fault plane (Fig. 4.20). From the topmost fabric sampled to the most distant one in the footwall, calcite $\delta^{18}O$ values rise from −20.6 ‰ to −11.8 ‰. A trend in the same direction but with smaller magnitude is observed in $\delta^{13}C$ values. Both such trends are similar to those observed at the nearby Vorab Pign section of the Lochsite and upper footwall (Fig. 4.16). Calcite Δ_{47}-temperatures are uniform and similar to the apparent equilibrium blocking temperatures measured in other high-grade sections of the Lochsite calc-tectonite ($T_{\Delta 47}$ = 176 ± 7 °C). Thus, the temperatures on these mm-scale subsample are consistent with the lower limits on the temperature of final pervasive deformation in high-grade sections of the Glarus fault (see section 4.3). On the other hand, late, brittle deformation features in Nagens sample gl–lo–7 are clearly visible but have yet to be analyzed, and could possibly record lower final temperatures if these fine fracture-filling calcites can be isolated (Fig. 4.20a).

No significant variations in isotopic compositions are observed in two fabrics of the Risetenhoren sample (Fig. 4.21a). In the Schwanden sample, on the other hand, we find dramatic differences in calcite Δ_{47}-temperatures at a sub-cm scale (Fig. 4.21b). The entire sample is strongly foliated, with mm-sized alternating bands of grey, white, and tan carbonate. A strongly sheared white crystal from the most wavy section of the sample is relatively hot ($T_{\Delta 47}$ = 162 ± 18 °C). A tan sigmoidal enclave has a similar Δ_{47}-temperature (148 ± 16 °C). The sheared grey fabric between these two grains, however, is dramatically colder: $T_{\Delta 47}$ = 71 ± 9 °C

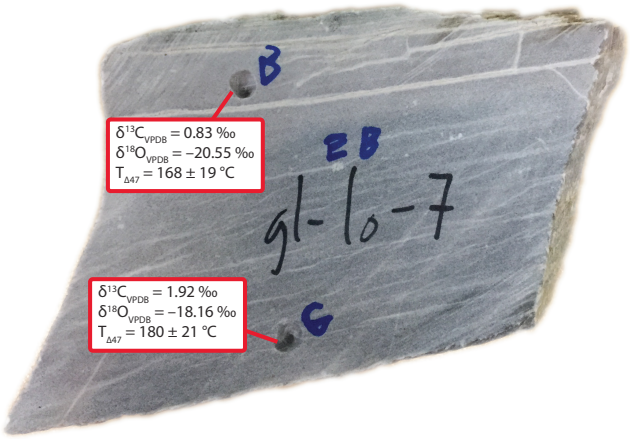

(a) Nagens, upper section

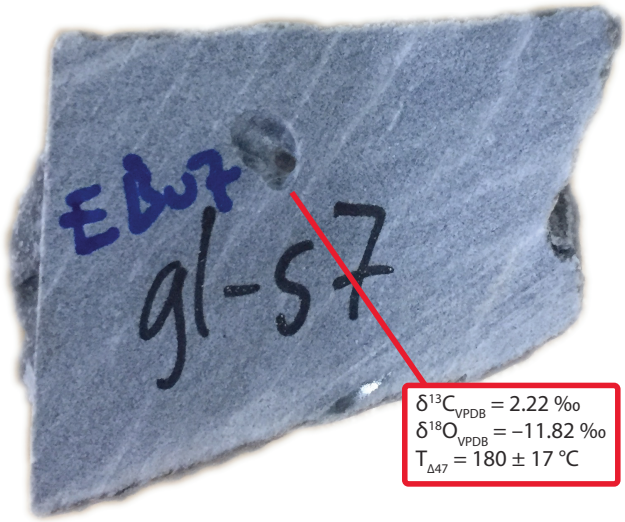

(b) Nagens, lower section

Figure 4.20: Photographs and isotopic data for microdrilled carbonate fabrics of the Lochsiten calc-tectonite at Nagens, where peak conditions exceeded 300 °C.

(Fig. 4.21b). That this grey fabric envelops the tan sigmoidal carbonate and is less undulose than the banding surrounding the white crystalline calcite suggests that it is the most recent fabric to recrystallize. If so, and if these data hold up to replication, then this suggests that dynamic recrystallization, and perhaps ductile deformation, persisted in the Lochsite calc-tectonite at Schwanden until ambient conditions cooled to at least ~70 °C.

4.4 Synthesis and suggestions for focus of future work

From these initial exploratory data sets, a few common questions emerge that could be good targets for further study. Of course, any other suggestions for directions to

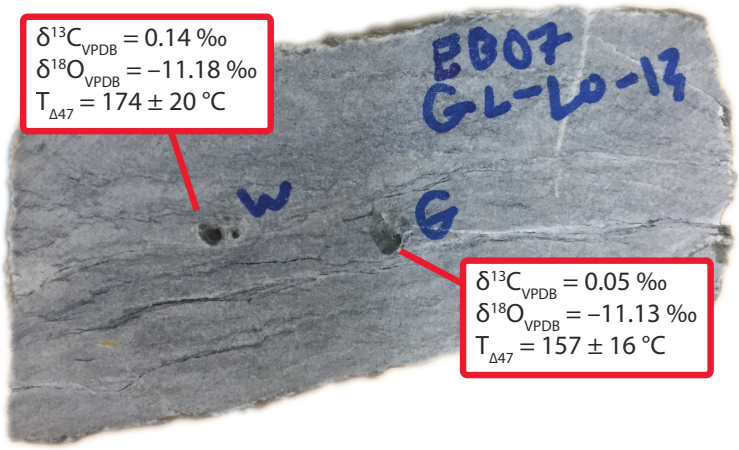

(a) Risetenhoren

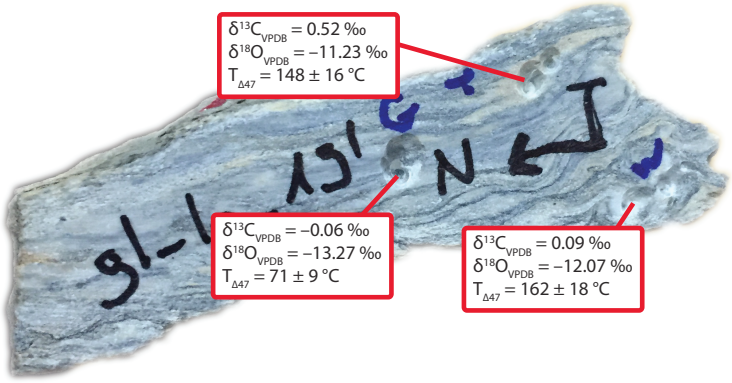

(b) Schwanden

Figure 4.21: Photographs and isotopic data for microdrilled carbonate fabrics from low-temperature sections of the Lochsiten calc-tectonite.

take these efforts are most welcome.

Causes of scatter in regional calcite Δ_{47} values from hot sections

It is not surprising that among the low-temperature carbonates of the Säntis nappe, large variations in calcite Δ_{47}-temperatures exist. Patchy, heterogenous recrystallization behaviors are a common feature of carbonate clumped isotope datasets in deeply-buried sedimentary sequences (eg., Bergmann, 2013; Shenton et al., 2015). Although a large effort *could* be directed to understanding why certain hand samples in the Säntis range recrystallized at 100 °C while others retained lower diagenetic temperatures at 50 °C, likely through detailed characterization of the microstructural, microcrystallographic, and geochemical differences in the samples, it is not clear that such answers would be particularly satisfying or applicable to other systems where carbonates are buried to moderate temperatures.

More surprising are the large differences in calcite Δ_{47}-temperatures in samples that are all believed to have been exposed to relatively high temperatures, at least above 200 °C. For instance, according to vitrinite reflectance, illite crystallinity, and fluid inclusion microthermometry studies, even the coldest, northernmost sections of the Infrahelvetic flysch were buried to 230 °C (M. Rahn et al., 1995; Wang, FREY, and STERN, 1996; Ebert, Herwegh, and A. Pfiffner, 2007). At such high temperatures, calcite Δ_{47} values should fully re-equilibrate in the solid state within just a few million years (Stolper and J M Eiler, 2015). To demonstrate this, we modeled calcite Δ_{47} reordering for T-t paths determined by previous apatite (U-Th)/He work in the Infrahelvetic complex (M. Rahn et al., 1995) (Fig. 4.22). These models show that except in the coldest, northernmost toe of the flysch units, prograde calcite should have fully reordered to typical blocking temperatures during metamorphism. The discrepancy is especially apparent when modeled calcite Δ_{47} temperatures are compared to measured ones in the flysch (Fig. 4.23). Although measured values the higher-grade marbles of the parautochthonous cover agree with the models, many Δ_{47} values in the flysch are far too cold (Fig. 4.23). The discovery of temperatures as low as ~100 °C in the Infrahelvetic flysch units and parautochthonous mesozoic carbonates, even in samples far removed from the Glarus fault plane, thus requires one of three peculiar situations: 1) peak temperatures in the Infrahelvetic complex were dramatically overestimated in previous studies, 2) the experimentally-derived reordering kinetics for Δ_{47} values in pure optical calcite are inaccurate when applied to natural samples of complex lithology in cold geologic settings, or 3) the capacity of calcites to recrystallize far into the retrograde metamorphic path is grossly under-appreciated.

Although interpreting qualitative thermal maturity indicators as accurate, absolute temperatures is notoriously problematic, it is unlikely that these proxies could have 'over-shot' temperatures in the flysch units by at least 50 °C. Even if peak conditions in the flysch units were so dramatically overestimated, multiple independent thermometers in the more southern parautochthonous Mesozoic carbonates (e.g., calcite–dolomite Mg thermometry (Ebert, Herwegh, and A. Pfiffner, 2007); dolomite Δ_{47}-thermometry (this study)) indicate that these units were exposed to at least 300 °C. And even in these hotter units, cold, heterogeneous calcite Δ_{47} values persist. Given the extreme unlikelihood that these calcites either resisted reordering during prograde metamorphism to 300 °C or fully reordered in the solid state on the retrograde path down to 100 °C, the only reasonable conclusion is that late retrograde-stage recrystallization is a pervasive, yet erratic, feature of calcite grains

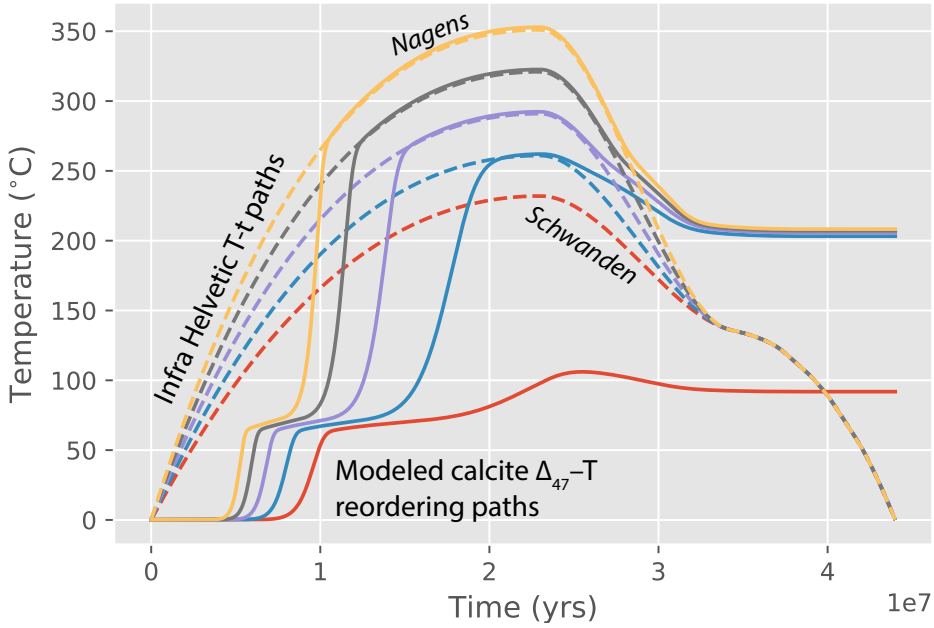

Figure 4.22: Calcite C – O reordering model for T-t paths in the Infrahelvetic complex.

in the tectonic blocks of the Glarus alps. This, too, is somewhat unusual because it has been widely discussed that during regional exhumation of the Glarus alps, strain and strain-induced dynamic recrystallization were focused on the out-of-sequence Glarus thrust and the few meters of rock immediately enveloping it. On the other hand, Dielforder, Vollstaedt, et al. (2015) recently documented the presence of late, extensional fractures throughout the Infrahelvetic complex, associated with the occurrence of cyclic seismicity along the Glarus thrust. However, these co-seismic extensional fractures were shown to occur at peak conditions of 210 – 290 °C through ^{18}O thermometry of vein-filling quartz and calcite, and confirmed by hot (180 – 230 °C) calcite Δ_{47} temperatures measured on these same veins in the present study (see attached Table 3). Thus, it would seem that anomalously cold calcite Δ_{47}-temperatures in the Infrahelvetic complex and (to some extent) Helvetic nappes document an even later stage of recrystallization during late retrograde cooling and exhumation of these units. This could recystallization could have been induced by regional stress due to the doming of the Aar massif, and is possibly associated with contemporaneous activity on the Glarus thrust fault, as evidenced by the cold Δ_{47}-temperatures in the latest fabrics of the Lochsite calc-tectonite at Schwanden and Kärpf. It is notable that such scattered, low-Δ_{47} heterogeneities are absent from the

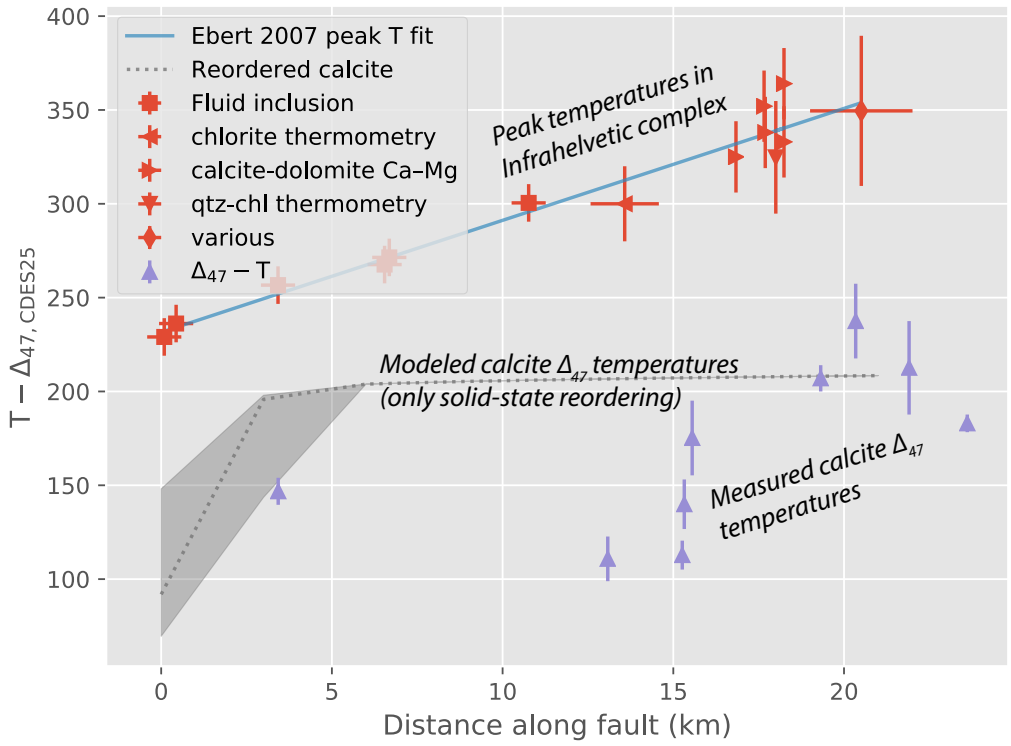

Figure 4.23: Synthesis of peak temperatures, measured and modeled calcite Δ_{47} temperatures in the Infrahelvetic complex.

southermost regional samples, which are unequivocally high-grade marbles. This contrast could suggest a textural/grain-size control on the susceptibility of exhumed carbonates to cold, late recrystallization. That is, granoblastic, coarse grained calcitic marbles may resist recrystallization when exposed to moderate stress under cold conditions, whereas in flysch units of lower grade and (often, but not exclusively) mixed lithologies, fine-grained matrix calcites will readily respond to regional strain by dissolving and re-precipitating.

The continuing search for dolomite-bearing samples

It is clear from the above discussion that one of the challenges of calcite Δ_{47}-thermometry is the limited range it has the ability to record. Many ambiguities above could be resolved with independent constraints on the peak temperatures of the studied samples from dolomite Δ_{47}-temperatures. The challenge is finding appropriate samples. Of the 32 samples screened so far by XRD, only 5 had sufficient dolomite for analysis. A concerted effort needs to be made to powder, scan, and discover more dolomite-bearing samples, especially from the Helvetic nappes and

the Lochsite calc-tectonites. An additional challenge of measuring bulk powders from pure calcite marbles is that at any tractable scale, resulting Δ_{47} values are inevitably mixtures of all the individual grains, microfabrics, and generations of calcite present in these complex samples. One advantage of extracting dolomite from bulk rocks where it is not abundant is that there is greater potential to reduce mixing effects and record the clumped and single-isotope composition of a single crystallization even. This aspect may be especially useful in the Lochsite samples, where if bulk calcite is accommodates most of the strain through dynamic recrystallization, perhaps scattered dolomite grains will retain the Δ_{47}-compositions of earlier events. The phase-specific Δ_{47} data from Venice's flysch samples already suggest that dolomite is uniquely resistant to recrystallization in tectonic environments. It would be worth exploring whether this principle holds when both strain rates and magnitudes are substantially increased. On the other hand, if dolomite Δ_{47}-temperatures dynamically recrystallize throughout the Lochsite shear zones, it will be possible to use this proxy for test the hypothesis of secular cooling-induced strain-localization from 300 °C to 200 °C in the exposed sections.

4.5 Supplementary data tables

Sample ID	Site	Easting	Northing	Elevation (m)	n	$\delta^{13}C$ (vpdb)	$\delta^{13}C$ stdev	$\delta^{18}O$ (min) (vpdb)	$\delta^{18}O$ stdev	Δ_{47} (CDES25)	Δ_{47} st dev	Δ_{47} std err	T (°C)	T (°C) (st err)	$\delta^{18}O$ (fluid, vs-mow)	Unit
16-BN-1	Bread Nestle	735464	225112	1259.5	2	1.756	0.001	-4.578	0.013	0.497	0.048	0.034	110.1	24.9	9.8	HN
16-BN-10	Bread Nestle	731635	224323	1241.4	1	3.696	0.1	-4.572	0.15	0.521	0.017	0.017	95.1	10.5	8.2	HN
16-BN-3	Bread Nestle	733816	225947	1512.8	2	1.777	0.097	-6.494	0.067	0.549	0.007	0.005	79.6	2.7	4.4	HN
16-CF-1	Churfirsten	744195	223268	1743.8	4	2.52	1.053	-4.309	0.073	0.443	0.016	0.014	152.2	13.5	13.7	HN
16-CF-13	Churfirsten	742048	223257	1502.8	4	1.212	0.707	-4.2	0.046	0.492	0.043	0.032	113.5	23.9	10.5	HN
16-CF-17	Churfirsten	743499	221374	731.7	2	2.717	0.002	-5.404	0.02	0.387	0.014	0.01	216.9	15.6	16.4	HN
16-CH-16	Chaserrug	725930	202853	1121.8	2	-0.886	0.015	-8.751	0.014	0.449	0.012	0.008	146.8	7.2	8.8	IF
16-CH-17	Chaserrug	725809	207609	874.5	2	1.144	0.028	-4.724	0.019	0.408	0.01	0.007	188.9	8.8	15.7	HN
16-CH-22	Chaserrug	724469	212297	855.3	1	1.347	0.1	-5.075	0.15	0.405	0.017	0.017	192.6	22.8	15.5	HN
16-CH-30	Chaserrug	728803	218132	1135.6	4	0.945	0.002	-3.812	0.021	0.396	0.033	0.017	204.2	25	17.4	HN
16-CH-32	Chaserrug	724001	218095	440.2	2	1.552	0.025	-3.16	0.062	0.461	0.011	0.008	136.6	6.7	13.7	HN
16-CS-21	Cassons	741649	192124	2305.9	2	1.709	0.008	-7.125	0.04	0.374	0.015	0.011	237.5	19.9	15.6	IF
16-CS-24	Cassons	742996	191090	1804.1	2	1.993	0.004	-4.803	0.052	0.39	0.022	0.016	212.6	24.9	16.8	IF
16-P-11	Pizol	754964	204625	1186.8	2	-0.881	0.543	-11.006	0.085	0.496	0.023	0.017	110.8	11.9	3.4	IF
16-ST-1	Santis Thrust	744012	235209	2433.3	2	3.112	0.055	-3.391	0.038	0.507	0.002	0.001	103.7	0.6	10.4	HN
16-ST-14	Santis Thrust	745059	234338	2271.6	2	2.731	0.012	-4.205	0.006	0.497	0.008	0.006	110.1	4.1	10.2	HN
16-ST-15	Santis Thrust	745103	234355	2256.1	2	1.727	0.004	-2.958	0.014	0.581	0.006	0.004	64	1.8	5.9	HN
16-ST-22	Santis Thrust	745950	233994	2302	2	2.752	0	-4.712	0.002	0.502	0.024	0.017	106.9	11.5	9.4	HN
16-ST-25	Santis Thrust	746056	233814	2234.9	1	3.573	0.1	-3.978	0.15	0.627	0.017	0.017	44.4	6.9	1.7	HN
16-ST-31	Santis Thrust	746760	232411	1728.6	2	2.74	0.005	-5.048	0.027	0.528	0.026	0.018	91.1	10.7	7.3	HN
16-ST-32	Santis Thrust	746544	232146	1549.3	2	3.307	0.036	-4.392	0.009	0.556	0.004	0.003	76.1	1.5	6.1	HN
16-ST-7	Santis Thrust	744197	234743	2445.4	2	2.254	0.014	-3.864	0.005	0.556	0.023	0.016	76.1	8.3	6.6	HN
16-VP-10	Vorab	733048	193819	2592.7	2	1.279	0.609	-6.644	0.061	0.493	0.036	0.011	112.8	7.7	8	IF
16-VP-11	Vorab	733043	193758	2596.6	6	1.866	0.931	-5.402	0.241	0.457	0.027	0.015	139.9	13.2	11.6	IF
16-VP-14	Vorab	733138	193564	2606.5	1	1.661	0.1	-5.998	0.15	0.42	0.017	0.017	175.2	19.9	13.5	IF
16-VP-50	New Vorab Contact	736714	191207	2041	2	1.211	0	-5.664	0.039	0.394	0.008	0.005	207	7	15.7	IF
16-VP-55	New Vorab Contact	739149	187872	1211.7	2	1.946	0.549	-5.597	0.088	0.413	0.015	0.004	183	4.7	14.4	IF
VS-16EN1A	Venice_Flysch				2	0.802	0.911	-7.628	0.012	0.442	0.012	0.009	153.1	8.6	10.4	IF
VS-16MM01	Venice_Flysch				1	2.063	0.1	-6.97	0.15	0.364	0.017	0.017	255.5	36.6	16.5	IF
VS-16SCH01B	Venice_Flysch				1	0.571	0.1	-8.35	0.15	0.51	0.017	0.017	101.8	11	5.1	IF
VS-16W01	Venice_Flysch				1	1.028	0.1	-5.382	0.15	0.389	0.017	0.017	214	26.9	16.3	IF

Table 4.1: Mean calcite Δ_{47} data for the Glarus alps.

Sample ID	Site	Easting	Northing	Elevation (m)	n	$\delta^{13}C$ (vpdb)	$\delta^{13}C$ stdev	$\delta^{18}O$ (min) (vpdb)	$\delta^{18}O$ stdev	Δ_{47} (CDES25)	Δ_{47} st dev	Δ_{47} std err	T (°C)	T (°C) (st err)	$\delta^{18}O$ (fluid, vsmow)	Unit
16-VP-11	Vorab	733043	193758	2596.6	1	2.144	0.1	-2.739	0.15	0.316	0.017	0.017	392.9	95.6	24.1	HN
16-VP-50	Vorab Contact	736714	191207	2041	1	2.466	0.1	-3.297	0.15	0.264	0.017	0.017	1140.5	1838.1	29.1	HN
VS-16EN1A	Venice_Flysch				2	2.46	0.251	-5.71	0.701	0.619	0.038	0.027	47.6	11.4	-2.7	IF
VS-16SCH01B	Venice_Flysch				1	1.141	0.1	-5.524	0.15	0.631	0.017	0.017	42.9	6.8	-3.4	IF
VS-16W01	Venice_Flysch				1	1.524	0.1	-4.964	0.15	0.607	0.017	0.017	52.6	7.3	-1	IF

Table 4.2: Mean dolomite Δ_{47} data for the Glarus alps.

Sample ID full	Sample ID	Site	Easting	Northing	Elevation (m)	Distance above contact (m)	n	$\delta^{13}C$ (vpdb)	$\delta^{13}C$ stdev	$\delta^{18}O$ (min) (vpdb)	$\delta^{18}O$ stdev	Δ_{47} (CDES25)	Δ_{47} st dev	Δ_{47} std err	T (°C)	T (°C) (st err)	$\delta^{18}O$ (fluid, vsmow)
GL-Lo-13_G	GL-Lo-13	Risetenhoren	737250	204350			2	0.052	0.078	-11.135	0.461	0.438	0.022	0.016	156.8	16.2	7.082
GL-Lo-13_W	GL-Lo-13	Risetenhoren	737250	204350			1	0.136	0.1	-11.185	0.15	0.421	0.017	0.017	174.1	19.8	8.184
GL-Lo-19p_G	GL-Lo-19p	Lochsiten	726000	206350			1	-0.058	0.1	-13.265	0.15	0.567	0.017	0.017	70.6	8.5	-3.608
GL-Lo-19p_T	GL-Lo-19p	Lochsiten	726000	206350			1	0.515	0.1	-11.228	0.15	0.448	0.017	0.017	147.7	16	6.323
GL-Lo-19p_W	GL-Lo-19p	Lochsiten	726000	206350			1	0.094	0.1	-12.069	0.15	0.433	0.017	0.017	161.7	17.9	6.471
GL-Lo-7_B	GL-Lo-7	Nagens	736750	191980			1	0.829	0.1	-20.55	0.15	0.427	0.017	0.017	167.8	18.8	-1.765
GL-Lo-7_G	GL-Lo-7	Nagens	736750	191980			1	1.924	0.1	-18.157	0.15	0.416	0.017	0.017	179.6	20.7	1.413
GL-S-7	GL-S-7	Nagens	736750	191980			2	2.222	0.067	-11.815	0.251	0.415	0.02	0.014	180.8	16.9	7.954
13F89_G3	13F89	Globotruncana	736075	196097	2626.2		1	1.163	0.1	-8.777	0.15	0.397	0.017	0.017	202.9	24.7	12.294
14F37_G2	14F37	Globotruncana	734331	196097	1995		2	2.095	0.072	-8.051	0.071	0.41	0.015	0.01	186.6	12.4	12.136
16-CH-1	16-CH-1	Chaserrug	726740	199933	1833.4	5	1	2.606	0.1	-9.135	0.15	0.399	0.017	0.017	200.3	24.2	11.791
16-CH-10	16-CH-10	Chaserrug	726740	199933	1833.4	-2	1	0.642	0.1	-11.71	0.15	0.532	0.017	0.017	88.8	9.9	0.274
16-CH-5	16-CH-5	Chaserrug	726740	199933	1833.4	1	2	2.086	0.043	-11.592	0.009	0.374	0.033	0.023	237.5	45.2	11.047
16-CH-7	16-CH-7	Chaserrug	726740	199933	1833.4	0.3	1	2.084	0.1	-10.913	0.15	0.389	0.017	0.017	214	26.9	10.673
16-CH-8	16-CH-8	Chaserrug	726740	199933	1833.4	-0.1	2	1.419	0.092	-11.742	0.048	0.46	0.006	0.004	137.4	3.3	4.996
16-PS-10	16-PS-10	PizSegans	736563	196585	2740.3	-0.45	1	1.334	0.1	-12.469	0.15	0.411	0.017	0.017	185.4	21.6	7.559
16-PS-14	16-PS-14	PizSegans	736563	196585	2740.3	-1.05	1	1.504	0.1	-11.59	0.15	0.421	0.017	0.017	174.1	19.8	7.771
16-PS-7	16-PS-7	PizSegans	736563	196585	2740.3	0	1	-0.595	0.1	-13.351	0.15	0.432	0.017	0.017	162.7	18.1	5.233
16-PS-8	16-PS-8	PizSegans	736563	196585	2740.3	-0.15	1	0.238	0.1	-13.825	0.15	0.407	0.017	0.017	190.2	22.4	6.45
16-VP-28	16-VP-28	Vorab Pign	732335	192622	2582.3	0.1	1	0.264	0.1	-9.786	0.15	0.405	0.017	0.017	192.6	22.8	10.707
16-VP-30	16-VP-30	Vorab Pign	732335	192622	2582.3	0	2	0.465	0.027	-14.809	0.088	0.415	0.007	0.005	180.8	5.8	4.9
16-VP-31	16-VP-31	Vorab Pign	732335	192622	2582.3	-0.02	1	0.626	0.1	-16.298	0.15	0.407	0.017	0.017	190.2	22.4	3.926
16-VP-32	16-VP-32	Vorab Pign	732335	192622	2582.3	-0.1	2	2.372	0.009	-15.841	0.015	0.4	0.006	0.004	199	5.2	4.875
16-VP-34	16-VP-34	Vorab Pign	732367	192647	2578.3	-5	2	3.294	0.006	-9.868	0	0.398	0.014	0.01	201.6	13.8	11.112
16-VP-44_B	16-VP-44	New Vorab	735706	192097	2283.8	0	1	1.522	0.1	-18.842	0.15	0.421	0.017	0.017	174.1	19.8	0.377
16-VP-44_BT	16-VP-44	New Vorab	735706	192097	2283.8	0	1	1.408	0.1	-18.804	0.15	0.416	0.017	0.017	179.6	20.7	0.753
16-VP-44_T	16-VP-44	New Vorab	735706	192097	2283.8	0	1	1	0.1	-20.48	0.15	0.44	0.017	0.017	155	16.9	-2.562
16-VP-49_G	16-VP-49	New Vorab	735706	192097	2283.8	-0.5	1	1.851	0.1	-17.887	0.15	0.436	0.017	0.017	158.8	17.5	0.345
16-VP-49_T	16-VP-49	New Vorab	735706	192097	2283.8	-0.5	1	1.748	0.1	-19.648	0.15	0.416	0.017	0.017	179.6	20.7	-0.108

Table 4.3: Mean calcite Δ_{47} data for the Lochsited calc-tectonite

References

Badertscher, N P and M Burkhard (2000). "Brittle-ductile deformation in the Glarus thrust Lochseiten (LK) calc-mylonite". In: *Terra Nova* 12.6, pp. 281–288.

Badertscher, Nicolas P, Rainer Abart, et al. (2002). "Fluid flow pathways along the Glarus overthrust derived from stable and Sr-isotope patterns". In: *American Journal of Science* 302.6, pp. 517–547.

Badertscher, Nicolas P, Georges Beaudoin, et al. (2002). "Glarus overthrust: A major pathway for the escape of fluids out of the Alpine orogen". In: *Geology* 30.10, p. 875.

Bergmann, Kristin Diane (2013). "Constraints on the carbon cycle and climate during the early evolution of animals". PhD thesis. California Institute of Technology.

Brand, Willi A, Sergey S Assonov, and Tyler B Coplen (2010). "Correction for the 17O interference in δ(13C) measurements when analyzing CO2 with stable isotope mass spectrometry (IUPAC Technical Report)". In: *Pure and Applied Chemistry* 82.8.

Daëron, M et al. (2016). "Absolute isotopic abundance ratios and the accuracy of Δ47 measurements". In: *Chemical Geology* 442 IS -, pp. 83–96.

Dielforder, Armin (2016). "The accretion of underfilled foreland basin sediments and its implication for the prograde evolution of collisional orogens: An integrative structural, mechanical and geochemical perspective". PhD thesis. University of Bern.

Dielforder, Armin, Alfons Berger, and Marco Herwegh (2016). "The accretion of foreland basin sediments during early stages of continental collision in the European Alps and similarities to accretionary wedge tectonics". In: *Tectonics*.

Dielforder, Armin, Hauke Vollstaedt, et al. (2015). "Linking megathrust earthquakes to brittle deformation in a fossil accretionary complex". In: *Nature Communications* 6, p. 7504.

Ebert, A (2006). "Microfabric evolution in pure and impure carbonate mylonites and their role for strain localization in large-scale shear zones". PhD thesis. University of Bern.

Ebert, A, M Herwegh, and A Pfiffner (2007). "Cooling induced strain localization in carbonate mylonites within a large-scale shear zone (Glarus thrust, Switzerland)". In: *Journal of Structural Geology* 29.7, pp. 1164–1184.

Ebert, Andreas et al. (2008). "Grain coarsening maps for polymineralic carbonate mylonites: A calibration based on data from different Helvetic nappes (Switzerland)". In: *Tectonophysics* 457.3-4, pp. 128–142.

Friedman, Irving and J R O'neil (1977). *Compilation of stable isotope fractionation factors of geochemical interest: United States Geological Survey Professional Paper, v. 440-KK*. United States Geological Survey.

Herwegh, Marco, Alfons Berger, and A Ebert (2005). "Grain coarsening maps: a new tool to predict microfabric evolution of polymineralic rocks". In: *Geology*.

Herwegh, Marco, Jean-Pierre Hürzeler, et al. (2008). "The Glarus thrust: excursion guide and report of a field trip of the Swiss Tectonic Studies Group (Swiss Geological Society, 14.–16. 09. 2006)". In: *Swiss Journal of Geosciences* 101.2, pp. 323–340.

Horita, Juske (2014). "Oxygen and carbon isotope fractionation in the system dolomite–water–CO2 to elevated temperatures". In: *Geochimica et Cosmochimica Acta VL - IS - SP - EP - PY - T2* - 129 IS -.C, pp. 111–124.

Lloyd, Max K, John M Eiler, and Peter I Nabelek (2017). "Clumped isotope thermometry of calcite and dolomite in a contact metamorphic environment". In: *Geochimica et Cosmochimica Acta* 197, pp. 323–344. DOI: 10.1016/j.gca.2016.10.037.

Pfiffner, O A (1985). "Displacements along thrust faults". In: *Eclogae Geologicae Helvetiae*.

– (1986). "Evolution of the north Alpine foreland basin in the Central Alps". In: *Foreland basins*.

Pfiffner, O Adrian (1993). "The structure of the Helvetic nappes and its relation to the mechanical stratigraphy". In: *Journal of Structural Geology* 15.3-5, pp. 511–521.

Poulet, Thomas et al. (2014). "Modeling episodic fluid-release events in the ductile carbonates of the Glarus thrust". In: *Geophysical Research Letters* 41.20, pp. 7121–7128.

Rahn, M K and B Grasemann (1999). "Fission track and numerical thermal modeling of differential exhumation of the Glarus thrust plane (Switzerland)". In: *Earth and Planetary Science Letters*.

Rahn, M K, A J Hurford, and M FREY (1997). "Rotation and exhumation of a thrust plane: Apatite fission-track data from the Glarus thrust, Switzerland". In: *Geology* 25.7, pp. 599–602.

Rahn, M et al. (1995). "Alpine Metamorphism in the North Helvetic Flysch of the Glarus-Alps, Switzerland". In: *Eclogae Geologicae Helvetiae* 88.1, pp. 157–178.

Ryb, U et al. (2017). "The clumped-isotope geochemistry of exhumed marbles from Naxos, Greece ". In: *Earth and Planetary Science Letters* 470, pp. 1–12.

Schmid, S (1975). "The Glarus overthrust: field evidence and mechanical model". In: *Eclogae Geologicae Helvetiae* 68.2, pp. 247–280.

Shenton, Brock J et al. (2015). "Clumped isotope thermometry in deeply buried sedimentary carbonates: The effects of bond reordering and recrystallization". In: *Geological Society of America Bulletin*.

Stolper, D A and J M Eiler (2015). “The kinetics of solid-state isotope-exchange reactions for clumped isotopes: A study of inorganic calcites and apatites from natural and experimental samples”. In: *American Journal of Science* 315.5, pp. 363–411.

Swanson, Erika M et al. (2012). “Temperatures and fluids on faults based on carbonate clumped–isotope thermometry”. In: *American Journal of Science* 312.1, pp. 1–21.

Wang, H J, M FREY, and W B STERN (1996). “Diagenesis and metamorphism of clay minerals in the helvetic Alps of eastern Switzerland”. In: *Clays and Clay Minerals* 44.1, pp. 96–112.

York, Derek (1968). “Least squares fitting of a straight line with correlated errors”. In: *Earth and Planetary Science Letters* 5.0, pp. 320–324.

Chapter 5

EXTRACTION AND DETEMINATION OF COMBINED $^{13}C-^{2}H$ AND $^{2}H_2$ CLUMPING OF METHOXYL GROUPS FROM ORGANIC MONOMERS, PLANT TISSUES, AND COAL

5.1 Introduction

Measurements of the abundances of multiply-substituted ('clumped') isotopologues of simple organic and inorganic molecules can provide unprecedented constraints on the temperatures and conditions (e.g., source composition, H_2 availability, biosynthetic pathway) of their formation (J. M. Eiler, 2007; J. M. Eiler, 2013; Stolper, Lawson, et al., 2014; Stolper, Martini, et al., 2015; Yeung, Ash, and Young, 2015; Magyar, 2017). To date, however, application of these techniques has been limited to compounds that are room-temperature gases (e.g., CH_4, CO_2, O_2, N_2O, C_2H_6) or carbonate and phosphate minerals, which can be degraded to CO_2 by established techniques. (J. M. Eiler and E. Schauble, 2004; Ghosh et al., 2006; Yeung, Young, and E. A. Schauble, 2012; Clog and J.M. Eiler, 2014; Stolper, A L Sessions, et al., 2014; Magyar, Orphan, and J. M. Eiler, 2016). Raising the operating temperature of analytical equipment to volatilize larger molecules is insufficient to overcome this obstacle, however, because formally resolving substituted isotopologues with shared cardinal masses at molecular weights much above ~50 Da requires mass resolving power that exceeds the upper limits of what multicollector sector isotope ratio mass spectrometers (IRMS) can currently (and likely ever) achieve. To surpass this limit, there is an ongoing effort to developing techniques to accurately, precisely determine the intramolecular isotopic anatomy of larger organic molecules by Orbitrap mass-spectrometry (John Eiler et al., 2017). Such Fourier Transform-type mass spectrometers can routinely observe hundreds of isotopologues at mass resolutions in excess of 1,000,000 ($M/\Delta M$), but still require analytes that are soluble in common organic solvents, and elute through a gas chromatograph at temperatures below ~250 °C. And the mass spectrum of such larger molecules contain a litany of fragments that must be exhaustively identified for each new compound in order to design measurements that target sites of interest.

The vast majority of sedimentary organic matter, however, is polymeric, solid, and resists dissolution in most organic solvents (i.e., kerogen). To some extent, it is this

same recalcitrance to biodegradation and breakdown, which causes organic carbon to be preserved in the rock record, that makes it challenging to characterize by conventional geochemical and mass-spectrometric techniques. Analogous to the carbonate–CO_2 extraction, an alternative approach is to chemically extract volatile, manageable moieties from larger, analytically-intractable structures. If such chemical extractions are site-specific, quantitative, and do not induce isotopic exchange during sample workup, then combined with high-resolution mass spectrometry of the derivatives, then this approach can provide intramolecular and clumped isotopic information from subsets of complex, (otherwise) inscrutable organic structures. Indeed, since long before development of high-resolution mass spectrometers or nuclear magnetic resonance capable of extracting site-specific isotopic information from intact molecules, chemical degradations have been the principal method by which intramolecular isotope distributions have been determined (e.g., Abelson and Hoering (1961), DeNiro and Epstein (1977), Monson and Hayes (1982), and Rossmann, Butzenlechner, and H. L. Schmidt (1991)).

Here, I describe the chemical and mass spectrometric methods for extracting, purifying, derivatizing, and analyzing the clumped isotope compositions of methoxyl groups ($R-O-CH_3$) from simple organic molecules and more complex organic compounds. My approach integrates a modified version of the Zeisel (1885) reaction for converting ether-bound methyl groups to iodomethane (CH_3I) in hydriodic (HI) acid, new cryogenic techniques for quantitatively extracting and purifying product CH_3I, a new bond-specific soft fluorination for conversion of iodomethane to fluoromethane (CH_3F) on Cobalt trifluoride (CoF_3), and a pioneering dual high-resolution IRMS technique for determining the $\delta^{13}C$, $\delta^{2}H$, and Δ_{36} values of fluoromethane. Together, these techniques enable the accurate determination of the singly-substituted and clumped isotope composition of methoxyl groups with sub-permil precision, over a thousand-fold range in abundances, in a variety of natural and synthetic materials. Although time-consuming and resource-intensive, this flexible method dramatically expands the range of compounds available for study by clumped isotope geochemistry. I additionally present two initial applications of this method: 1) forensic discrimination among sources of vanillin, a globally-traded and often-counterfeited flavoring agent; and 2) characterization of the variability of methoxyl clumped isotope compositions of the biopolymer lignin in natural woods. Finally, in light of these data and what is known of the pathways of methyl group biosynthesis, I discuss whether these moieties are likely to be assembled reversibly and, if so, bear clumped isotope compositions in thermodynamic equilibrium with

their formation temperature.

5.2 Background

Why methoxyl groups?

In order to be a useful recorder of primary biosynthetic conditions, a moiety must have widespread occurrence, persist in the sedimentary record, and resist isotopic modification during senescence and diagenesis. To the extent that these properties have been interrogated, methoxyl groups appear to be all three. Lignin, the structural 'skeleton' of wood, bark, and leaves, is a polymerized network of the phenolic monomers ρ-hydroxyphenyl, guaiacyl, and syringyl, which contain zero, one, and two methoxyl groups for each benzene ring (Campbell and Sederoff, 1996; Boerjan, Ralph, and Baucher, 2003; Vanholme et al., 2010), respectively. The relative abundances of each monomer vary substantially within plant species, or even among different tissues within an individual plant (Campbell and Sederoff, 1996). But generally, gymnosperm lignin is primarily composed of interconnected guaiacyl units, whereas angiosperms contain subequal amounts of guaiacyl and syringyl monomers (Campbell and Sederoff, 1996; Boerjan, Ralph, and Baucher, 2003). Since lignin is a relatively large component of wood (~15–36%, dry weight; Campbell and Sederoff (1996)), methoxyl groups are a substantial component of woody tissue in all living plants.

Relative to other major plant compounds (e.g, cellulose, hemicellulose), lignin is highly resistant to degradation. In aerobic environments it can be broken down by the enzyme lignin peroxidase, secreted by white-rot fungi among others (Tien and Kirk, 1988). In anaerobic environments this enzyme cannot activate, so lignin resists degradation and can be preserved with minimal alteration (Schink and Zeikus, 1982; Benner et al., 1987). For example, the peatification process is notable for its highly-selective removal of some plant compounds (e.g., cellulose) while leaving the lignin structure (largely including its methoxyl groups but see Chapter 6) essentially intact (Hatcher and Clifford, 1997). As a result, lignin contents are enriched to ~ 80% (dry weight) of anoxic plant litter after as little as a decade (Benner et al., 1987), constituting a sizeable flux of methoxyl groups to the subsurface. Although ^{13}C – NMR studies detect the progressive loss of methoxyl groups during coalification with increased thermal maturity (Hatcher and Clifford, 1997), lignin methoxyl groups should persist in the sedimentary record as long as diagenetic conditions remain moderate.

In addition to apparently resisting methoxyl loss during diagenesis, methoxyl C – H bonds should resist exchange as well. Although the rates of methoxyl hydrogen isotope exchange have not been directly measured, they are among the slowest H exchange rates in sedimentary organic compounds (Alex L Sessions et al., 2004; Alex L Sessions, 2016). Because the thermal maturities at which methyl hydrogens (in general) empirically exchange in geologic settings ($R_0 \geq 0.4$; Alex L Sessions (2016)) are similar to those at which methoxyl groups (specifically) are lost (Hatcher and Clifford, 1997), it stands to reason that if lignin methoxyl groups are found in sedimentary rocks in abundances similar to those expected for primary woody tissue, then their internal isotopic structure is likely unmodified.

Progress from and pitfalls of previous extraction techniques

For these reasons, there has been burgeoning interest in developing the δ^2H of lignin methoxyl groups as a robust, widespread paleoclimate proxy (Keppler et al., 2007; Gori et al., 2012; Mischel et al., 2016; Anhäuser, Greule, Polag, et al., 2017; Riechelmann et al., 2016; Feakins, Ellsworth, and Silveira Lobo Sternberg, 2013). Researchers have accordingly developed rapid, 'one-pot' methods to extract and measure the isotope composition of methoxyl groups from lignin (Keppler et al., 2007; Greule, Mosandl, et al., 2008; Greule and Keppler, 2011; Feakins, Rincon, and Pinedo, 2012). Differences between these methods are subtle; generally, 1–2 mL of 57% HI acid are directly added to the 0.4–15 mg of wood in 2–5 mL vials and sealed with caps containing gas-tight polytetrafluroethylene (PTFA) septa. Vials are incubated at 105 – −110°C for 30 minutes, during which methoxyl groups are converted to iodomethane by the reaction:

$$\mathrm{R{-}O{-}CH_3 + HI \rightarrow R{-}OH + CH_3I.} \tag{5.1}$$

This is an S_{N2} reaction in which the oxygen atom is protonated, freeing the methyl group to bond with the iodine anion, thus cleaving the ether bond (Goto et al., 2006). After 30 minutes, vials are removed to room-temperature for at least 30 minutes to allow product CH_3I to equilibrate in the headspace. Some, but not all, workers neutralize the hydriodic acid by injecting a KOH solution through the septa (Feakins, Ellsworth, and Silveira Lobo Sternberg, 2013). CH_3I is then directly introduced to an analytical instrument by injecting an aliquot of the vial headspace. Depending on the application, this instrument could be a GC-combustion-IRMS setup for converting CH_3I to CO_2 for δ^{13}C determination (Greule, Mosandl, et al., 2009), or a GC-pyrolysis-IRMS interface for reduction to and measurement of H_2

(Greule, Mosandl, et al., 2008; Keppler et al., 2007; Feakins, Rincon, and Pinedo, 2012). Because iodomethane incompletely reduces to H_2 during pyrolysis, with $\sim 3\%$ forming HI, a cold trap can be added such that only dihydrogen is introduced into the IRMS (Feakins, Rincon, and Pinedo, 2012).

Although these experimental procedures are suitable for efficient, high-throughput analyses of many tens of wood samples, they are unsuitable for high-precision clumped isotope measurement of intact methoxyl groups for a number of reasons:

1. *Sample size*: In order to support dual-inlet IRMS measurements with long integration times (5–10 hours), tens of micromoles of analyte are needed. This is 1–2 orders of magnitude more iodomethane than is produced using the above methods. For complex materials with low methoxyl contents, the mass of sample required (hundreds of milligrams to grams), and volume of hydriodic acid needed to fully immerse this mass, greatly exceed the capacity of 2–5 mL vials.

2. *Potential for contamination*: The above procedure has atmosphere in the headspace. The major atmospheric gases are all more volatile than iodomethane, and thus elute before the analyte on the GC-IRMS and would not interfere with the iodomethane peak. Lacking a chromatrographic separation procedure, dual-inlet IRMS requires extremely pure gas samples ($> 99\%$) in order to ensure that sample and reference gases fragment and fractionate in the same way in the ion source. Therefore, the above procedure is inadequate for dual-inlet methods.

3. *Incomplete recovery of iodomethane*: The headspace-GC vial sampling procedure analyzes a relatively small proportion of the total iodomethane generated. Iodomethane is moderately soluble in water (14 g/L at 20 °C; Horvath (1972)), so if there is an equilibrium isotope effect between vapor-phase iodomethane in the vial headspace and that dissolved in the aqueous acid solution, then retrieving solely part of the headspace will isotopically fractionate the sample.

4. *Inaccurate yield calculation*: Quantitative concentrations of compounds analyzed by GC-IRMS are commonly obtained using calibration lines that correlate injections of known amounts of standards to peak area. In principle, it should be possible use such an approach to calculate iodomethane yields, if the same proportion of iodomethane partitions into the gas phase and the

same volume of gas is sampled each time. However, the vapor pressure of iodomethane will depend on the volume of the headspace, which in turn will depend on the exact volumes of acid and organic material added. Both of these will vary substantially depending on the methoxyl content of the target material. Previous workers have attempted quantitation by adding known amounts of ethyl cellulose to each sample, which produces iodoethane (C_2H_5I) during the HI reaction, and comparing the abundances of the of the molecular ions of iodomethane and iodoethane (142 and 156 m/z, respectively) when the vial headspace is sampled and analyzed by GC-MS (Anhäuser, Greule, Zech, et al., 2015). This method, too, is problematic because these two compounds have different solubilities in aqueous solutions (off by a factor of 3; (Horvath, 1972)) and (presumably) different, nonlinear, relationships between analyte size and ionization yield. Thus, again, variations in relative compound abundance, and net headspace pressure, should affect the predicted concentrations calculated by this method.

5. *No independent check of quantitation*: The assertion that the HI-induced demethoxylation is quantitative arises from the observation that CH_3I peak areas from a vanillin, a lignin, and a wood standard were largely invariant after carrying out the reaction for 30 minutes at 110 °C (Greule, Mosandl, et al., 2008). Such a test is insufficient to prove quantitation however. The CH_3I-producing reaction (Eqn. 5.1) could be competing with a secondary reaction, perhaps involving the R–O ether bond in $R-O-CH_3$ groups. And, there is no guarantee that the reaction will be similarly efficient in more complex materials like kerogen and coal. Indeed, Goto et al. (2006) observed a sevenfold variation in the relative rate of reaction 5.1 depending on the molecular structure of the methoxyl-bearing compound. One recourse is to demonstrate that no additional CH_3I is generated by continued reaction after the initial 30 minutes. This requires that initial CH_3I is removed from the reaction chamber, which the 'one-pot' vial method does not do.

6. *Analytical shortcomings of iodomethane*: Measurement of $^{13}C-^{2}H$ clumping requires an analyte in which the original methyl groups remain intact. Although iodomethane would be the simplest choice, it is only moderately volatile under laboratory conditions (boiling point = 40 °C at atmospheric pressure). Bellows, capillaries, and inlet systems can be heated to fully volatilize CH_3I, but such resistance-heated apparatuses rarely have uniform

temperatures, creating 'cold spots' where this analyte could condense. And, even at elevated temperatures of the electron-ionization source, the residence time of residual CH_3I is on the order of minutes, which precludes the rapid switches between sample and reference gases that dual-inlet mass spectrometry typically requires. Finally, resolving the singly-substituted isotopologues $^{13}C^1H_3I$, $^{12}C^1H_2^2HI$, and the H-adduct $^{12}C^1H_4$ at cardinal mass 143 Da requires a formal mass resolution of ~90,000 (and practically, much greater), which greatly exceeds the capabilities of current sector MS instruments. Although this mass resolution problem is tractable at cardinal mass 16 Da if isotopologues of the methyl fragment are analyzed, the instability of these fragments and related isobars complicate this approach (see below).

Advances and limits in high-resolution mass spectrometry

Determining the clumped $^{13}C-^2H$ composition of an organic molecule at a useful precision (≤ 1 ‰) requires, at a minimum, accurately measuring the relative abundances of the ^{13}C- and ^2H-substituted isotopologues and the clumped $^{13}C-^2H$ isotopologue of molecular ions (or fragments) normalized to the unsubstituted species at even greater precisions. Maximum mass resolving powers (MRP) of cutting-edge multicollector, normal-geometry gas-source sector-MS instruments (e.g., Thermo MAT 253 Ultra, Nu Panorama) are ~50,000 (5/95% definition). These is suitable for cleanly separating the 13 C- and ^2H-substituted species at ~32 Da but no higher. The Thermo DFS is a single-collector, reverse-geometry MS that can reliably exceed such mass resolutions, but only when observing a very small mass window (on the order of hundreds of miliDaltons, at most). Thus separately, neither instrumental format is capable of making clumped isotope measurements of molecules much heavier than ethane. It may be possible to exceed this limit if, however, the strengths of these instruments are combined. Specifically, the Thermo MAT253 Ultra is able to precisely determine the ratios:

$$\frac{^{13}C^1H\text{–}R + {}^{12}C^2H\text{–}R}{^{12}C^1H\text{–}R}, \text{ and } \frac{^{13}C^2H\text{–}R}{^{12}C^1H\text{–}R} \tag{5.2}$$

at masses up to ~80 Da. The Thermo DFS should be able to precisely measure the ratio:

$$\frac{^{12}C^2H\text{–}R}{^{13}C^1H\text{–}R} \tag{5.3}$$

up to a similar mass limit. By combining these measurements on a single sample gas, it should be possible to derive $\delta^{13}C$, δ^2H, and $\Delta_{^{13}C-^2H}$ values for moderately heavy organic molecules beyond methane and ethane. Demonstration that these

measurements can be performed accurately relative to a working reference gas of known composition would thus represent a significant advance in the development of analytical strategies for the field of clumped isotope geochemistry.

5.3 Methods for chemical extraction and purification

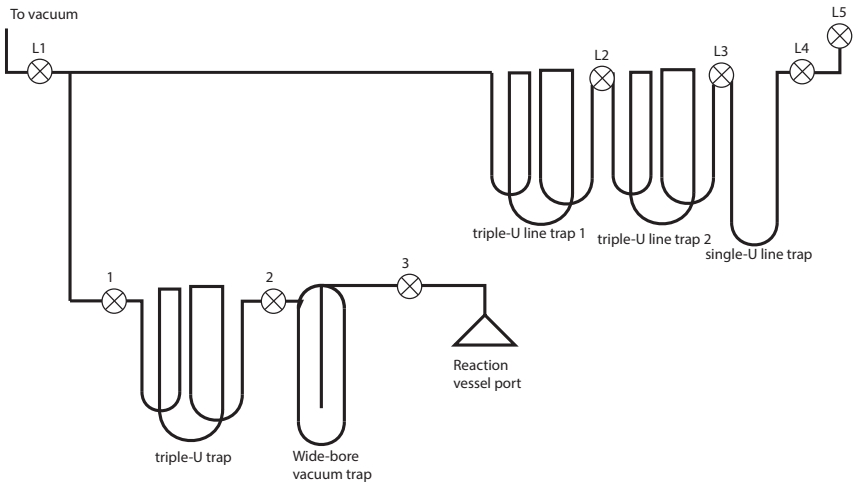

Figure 5.1: Schematic of the vacuum line setup for extracting and purifying iodomethane

To remedy the issues of previous methods discussed in section 5.2, two new procedures were developed to quantitatively react, extract, and isolate iodomethane generated by the reaction of methoxyl-bearing compounds with hydriodic acid. The first procedure uses a gas-tight McCrea (1950)-style two-legged reaction vessels heated in a silicone oil bath. It has a lower procedural blank and is suitable for small amounts of material with high methoxyl contents. The second employs a glass reflux reactor with a water-cooled condenser, heated by a resistance heating mantle. Inspired by the reaction setup of D. A. Krueger and H. W. Krueger (1983), it uses N_2 as a carrier gas to continuously separate and condense evolved iodomethane as it is generated. It has a larger procedural blank, but is methodologically simpler and suitable for larger samples with lower methoxyl contents. Because both procedures were developed expressly for this project, they are described in detail, along with justifications of critical steps.

Reaction vessel procedure

For solid samples, 20–200 mg of material are weighed and added to one leg of a clean, baked, open, two-legged reaction vessel. The vessel is chilled to −77 °C by immersing it in a ethanol–CO_2 ice slush for 5 minutes, after which 4 mL of 57% hydriodic acid are added to the other leg of the vessel to freeze. If analyzing a liquid sample (e.g., methanol, anisole), 2–12 μL are then added directly on top of acid once frozen. While still immersed in the slush, the reaction vessel is assembled with a head-top valve sealed with silicone high-vacuum grease (Dow Corning), and evacuated on a glass, greaseless vacuum line backed by an Hg diffusion pump. The ethanol–CO_2 ice slush is necessary to ensure that the aqueous hydriodic acid and (if applicable) liquid samples does/do not evaporate while evacuating the reaction vessel, and that the reaction does not commence before the vessel is evacuated and sealed. Hydrocarbon-based greases are avoided to preclude their reaction with the acid, which could generate additional CH_3I. Once the reaction vessel is evacuated but still affixed to the line, ∼3 mMol of N_2 are added to it by injection through a butyl-rubber septa using a gas-tight, locking syringe. This N_2 addition is necessary to prevent an excess of hydriodic acid from volatilizing during the reaction at reflux conditions. The vessel is then sealed, warmed to room temperature in a water bath, and (if applicable) the solid sample and acid are thoroughly mixed by swirling and sonicating for 3–5 minutes. Once mixed, sample and acid are reacted for 90 minutes at 130°C by immersing the vessel legs in a silicone oil bath heated by hot plate.

After 90 minutes, the vessel is cooled in a 25 °C water bath to condense the HI acid and allow CH_3I to equilibrate in the headspace. Next, CH_3I is extracted from the hydriodic acid mixture in the reaction vessel using a series of cryogenic separations conducted on a custom assembly of glass vacuum traps and glass valves with Viton® O-rings, connected by 3/8" Cajon® fittings (Fig. 5.1). First, N_2 is stripped off while retaining the CH_3I by exposing the reaction vessel to two traps connected in series: a wide-bore vacuum trap, immersed in an ethanol–CO_2 ice slush (−77 °C), followed by a triple-U trap immersed in liquid N_2 (LN_2, −196 °C) (Fig. 5.1). Iodomethane has a small but significant vapor pressure at −77 °C (∼110 Pa), but fully freezes at −196 °C. Hydriodic acid will evaporate at room temperature and low pressure, but freeze at −77 °C. So, after allowing these three volumes to equilibrate for 5 minutes, the LN_2 level is raised and valve 1 (see Fig. 5.1) is opened to pump across the LN_2 trap, removing N_2 while retaining CH_3I. Pumping continues until pressures returned to baseline and all N_2 was removed (approx. 5 mins). Without the N_2 pressure, both CH_3I and HI evaporate at 25 °C, and while CH_3I can pass through the

ethanol–CO_2-cooled trap at low vapor pressures, HI is retained. So, the apparatus is held at this condition for 60 minutes to separate these two compounds on the LN_2 and ethanol–CO_2 traps, respectively. Exhaustive testing revealed that no CH_3I remained in the reaction vessel or wide-bore vacuum trap after this time. Note, however, that because of the low volatility of CH_3I, this elution time depends on both the size of the sample and the particular geometry of the setup, and will not necessarily be sufficient for other applications on different apparatuses. Note as well that, for the duration of this separation, it is essential to both keep the legs of the reaction vessel at room temperature in a water bath (else evaporative cooling will slow the exsolution of CH_3I), and to periodically evacuate any gaseous incondensibles that also exsolve through valve 1 (else headspace pressure will slow the transfer of CH_3I over the ethanol–CO_2 trap). With the majority of HI removed, the triple-U trap is thawed and CH_3I is transferred to the single-U trap on the glass vacuum line, by immersing this in LN_2, for further cleaning and purification (see below, section 5.3). Again, because of the low volatility of this analyte, this transfer step is conducted for a full 10 minutes while heating glass surfaces with a resistance heat gun throughout.

Once CH_3I is transferred to the vacuum line, the custom extraction apparatus is disassembled and cleaned in the following manner: Residual HI acid and reacted materials are thawed, filtered, neutralized with sodium bicarbonate, and discarded. Glassware that came into contact with acid is thoroughly rinsed, first with de-ionized water (DIW), then acetone. Metal fittings and O-rings are wiped clean with Kimwipes®, first dry, then once soaked in acetone. Despite this initial cleaning protocol, slow buildup of a brown, iodine-bearing coating occurs on all metal surfaces exposed to volatile hydriodic acid. These are periodically removed by sonicating contaminated fittings in acetone for > 4 hrs, followed by further physical cleaning with wipes and brushes, and final rinses in fresh DIW and acetone. Once clean, all parts of the extraction apparatus are dried at 130 °C for > 1 hr, and stored until the next use.

This procedure is simple to execute and maintain leak-free. Still, it has three major drawbacks:

1. The extended transfer step required to separate CH_3I from HI by evaporative distillation at -77 °C is time-consuming and imprecise. Samples with unknown methoxyl contents require secondary transfer steps to ensure that all CH_3I is collected.

2. Evaporation of such a large volume of hydriodic acid across two Cajon Ultra-Torr® fittings dramatically accelerates the corrosion rate and buildup of brown, recalcitrant residue on these metal surfaces. There is reason to worry that even once cleaned, small amounts of CH_3I could be retained in this residue or etched faces.

3. This setup is incapable of handling large amounts of material. Although far more than 300 mg of powder can fit in this reaction vessel, the volume of acid required to fully immerse such an amount causes the reaction vessel to overpressurize when heated to reflux at 130 °C. Once overpressurized, reaction vessels are prone to 'burping' by spontaneously, violently degassing through the silicone grease-lined coupling between the vessel legs and valve components. Although the hazards of such a procedure are mitigated by conducting this reaction behind a blast shield in a fume hood, it is nonetheless unacceptable because this degassing will fractionate CH_3I in the headspace.

Reflux condenser procedure

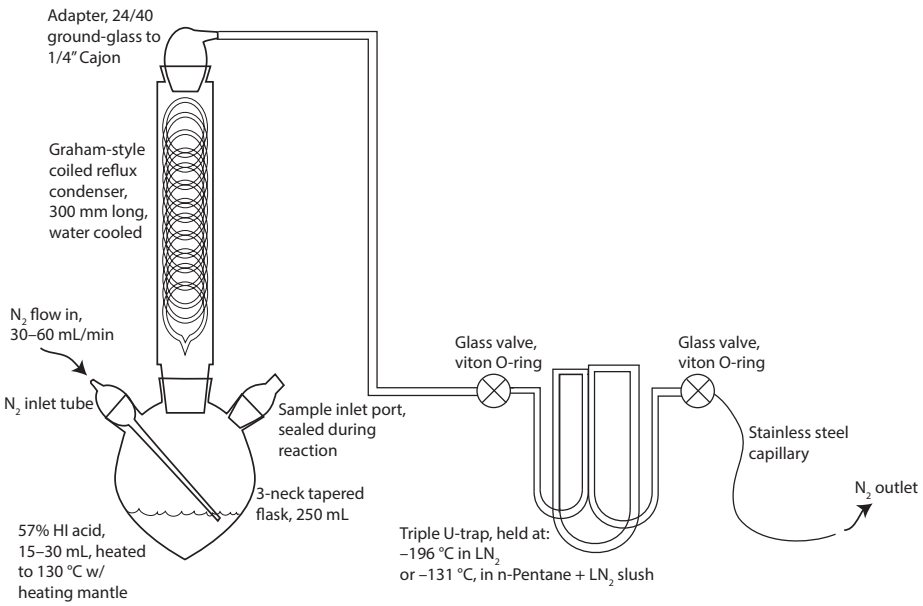

Figure 5.2: Schematic of the experimental setup for evolving and concentrating CH_3I in a reflux reactor in a continuous N_2 stream

To address the drawbacks described above, an additional reaction protocol was developed. Inspired by the experimental design of D. A. Krueger and H. W. Krueger (1983), this setup uses a reflux reactor to react large volumes of acid and material in a

gas-tight 250 mL tapered reaction vessel (Fig. 5.2). Here, a flow of N_2 continuously entrains evolved CH_3I, carries it beyond a water-cooled reflux condenser to condense on a triple-U trap. This continuous separation drastically reduces the amount of residual HI that is exposed to metal surfaces, reaches the CH_3I trap, and must later be removed. And, the capillary bleed at the N_2 outlet beyond the CH_3I trap prevents overpressurization and enables reaction of these larger volumes of methoxyl-depleted material. Although it is more challenging to assemble, clean, and maintain leak-free, it reduces the experiment time and expands the range of materials that can be safely explored. The procedure is described in detail below.

The assembled apparatus is diagrammed in Fig. 5.2. Upstream of the adapter, all couplings are 24/40 ground glass fittings sealed with Dow Corning® silicone grease. Downstream, three Cajon Ultra-Torr® fittings connect the Pyrex® 1/4" and 3/8" components. Before each run, the setup is assembled and monitored for leaks by verifying that the flow rate at the N_2 outlet capillary matches the expected value for the setting on the regulator at the apparatus inlet. Atmospheric contaminants are removed by purging the assembled apparatus at an elevated flow rate (~200 mL/min) for > 5 mins. Then, 15–30 mL of cold (−10 °C) 57% HI acid and 10–10,000 mg of powdered sample are quickly added through the sample inlet port. The minimum acid volume (15 mL) is governed by the level at which the end of the N_2 inlet tube is immersed in the liquid so that N_2 is bubbled through the acid for the course of the reaction. After the addition of the sample and 3 more minutes of purging, the N_2 flow rate is reduced to 30–60 mL/min and the triple-U trap is immersed in either an LN_2 bath (−196 °C) or an LN_2–n-pentane slush (−131 °C) to begin capturing evolved CH_3I. Both cooling baths are capable of quantitatively freezing CH_3I, but the colder bath additionally captures evolved CO_2. The latter is preferable, because maintaining the LN_2–n-pentane slush at temperature requires the frequent addition of small amounts of LN_2. And, carbon dioxide is a major byproduct of the HI reaction with complex natural materials, and there is considerable merit in sampling this gas and determining the moieties in kerogen from which this CO_2 originates. However, capturing the CO_2 here means it must later be separated from the CH_3I on the vacuum line. This procedure is described in the next section. No difference in the yield or composition of captured CH_3I is detected with either cooling bath.

For the reaction, the tapered reaction bulb is heated to 130 °C in a hemispherical heating mantle powered by a Variac® at 80 V. The reaction proceeds for 90 minutes. After 90 minutes, the N_2 flow is interrupted and the triple-U trap valves are quickly

closed off, capturing the frozen CH_3I, CO_2 (if applicable), and both condensed and gaseous N_2 inside. This triple-U trap is then attached to inlet port of the cleaning apparatus shown in Fig. 5.1 and described above. The cleaning procedure is identical to that described for the McCrea (1950)-style vessel method with two key differences:

1. Because a large amount of N_2 is captured in the triple-U trap at the end of the reaction, immediately warming the sealed volume to room temperature could over-pressurize it, or cause the rapid evacuation of N_2 across the ethanol–CO_2 and LN_2 traps to entrain CH_3I and fractionate the sample. So the triple-U trap from the reaction line is left immersed in LN_2 while transferred to the cleanup line (Fig. 5.1) and initially evacuated across the traps. Due to the relatively low vapor pressure of N_2 at -196 °C, this evacuation can take up to ~20 mins to reach baseline. Once all incondensible gases are removed, the trap is sealed, thawed to 25 °C in a water bath, and slowly re-opened to the cleanup line to allow H_2O and HI to freeze in the ethanol–CO_2 trap and CH_3I (and CO_2) to freeze in the LN_2 trap.

2. Because little HI acid reaches the triple-U trap in the reflux reaction setup, a full 60 min transfer cycle is not necessary to ensure that all CH_3I is exsolved. Once the triple-U trap is thawed to RT, 15 minutes of exposure to the ethanol–CO_2 and LN_2 traps is sufficient to quantitatively capture CH_3I in the latter trap.

Secondary purification on glass vacuum line

Once CH_3I is transferred to the glass vacuum line, it is further purified, measured, and aliquoted. First, any residual HI or water that persists in the sample is removed with the following procedure: the gas is thawed onto the single-U line trap (Fig. 5.1) and its pressure measured by manometer. It is then frozen to the bottom the trap by immersion in LN_2. Once completely frozen and the manometer reads no pressure above baseline, the LN_2 trap is replaced with an ethanol–CO_2 ice trap at a higher level, and allowed to equilibrate for 2 mins. Because the vapor pressure of CH_3I at -77 °C is independent of sample size but that of CO_2 is not, any pressure reading above the vapor pressure of CH_3I (110 Pa) indicates the presence of CO_2 (or another volatile gas?) in the gas mixture, which can be separated out below. Once equilibrated, the headspace CH_3I is exposed to the adjacent triple-U line trap, which is immersed in LN_2. Volatile CH_3I is thus continuously evaporated off of the

single-U line trap and frozen onto the triple-U line trap, while leaving water and HI frozen behind. This transfer continues for 15 minutes, during which time the progress can be monitored by the headspace pressure reading on the manometer. At the end of the transfer, residual HI and water are pumped away by thawing the ethanol–CO_2 ice trap and heating it with a resistance heat gun.

The reaction of large (> 100 mg) amounts of thermally mature, methoxyl-depleted, organic-rich material in HI acid at 130 °C generates abundant CO_2, in some cases more than 100 times the amount of CH_3I that is produced. If CO_2 is detected during the condensation step at −77 °C (see above), it is separated without fractionating iodomethane using a second cryogenic step over an LN_2–n-Pentane slush (−131 °C). As above, the sample gas is first condensed at the bottom of the trap in LN_2. Next, the trap is thawed to −131 °C in the n-pentane slush, and volatilized CO_2 (CO_2 vapor pressure at −131 °C ≈ 0.4 kPa) is frozen into the adjacent trap in LN_2, leaving CH_3I behind. This transfer is conducted for 5 minutes. Then, the valve between the traps is closed, the LN_2–n-pentane trap is warmed to 25 °C, and the new CH_3I pressure is recorded. This cleanup cycle is repeated until the CH_3I pressure between cycles drops by no more than 1%, indicating that the vast majority of CO_2 has been removed.

Site-specific fluorination of iodomethane

To overcome the analytical shortcomings of iodomethane, once cleaned, this gas is converted to fluoromethane (CH_3F) by reaction with cobalt(III) trifluoride (CoF_3) by the reaction:

$$CH_3I + \frac{1}{3}CoF_3 \rightarrow CH_3F + \frac{1}{3}CoI_3. \tag{5.4}$$

Fluoromethane is a stable, non-toxic gas with a vapor pressure similar to CO_2. And, fluorine has only one stable isotope (^{19}F), so the substitution of the iodine atom for fluorine will not create any additional isobaric interferences 1 and 2 Da above the unsubsituted molecular ion. For this fluorination reaction to be suitable for high-precision clumped isotope work, it must be quantitative, not introduce other contaminants, and not induce C–H bond exchange in the transition state. Finding a suitable reagent is non-trivial; initial attempts to selectively fluorinate iodomethane on a variety of other fluorinating agents failed to meet one or another of these criteria. Iodomethane quantitatively reacted with silver(I) fluoride (AgF), a classic soft fluorinating agent (Filippo Jr and Romano, 1975; Mann, 1987), at 25 °C within 12 hours. However, this reaction produced subequal amounts of fluoromethane and

ethanol, presumably due to the reaction with residual water adsorbed to the surface of the fluorinated salt. Indeed, when exposed to vacuum in preparation for sealing it in Pyrex® break-seals with iodomethane, AgF continued to degas, even after up to 30 minutes of heating at ~100 °C. Attempts were made to quantitatively remove this adsorbed water by pre-fluorinating AgF with bromine pentafluoride (BrF_5) for 30 minutes at 25 °C, because this strong fluorinating agent should readily oxidize any H_2O to HF and O_2 at these conditions. Although the conversion rate from CH_3I to CH_3F was higher using this pre-treated AgF (~90%), substantial ethanol was still generated, suggesting that some of this H_2O is a structural impurity inaccessible by the BrF_5 treatment. Two other fluorinating agents, potassium fluoride (KF) and xenon difluoride (XeF_2) were found to be free of water and could be fully degassed on a vacuum line in a matter of minutes. However, reaction with each of these salts was slow and non-quantitative. At best, 10% conversion of CH_3I to CH_3F was observed at 40 °C after 1 week in the case of XeF_2. This was likely due to the creation of metastable intermediates (e.g., CH_3IF_2), which did not immediately degrade to CH_3F (Forster and Downs, 1985).

Cobalt(III) trifluoride, unlike the above salts, quantitatively, cleanly fluorinates iodomethane at 25 °C in 24 hours. CoF_3 is a (relatively) safe, stable, selective soft fluorinating agent, most commonly used in the geosciences for the conversion of liquid water to O_2 for the analysis of $\delta^{18}O$ and $\Delta^{17}O$ by IRMS (Baker et al., 2002; Barkan and Luz, 2005; Barkan and Luz, 2012; Passey et al., 2014). For each sample, 50–100 mg of CoF_3 (i.e., a ~10–20-fold excess of CoF_3) is loaded into a Pyrex® break-seal and evacuated. To encourage the release of adsorbed water and other contaminants, the tube is heated by heat gun until baseline pressures are reached (5–10 mins). Then, sample CH_3I is frozen into the tube in LN_2 and flame-sealed.

The conversion proceeds at room temperature for 1–4 days. At the end of the reaction, CH_3F is isolated from the residual salt and other condensible contaminants with a cleaning procedure analogous to the separation of CH_3I from HI and H_2O described above. Briefly, the break-seal is cracked onto a custom two-trap apparatus, the first trap held at −77 °C, and the second at −196 °C. For 20 mins, CH_3F desorbs from the salt, passes through the ethanol–CO_2 ice trap, and freezes in LN_2. Continuous heating of the reaction tube accelerates this desorption. Meanwhile, H_2O, HF, and any volatile CoF_3 are trapped at −77 °C. Following this initial cleanup, CH_3F is further purified by cryogenic distillation on a liquid-He cryostat: first, CH_3F is fully condensed onto the the cryostat at 80 K, and any residual incondensibles are

pumped away. Then, the temperature of the cryostat is cycled thrice between 140 K and 80 K, pumping away the residue at 80K each time. Finally, the temperature is raised to 110 K, where CH_3F is moderately but significantly volatile, and this gas, alone, is frozen off the cryostat and into two aliquots of identical break seals for dual, dual-inlet IRMS analysis.

5.4 Methods for dual-mass spectrometric measurement

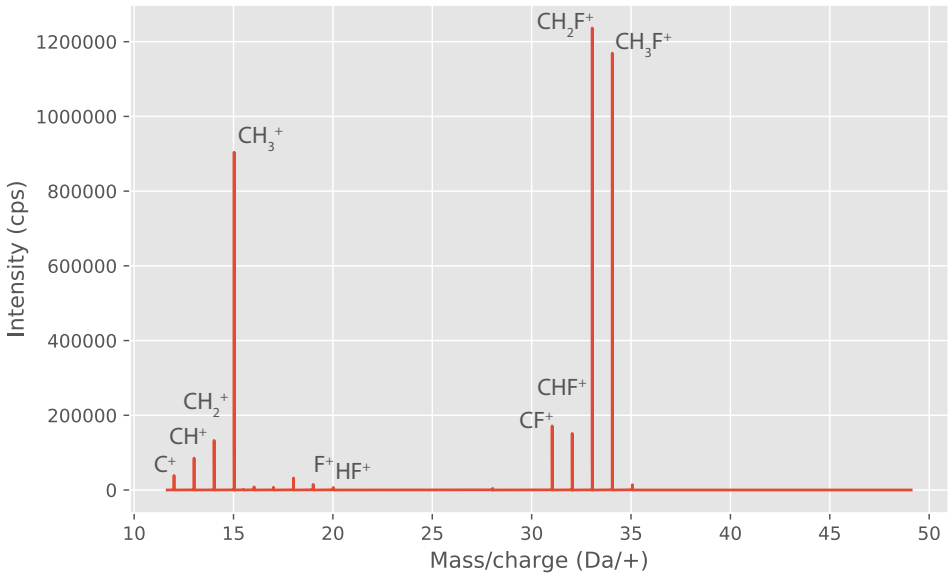

Figure 5.3: Mass spectrum of fluoromethane, acquired on a Thermo DFS IRMS, with electron energy at 55 eV, filament current at 1.5 mA, on a 1e5 SEM amplifier. Peaks are labeled by the most abundant unsubstituted species at each cardinal mass.

The mass spectrum of fluoromethane contains two main families of peaks where determination of the isotopic composition of its methyl group is possible (Fig. 5.3). The most abundant peaks are the full molecular ion (CH_3F^+) and its -1 H fragment (CH_2F^+). Under most conditions the methyl fragment ($CH_3{}^+$) is ~25 % of the full molecular ion, but at low electron ionization energies a larger relative proportion of the sample gas fragments to methyl ions (Fig. 5.3). Because the mass resolution requirements for separating isotopologues of similar masses are lower at 15, 16, and 17 Da, exhaustive attempts were made to develop precise, reproducible methods to characterize the clumped isotope composition of methyl fragments. Such procedure would be especially desirable because it would enable precise, potentially accurate, determination of the $\delta^{13}C$, δ^2H, and clumped $^{13}C-{}^2H$ compositions of methyl groups in any moderately volatile molecule that produces

this fragment. This measurement is only feasible, however, if it can be made stably, reproducibly, and while resolving or correcting for all other isobaric interferences that could contaminate these measurements.

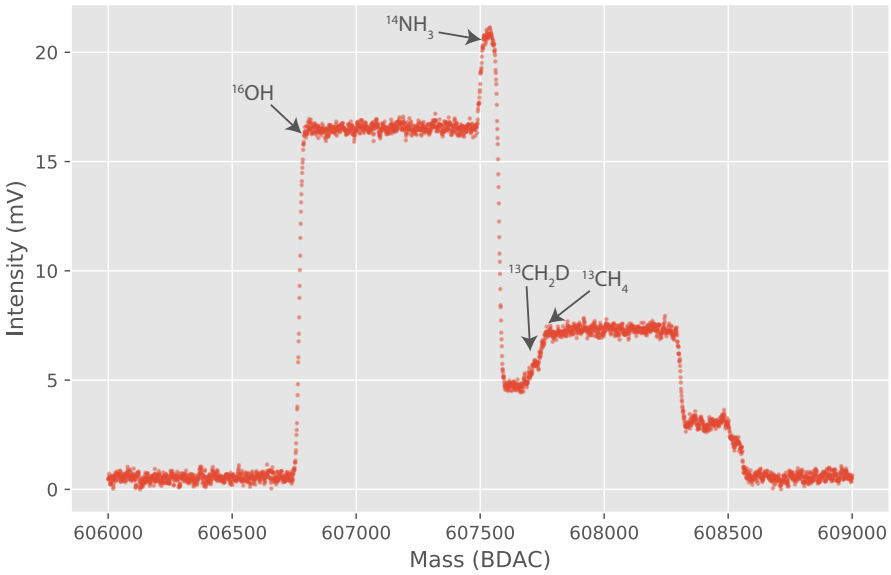

Figure 5.4: Mass spectrum of methyl fragment isotopologues and other isobaric interferences at mass 17 Da. Mass scan acquired on the prototype Thermo MAT 253 Ultra, 2.0 mA filament current, 100 eV electron energy, medium resolution entrance slit, on a Faraday cup with a 10^{12} Ω amplifier. Low-mass edge of major isotopologues are labeled. $^{12}CH_2D_2$ is not resolvable at this scale.

Prohibitive impedances to the accurate mass spectrometric measurement of methyl fragment ions

The mass spectrum at cardinal mass 17 Da illustrates the unique challenge of such measurements (Fig. 5.5). Due to its high abundance sensitivity and ability to stably measure isotope ratios in multicollector mode for long integration times, high-precision determination of the relative abundance of $^{13}CH_2D$ is best obtained on the prototype Thermo MAT 253 Ultra. However, the wide exit slits on this instrument that enable integration on flat-topped peaks also prevent measurement of the doubly-substituted methyl fragment alone: on the low-mass side $^{13}CH_2D$ overlaps with $^{14}NH_3$, while on the high-mass side it overlaps with the H-adduct $^{13}CH_4$. Previous workers have shown that although the abundance of ammonia ions in the MAT253 Ultra is sample-specific and evolves with time, it is sufficiently stable on ~hour-long timescales that it can be accurately corrected for by bracketing each

analysis of the sum of the target species and the ammonia ion with measurements of the ammonia ion alone (Clog et al., in prep). However, because the ammonia ion here is ~3 times the abundance of the target species, optimal counting statistics require spending $\sqrt{3}$ times as long integrating on this contaminant species as opposed to the target ion. And since such a measurement must be done at high resolution in order to resolve $^{13}CH_2D$ + $^{14}NH_3$ from the shoulder of $^{13}CH_4$, given the low count rates this measurement condition produces, achievement of 0.5 ‰ precision on the ratio of $^{13}CH_2D$ to $^{12}CH_3$ requires ~16 hours of total integration time on sample and reference gases. Including the time required for periodically scanning to find the shoulder of a moving peak, and the deadtime during sample-standard switches in each cycle, such a measurement requires upwards of 24 hours and is unfeasible given the manual work required.

On the high-mass side, the sum of $^{13}CH_4$ and $^{13}CH_2D$ can be measured, or $^{13}CH_4$ can be measured alone. Because these two peaks are subequal in intensity, subtraction of $^{13}CH_4$ from the sum in bracketed acquisitions is more favorable than the NH_4 subtraction from a counting statistics perspective, but only if the ratio of $^{13}CH_4$ to $^{12}CH_3$ is stable over the course of a single bracketed acquisition block. However, because the abundances of H-adducts typically have second-order dependencies on those of their source ions, H-adducts will decay in a non-linear manner due to the intensity drop over the course of a single acquisition (c.f., Stolper, A L Sessions, et al. (2014)). Because the adduct intensity is larger than the target ion, these non-linearities are significant and must be calibrated prior to measurement. Thus, these calibrations must be valid and stable over the course of a measurement block. If this latter condition is met, however, it is more efficient to measure solely the sum of $^{13}CH_4$ and $^{13}CH_2D$ at a lower resolution and higher count rate, and exploit the non-linearity in the dependence of $^{13}CH_4$ on $^{13}CH_3$ to implicitly subtract out its contribution to each measurement. This strategy is analogous to that used for the subtraction of $^{13}CH_5$ from $^{13}CH_3D$ in methane (Stolper, A L Sessions, et al., 2014), but more advantageous here because this $^{13}CH_4$ adduct is so large.

It is apparent, however, that at least for the gases analyzed to-date (CH_3F and CH_3Cl), adduction rates on methyl fragments, and even methyl fragmentation rates in general, are insufficiently stable over the course of a single measurement session to allow for accurate calibration and subtraction. Methyl fragmentation exhibits significant hysteresis; over the course of an hour, the size of the methyl fragment at the same delivery pressure can drop by at least 15%. Although such instabilities can

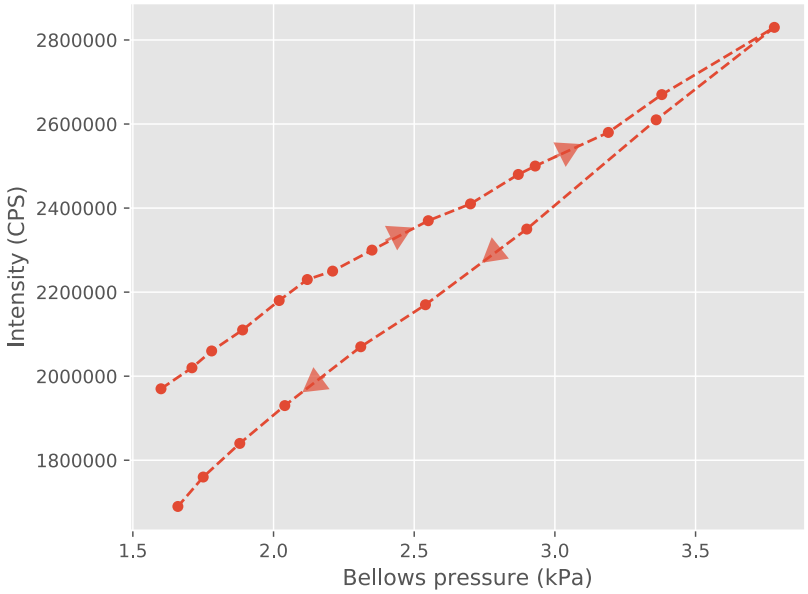

Figure 5.5: Hysteresis in intensity of unsubstituted methyl fragment $^{12}CH_3^+$ vs. bellows pressure for CH_3F working gas, over the course of ~1 hour. Mean intensities integrated for 3 minutes, and allowed to equilibrate for 1 minute after each change in bellows compression. Data acquired on the Thermo DFS, 1.49 mA filament current, -80 eV electron energy, an SEM with 10^5 amplification. Arrows denote direction in which data points were collected.

be normalized if they occur in both sample and reference gases, they are nonetheless concerning. More problematic is the unstable, antithetical behavior of the $^{12}CH_4$ and $^{13}CH_4$ adducts. If H-adduction of methyl fragments occurs analogously to H-adduction of methane, it should be described by the reaction:

$$CH_3^+ + CH_3 \rightarrow CH_4^+ + CH_2. \tag{5.5}$$

Given an adduction rate k, the concentration of the CH_4^+ adduct should thus have a second-order dependence on the concentration of the methyl fragment. Or,

$$[CH_4] = k[CH_3]^2. \tag{5.6}$$

Therefore, when $^{13}CH_3$ and $^{12}CH_4$ are measured together at mass 16 ($i^{16} = {}^{13}CH_3 + {}^{12}CH_4$, and $^{12}CH_3$ is the only major ion at mass 16, the ratio of counts on mass 16 to mass 15 should depend on the intensity on mass 16 by the equation:

$$\frac{i^{16}}{i^{15}} = k \times i^{15} + \frac{^{13}CH_3}{^{12}CH_3}. \tag{5.7}$$

Thus, an array of raw measurements of $\frac{i^{16}}{i^{15}}$ at a range of source pressures should define a line with a positive slope equal to k and a y-intercept that is the true ratio

of $\frac{^{13}CH_3}{^{12}CH_3}$. If k is stable over the course of a measurement session, then it can be determined once by this approach, and used to correct all subsequent analyses. This is the principle upon which the prototype Ultra-based measurement of $\delta^{13}C$, $\delta^{2}H$, and Δ_{18} in methane relies.

Extensive testing has revealed, however, that methyl fragments do not adhere to this rule. When chloromethane (CH_3Cl) is the analyte gas, adduct slopes are positive, but highly unstable: over the course of two hours, the adduction rate can readily drift enough to change the measured 16/15 ratio at a single mass15 intensity by 2% (Fig. 5.6). With fluormethane as the analyte, k values are observed to be negative (Fig. 5.7). This negative slope suggests that for fluoromethane, formation of the H-adduct CH_4^+ is not governed by Reaction 5.5. Instead the primary donor of H must be another molecule, such as a persistent background contaminant like water. If the primary source of H atoms is H_2O, then the adduction reaction is more accurately:

$$CH_3^+ + H \rightarrow CH_4^+, \tag{5.8}$$

and the adduct concentration will be described by the equation:

$$[CH_4] = k[CH_3] \times [H_2O]. \tag{5.9}$$

Because H_2O is a persistent source contaminant, increasing the delivery rate of CH_3F by increasing source pressure will dilute the activity of $[H_2O]$. If the delivery of reactive protons from water is the rate-limiting step, then by increasing source pressure, the adduction rate will decrease. This behavior may be exclusive to fluorinated compounds because of the exceptional electronegativity of fluorine. This ectronegativity might mean that the ion-producing fragmentation reaction in fluoromethane,

$$CH_3F \rightarrow CH_3^+ + F^-, \tag{5.10}$$

is unusually common. This could produce an excess of methyl fragment ions that can readily incorporate an additional H at rates above what could occur if they originated from fluoromethane alone.

In any case, these observations render conventional adduct corrections on methyl fragments of fluoromethane prohibitively complicated. The abundances of contaminant species will inevitably vary per sample and perhaps also with time over the course of a single measurement. Real-time monitoring of their abundances is challenging, and even so, there is no guarantee that an acceptably accurate adduction model could even be produced. Instead, since methyl fragments cannot be measured

in isolation from either its adduct or a low-mass contaminant, a different analytical strategy is required.

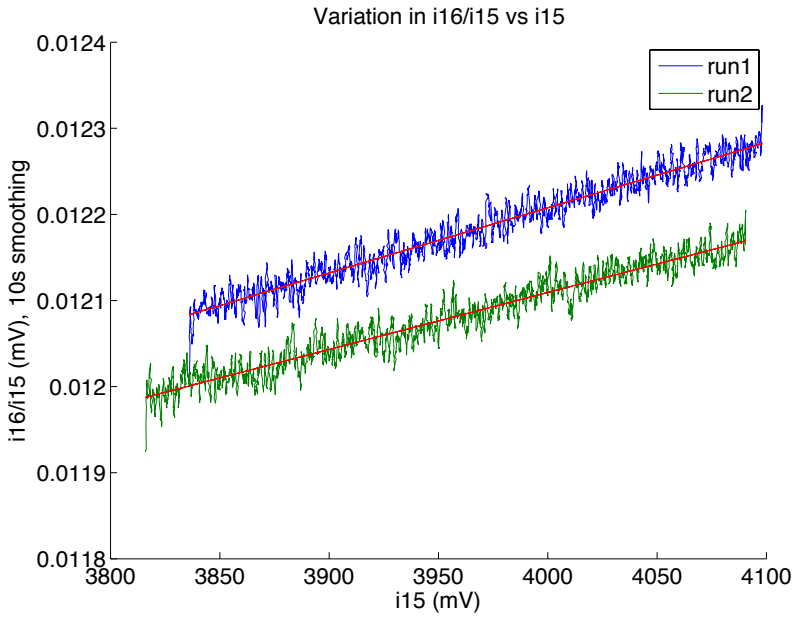

Figure 5.6: Drift in adduction rate of methyl groups when CH_3Cl is the analyte. Runs were each acquired by constantly measuring reference gas over the course of an hour. During the 2 hr break in between, all that was changed about the instrument state was the compression percentage of the bellows.

High-resolution multicollector MS measurement of fluoromethane

Instead, we opted to make our measurements on isotopologues of the full molecular ions of fluoromethane at masses 34, 35, and 36. The mass spectra for these peaks on the prototype 253 Ultra are shown in Figs. 5.8 5.9, and 5.10. Here, adduction rates are well-behaved and stable over the course of a day. This should permit precise correction for adduct input by measuring adduct lines daily, and using these relationships to correct all measurements (Figs. 5.11, 5.12. Accurate determination of adduct slopes is essential because fluromethane adduction rates are at least 10 times those of methane. That is, on the 253 Ultra, the intensity of $^{12}CH_4F$ is approximately equal to than the intensity of $^{12}CH_2DF$. And this is after extensive tuning of source conditions to optimize for low adduction rates; in a tune state that maximizes sensitivity of the full molecular ion, adduct abundance is five times that of $^{12}CH_2DF$. This relatively large adduct likely prohibits sufficiently-precise adduct-corrected measurements of $^{12}CH_2DF/^{12}CH_3F$ alone. However, the point is moot; the prototype 253 Ultra lacks the mass resolution to fully resolve $^{12}CH_2DF$ from

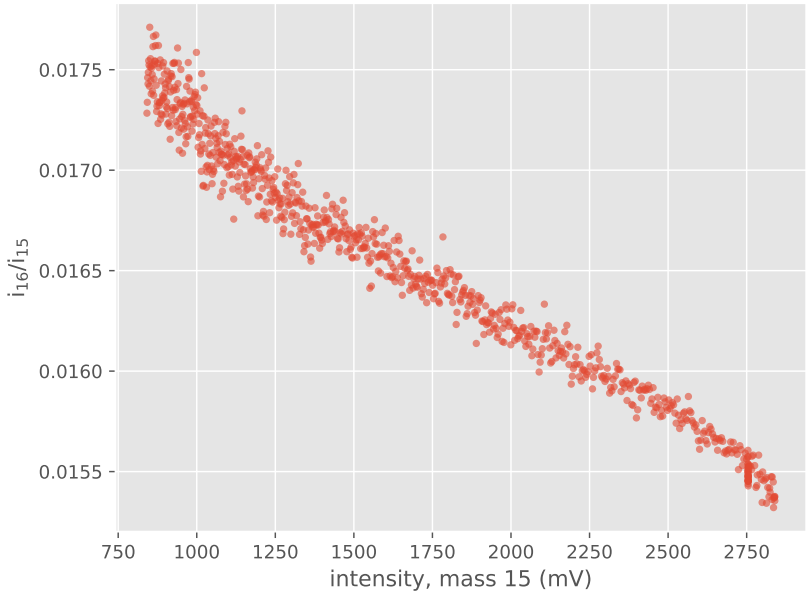

Figure 5.7: Inverse dependence of methyl fragment adduction rate on methyl fragment intensity when CH_3F is the analyte gas.

$^{13}CH_3F$ at mass 35 (Fig. 5.9). Interestingly, although mass resolutions in excess of 30,000 are regularly achievable for symmetric n-alkanes on this instrument, it was never possible to tune the machine to a resolution greater than 28,000 with fluoromethane as the analyte.

Nonetheless, precise determination of the ratio of the sum of [$^{13}CH_3F$] and [$^{12}CH_2DF$] to [$^{12}CH_3F$] is achievable, reproducible, and conforms to shot noise limits, provided the adduct line is accurately determined and background scattered ion load is corrected for. With this ratio, it is possible to correct the $^{13}CH_4F$ adduct contribution to mass 36 intensity, and the ratio of the sum of [$^{13}CH_2DF$] and [$^{12}CHD_2F$] to [$^{12}CH_3F$] can be measured with acceptable precision, provided the same conditions (accurate adduct and background dependencies) are met. The importance of signal-dependent background corrections should not be underappreciated. When analyzing fluoromethane, it is regularly observed that the scattered ion load—that is, the intensity of background when measured far off-peak—is linearly dependent on the on-peak intensity of mass 34. This phenomenon is true to some extent for all masses of interest (Figs. 5.14, 5.16, 5.15). Accurate determination of this dependence is especially important at mass 36, where scattered ion intensities are at least 2% of the intensities of the clumped isotopologues. The size of these scattered ion loads varies from sample to sample. They appear to be caused by minor but vari-

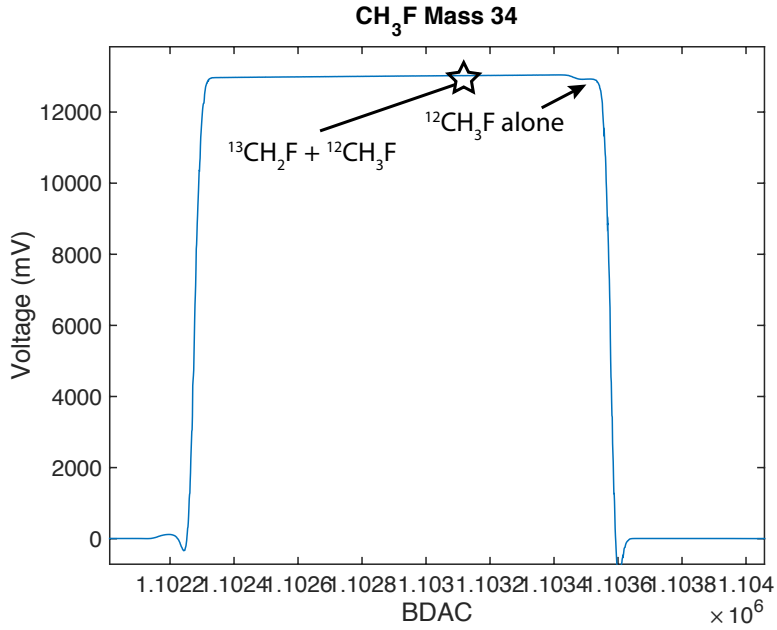

Figure 5.8: Mass spectrum of mass 34 of fluoromethane on the MAT 253 Ultra. Star denotes location of measurement.

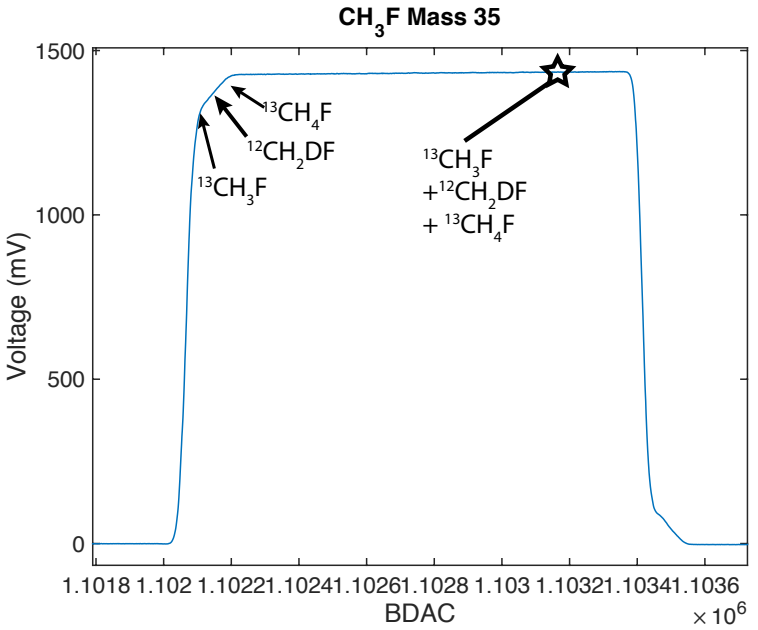

Figure 5.9: Mass spectrum of mass 35 of fluoromethane on the MAT 253 Ultra. Star denotes location of measurement.

able amounts of contaminant species that are produced during the demethoxylation reaction of complex materials, and cannot be stripped by our cryogenic distillation procedure. Indeed, it was noted that scattered ion loads were usually larger for

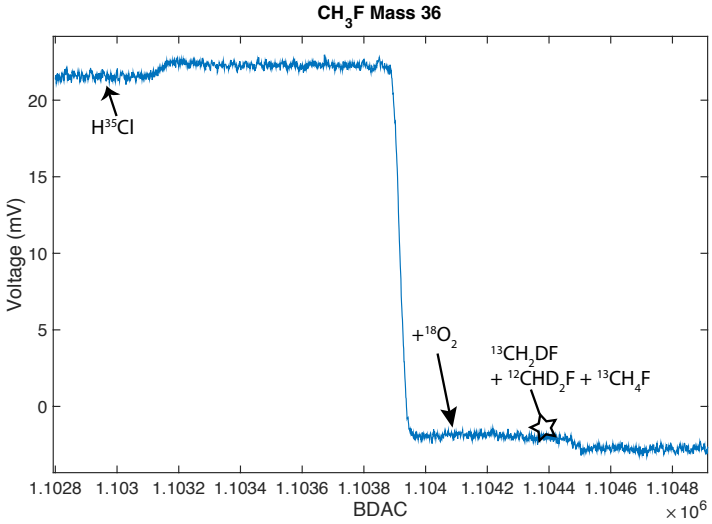

Figure 5.10: Mass spectrum of mass 36 of fluoromethane on the MAT 253 Ultra. Star denotes location of measurement.

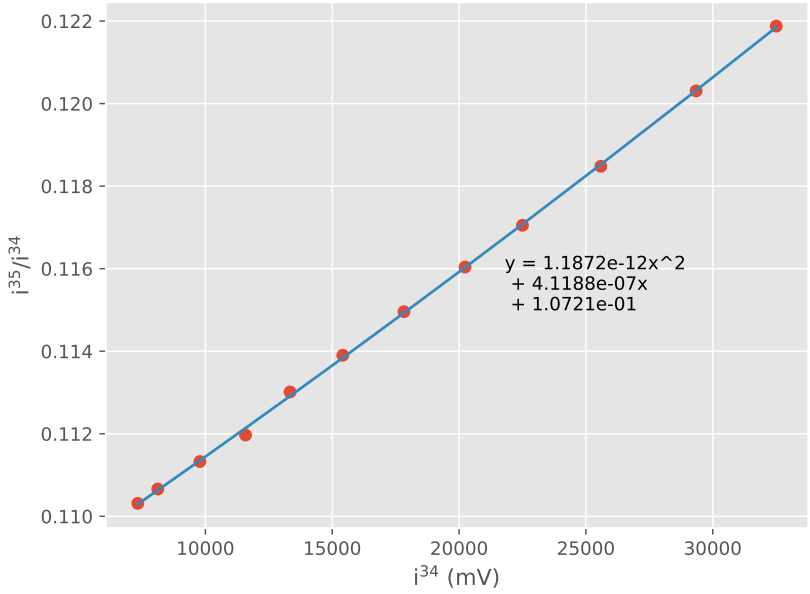

Figure 5.11: Example adduct line of $r35$ vs. $i34$ of fluoromethane on the MAT 253 Ultra.

CH_3F samples sourced from more complex and thermally mature starting materials. For this reason, these background dependencies need be determined daily for every sample and working gas separately, and applied to every measurement cycle invididually. No clumped isotope measurements of mature materials with prohibitively high scattered ion loads are reported here.

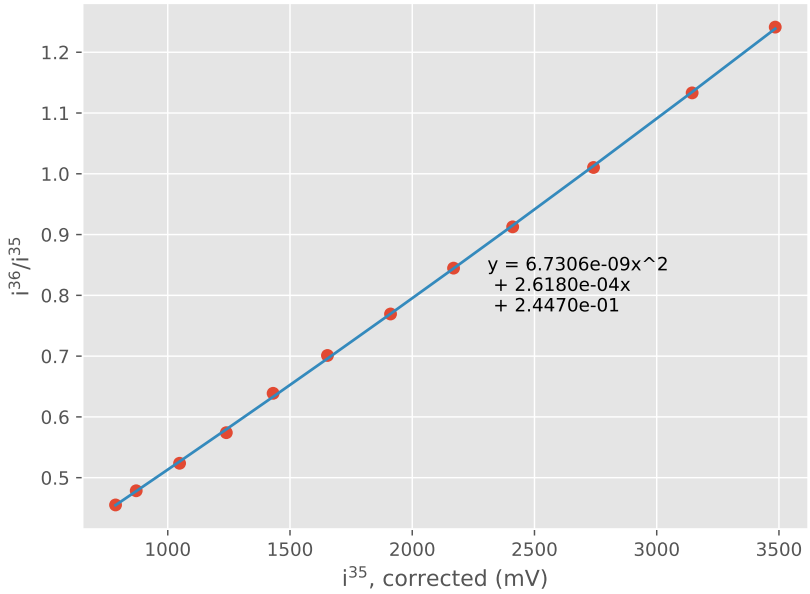

Figure 5.12: Example adduct line of $r36$ vs. $i35$ of fluoromethane on the MAT 253 Ultra. Note that for this relationship to be accurate, the adduct contribution to the intensity on mass 35 must first be subtracted.

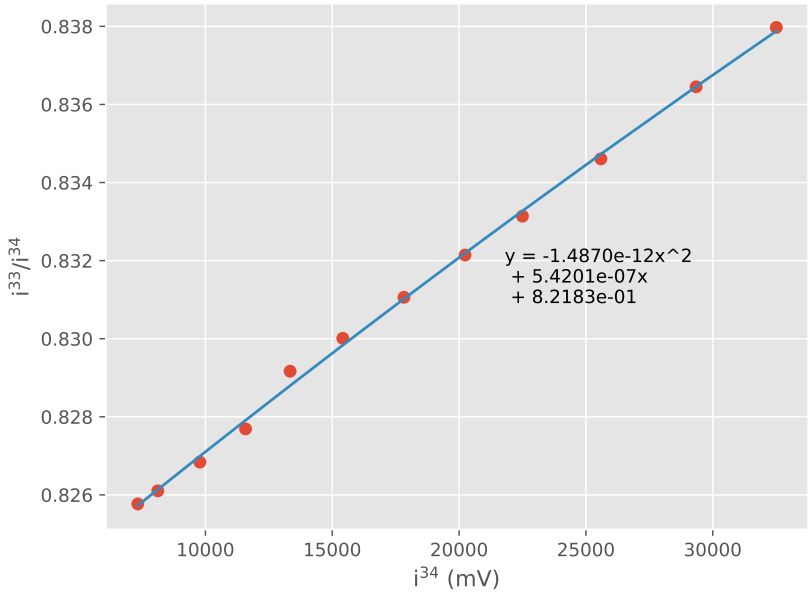

Figure 5.13: Dependence of fragmentation rate ($i33/i34$) on intensity of mass 34. Note that our correction scheme assumes that the fragmentation rate is effectively constant over the intensity range of actual measurements.

Single-collector measurements of D/^{13}C in fluoromethane

The Prototype MAT 253 Ultra is capable of precisely determining the relative abundances of of the sum of the two singly-substituted istopologues at mass 35, and the

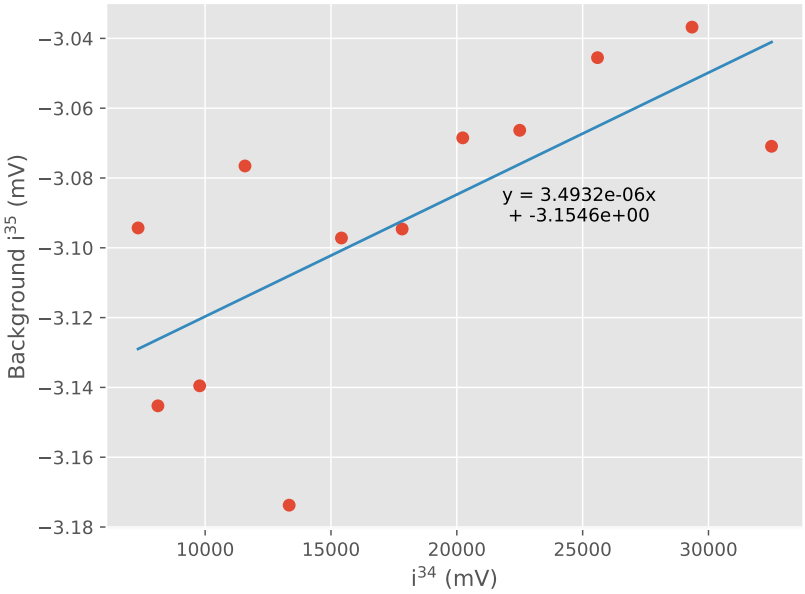

Figure 5.14: Example off-peak background line near mass 35 vs. $i34$ of fluoromethane on the MAT 253 Ultra.

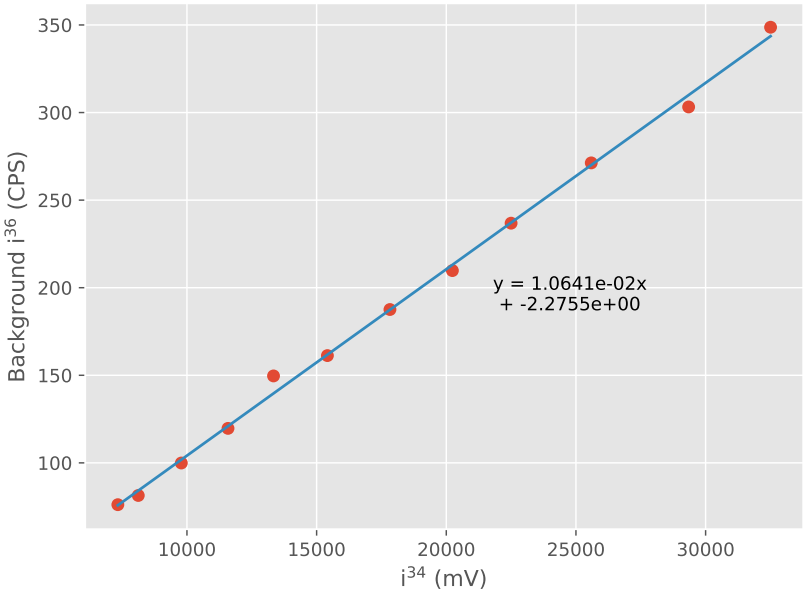

Figure 5.15: Example off-peak background line near mass 36 vs. $i34$ of fluoromethane on the MAT 253 Ultra.

doubly substituted species at mass 36. In order to calculate a Δ_{36} value, describing the measured abundance of the clumped species relative to a stochastic distribution, however, precise values for δ^{13}C and δ^{2}H must be determined. To accomplish this,

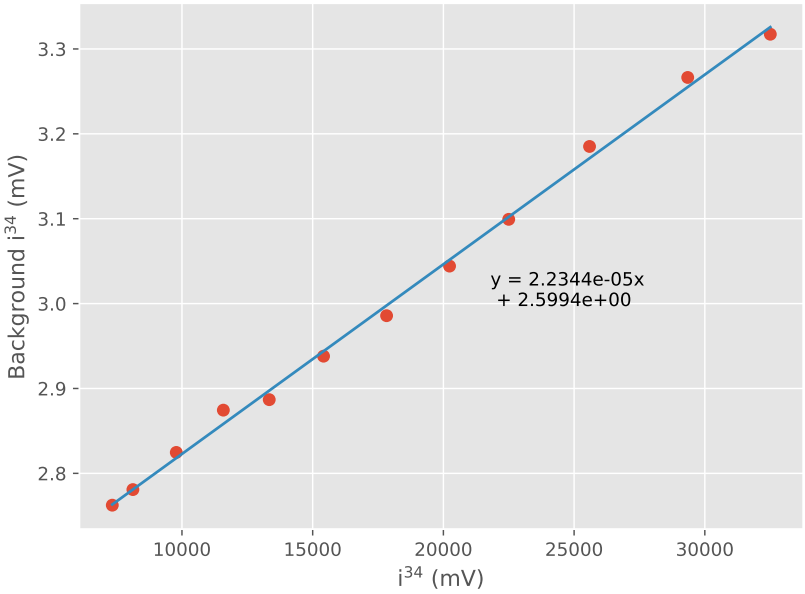

Figure 5.16: Example off-peak background line near mass 34 vs. $i34$ of fluoromethane on the MAT 253 Ultra.

we employ an additional measurement of a second aliquot of sample gas, relative to the same working reference gas, on a Thermo DFS modified to perform dual-inlet measurements with long integration times. The DFS has a single collector, so making measurements at multiple cardinal masses requires peak hopping schemes which are potentially feasible but challenging to do accurately (see Dallas et al., in prep). However, the instrument can rapidly, repeatedly scan over a very small mass window (100s of mDa, at most) at an extremely high mass resolution (upwards of 60,000 in some cases). Thus it is possible to generate precise peak scans of isotopologues that would be irresolvable by any other existing sector MS instrument. By producing many such scans, regularly switching between sample and working gas for long integration times, and fitting the results using peak shape models, it is possible to produce precise determinations of the ratios of peaks at the same cardinal mass. We exploit this capability for two measurements: 1) at mass 35, the ratio of $^{12}CH_2DF$ to $^{13}CH_3F$ can be determined at mass resolutions above 45,000; and 2) at mass 16, the ratio of $^{12}CH_2D$ to $^{13}CH_3$ can be determined in nearly any instrument state with mass resolution above 20,000. Example scans of each measurement, and fits from our custom peak-fitting software, are shown in Figs. 5.17, 5.18. Each measurement has its benefits and drawbacks. The measurement at mass 35 uses the exact same species analyzed on the MAT 253 Ultra. Risk of contamination, or mass

fractionations due to instability of the methyl fragment, is low. On the other hand, because the adduct peak is exceptionally large, an instrument with extremely narrow entrance and exit slits must be used in order to resolve $^{12}CH_2DF$ from the low-mass tail of $^{12}CH_4F$. This reduces count rates to the extent that a single, hourlong measurement has a shot noise-limited error of $\sim 3‰$. Both because of the larger relative mass differences and the smaller adduct size, measurement of the ratio of $^{12}CH_2D$ to $^{13}CH_3$ is comparatively straightforward and can be done with wide slits at a much lower mass resolution. In fact, although methyl fragmentation rates on the DFS are comparatively low ($\sim 25\%$ of the CH_3F peak), the wider entrance and exit slits permit running this measurement with $\sim$ thrice the count rates, reducing the integration times required to achieve suitable precision. On the other hand, as discussed above, methyl fragmentation rates are unstable on timescales of hours. Of course, by only considering the ratio of one methyl fragment isotopologue to another, any drift in absolute fragment abundance should cancel out. More insidious is the persistent worry of cryptic contamination; many potential contaminant species contain methyl groups, and by measuring solely methyl fragments, multiple potential sources of these isotopologues are indistinguishable.

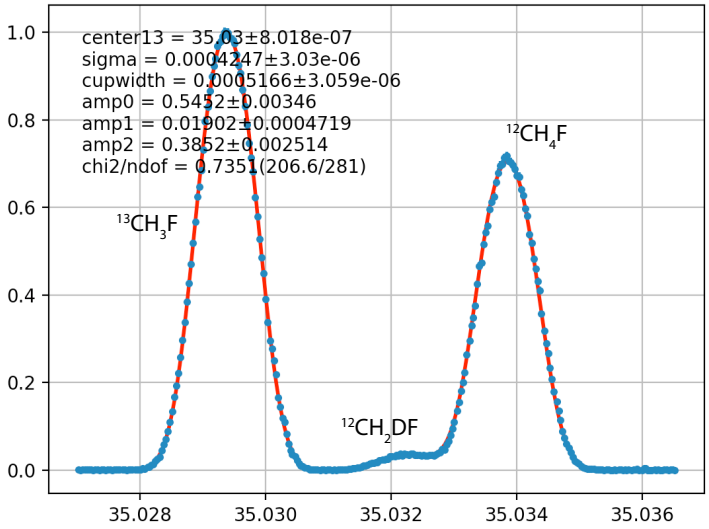

Figure 5.17: Example of peak shape and model fit of methyl fragment isotopologues at mass 35.

As a compromise between these needs, we used a measurement scheme that employed both families of peaks. For a given measurement session, the relative isotope ratio of D to ^{13}C was first determined on the full molecular ions at mass 35. After

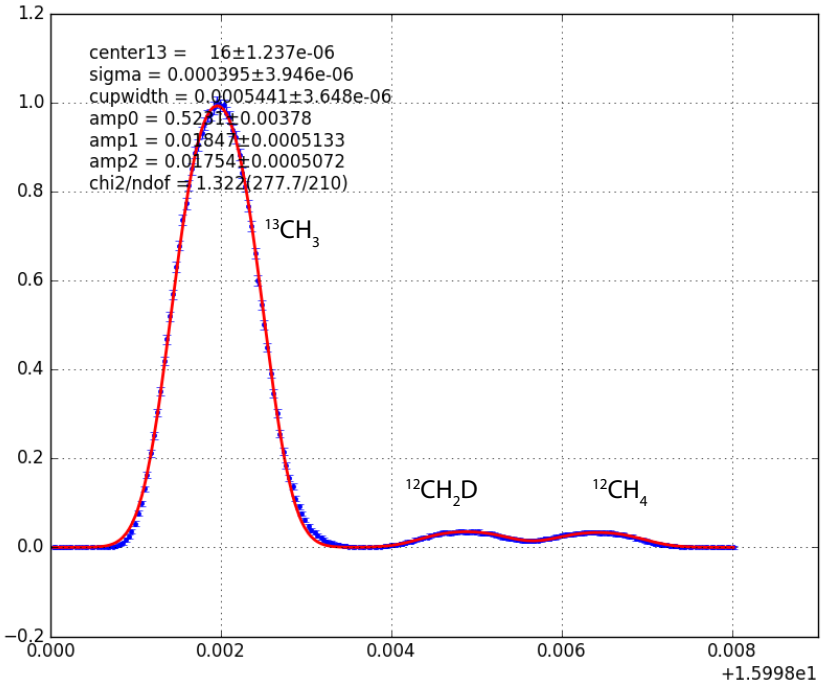

Figure 5.18: Example of peak shape and model fit of methyl fragment isotopologues at mass 16.

2–5 such hourlong measurements, the instrument was re-tuned to optimize counts on the methyl fragment, and additional hourlong D to ^{13}C determinations were made (typically 4–8). Mean values of each were compared to demonstrate that the isotope ratios were indistinguishable within uncertainty. Then the weighted average of these separate measurements was used to calculate the final value of D to ^{13}C in the sample, relative to the working reference gas. Over the course of tens of such measurements, no sample was found where D to ^{13}C isotope ratios from the methyl fragment and molecular ion difference significantly. And, shot noise plots demonstrate that counting-statistics limits were regularly approached (Fig. 5.19).

Data processing and correction

A single methoxyl clumped isotope measurement requires 2–3 days of analytical time. On the MAT 253 Ultra, after applying intensity-dependent background corrections and adduct corrections, the ratios:

$$\frac{^{13}C^{1}H_3F + {}^{12}CH_2DF}{^{12}CH_3F + {}^{13}CH_2F + {}^{12}CHDF}, \text{ and } \frac{^{13}CH_2DF + {}^{12}CHD_2F}{^{12}CH_3F^{+} {}^{13}CH_2F + {}^{12}CHDF} \tag{5.11}$$

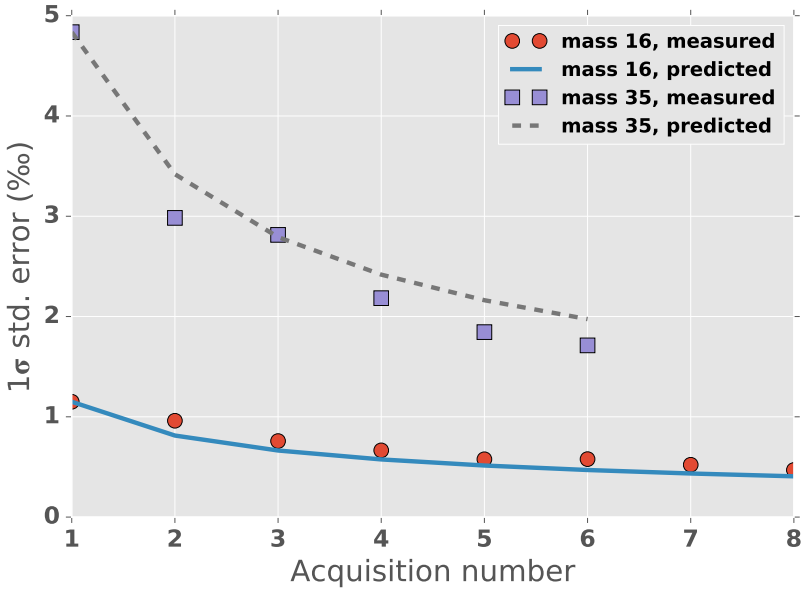

Figure 5.19: Sample measured 1σ standard errors, and expected shot noise limits, for the described DFS measurements at masses 35 and 16.

are measured, relative to the working gas, to precisions of $\sim 0.01‰$ and $\sim 0.5‰$, respectively. On the Thermo DFS, the ratio

$$\frac{^{12}CH_2DF}{^{13}CH_3F} \tag{5.12}$$

is determined, through long integration times (10–15 hours), to a precision of $\sim 0.5‰$. The $\delta^{13}C_{VPDB}$ and $\delta^{2}H_{VSMOW}$ values of the working gas were measured by A. Schimmelmann, by sealed-tube combustion and reduction, to be $-67.79 \pm 0.05‰$ and $-113.6 \pm 1.3‰$, respectively. The H-fragmentation ratio, measured as: $^{12}CH_2F/^{12}CH_3F$, was determined daily, but was commonly close to 0.866. By assuming that this fragmentation rate applies to singly-substituted fragments as well, and given the true isotope composition of the working gas, the *root* solver from the *scipy.optimize* python module is used to find an analytical solution to this system of equations and determine the $\delta^{13}C$ and $\delta^{2}H$ values of the sample relative to VPDB and VSMOW standards, and the Δ_{36} value relative to that of the working gas. Uncertainties on these values are found using a Monte Carlo scheme where each of the three raw measurements are independently randomly perturbed by their gaussian measurement uncertainty and the three derived values are recalculated. This exercise is repeated for 10,000 iterations. The reported $\delta^{13}C$, $\delta^{2}H$, and Δ_{36} values are the means of these distributions. The reported errors are the standard deviations of

the distributions of these simulater $\delta^{13}C$, $\delta^{2}H$, and Δ_{36}values. Obviously, this approach assumes that measurement errors are perfectly uncorrelated. Since the two measurements with the largest errors are made on separate aliquots on different mass spectrometers, this is likely a reasonable assumption.

5.5 Results and Discussion

To date, 38 measurements of the $\delta^{13}C$, $\delta^{2}H$, and Δ_{36} values of methoxyl-bearing compounds or our in-house iodomethane standard have been measured over the course of four analytical sessions. However, due to issues involving incomplete fluorination using degraded Co(III)F_3 in the most recent session, only fourteen measurements are reported here. Below we present results demonstrating the accuracy and precision of both the chemical extraction procedure and the mass spectrometric methods.

Tests of yield and purification

Yields from the chemical extraction procedure can be determined using measured amounts of simple compounds with known methoxyl contents. Using both methods, the yields of iodomethane (measured as manometer pressure at room temperature of this gas expanded into a known volume) are commonly near 100%. A notable exception is the relatively poor yield of methionine. Methionine contains an S-bound methyl group, not an O-bound one. It is conceivable that the Hydriodic conversion of methyl-thiol groups to iodomethane is substantially slower than methoxyl groups. If so, CH_3I yield from methionine could be improved with a longer reaction time.

Accuracy and reproducibility of complete procedure

The accuracy of our complete chemical and mass spectrometric procedure can be efficiently tested by performing it on compounds where the isotope compositions of methoxyl group are independently known.

$\delta^{13}C$ *accuracy*: $\delta^{13}C$ values of a CH_3I standard from Sigma Aldrich and a methanol standard were independently determined by conventional sealed-tube combustion. Briefly, CH_3I, or CH_3OH was heated at 850 °C in the presence of CuO wire, with Ag foil added to scavenge iodine. Product CO_2 was separated from water on a vacuum line and measured on a Thermo Delta V IRMS in dual-inlet mode. Expected $\delta^{13}C$ values shown in Fig. 5.20 are the means and standard errors of four and three replicate combustions of methanol and CH_3I, respectively. Three measurements each of the methanol and CH_3I standard were made over the course of the two

Reaction date	Compound	Extraction method	Amount (mg)	Yield (%)
4/8/16	Methionine	V	25	68.37
4/12/16	Methanol	V	2.20	103.34
5/5/16	Vanillin	V	35.7	92.90
5/6/16	Vanillin	V	17.6	83.48
5/6/16	Vanillin	V	17.2	93.71
5/10/16	Methanol	V	2.52	104.66
5/12/16	Vanillin	V	28.5	96.47
5/14/16	Vanillin	V	27.6	93.64
5/17/16	Vanillin	V	21.4	97.64
5/17/16	Methanol	V	2.21	116.49
6/2/16	Vanillin	V	28.8	93.92
6/11/16	Methanol	C	2.75	97.79

Table 5.1: Iodomethane yields from methoxyl extractions of pure compounds. 'V' samples used the reaction vessel method. 'C' samples used the reflux condenser.

Date	Type	Sample	δ^{35}	δ^{35} (1σ s.e.)	δ^{36}	δ^{36} (1σ s.e.)	δD/^{13}C	δD/^{13}C (1σ s.e.)
2/2/16	Bamboo	Bamboo_USC	35.441	0.007	-58.20	0.49	-109.50	0.30
11/15/15	CH_3I	CH3I-F_std	16.388	0.007	35.89	0.40	9.36	1.08
2/5/16	CH_3I	CH3I-F_std	17.564	0.009	35.42	0.47	4.38	0.56
2/4/17	CH_3I	CH3I-F_std	17.140	0.009	20.48	0.40	-10.25	0.45
2/1/16	Lignin	Lignin_USC	37.607	0.009	-131.22	0.67	-192.78	0.40
11/10/15	MeOH	MeOH_orphan	39.615	0.010	-24.86	0.45	-107.26	1.43
11/12/15	MeOH	MeOH_orphan	40.853	0.007	-23.04	0.40	-103.83	0.71
2/4/16	MeOH	MeOH_orphan	42.169	0.006	-28.21	0.38	-111.00	0.20
6/20/16	MeOH	MeOH_orphan	43.402	0.007	-17.50	0.53	-102.17	0.46
2/3/16	Syringic Acid	SyringicAcid_USC	23.317	0.006	-46.33	0.43	-91.51	0.35
6/18/16	Vanillin, natural	SAV-N	27.767	0.006	-40.36	0.43	-102.45	1.49
6/15/16	Vanillin, synthetic	RRV-2	47.494	0.006	-179.27	0.44	-280.72	0.62
6/17/16	Vanillin, synthetic	SAV-S	50.288	0.010	337.71	0.67	190.26	1.07
6/23/16	Vanillin, synthetic	RRV-1	47.205	0.008	-172.30	0.46	-276.81	1.10

Table 5.2: Adduct-corrected, background-corrected δ^{35}, δ^{36}, and δD/^{13}C measurements, relative to the working gas composition.

measurement sessions. Methanol measurements are full procedural replicates of the entire extraction, purification, fluorination, and analysis procedure. CH_3I standard measurements are separate conversions of CH_3I to CH_3F over CoF_3. Although the calculated δ^{13}C values generally agree with the offline sealed-tube combustion values, the replicate variation is on the order of 1‰, considerably larger than the measurement error. This is especially true among the full procedural replicates. It is not immediately apparent why this variation is so large. One possibility is that the lack of perfect 100% yields causes some fractionation in the extractions. If so, further refinement of procedural technique will be required to reduce this variation.

δ^2H *accuracy*: δ^2H values of standard compounds were determined in a number

Date	Type	Sample	δ^{13}C	δ^{13}C (1σ s.e.)	δ^{2}H	δ^{2}H (1σ s.e.)	Δ_{36}	Δ_{36} (1σ s.e.)
2/2/16	Bamboo	Bamboo_USC	-30.38	0.01	-178.98	0.26	-20.67	0.58
11/15/15	CH_3I	CH3I-F_std	-52.71	0.04	-90.85	0.92	-6.08	1.05
2/5/16	CH_3I	CH3I-F_std	-51.42	0.02	-94.07	0.48	-4.30	0.67
2/4/17	CH_3I	CH3I-F_exp3	-51.29	0.02	-107.16	0.39	-4.20	0.58
2/1/16	Lignin	Lignin_USC	-25.22	0.02	-251.80	0.38	-12.84	0.92
11/10/15	MeOH	MeOH_orphan	-26.52	0.05	-173.61	1.25	3.40	1.58
11/12/15	MeOH	MeOH_orphan	-25.48	0.03	-169.57	0.64	-0.71	0.87
2/4/16	MeOH	MeOH_orphan	-23.96	0.01	-174.95	0.18	-0.99	0.45
6/20/16	MeOH	MeOH_orphan	-23.13	0.02	-166.05	0.40	-1.72	0.68
2/3/16	Syringic Acid	SyringicAcid_USC	-42.50	0.01	-172.87	0.31	-3.58	0.58
6/18/16	Vanillin, natural	SAV-N	-37.89	0.06	-178.95	1.33	5.43	1.66
6/15/16	Vanillin, synthetic	RRV-2	-12.50	0.02	-324.61	0.54	21.01	0.96
6/17/16	Vanillin, synthetic	SAV-S	-27.52	0.04	100.58	0.96	30.68	0.99
6/23/16	Vanillin, synthetic	RRV-1	-12.93	0.04	-321.21	0.96	24.93	1.54

Table 5.3: Derived δ^{13}C (vs. VPDB), δ^{2}H (vs. VSMOW), and Δ_{36} (vs. wg) measurements of methoxyl groups from synthetic and natural materials.

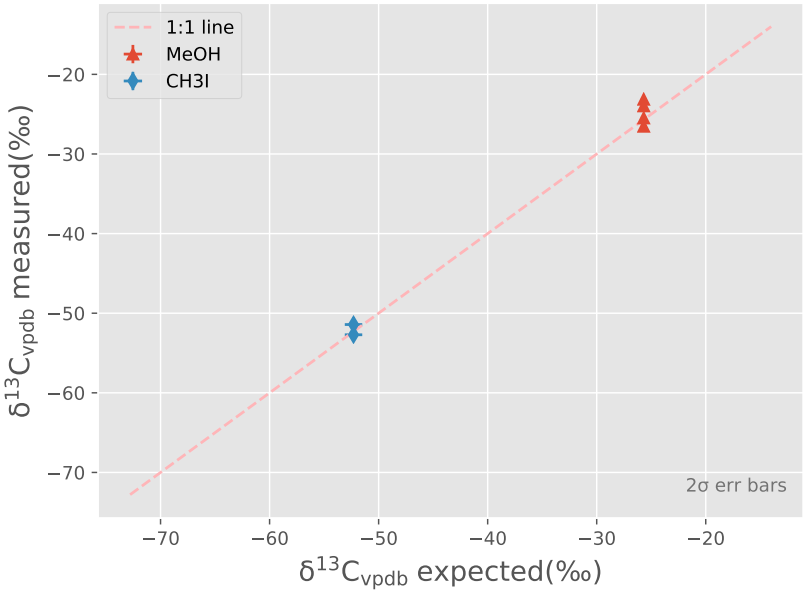

Figure 5.20: Accuracy tests for δ^{13}C measurements of methoxyl groups in methanol and iodomethane standards.

of ways. Accepted values for the lignin and bamboo standards shown were are results obtained by C. Ponton from the same materials using the standard GC-vial methoxyl extraction + GC-pyrolysis-IRMS technique in the Feakins Lab at USC. Uncertainties were not reported for these values, so here we assume a 1σ standard error of 2‰ for these measurements. The δ^{2}H value of the methoxyl group in our methanol standard was determined by P. Douglas by affixing this methyl group to a phthalic acid standard of known δ^{2}H composition. By measuring the δ^{2}H value of the resulting phthalic acid methyl ester by online GC-pyrolysis-IRMS, the

δ^2H value of the methanol-derived methyl group can be calculated by subtraction. This approach is only robust, however, if both methanol and phthalic acid are quantitatively reacted to phthalic acid-ME. Yields were not assessed here, nor were replicate measurements made, so large uncertainties are assigned to this value. The δ^2H value of our specific CH_3I standard has not yet been determined. However, both the carbon and hydrogen compositions are extremely similar to those of a separate batch of CH_3I standards, also purchased from Sigma Aldrich, measured by A. Schimmelmann. So, the reported δ^2H value of this CH_3I is used here. Such an approach is inherently circular and clearly problematic. However, all measurements of methanol, bamboo, and lignin fall on a 1:1 line with accepted values within 2-sigma uncertainty (Fig. 5.21), suggesting that even lacking a true determination of the δ^2H of our CH_3I standard, our extraction and dual-MS measurement procedure is reasonably accurate. Note, again, however, that the replicate variability is larger than the measurement uncertainty for methanol and iodomethane.

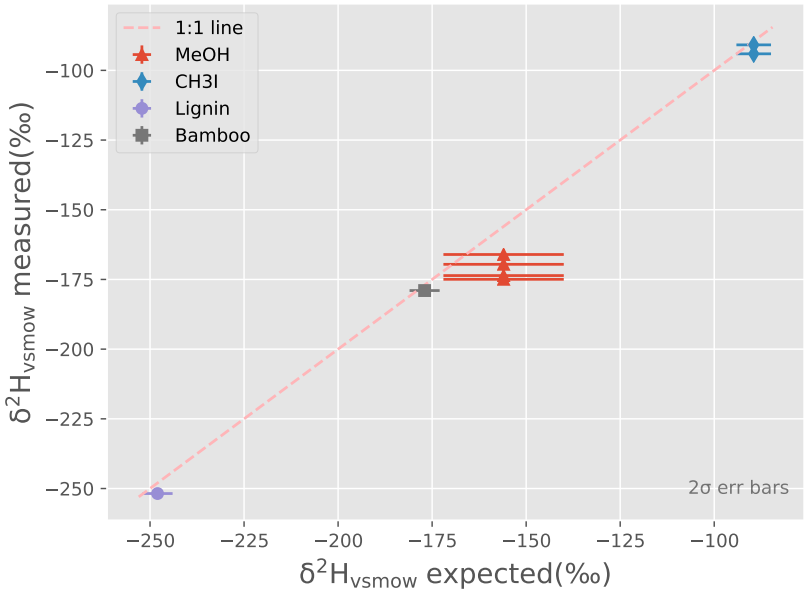

Figure 5.21: Accuracy tests for δ^2H measurements of methoxyl groups in methanol and iodomethane standards.

Δ_{36} *reproducibility*: Robust demonstration of absolute accuracy in Δ_{36} requires re-equilibrating C–H bonds in fluoromethane at different temperatures and approaching equilibrium from opposite directions. Such an approach is analogous to those used to report multiply-substituted and intramolecular isotope configurations of simple n-alkanes (methane, ethane, propane) in stochastic reference frames. However,

when fluoromethane is exposed to the the same activated-carbon catalysts used to promote C – H exchange in these compounds (e.g., nickel-carbon, palladium-carbon, alumina), it rapidly degrades to form other species, notably methane, HF, and F_2. Analogous catalyzed exchange experiments using other methyl-bearing compounds have failed for similar reasons: at moderately elevated temperaures, methanol and iodomethane also degrade in the presence of nickel and palladium catalysts.

Because we have not yet been able to re-equilibrate the C-H bonds in methoxyl groups, we cannot yet report our clumped C-H measurements in the stochastic reference frame. Instead, these values are reported relative to the clumped C-H enrichment of the working gas (Fig. 5.22). So although absolute accuracy of our Δ_{36} measurements cannot be established, we can at least assess whether replicate measurements are reproducible, and different materials are resolved from one another. Generally, Δ_{36} values of replicates of the CH_3I and MeOH standard are reproducible both within and between analytical sessions. And, variations do not correlate with $\delta_{36,wg}$ (Fig. 5.23). This suggests that instrumental drift and 'stretching' of the working-gas reference frame are minor, at least relative to the uncertainties of our measurements. It is notable that Δ_{36} values of standards are in good agreement even when $\delta^{13}C$ and $\delta^{2}H$ compositions vary beyond analytical uncertainty. This phenomenon is analogous to one commonly observed in the reaction and measurement of $\delta^{13}C$, $\delta^{18}O$, and Δ_{47} values of CO_2 from acid-digested carbonates: $\delta^{18}O$ values of carbonates drift between analytical sessions and batches of phosphoric acid by $\sim 0.1‰$, but the measurement uncertainty of a single CO_2 aliquot is better than $0.01‰$, and Δ_{47} values of multiple extractions can agree within measurement error once mass spectrometric non-linearities are corrected for. In both cases, this suggests that moderate isotopic fractionations associated with our multi-step chemical extraction, purification, and fluorination procedure do not significantly fractionate Δ_{36} values. In other words, the Δ_{36} value of a methoxyl group is 'buffered' to fractionations during our sample workup procedure in a way that $\delta^{13}C$ and $\delta^{2}H$ values are not.

Clumped $^{13}C-^{2}H$ variation among simple monomers and complex polymers

Among natural and synthetic materials measured so far, a remarkably wide range in Δ_{36} is observed (Fig. 5.24). Three aspects of these data are notable. As with the standards, Δ_{36} measurements are independent of $\delta_{36,wg}$, suggesting that this variation is not the result of a faulty analytical procedure or data processing scheme (Fig. 5.25). Instead, the $\sim$ 50 permil range in Δ_{36} appears to be robust. It is the

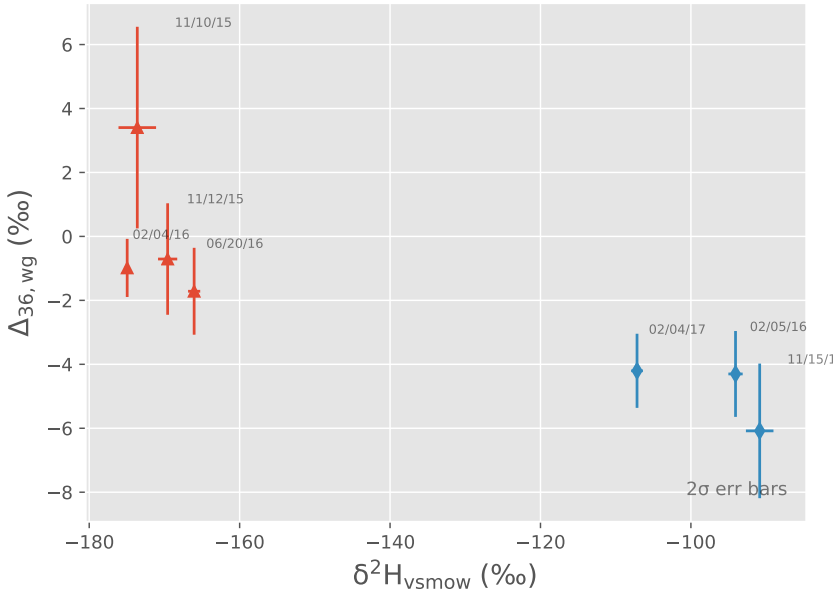

Figure 5.22: Reproducibility of Δ_{36} measurements of methoxyl groups in methanol and iodomethane standards across multiple analytical sessions.

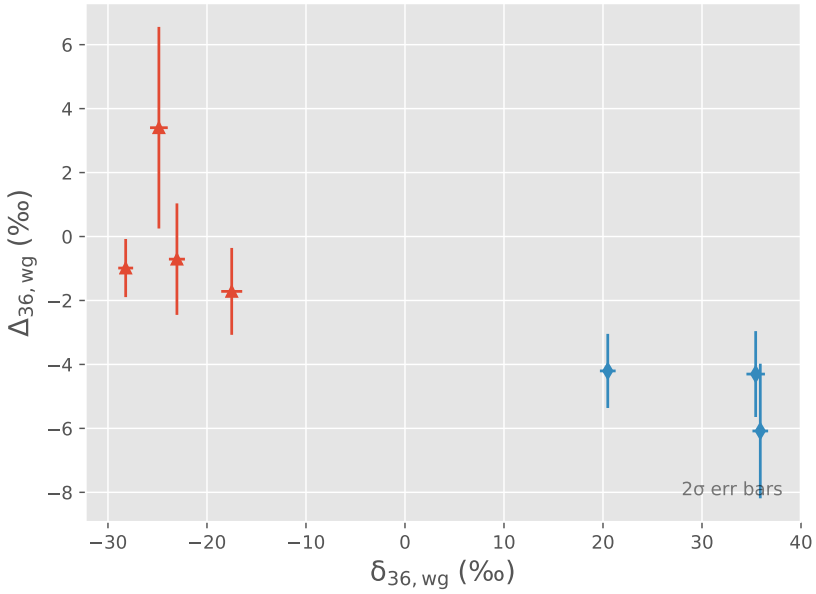

Figure 5.23: Reproducibility of Δ_{36} measurements of methoxyl groups in methanol and iodomethane standards across multiple analytical sessions, relative to $\delta_{36,wg}$.

largest range in the clumped isotope compositions of organic molecules observed to date. As discussed above, these data cannot yet be projected into a stochastic reference frame because the stochastic Δ_{36} value of the working gas is not known.

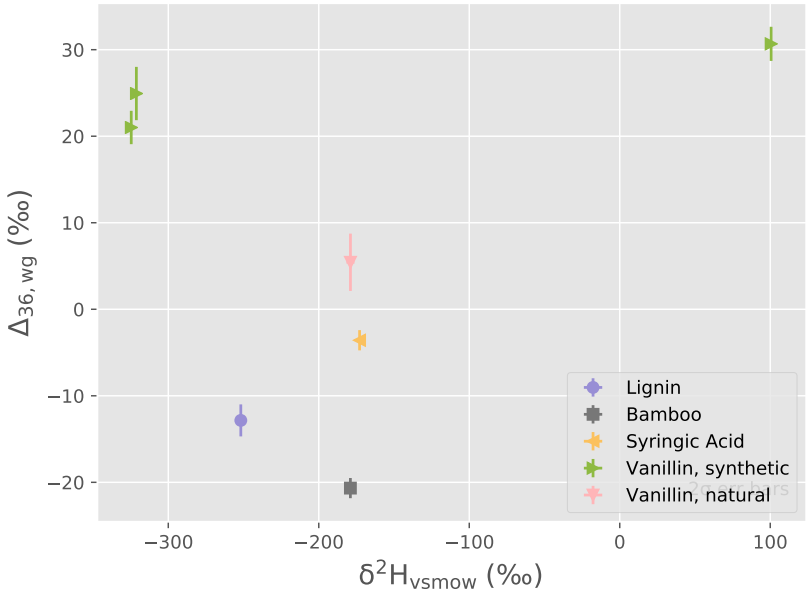

Figure 5.24: Variation in Δ_{36} values among natural and synthetic methoxyl-bearing monomers and polymers, compared to δ^2H.

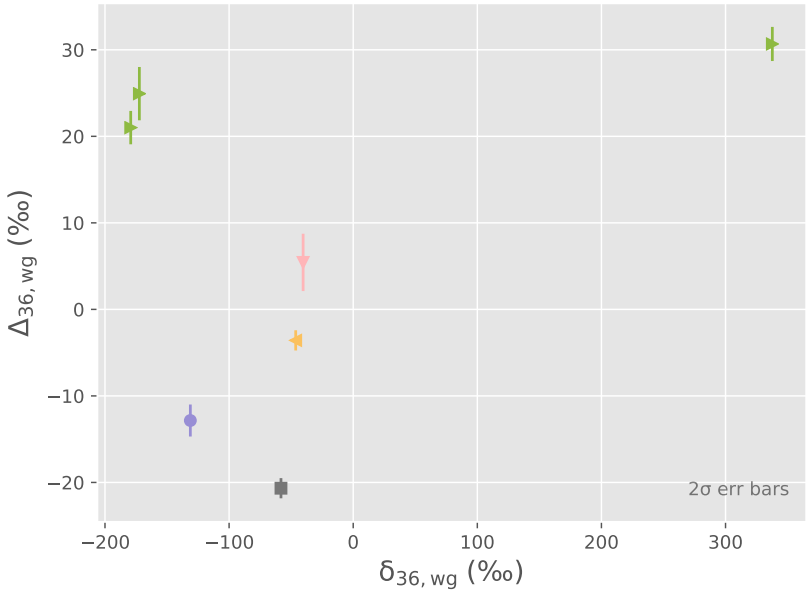

Figure 5.25: Variation in Δ_{36} values among natural and synthetic methoxyl-bearing monomers and polymers, compared to $\delta_{36,wg}$.

So which, if any, of these materials are in isotopic equilibrium with their formation environment cannot be assessed. In fact, even if the stochastic value of the working reference gas was known, expressing all data into their thermodynamic reference

frames is non-trivial because these methoxyl groups arise from different materials, and the Urey-Bigeleisen-style model for a given methoxyl group will depend on its bonding environment. So, e.g., methoxyl groups from vanillin and methanol will not have the same Δ_{36}-T relationship.

Nonetheless, these second-order (and third-order) isotope effects are subtle compared to the range of Δ_{36} values observed. In any reasonable natural compound, the full range of thermally-equilibrated Δ_{36} values should not exceed $\sim 15‰$. That we observe a range in values nearly 4 times that indicates that kinetic isotope effects dominate the landscape of methoxyl $^{13}C-^{2}H$ configurations in natural materials. This is perhaps not surprising given how we believe these methoxyl groups are formed. In higher plants, methoxyl groups, like all C1 compounds, originate from the C3 group of serine, which is cleaved by serinehydroxy methyltransferase to the tetrahydrofolate-bound (THF) C1 pool (H. L. Schmidt and Gleixner, 1998; H.-L. Schmidt, Robins, and Werner, 2015). A subset of these are methylated, transferred by S-adenosyl methionine and attached to the aromatic acids and alkaloids by Catechol-O-methyltransferase (H. L. Schmidt and Gleixner, 1998; H.-L. Schmidt, Robins, and Werner, 2015). Although THF-bound CH_2 groups might be reversibly exchanged during their residence in the transient C1-carbon pool, it has been argued that the methylation step, $CH_2 + H \rightarrow CH_3$ of methionine synthesis is one-way, largely-irreversible reaction (H. L. Schmidt and Gleixner, 1998; H.-L. Schmidt, Robins, and Werner, 2015).

Intriguingly, the apparent net fractionation between δ^2H of xylem water and lignin methoxyl groups is $\sim -180‰$ (Feakins et al., 2014). This fractionation is at least $100‰$ larger than that between xylem water and bulk wood (Keppler et al., 2007), and similarly larger than that between xylem water and cellulose (EPSTEIN, YAPP, and Hall, 1976). Most(?) hydrogen in bulk wood and cellulose is exists in CH_2 groups, and the plant C1 pool that is the likely source for all methyl groups is bound as CH_2 groups onto THF. If the CH_2 groups of the plant C1 pool have a similar composition to those of cellulose, then the addition of the third hydrogen must be accompanied by an extremely large isotope effect in order for methoxyl groups to be depleted by, on average, $-180‰$. Such a large, likely kinetic, isotope effect should generate distributions of deuterium among the three hydrogen sites in methoxyl groups (and more generally, methyl groups) that are extremely uneven (e.g., two hydrogens with δ^2H of $-100‰$ each, a third hydrogen with δ^2H of $-350‰$ in order to get the correct average bulk fractionation). If so, in addition

to the kinetic isotope effects we apparently observe in Δ_{36}, which is dominated by non-equilibrated $^{13}C-{}^{2}H$ concentrations, enormous excess should exist in the $\Delta_{^{12}CHD_2}$ values of methoxy groups as well. It is likely that the newest generations of high-resolution mass spectrometers could measure $\Delta_{^{12}CHD_2}$ values and observe such an effect. This would provide major insights into the reversibility of different steps in the assembly of methyl groups in higher plants.

References

Abelson, Philip H and T C Hoering (1961). "Carbon Isotope Fractionation in Formation of Amino Acids by Photosynthetic Organisms". In: *Proceedings of the National Academy of Sciences of the United States of America* 47.5, pp. 623–632.

Anhäuser, Tobias, Markus Greule, Daniela Polag, et al. (2017). "Mean annual temperatures of mid-latitude regions derived from δ2H values of wood lignin methoxyl groups and its implications for paleoclimate studies". In: *Science of The Total Environment* 574, pp. 1276–1282.

Anhäuser, Tobias, Markus Greule, Michael Zech, et al. (2015). "Stable hydrogen and carbon isotope ratios of methoxyl groups during plant litter degradation". In: *Isotopes in Environmental and Health Studies*, pp. 1–12.

Baker, L et al. (2002). "A Technique for the Determination of 18O/ 16O and 17O/ 16O Isotopic Ratios in Water from Small Liquid and Solid Samples". In: *Analytical Chemistry* 74.7, pp. 1665–1673.

Barkan, Eugeni and Boaz Luz (2005). "High precision measurements of 17O/16O and 18O/16O ratios in H2O". In: *Rapid Communications in Mass Spectrometry* 19.24, pp. 3737–3742.

– (2012). "High-precision measurements of 17O/ 16O and 18O/ 16O ratios in CO 2". In: *Rapid Communications in Mass Spectrometry* 26.23, pp. 2733–2738.

Benner, R et al. (1987). "Depletion of 13 C in lignin and its implications for stable carbon isotope studies". In: *Nature*.

Boerjan, Wout, John Ralph, and Marie Baucher (2003). "Lignin Biosynthesis". In: *Annual Review of Plant Biology* 54.1, pp. 519–546.

Campbell, M M and R R Sederoff (1996). "Variation in Lignin Content and Composition (Mechanisms of Control and Implications for the Genetic Improvement of Plants)." In: *Plant Physiology* 110.1, pp. 3–13.

Clog, M.D. and J.M. Eiler (2014). "C-H and C-C clumping in ethane by high-resolution mass spectrometry". In: *AGU Fall Meeting Abstracts*.

DeNiro, M J and Samuel Epstein (1977). "Mechanism of carbon isotope fractionation associated with lipid synthesis". In: *Science* 197, pp. 261–263.

Eiler, John M (2007). ""Clumped-isotope" geochemistry—The study of naturally-occurring, multiply-substituted isotopologues". In: *Earth and Planetary Science Letters* 262.3–4, pp. 309–327.

– (2013). "The Isotopic Anatomies of Molecules and Minerals". In: *Annual Review of Earth and Planetary Sciences* 41.1, pp. 411–441.

Eiler, John M and Edwin Schauble (2004). "18O13C16O in Earth's atmosphere". In: *Geochimica et Cosmochimica Acta* 68.23, pp. 4767–4777.

Eiler, John et al. (2017). “Analysis of molecular isotopic structures at high precision and accuracy by Orbitrap mass spectrometry”. In: *International Journal of Mass Spectrometry*.

EPSTEIN, S, C J YAPP, and J H Hall (1976). “The determination of the D/H ratio of non-exchangeable hydrogen in cellulose extracted from aquatic and land plants”. In: *Earth and Planetary Science Letters*.

Feakins, Sarah J, Patricia V Ellsworth, and Leonel da Silveira Lobo Sternberg (2013). “Lignin methoxyl hydrogen isotope ratios in a coastal ecosystem”. In: *Geochimica et Cosmochimica Acta* 121.C, pp. 54–66.

Feakins, Sarah J, Miguel Rincon, and Paulina Pinedo (2012). “Analytical challenges in the quantitative determination of 2H/ 1H ratios of methyl iodide”. In: *Rapid Communications in Mass Spectrometry* 27.3, pp. 430–436.

Filippo Jr, J San and L J Romano (1975). “Mechanism of the reaction of alkyl bromides and iodides with mercury (II) and silver (I) fluorides”. In: *The Journal of Organic Chemistry*.

Forster, A M and A J Downs (1985). “Reactions of Xenon Difluoride - Oxidative Fluorination of Methyl-Derivatives of the Para-Block Elements”. In: *Polyhedron* 4.9, pp. 1625–1635.

Ghosh, Prosenjit et al. (2006). “13C-18O bonds in carbonate minerals: A new kind of paleothermometer”. In: *Geochimica et Cosmochimica Acta* 70.6, pp. 1439–1456.

Gori, Y et al. (2012). “Carbon, hydrogen and oxygen stable isotope ratios of whole wood, cellulose and lignin methoxyl groups of Picea abiesas climate proxies”. In: *Rapid Communications in Mass Spectrometry* 27.1, pp. 265–275.

Goto, Hitoshi et al. (2006). “Interference of Carbohydrates in the Determination of the Methoxyl Content of Lignin in Woody Samples”. In: *Journal of Wood Chemistry and Technology* 26.1, pp. 81–93.

Greule, Markus and Frank Keppler (2011). “Stable isotope determination of ester and ether methyl moieties in plant methoxyl groups”. In: *Isotopes in Environmental and Health Studies* 47.4, pp. 470–482.

Greule, Markus, Armin Mosandl, et al. (2008). “A rapid and precise method for determination of D/H ratios of plant methoxyl groups”. In: *Rapid Communications in Mass Spectrometry* 22.24, pp. 3983–3988.

– (2009). “A simple rapid method to precisely determine 13C/ 12C ratios of plant methoxyl groups”. In: *Rapid Communications in Mass Spectrometry* 23.11, pp. 1710–1714.

Hatcher, Patrick G and David J Clifford (1997). “The organic geochemistry of coal: from plant materials to coal”. In: *Organic Geochemistry* 27.5-6, pp. 251–274.

Horvath, A L (1972). "Critical Properties of Halogenated Hydrocarbons - a Correlation". In: *Ashrae Journal-American Society of Heating Refrigerating and Air-Conditioning Engineers* 14.7, pp. 46–&.

Keppler, Frank et al. (2007). "Stable hydrogen isotope ratios of lignin methoxyl groups as a paleoclimate proxy and constraint of the geographical origin of wood". In: *New Phytologist* 176.3, pp. 600–609.

Krueger, Dana A and Harold W Krueger (1983). "Carbon isotopes in vanillin and the detection of falsified natural vanillin". In: *Journal of Agricultural and Food Chemistry* 31.6, pp. 1265–1268.

Magyar, Paul M (2017). "Insights into pathways of Nitrous Oxide generation from novel isotopologue measurements". PhD thesis. California Institute of Technology.

Magyar, Paul M, Victoria J Orphan, and John M Eiler (2016). "Measurement of rare isotopologues of nitrous oxide by high-resolution multi-collector mass spectrometry". In: *Rapid Communications in Mass Spectrometry* 30.17, pp. 1923–1940.

Mann, John (1987). "Modern methods for the introduction of fluorine into organic molecules: an approach to compounds with altered chemical and biological activities". In: *Chemical Society Reviews* 16, p. 381.

McCrea, J M (1950). "On the Isotopic Chemistry of Carbonates and a Paleotemperature Scale". In: *The Journal of chemical physics* 18.6, pp. 849–857.

Mischel, Maria et al. (2016). "δ2H, δ13C and δ18O from whole wood, α-cellulose and lignin methoxyl groups in Pinus sylvestris: a multi-parameter approach". In: pp. 1–17.

Monson, K D and J M Hayes (1982). "Biosynthetic control of the natural abundance of carbon 13 at specific positions within fatty acids in Saccharomyces cerevisiae". In: *Journal of Biological Chemistry*.

Passey, Benjamin H et al. (2014). "Triple oxygen isotopes in biogenic and sedimentary carbonates". In: 141.C, pp. 1–25.

Riechelmann, Dana F C et al. (2016). "Palaeogeography, Palaeoclimatology, Palaeoecology". In: *Palaeogeography, Palaeoclimatology, Palaeoecology* 445.C, pp. 60–71.

Rossmann, A, M Butzenlechner, and H L Schmidt (1991). "Evidence for a nonstatistical carbon isotope distribution in natural glucose". In: *Plant Physiology*.

Schink, B and J G Zeikus (1982). "Microbial ecology of pectin decomposition in anoxic lake sediments". In: *Microbiology*.

Schmidt, H L and G Gleixner (1998). *Carbon isotope effects on key reactions in plant metabolism and 13C-patterns in natural compounds*. Stable isotopes.

Schmidt, Hanns-Ludwig, Richard J Robins, and Roland A Werner (2015). "Multifactorial in vivostable isotope fractionation: causes, correlations, consequences and applications". In: *Isotopes in Environmental and Health Studies* 51.1, pp. 155–199.

Sessions, Alex L (2016). "Factors controlling the deuterium contents of sedimentary hydrocarbons". In: *Organic Geochemistry* 96, pp. 43–64.

Sessions, Alex L et al. (2004). "Isotopic exchange of carbon-bound hydrogen over geologic timescales". In: *Geochimica et Cosmochimica Acta* 68.7, pp. 1545–1559.

Stolper, D A, M Lawson, et al. (2014). "Formation temperatures of thermogenic and biogenic methane". In: *Science* 344.6191, pp. 1500–1503.

Stolper, D A, A M Martini, et al. (2015). "Distinguishing and understanding thermogenic and biogenic sources of methane using multiply substituted isotopologues". In: *Geochimica et Cosmochimica Acta* 161, pp. 219–247.

Stolper, D A, A L Sessions, et al. (2014). "Combined 13C-D and D-D clumping in methane: Methods and preliminary results". In: *Geochimica et Cosmochimica Acta* 126, pp. 169–191.

Tien, Ming and T Kent Kirk (1988). "Lignin peroxidase of Phanerochaete chrysosporium". In: *Methods in Enzymology* 161, pp. 238–249.

Vanholme, R et al. (2010). "Lignin Biosynthesis and Structure". In: *Plant Physiology* 153.3, pp. 895–905.

Yeung, Laurence Y, Jeanine L Ash, and Edward D Young (2015). "Biological signatures in clumped isotopes of O2". In: *Science* 348.6233, pp. 431–434.

Yeung, Laurence Y, Edward D Young, and Edwin A Schauble (2012). "Measurements of 18O 18O and 17O 18O in the atmosphere and the role of isotope-exchange reactions". In: *Journal of Geophysical Research* 117.18.

Zeisel, S (1885). "Über ein Verfahren zum quantitativen Nachweise von Methoxyl". In: *Monatshefte für Chemie* 6.1, pp. 989–997.

Chapter 6

THE THERMAL AND BIO-DEGRATION OF METHOXYL GROUPS IN COALS: IMPLICATIONS FOR ISOTOPIC HETEROGENEITY OF COMPLEX ORGANIC COMPOUNDS AND THE SUPPORT OF THE DEEP BIOSPHERE

6.1 Introduction

It is well-established that sediments rich in insoluble organic carbon compounds (i.e., kerogen) give a unique advantage to microbial assemblages in the deep biosphere (Head et al., 2003; Inagaki et al., 2015). Less clear is the makeup of these microbial assemblages, the key substrates supporting them, and the critical metabolisms involved. Are all kerogens similarly useful to microorganisms in extreme environments? Which functional groups regulate a community's activity? What happens when these are depleted? Understanding the relationships between deep-biosphere microbes and their organic carbon-rich energy sources has typically been challenging because of a variety of analytical roadblocks. These substrates are heterogeneous, insoluble organic polymers that are largely inscrutable to characterization by conventional isotopic and chemical techniques. The microbes utilizing them have extremely slow turnover rates, and require study using cutting-edge contamination procedures, lengthy (often multi-year) isotope-labeled incubations, and resource-intensive, cell-specific activity measurements (e.g., Trembath-Reichert et al., 2017).

Because most microbial metabolisms preferentially select for compounds that are both easily degradable and depleted in carbon-13, the biodegradation of liquid hydrocarbons in unsterilized oil reservoirs leaves fractionated residues that are enriched in δ^{13}C and disproportionately composed of more recalcitrant compounds (Stahl, 1977; Clayton, 1991; Clayton and Bjorøy, 1994; Head et al., 2003). Applying such strategies to type-III kerogens and coals, which are an increasingly important resource for natural gas in an evolving global energy landscape, has been hindered by analytical impedances that prevent the measurement of any isotopic properties other than bulk isotope compositions. As such, there currently exists an apparent contradiction in our understanding of the chemical and isotopic evolution of these materials: The total carbon isotope compositions of humic kerogens and their pre-

cursor polymers are largely invariant through maturation until the highest grades of metamorphism (> 400 °C) (Hoefs and Frey, 1976; Redding et al., 1980; Whiticar, 1996; Meyers and Simoneit, 1999; Kotarba and Lewan, 2004). In fact, the apparent invariance of coal δ^{13}C has been repeatedly used to fingerprint and map related coal deposits independent of thermal maturity (Meyers, 1994; Whiticar, 1996). On the other hand, the earliest stages of coalification are accompanied by dramatic changes in chemistry and structure. Over the transition from lignin to lignite, the loss of water and O-bearing moieties lead to substantial drops in the porosity, reactivity, and total O/C ratio of these materials (Tissot and Welte, 1974; Redding et al., 1980). At a molecular level, qualitative ^{13}C-NMR studies have documented the loss of key functional groups through dehydroxylation, ether cleavage, and demethoxylation reactions (Hatcher and Clifford, 1997).

Although the role of microbial degradation in these transformations remains uncertain, the ability of anaerobic subsurface microorganisms to utilize such substrates is undeniable; cooperative assemblages of fermentative and methanogenic microorganisms can remove key functional groups and reduce insoluble humic acids into metabolic intermediates which can be utilized as non-competitive substrates for microbial methanogenesis (Strapoc et al., 2011). Such assemblages can apparently produce major, commercially-significant quantities of methane from shallow coal beds and other organic-rich units too immature to be generating this gas by thermal processes alone (Martini et al., 2003; Flores et al., 2008; Strapoc et al., 2011). Importantly, this microbial methane is lower—often much lower—in δ^{13}C than the coals from which it is sourced (Whiticar, 1986). In order to conserve isotope mass balance, this incompatibility between carbon sources that appear invariant in carbon-13 content (δ^{13}C ≈ –28 ‰ vs. VPDB) and the ongoing production of methane that is substantially more depleted (δ^{13}C ≈ –60 to –40 ‰ vs. VPDB) must be resolved in one of two ways: either 1) the initial removal of carbon atoms from the coal matrix does not fractionate carbon isotopes, and isotopically light methane is generated either from a pool of intermediate metabolites that becomes progressively enriched in δ^{13}C, or in conjunction with a cryptic second carbon product that is enriched in δ^{13}C but never sampled (e.g., product CO_2 with δ^{13}C ≈ –20 to 0 ‰ vs. VPDB); or, 2) early, isotopically light microbial methane preferentially utilizes and fractionates a subset of carbon sites in low-grade coals, but these ^{13}C-enriched residues are diluted by unfractionated carbon sites and occluded to bulk isotope probing.

The resolution of this contradiction has key implications for the process by which

microbial methane is produced in coal beds, and the capacities of low-grade, organic-rich substrates to generate methane and support active deep biosphere populations. If hypothesis 1) predominates, then a major, cryptic pool of enriched carbon is missing from current models of the subsurface carbon cycle. If hypothesis 2) is more accurate, then the capacity of these substrates to generate methane at low thermal maturities and support microbial life will be substantially smaller than the total carbon contents of these materials. In essence, if not all carbon sites are equally accessible to microbes, then heavily biodegraded type-III coals will be effectively closed to further microbial methanogenesis without perceptibly altering other intrinsic properties of the materials. The methane-producing capacity of low-grade coals and shales has been investigated previously using laboratory-based artificial maturation experiments at elevated temperatures. However such techniques cannot replicate environmental conditions due to omitting the effects of microbial degradation, and the products of such experiments are notoriously poorly representative of those found in natural settings (Lewan, 1985; Kotarba and Lewan, 2004).

Here, we present the first site-specific carbon isotope measurements of methoxyl ($R--O--CH_3$) groups from an array of humic materials spanning the transition from extant lignin to sub-bituminous coal. We observe the loss of methoxyl groups with increasing maturation and biodegradation. This loss imparts a normal kinetic isotope effect that generates residual pools of methoxyl carbon that are among the heaviest in $\delta^{13}C$ ever measured in biotic organic carbon. Using these and related measurements, we explore the role of microbial degradation in the loss of these moieties, and discuss implications for the existence of a global pool of readily-releasable methane precursors in low-grade humic deposits.

6.2 Background

The delivery and degradation of methoxyl groups to subsurface environments

Methoxyl groups, affixed to ether-linked aromatic acids such as vanillic acid and syrngic acid, are commonly 10–20% by weight of the biopolymers lignin and pectin, and thus are ubiquitous components of the woody and leafy tissue of higher plants (Benner et al., 1987). Although pectin, along with other major vascular plant components (cellulose and hemicellulose), is readily degraded, lignin is highly recalcitrant and can be preserved with minimal alteration by rapid burial in anoxic environments (Hatcher et al., 1981; Schink and Zeikus, 1982; Benner et al., 1987; Hatcher and Clifford, 1997). For example, the peatification process is notable for its selective removal of major plant components while leaving the lignin structure

essentially intact (Hatcher and Clifford, 1997). As a result, lignin contents in anoxic plant litter are enriched to up to ~80% of dry weight after as little as a decade (Benner et al., 1987), constituting a sizeable flux of methoxyl groups to the subsurface environment. Following peatification, ^{13}C-NMR studies detect the progressive loss of methoxyl groups during the early stages of coalithification from peat to subbituminous coal (Hatcher et al., 1982; Hatcher and Clifford, 1997). However, since this technique is non-quantitative and insensitive to isotopic enrichments, it remains an open question whether microbial mediation is required for the loss of methoxyl groups at these low-temperatures, or simply coincident with it.

It is clear, however, that methoxyl groups are an attractive substrate for microbial growth. Fermentative bacteria can anaerobically cleave methoxyl groups from insoluble humic acids and convert them to methanol (Donnelly and Dagley, 1980), an intermediate metabolite that is of particular interest as a non-competitive substrate for methanogenesis. Indeed, there is mounting evidence that this pathway (methylotrophic methanogenesis) may fluorish in extreme environments (e.g., hypersaline ocean sediments: Zhuang et al., 2016; subsurface coal beds: Guo et al., 2012). Moreover, it has recently been demonstrated that some archaea can generate methane directly from methoxylated coal and coal-like monomers (Mayumi et al., 2016). Given the challenge of distinguishing methylotrophic methanogenesis from aceticlastic based on the isotopic composition of the product methane alone (Whiticar, 1999), and the relative prevalence of such non-competitive substrates in the environment (Summons et al., 1998), the role of this pathway in the global methane budget may be underappreciated (Penger et al., 2012; Welte, 2016).

Sample descriptions and origins

To observe the role of microbial degradation along the early maturation path of Type-III kerogens, we analyzed samples of varying degrees of biodegradation that span a range of thermal maturities from pristine wood to high-volatile bituminous coal. The origin and history of these materials are described briefly below:

Undegraded woods and lignin: Gram-sized quantities of powdered poplar and bamboo were obtained from the USC Stable Isotope Laboratory, where both materials serve as secondary standards for the determination of δ^2H values of methoxyl groups. The bamboo was milled and homogenized from a batch of chopsticks obtained from USC Dining Services. The poplar is of unknown origin. A pure lignin powder (Sigma Aldrich) was obtained from this lab as well. Two additional

milled wood powders, from tinea and beech trees, were obtained from the Analytical Biogeochemsitry Laboratory and the University of Heidelberg.

Polish brown coals/lignites: Two low-grade brown coals were obtained from the Belchatow coal deposit, Poland (Drobniak and Mastalerz, 2006). The coals were deposited in a freshwater environment and rapidly buried in a band of tectonic grabens 40 km long and ~1.5 km wide in the late Miocene (Drobniak and Mastalerz). Reflectances of different macerals vary systematically within samples, but a narrow range of ulminite-B reflectances of 0.26 to 0.29 % categorizes these samples as low-maturity lignites (Drobniak and Mastalerz).

Shimokita lignites/sub-bituminous coals: Six lignites and sub-bituminous coals were retrieved from 1.9–2.0 km below the sea floor ~50 km off the coast of the Shimokita peninsula, Japan (Gross et al., 2015). These 1–7 m thick coal horizons were deposited in a coastal, black marsh in the early/middle Miocene, and then buried to their current depth by slow subsidence in a forearc basin of the NE Japan Arc through the rest of the Cenozoic (Gross et al., 2015). These materials were retrieved from IODP site C0020 as part of IODP Expedition 337, the first cruise dedicated to the exploring the in situ microbial activity of the deep biosphere (Inagaki et al., 2016). In addition to observing active methanogenesis in these coal beds in equilibrium with the current ambient temperatures, 16S rRNA sequencing revealed microbial assemblages in these coal beds that are distinct from overlying shallow marine communities and more closely resemble those found in coastal marshes, suggesting that the current microbial assemblages are indigenous descendants of the primary microbial community entombed at the time of deposition, and that these assemblages have been degrading these coals in a closed system for the intervening ~20 Myrs (Inagaki et al., 2015). Recent incubations of these coals on environmentally-representative substrates suggest that fermentative bacteria, not methanogenic archaea, dominate these assemblages, and are most active on methoxyl-like substrates such as trimethylamine and dimethylsulfide (Trembath-Reichert et al., 2017). Mean random ulminite reflectances of these coals are 0.37 to 0.43 %, and generally correlate with depth (Gross et al., 2015).

Powder River sub-bituminous coals: Two sub-bituminous coals from the Powder River Basin, WY, were also considered. Although vitrinite reflectance suggests that these coals are only marginally more thermally mature than the Shimokita coals (vitrinite Rr of 0.45–0.47 %), they have experienced a more complex geologic history over a longer period of time (Formolo et al., 2008). The Fort Union member

sourcing these materials was deposited in a freshwater, fluvial environment in the Paleocene, after which the unit was buried under erosional basin fill due to uplifts of the surrounding ranges associated with the Laramide Orogeny (Flores, 1986; Flores et al., 2008). The unit reached at most 100 °C in the Miocene, after which continued uplift and erosion exposed the flanks of the basin to fresh infiltrations of nutrient-rich groundwaters, which continued until recent times (Flores et al., 2008). This marginal groundwater incursion may have been exacerbated by the natural combustion of exposed coal beds, forming clinker that enhanced permeability and the delivery of key nutrients (e.g., organic acids, SO_4) to shallow subsurface coal beds along the flanks of the basin (Flores et al., 2008). This incursion stimulated a surge of secondary methanogenic activity along the basin rim, diluting 'old' methane, generated largely through hydrogenotrophic methanogenesis during the initial maturation phase, by the addition of 'new' methane, which bulk isotopic evidence suggests was produced by the methyltrophic pathway (Flores et al., 2008). This complex, spatially-varying history is also recorded in the scattered, contradictory biomarker biodegradation indices throughout the basin: exhaustive characterization of soluble organic components in the Powder River Basin suggests that local geology and hydrology (i.e., permeability, recurring freshwater input) control the degree of biodegradation and methane production in any given site, not burial depth or vitrinite-based thermal maturity (Formolo et al., 2008). Here, we consider samples from both endmembers: a sub-bituminous coal cored from the center of the basin where little secondary fluid is through to have reached, and a less mature, more biodegraded sample from the northwestern basin margin with ample evidence for secondary microbial stimulation by shallow subsurface freshwater incursions (Formolo et al., 2008).

High-volatile bituminous coals from the Midwestern US: In addition to the above low-grade coals, we analyzed methoxyl contents from 6 more mature, high-volatile bituminous coals from the San Juan and Michigan basins (vitrinite reflectances of 0.51–0.82 %). These more mature coals did not contain sufficient methoxyl groups to determine δ^{13}C values with high confidence. Moreover, the concentrations of iodomethane generated from these materials were not significantly larger than those produced when an overmature, methoxyl-free anthracite 'blank' was submitted to our extraction procedure. Because these materials did not contain concentrations of methoxyl groups above blank levels, we do not consider them further, other than to highlight that this observation is consistent with previous ^{13}C-NMR based studies of methoxyl loss during coalification, which suggest that no detectable methoxyl groups remain following the transition from sub-bituminous coal to high-volatile

bituminous coal (Hatcher et al., 1983; Hatcher and Clifford, 1997).

Living tree and grass tissues: Recalcitrant woody tissue is thought to be the primary source material for coal and humic kerogens. Nonetheless, we sampled other tissues from living plants to observe the variation in methoxyl content and composition that exists in a single ecosystem, or even a single organism. From the branch of a Jacaranda tree (Jacaranda mimosifolia) at Caltech, we sampled leaflets, petioles anchoring these leaflets, and the stem running along the entire compound leaf (Fig. 6.8). The woody branch was cross-sectioned, and three separate tissues were sampled: the green bark containing the phloem, the primary wood making up the bulk of the branch, and the secondary xylem running along the core (Fig. 6.7). We also sampled blades of two different grasses growing at the base of the Jacaranda tree. Living plant tissues were sectioned with a razor blade, ground by mortar and pestle under liquid N_2, and acidified by the below procedure within three hours after sampling them.

Santa Barbara basin sediment: Lignin-rich woody tissue is believed to be the primary source of methoxyl groups to degrading organic matter. So, marine organic-rich deposits, which are fed by marine organisms depleted in lignin, should be devoid of methoxyl groups. To test this, we attempted our extraction procedure with organic-rich sediments from the Santa Barbara basin, off the California coast. Here, high productivity in the surface ocean has left the benthic zone anoxic, leading to high preservation rates of organic matter. Frozen sediment from the top 10 cm of a core provided by A.P. Phillips were directly measured, wet, using the procedure outlined below.

6.3 Methods

Complementary procedures for extraction, purification, and measurement of methoxyl groups in degraded materials

We used two separate extraction and analysis procedures two measure, and replicate, the $\delta^{13}C$ values of natural woods, lignins, and coals. Each procedure has its benefits and drawbacks. The first uses a large-format reflux condenser to continuously capture evolved CH_3I, multiple cryogenic steps on a glass vacuum line to purify it, and offline sealed-tube combustions to oxidize CH_3I to CO_2 for analysis by dual-inlet IRMS. Because this approach extracts all generated CH_3I and quantifies by manometry, it has the advantage of generating accurate measurements of the amount of CH_3I evolved from a material. However, because further purification

of CH_3I from other compounds (e.g., CO_2, acetone) is performed 'blind' with cryogenic distillations, it is vulnerable to contamination, as other gases of similar vapor pressures could remain in the gas mixture and also be combusted to CO_2. Once combusted to CO_2, any contaminants are indistinguishable from CH_3I, and the resulting $\delta^{13}C$ will be a modal mixture of the $\delta^{13}C$ of all components.

To verify the purity of these extractions, we developed a separate procedure for CH_3I production and online purification and measurement by compound-specific GC-combustion-IRMS. Because this GC method temporally isolates CH_3I from other reaction products, resulting $\delta^{13}C_{CH3I}$ values are more robust. However since only a small fraction of CH_3I is analyzed, true quantitation of methoxyl abundance is challenging. Thus, by combining the strengths of both methods, we can obtain reliable, accurate measurements of both methoxyl abundance and carbon isotope composition in a wide variety of materials with a thousandfold range in methoxyl concentration. Both procedures are described in turn below.

In order to perform the Zeisel reaction, which converts ether and ester-bound methyl groups to iodomethane (CH3I) in hydriodic (HI) acid (Zeisel, 1885), with a setup that can accommodate larger samples, we constructed a gas-tight reflux/condensation reactor inspired by the experimental setup originally used for the determination of methoxyl $\delta^{13}C$ in vanillin (Krueger and Krueger, 1983). This apparatus is described in greater detail in Chapter 5. Prior to extraction, all starting materials were crushed to < 300 μm grain size using a manual steel ball mill, followed by a 'chipmunk' jaw crusher. For each extraction, 2 to 20 mL of cold (–4 °C) 57% HI acid (Sigma Aldrich) were added to the reaction vessel, followed by 45 mg to 9.4 g of sample material through the side-port. Immediately following the addition of the sample, the side-port was sealed, and the entire system was purged with 80–100 SCCM of N_2 through the bleed-out capillary for 5 minutes. Following this purge, the N_2 flow rate was reduced to 30–80 mL/min and maintained in this range for the duration of the extraction. The glass triple U trap was then immersed in either liquid N_2 (–196 °C, capturing both CH_3I and CO_2) or a slush of n-pentane and liquid N_2 (–131 °C, which retains CH_3I but not CO_2). Once the triple U trap was cooled to the target temperature, the HI acid was heated to reflux (130 °C) using a hemispherical resistance heating mantle powered by a Variac® transformer set at 60–80 V.

The CH_3I reaction was run for 120 minutes. Preliminary tests where methoxyl groups were re-extracted from coal residues that had already undergone this reaction demonstrated that no detectable quantities of CH_3I are released after this time.

Further tests using known quantities of the monomers methanol, vanillin, syringin, and guiacol were also used to verify the yield of the reaction. In all cases, yields exceeded 90%. Captured CH_3I was concentrated and purified from similarly-volatile products on a greaseless vacuum line using a series of cryogenic separations: first, residual N_2 was evacuated by gradually exposing the U-trap to high vacuum, while still immersed in liquid N_2, over the course of 30 minutes. Next, the gas mixture was passed across a vacuum trap immersed in an ethanol + CO_2 slush (–77 °C), which retains water and residual HI, while permitting the passage of CH_3I at a low vapor pressure (~100 Pa) for 20 minutes. To separate CO_2, the mixture was frozen in liquid N_2, then thawed in an n-pentane + liquid N_2 slush to gradually sublimate CO_2 but leave CH_3I condensed. Five cycles, each 15 minutes, of this sublimation procedure were conducted to completely remove CO_2 while retaining all CH_3I. Once purified, 10 to 100 μmoles of CH_3I were sealed in a quartz break-seal with 40 to 200 mg of cupric oxide and 40 mg of silver foil for combustion. Prior to this step, these oxidized and reduced metal substrates were relieved of all contaminants by flame-heating these materials with a natural gas torch under high vacuum for at least 5 minutes.

Quartz tubes were combusted at 780 °C for 2 to 10 hours to quantitatively convert the carbon in CH_3I to CO_2 by the reaction:

$$2\,CH_3I + 2\,Ag + 7\,CuO \rightarrow 2\,CO_2 + 2\,AgI + 3\,H_2O + 7\,Cu. \qquad (6.1)$$

Although similar combustions are typically performed at 1000°C, we note that at such higher temperatures, silver foil melts and adheres to the walls of the tube, which can cause the ampoule to fracture with cooling and thermal contraction. Product CO_2 was separated from H_2O using standard cryogenic procedures on a vacuum line, and sealed into a new, clean Pyrex® break-seal. $\delta^{13}C$ and $\delta^{18}O$ values of CO_2 were measured on a Thermo Delta V or MAT 253 IRMS in dual-inlet mode, by comparing against an Oztech® reference CO_2 tank of known isotopic composition. We note that $\delta^{18}O$ values of these gases vary by 10 ‰, with no obvious correlation with $\delta^{13}C$ or methoxyl content. The cause of this variation is still unknown, but may be due to 1) variation in Ag:CuO ratio, if the silver foil is itself partially oxidized with O of a different isotopic composition; 2) slight amounts of N_2O, generated by the incomplete reduction of N-bearing organic compounds, because major N_2O isobars exist at 44, 45, and 46 Da ($^{14}N^{16}_2O$, $^{15}N^{14}N^{16}O$, and $^{14}N^{18}_2O$, respectively); or 3) variation in time heating CuO on the vacuum line (an inherently reducing

environment), inducing the loss of O_2 with an isotopic fractionation in the residual CuO.

The accuracy of $\delta^{13}C$ values determined by this complete extraction, combustion, and measurement procedure was verified by comparing results for an anhydrous methanol standard subjected to the treatment with direct combustion of the same material by conventional seal-tube combustion. Because all carbon atoms in methanol are bound as methoxyl groups, such a test elucidates any fractionations induced by the full procedure of CH_3I conversion, extraction, purification, combustion, and analysis. It does not, however, test for the ability to resolve other contaminants produced during the reaction of HI acid with more complex materials.

To additionally verify the purity of our analytes, separate aliquots of each sample, and a few additional coals and woods, were measured using a 'one-pot' CH_3I production procedure coupled to headspace injection into a GC-combustion-IRMS interface. This procedure is largely similar to the GC-vial method employed by previous workers (c.f., Greuele et al., 2007), but with a few key improvements to enable the accurate determination of methoxyl $\delta^{13}C$ values in degraded materials with low methoxyl concentrations. Briefly, 2–1200 mg of material were loaded into 12 ml borosilicate Labco Exetainer® vials with heat-resistant screw-caps and gas-tight chlorobutyl septa. These were sealed and purged with helium for 5 mins. Next, 0.5–4 mL of 57% Hydriodic acid were added to cover by syringe injection. The CH_3I reaction was conducted by immersing the lower half of the vials (to cover) in a silicone oil bath held at 130 °C with a heating plate. The reaction proceeded for 2 hours to ensure complete conversion of methoxyl groups to iodomethane. Samples were cooled to room temperature and allowed to equilibrate for at least 30 mins prior to analysis.

On-line determination of methoxyl $\delta^{13}C$ was performed on a Thermo GC-combustion-IRMS interface with the following methods. For each analysis, 25–250 μL of vial headspace were sampled, after flushing the plunger >10x, with a Hamilton Gastight® locking syringe and manually injected into a Finnigan TraceGC Ultra with an inlet chamber held at 120 °C in a He split flow of 10 mL/min (7:1 split ratio). CH_3I and other compounds were separated on a DB-5 column with a He carrier flow of 1.4 mL/min. The GC was held at 30 °C for 15 minutes to separate all volatile gases, then ramped at 20 °C/min to 120 °C to elute less volatile compounds and preclude memory effects. To further combat memory effects, the syringe was cleaned by repeatedly purging the needle and chamber after each injection in a 400 mL flow-

through vessel of pure He that was refilled daily. Eluted compounds were converted to CO_2 in a CuO oxidation furnace at 1000 °C, dried on a Naflon column, and analyzed for $\delta^{13}C$ and $\delta^{18}O$ on a Delta V IRMS in continuous-flow mode. MS drift was corrected for by measuring reference tank CO_2 at the beginning and end of every GC run. Accuracy of the complete GC-combustion-IRMS procedure was verified by analyzing the headspace from a 400 mL gas-tight vessel containing a mixture of CO_2, methanol, CH_3I, and toluene standards daily. The $\delta^{13}C$ of each compound of this standard mixture was independently determined by sealed-tube combustion + dual-inlet IRMS, as above. Measured $\delta^{13}C$ of standard compounds were never more than 1‰ discrepant from their accepted values, so daily $\delta^{13}C$ corrections were not applied. To improve precision, multiple headspace extractions from individual sample vials were performed, up to 5 times. Successfully resampling and analyzing the same vial 10 days after initially piercing the septa demonstrated that 1) CH_3I is stable over day-to-week timescales while remaining in contact with residual HI acid and 2) any leakage of the vial that occurs during this time is minor and apparently does not fractionate isotopologues of CH_3I. Because no nonlinearities in CH_3I $\delta^{13}C$ were observed for peaks with total areas between 1 and 120 Vs, no linearity corrections were applied.

Site-specific carbon isotope measurements were complemented by determinations of bulk C contents and $\delta^{13}C$ values by Costech Elemental Combustion System + Thermo Delta IRMS. Standard procedures for sample preparation, combustion, and analysis were followed for these bulk measurements.

Artificial maturation experiments

In order to directly observe a carbon isotope effect associated with methoxyl group loss and make prediction about the rate of thermal loss in natural systems, we also subjected our poplar standard described above to artificial maturation experiments. Specifically, 298.1 to 416.0 mg of ground poplar were packed into a 3/8" Pyrex® tube and sealed on one end. The apparatus was evacuated on a vacuum line across a single-use Pyrex® U-trap immersed in an Ethanol–CO_2 ice slush in order to prevent volatile reaction products (e.g., water, saccharides) from contaminating the line. Once evacuated, the tube was heated in a copper block at 280–300 °C for 10–30 hours. Removal of volatile components by condensation and high-vacuum persisted for the duration of the experiments. Within the first few hours, water evaporated and cellulose depolymerized, volatized, and caramelized, coating the upper portions of the tube with a golden-brown residue. At the end of the experiments, the tube was

opened and charred lignin was quantitatively recovered. The remaining methoxyl content and $\delta^{13}C$ values from these maturation experiments were determined by subjecting these chars to the same procedure described above.

Cross-calibration of methoxyl $\delta^{13}C$ methods

To report $\delta^{13}C$ and methoxyl contents that are robust and contaminant free, it is first necessary to validate that methoxyl $\delta^{13}C$ values can be replicated by both techniques. For half of all samples, the methoxyl $\delta^{13}C$ values from each method agree within 3‰ (Fig. 6.6). For the other half, large discrepancies of up to 25 ‰, exist (Fig. 6.6). These large discrepancies occur in samples depleted in methoxyl content, where the small relative amounts of product CH_3I are vulnerable to contamination by other compounds. Because these samples also tend to be most strongly enriched in methoxyl $\delta^{13}C$ (see below), small amounts of contamination by compounds with typical organic $\delta^{13}C$ values can drastically shift the $\delta^{13}C$ of the mixture. We observed this effect using aliquots of gas purified by the reflux procedure and analyzing them by GC-MS and GC-IRMS (Table 6.2, 6.4). Headspace injections of purified gases from Powder River Basin coals, ostensibly all CH_3I, instead contained subequal amounts of CO_2, acetone, and CH_3I. CO_2 is a major byproduct of the HI acid reaction and challenging to completely strip from CH_3I (see Chapter 5). Acetone is the solvent used to clean the reflux reactor between runs, and difficult to completely remove without long bakes at elevated temperatures. Both of these contaminants have 'typical' organic carbon $\delta^{13}C$ values (–22 to –30‰ vs. VPDB), while the residual CH_3I from these impure samples has anomalous, enriched values that are in far better agreement with the data obtained by compound-specific GC-IRMS. Because of this demonstrable susceptibility of sealed-tube combustion methods to contamination, only methoxyl $\delta^{13}C$ data from compound-specific online separations are discussed below.

Despite this, the reflux reactions are still useful. For samples where methoxyl $\delta^{13}C$ from both methods do agree, suggesting that neither sample is contaminated by other compounds, the peak areas from GC-IRMS runs can be compared to manometer readings from reflux reactions to directly calibrate yields from the gas bench vial runs to true methoxyl concentrations (Fig. 6.5). Specifically, normalized peak areas (Peak area/injection size/sample amount) are strongly correlated with normalized methoxyl content (wt. % methoxyl*TOC), so a calibration line can be used to correct any gas bench vial run during this session to true methoxyl content, as long as the total carbon content of the material is known. These derived methoxyl contents

Sample_Name	N	R0	TOC%	Type	Wt. % methoxyl	δ^{13}C	δ^{13}C (1σ s.e.)
HU-1_Tinea	2	0.2	50	wood	15.0	-22.80	0.17
HU-1_beech	1	0.2	50	wood	16.7	-26.38	0.50
USC_bamboo	1	0.2	54	wood	20.7	-27.67	0.50
USC_poplar	5	0.2	53	wood	19.3	-27.27	0.04
SBB_BC1_0-10cm	2			SBB_seds	0.017	-10.57	0.09
PRB_S352	3	0.47	57.84	PRB_coal	0.013	13.21	0.14
PRB_S939	1	0.45	58	PRB_coal	0.007	5.26	0.50
PL-11/384	2	0.28	60	polish brown coal	9.8	-12.45	0.01
PL-4/384	2	0.27	64	polish brown coal	11.1	-18.26	0.04
USC_lignin	2	0.2	55	lignin	36.3	-20.59	0.01
15R2	1	0.38	45	IODP-337_coal	0.172	7.21	0.50
15R3	2	0.38	61	IODP-337_coal	0.047	14.56	0.21
15R7	3	0.38	57	IODP-337_coal	0.017	13.42	1.46
18R2	3	0.37	46	IODP-337_coal	0.285	23.22	0.19
22R5	5	0.43	26	IODP-337_coal	0.057	28.34	0.25
25R	2	0.43	45	IODP-337_coal	0.755	18.83	0.02
Jac_green_bark	2			CIT_tree	0.963	-59.08	0.01
Jac_leaves	2			CIT_tree	0.855	-70.08	0.05
Jac_outer_wood	1			CIT_tree	0.797	-32.10	0.50
Jac_petiole	2			CIT_tree	2.2	-48.31	0.25
Jac_stem	1			CIT_tree	4.2	-36.62	0.50
Jac_xylem_wood	2			CIT_tree	6.8	-32.00	0.09
CIT_grass_A	1			CIT_grass	0.445	-60.93	0.50
CIT_grass_B	2			CIT_grass	0.271	-52.97	0.05

Table 6.1: Thermal maturities, methoxyl concentrations, and methoxyl δ^{13}C values, determined using the Gas Bench bottle reaction + GC-combustion-IRMS method.

are reported for all samples below. With this calibration line, is also possible to relate the disagreements between methoxyl contents and methoxyl δ^{13}C generated by each procedure (Fig. 6.6). It is apparent that samples with the largest relative discrepancies in apparent methoxyl content also have the largest discrepancies in methoxyl δ^{13}C, further implicating a role of contamination in the problematic δ^{13}C data derived from sealed-tube combustions.

6.4 Results

Bulk chemical and isotope compositions

Bulk carbon contents of all woods, lignites, and sub-bituminous coals are largely restricted to a narrow range of 45 to 64 wt. % (Table 6.1). The only exception is a Shimokita sub-bituminous coal with (apparently) significant siliciclastic input. Bulk δ^{13}C values are similarly uniform (Table 6.5); most humic coals have $\delta^{13}C_{VPDB}$ values $\approx$ –25 ‰, with slightly more depleted values in some undegraded woods ($\sim$–27 ‰), and slightly enriched in the Polish lignites (–23 to – 21 ‰). Such carbon-13 contents are typical for organic-rich deposits derived from Cenozoic C3-photosynthesizing terrestrial plant matter. There are no significant correlations

Sample_Name	N	R0	TOC%	Type	δ^{13}C	δ^{13}C ($1\sigma s.e.$)
DM-P-2	3			DM	-11.98	0.02
PRB_S352	3	0.47	57.84	PRB_coal	22.63	0.13
PRB_S939	3	0.45	58	PRB_coal	4.28	0.26

Table 6.2: Iodomethane δ^{13}C values samples purified by the reflux condenser procedure but analyzed by GC-combustion-IRMS

between organic carbon content, δ^{13}C value, and vitrinite reflectance.

Methoxyl contents and isotopic compositions

Methoxyl contents dramatically decrease with increasing maturity (Table 6.1). Methoxyl groups ($O--CH_3$) make up 15–24 wt. % of the mass of lignin in undegraded bamboo, poplar, tinea, and beech. Methoxyl contents are even larger in the purified lignin standard, but because the source of this lignin is unknown, its content is not interpreted further. In the Polish lignites, total methoxyl concentrations are 10–11 wt. %. Substantially lower concentrations are observed in shallowest sub-bituminous coals from the Shimotika peninsula: 0.017–0.29 wt. %. The lowest concentrations that can be confidently observed at least 20 times the size of the methoxyl blank are in the deeper Shimokita coals and those from the Powder River basin, at 0.007 to 0.06 wt. %.

Methoxyl δ^{13}C values ($\delta^{13}C_{methoxyl}$) of undegraded woods are similar to or up to 3 ‰ lighter than their respective bulk δ^{13}C values. Methoxyl δ^{13}C values in all coals are heavier than their bulk compositions, in many cases dramatically so. Among the Polish lignites, $\delta^{13}C_{methoxyl}$ values are 3 to 10 ‰ higher than $\delta^{13}C_{bulk}$ (Tables 6.1, 6.5). In the Powder River basin, sub-bitiminous coal $\delta^{13}C_{methoxyl}$ values are up to 38‰ heavier. The sub-bituminous coals from the Shimokita peninsula IODP core contain both the highest $\delta^{13}C_{methoxyl}$ values and the largest amount of scatter: $\delta^{13}C_{methoxyl}$ values are +7 to +28 ‰ vs. VPDB, corresponding to isotopic enrichments in the methoxyl site of 32 to 53 ‰ above their bulk values.

In the Jacaranda tree, nearly 40‰ variation in methoxyl δ^{13}C is observed (Figs 6.7, 6.8, 6.9). Woody tissues have methoxyl δ^{13}C values similar to bulk δ^{13}C typical of terrestrial C3 plants. More delicate tissues (leaflets, petioles, and phloem/green bark) are extremely depleted in methoxyl δ^{13}C, to values as low as –70‰ vs. VPDB in the leaflets. With one exception, methoxyl δ^{13}C correlates with estimated methoxyl content (Fig. S6.9).

Somewhat surprisingly, significant iodomethane was also produced from the HI acid reaction with Santa Barbara basin sediment. It is in relatively low abundance, but has an unusually-enriched δ^{13}C composition ($\sim -10‰$).

sample_ID	N	R0	TOC%	Type	Wt. % methoxyl	δ^{13}C	δ^{13}C(1σs.e.)
15R3	1	0.38	61	IODP-337_coal	0.1487	20.57	0.5
15R4	1	0.38	55	IODP-337_coal	0.1416	6.73	0.5
15R7	1	0.38	57	IODP-337_coal	0.1277	-13.98	0.5
18R2	3	0.37	46	IODP-337_coal	0.1235	25.21	2.26
22R5	1	0.43	26	IODP-337_coal	0.0628	16.69	0.5
DM-P-1	1			DM	6.6977	-21.67	0.5
DM-P-2	1			DM	6.8491	-14.66	0.5
PL-11/384	1	0.28	60	polish_brown_coal	6.6842	-13.59	0.5
PL-4/384	1	0.27	64	polish_brown_coal	9.6116	-20.5	0.5
PRB_S352	1	0.47	57.84	PRB_coal	0.0435	-2.02	0.5
PRB_S939	1	0.45	58	PRB_coal	0.0403	-21.45	0.5
SWL	1	0.45	53	PRB_coal	0.0477	-11.21	0.5
USC_bamboo	1	0.2	54	wood	24.3824	-30.36	0.5
USC_poplar	1	0.2	53	wood	22.8466	-27.77	0.5

Table 6.3: Methoxyl contents and δ^{13}C values determined by offline reflux condenser reaction + sealed tube combustion/IRMS.

Poplar demethoxylation experiments

Charred materials recovered from the 10 and 30 hour 300 °C treatments experienced total mass losses of 60–80% relative to starting material weight, likely through the loss of water and saccharides from cleaved cellulose (Fig. 6.3, Table 6.5). Relative to the amount of lignin that remained, these materials were depleted in methoxyl content, and enriched in $\delta^{13}C_{methoxyl}$, relative to the composition of untreated poplar. All of these variations correlate with treatment time: that is, the 30 hour experiment experienced greater net mass loss, greater relative loss of methoxyl groups, and greater enrichment in residual methoxyl δ^{13}C than the 10 hour experiment.

Using the starting material weight for each experiment and measured methoxyl content from the undegraded poplar measurement, we can calculate a reaction progress variable, (F = relative amount of methoxyl groups remaining), for thermal demethoxylation of poplar at 300 °C. These data can be fit by a Rayleigh model, where the observed enrichment in δ^{13}C of residual methoxyl groups is induced by the one-way loss of these moieties with an instantaneous isotopic fractionation ($\epsilon_{product-residue}$) of –12.3‰ (Fig. 6.4).

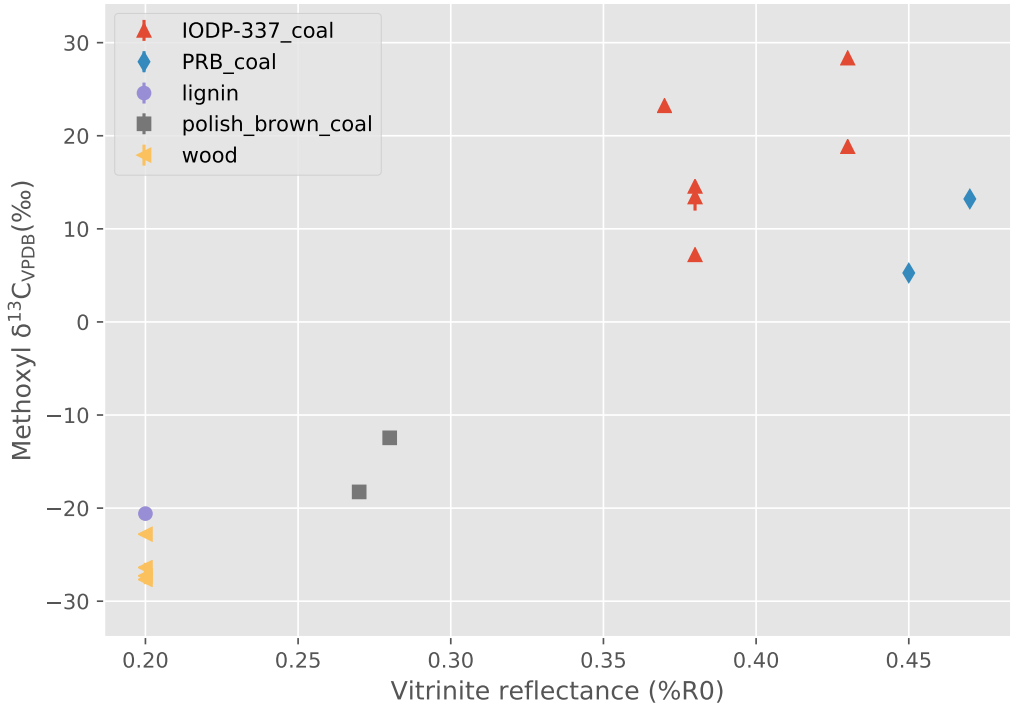

Figure 6.1: Variation in methoxyl δ^{13}C with vitrinite reflectance. Vitrinite reflectances of undegraded materials were not measured, but are assigned a nominal value of 0.2 in order to be shown here.

6.5 Discussion

In general, we observe a strong correlation between methoxyl δ^{13}C and thermal maturity (Fig. 6.1). Immature organic materials (assigned a vitrinite reflectance of 0.2 for plotting purposes) have methoxyl δ^{13}C similar to bulk organic matter of terrestrial C3 plants, while more mature materials (lignites and sub-bituminous coals, %R0 of 0.25–0.5) are dramatically enriched in this measurement (Fig. 6.1). Notably, these enrichments occur over an extremely narrow range in thermal maturity. In even marginally more mature materials (e.g., the San Juan basin high vol. bituminous coals, R0 = 0.5–0.7%), no methoxyl groups were found. However, the chemical composition and physical properties of coals continue to evolve to much higher maturities during catagenesis and metagenesis, corresponding to virtrinite reflectances well beyond 2.0% (Killops and Killops, 2005). A wide variety of maturity parameters can be used to distinguish more mature coals and kerogens. In comparison, methoxyl δ^{13}C values appear to be extremely sensitive to subtle differences in maturity over a range where few other accurate, precise proxies exist. Thus, this proxy may be extremely useful for discriminating among largely imma-

ture terrestrial organic materials, provided the mechanism by which methoxyl δ^{13}C values are enriched is understood.

A Rayleigh model for thermal methoxyl loss

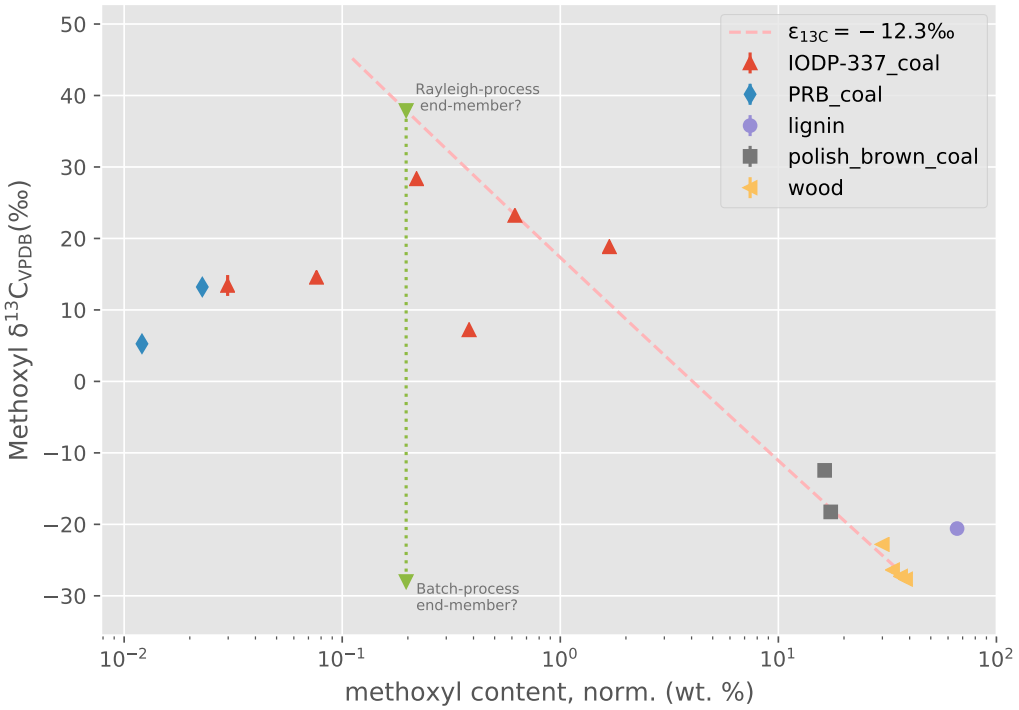

Figure 6.2: Variation in methoxyl δ^{13}C with methoxyl concentration. Dashed pink line denotes the expected trend of a Rayleigh fractionation model, given an initial composition of poplar wood and an isotope effect of $-12.3‰$. Green boxes denote hypothesized demethoxylation process endmembers, which could be mixed in single samples to explain the variance among degraded samples (see text for details).

A distillation process that isotopically enriches residual methoxyl groups is implicated by the strong relationship between methoxyl δ^{13}C and methoxyl concentration (Fig. 6.2). Relative methoxyl contents drop by nearly four orders of magnitude over the range of our dataset, and the most enriched methoxyl δ^{13}C values occur in lignites and sub-bituminous coals with the lowest methoxyl concentrations. This suggests a Raleigh-style effect, where irreversible loss that imparts a normal isotope effect leaves the residue remarkably enriched at low values of F. Specifically, for irreversible reactions in an open system that impart an isotope fractionation, the ${}^{13}R$ of the residual species will be defined by:

$$ {}^{13}R = {}^{13}R_0 \times F^{\epsilon}, \tag{6.2}$$

where $^{13}R_0$ is the initial isotope ratio of the reactant, and F is the fraction of reactant remaining. If all coal-precursors start with similar methoxyl contents and compositions, and undergo Rayleigh-style loss with the same, constant, isotope fractionation, then in the space of $\delta^{13}C_{methoxyl}$ vs. log(wt.‰ methoxyl), degraded materials will evolve along an (approximately) straight line with a slope related to the size and sign of the isotope effect (Fig. 6.2).

But what is the fractionation mechanism? And, is such a simple model even reasonable for describing the variation in methoxyl content and composition in varied materials from this global dataset? A logical first test is the isotope effect of thermal demethoxylation measured during our poplar vacuum heating experiments. Assuming a starting composition identical to poplar wood and an isotope effect of –12.3‰, thermal demethoxylation will enrich the residue along a Rayleigh line to $\delta^{13}C_{methoxyl}$ of +1‰ at when 10% of initial methoxyl groups remain, and +30.5‰ when only 1% do. In the space of $\delta^{13}C_{methoxyl}$ vs. log(wt.% methoxyl), such a vector is a decent fit to the polish brown coals, and the most ^{13}C-enriched IODP-337 coals. This suggests that methoxyl loss during thermal maturation may explain some of the enrichments that are observed (Fig. 6.2).

However, because nearly identical coal $\delta^{13}C_{methoxyl}$ values are observed over a hundred-fold range in methoxyl concentration, no single Rayleigh model can explain all these data. How then to interpret the scatter? One possibility is variation in the methoxyl isotope composition and content of starting materials. Given the natural variation in these parameters we find even within separate tissues of a single tree (Fig. 6.9), it is worth considering whether all these coals can even be projected into the same reference frame. After all, raw wt.% methoxyl contents do not monotonically decrease with increasing maturation. Lignin is rich in methoxyl groups but other, more degradable, plant compounds are not. Indeed, the loss of water, cellulose, and hemicellulose during peatification result in an apparent increase in raw methoxyl content across this transition. This effect is observed in our thermal demethoxylation experiments (Fig. 6.3), and in the invariance of raw methoxyl content between wood and the polish brown coals. To correct for this effect, we assume that pristine lignin has a constant methoxyl concentration, but that lignin content is diluted in starting materials by 50 to 80%. All materials that are not pristine plant matter are assumed to originate completely from lignin with a uniform methoxyl concentration.

It is easy to conjure up ways that this assumption could be violated in our coals. Syringyl contains two methoxyl groups per unit and guiacyl has one, so variation in

ratio of these two monomers in different lignins—a phenomenon documented within individual tissues, organisms, and especially gymnosperms vs. angiosperms (see Chapter 5)—will change the initial methoxyl content of lignin. And, of course, coals and kerogens need not be sourced entirely from lignin. At some level, other organic compounds will always survive degradation and be incorporated into kerogens. At the low-methoxyl extreme, sapropels (marine coals) should have little to no lignin in their precursor organic matter.

However, stratigraphic and palynological data suggest that all these coals are terrestrially-sourced (Drobniak et al., 2011; Gross et al., 2015; Flores et al, 2008). Their O/C and H/C ratios and locations on Van-Krevelen diagrams further confirm that type-III kerogen (lignin-derived) is the primary source of organic matter here (Drobniak et al., 2011; Gross et al., 2015; Flores et al, 2008). Since the methoxyl concentrations plotted in Fig. 6.2 are normalized to total carbon content, dilution by siliciclastic input should also not affect these data. So, while some variation in initial methoxyl content is inevitable, this is unlikely to explain the hundred-fold variation observed in methoxyl concentration at the same enriched $\delta^{13}C_{methoxyl}$ values.

These data could also be explained by 20–40‰ depletion in the initial isotope composition methoxyl groups of some coal precursors. After all, we can find such depletion between the leaves and wood of a single Jacaranda tree (Figs. 6.7, 6.8, 6.9). Such an argument is only plausible given a preservation mechanism by which leaf methoxyl groups are retained while wood methoxyl groups are lost. This is extremely unlikely. The exact source of these leaf methoxyl groups is yet unknown, however previous workers have reported similar $\delta^{13}C$ values for methanol and chloromethane emitted from both living and senescent leaves (Keppler et al., 2004). Chloromethane is too volatile to be trapped in sediments, and methanol is highly susceptible to degradation, or utilization for methanogenesis in anoxic environments. Microbial methanogenesis is implicated in both coal systems studied, so it is hard to imagine how primary methanol could persist for this long. Other potential sources of leaf methoxyl groups are pectin or methionine (technically a methyl-thiol group, but our procedure cannot discriminate between these), but these are also rapidly degraded during senescence. Critically, even if such hypothesized low-^{13}C methoxyl compounds were incorporated into these coals, their contribution to the bulk methoxyl pool would still be overwhelmed by those of lignin. Methoxyl contents are nearly 10x higher in woody tissues vs. vascular or mesophyllic ones, and there is no known environmental condition that selectively degrades lignin

while leaving simpler organic compounds intact (Fig. 6.9). So, not only are these peculiar ^{13}C-depleted methoxyl pools unlikely to persist during coalification, but they especially unlikely to do it alone, without having the initial δ^{13}C methoxyl pool overwhelmed by lignin methoxyl groups with typical (–22 to –32‰) values.

A biologic mechanism for methoxyl loss in degraded coals

Because neither variation in initial methoxyl concentration nor carbon isotope composition are likely to explain the observed scatter in Fig. 6.2, the remaining option is variation in the net isotope effect associated with methoxylation. Specifically, since the most enriched $\delta^{13}C_{methoxyl}$ values are well-described by the thermal loss of these groups, a separate mechanism is needed that is capable of reducing methoxyl content without imparting a major isotope effect on the residue. It may be initially counterintuitive that biodegradation be such a mechanism. In surface environments and laboratory cultures, microbial utilization of methoxyl groups from smaller, soluble compounds imparts an isotope effect similar to, or often much larger than, –12‰. The de-methoxylation of methyl tert-butyl ether has a normal isotope effect of 12–14‰ (Gray et al., 2002; Kuder et al., 2005). Methylotrophic methanogenesis on methanol results in residual carbon enriched by up to 60‰ (Summons et al., 1998; Whiticar, 1999). The carbon isotope effect of direct methanogenesis from methoxyl-bearing coal analogs has not been measured (Mayumi et al., 2016), but is likely to be similarly large. However, the extreme isotope enrichments of residual methoxyl groups that Rayleigh-style microbial degradation predicts would be expected if the assumptions of the Rayleigh model are met. Specifically, in the context of microbial degradation, open system-fractionation will only be observed if microbes have equal access to, and ability to discriminate among, all the methoxy groups in a volume of material. While such conditions may be met for batch cultures degrading dissolved species, they should not hold for subsurface kerogen, where insoluble carbonaceous matrices with restricted porosity could hamper the accessibility of all methoxyl sites. Moreover, deep biosphere microbes are not motile. This is both due to energy limitations—self-propelled movement is an energetically expensive process and unfeasible for organisms living on fermentative metabolisms with meager energetic outputs (c.f., Trembath-Reichert et al., 2017)—and porosity restrictions that impede transport through their 'coaly cages.' Given these limitations to mobility, it is reasonable to expect that coal-bound microbes would completely utilize the substrates physically available to them. By physically mixing areas barren of methoxyl groups with those that are undegraded, it would be possible to observe dra-

matic losses in methoxyl concentration with no apparent fractionation. Essentially, if degradation of organic subtracted by deep biosphere microbes is a closed-system process, then the isotope effect of their metabolisms will not be expressed. Mixing between these two end-members (closed-system and Rayleigh-style) could produce an array of methoxyl δ^{13}C values at similar methoxyl concentrations, or an array of methoxyl concentrations with similar δ^{13}C values. If this hypothesis is correct, then not only can these data be explained by closed-system degradation by deep biosphere microbes, but they require it. Moreover, if thermal de-methoxylation always functions as a Rayleigh-style process with a similar isotope effect, then the degree of departure from the thermal trend for coals with similar thermal histories records variations in the time-integrated activity of subsurface methoxyl-utilizing microorganisms. Unlike isotope labeling incubation studies, which measure the activity of deep biosphere microorganisms today, these measurements may be a new window into the complete history of deep biosphere activity in studied sections.

These data also make a statement on the distribution of microbes within organic-rich sections. Due to technological limitations to imaging individual cells with low-turnover rates, the spatial distribution of cells in deep biosphere is largely an open question. Are microbes organized into co-operative aggregates, analogous to the consortia of methanotrophic archaea and sulfate-reducing bacteria found in shallower marine sediments? Or, are they isolated and distributed throughout the coal matrix, so that complementary metabolisms are linked through longer diffusive pathways as opposed to nearest-neighbor transfer? If the above interpretation is correct, it requires that at some scale smaller than a single sample, methoxyl-utilizing microbes be heterogeneously distributed. In order for the non-fractionating mechanism to be expressed, there must be enclaves where methoxyl gourps are completely lost and others that are undisturbed. The relatively poor reproducibility of replicate extractions from the same coals from IODP-337 may speak to this as well. Barring cryptic contamination, the ~6 ‰ variation in methoxyl δ^{13}C from replicate aliquots of 18R2 suggests that the material is poorly homogenized (Table S2). This may be because at a scale finer than the grain size of the powdered material, microbial enclaves that have degraded these moieties are heterogeneously distributed. If so, repeating these extractions with different grain sizes could constrain the spatial scale over which microbial activity varies.

Implications for production of microbial methane from low-grade lignites

We have shown that methoxyl groups are quantitively lost from type-III kerogens and coals by the earliest bituminous grades. In order to maintain oxidative balance, regardless of the intermediate metabolism, the stable end products of cleaved $O--CH_3$ groups will be methane and CO_2, in a ratio of 3:1. Given the relatively high concentrations of methoxyl groups in immature precursors, these results suggest that major amounts of methane (on the order of 10% by weight) will be readily generated during early coalification and diagenesis. This is significant for two reasons. First, because we show that this process leaves residual methoxyl groups remarkably enriched in $\delta^{13}C$, we resolve an apparent contradiction between the isotopic evolution of methane during catagenesis, and the isotopic invariance of its source material. The $\delta^{13}C$ of early methane is 10–30 ‰ lighter than its source kerogen and evolves with continued maturation, but the total carbon isotope compositions of source kerogens do not change. Our work shows that some sites do get enriched, but that these effects are diluted by the overabundance of carbon sites that do not participate in early methane generation. We note, however, that thermal demethoxylation alone cannot generate methane with $\delta^{13}C$ values as low as –60‰; some addition fractionation in an intermediate step is required, which our technique cannot detect.

Second, although methoxyl groups are a reactive moiety for early methanogenesis and a favorable substrate for microbial metabolism, they are a finite pool that is rapidly exhausted. Thus, the capacity of lignites to generate early methane is tied to their history of thermal and bio-degradation: low-grade kerogens that have experienced extensive early subsurface biodegradation should not produce as much natural gas until higher maturities when other mechanisms are in play. Conversely, all coals will not be similarly fertile for supporting deep biosphere microbes: coals of higher maturity that have lost all methoxyl groups through thermal degradation will not support the same metabolisms as more immature strata, even when the former are exhumed to shallower depths. Our work suggests that even in single units, the principal microbial metabolisms will evolve with time, as once methoxyl groups are exhausted, other substrates (if they exist) will favor different organisms. Once such evolution is already implicated for the IODP-337 coals, where contrasting lines of evidence suggest that while methanogens once populated these coal beds, fermentative microbes, which could utilize methoxyl groups, have since taken over (Inagaki et al., 2015; Trembath-Reichert et al., 2017). Our work suggests that the dominance of these fermenters may also be waning, as once the methoxyl groups

and similar substrates are depleted, another primary energy source will need to be found.

6.6 Conclusions

Heat, time, and subsurface microbial activity modify polymeric organic matter in ways that are cryptic and hard to detect. Here we have shown that by studying the concentration and carbon isotope composition of a single site within lignin, kerogen, and coals, rich histories of thermal and biodegradation can be unraveled that are inscrutable using bulk methods alone. We argue that methoxyl groups are a significant but ephemeral source of early thermogenic methane and an attractive substrate for deep biosphere microbes. We suggest that the capacity of organic rich sediments to support microbial life will depend on the specific molecular structures it contains, and that detection of the loss of these moieties can be used to study the evolution of subsurface microbial assemblages through time.

6.7 Supplementary data

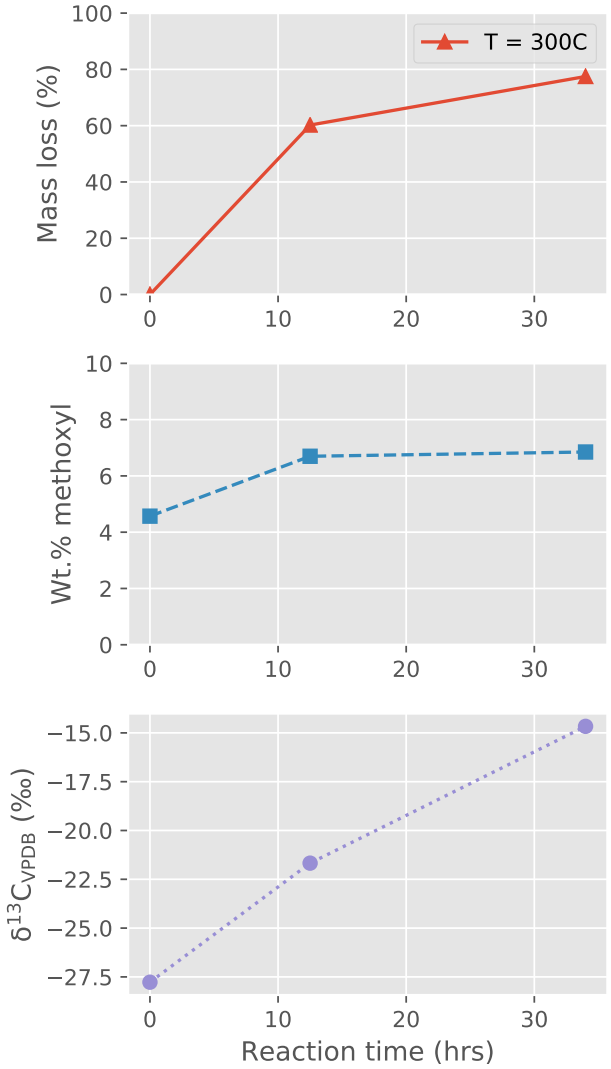

Figure 6.3: Thermal de-methoxylation experiments of poplar wood, showing the total mass loss, apparent enrichment in methoxyl groups of residues, and methoxyl δ^{13}Cvalues in these residues.

Date	Type	Sample_ID	Amount (mg)	Analysis #	Injection size (uL)	CO_2 area (Vs)	δ^{13}C (‰)	δ^{18}O (‰)
10/19/17	wood	1_USC_Poplar	9.2	16600	50	9.506	-27.195	-54.924
10/18/17	wood	1_USC_Poplar	9.2	16596	100	19.961	-27.392	-54.911
10/20/17	wood	1_USC_Poplar	9.2	16614	250	47.145	-27.311	-57.123
10/28/17	wood	1_USC_Poplar	9.2	16675	250	46.072	-27.226	-44.41
10/19/17	wood	10_USC_Poplar	9.8	16611	250	59.459	-27.226	-56.31
10/20/17	IODP-337_coal	16_18R2	343	16623	25	2.397	23.495	-54.816

Table 6.4 continued from previous page

Date	Type	Sample_ID	Amount (mg)	Analysis #	Injection size (uL)	CO_2 area (Vs)	$\delta^{13}C$ (‰)	$\delta^{18}O$ (‰)
10/20/17	IODP-337_coal	16_18R2	343	16624	250	19.912	23.31	-54.667
10/20/17	IODP-337_coal	16_18R2	343	16622	250	30.545	22.844	-54.917
10/22/17	IODP-337_coal	17_15R7	1168	16634	250	3.579	15.19	-52.446
10/22/17	IODP-337_coal	17_15R7	1168	16632	250	4.511	14.548	-53.076
10/21/17	IODP-337_coal	17_15R7	1168	16629	250	6.176	10.515	-52.534
10/23/17	PRB_coal	19 FortUnion S352	1132	16640	250	3.837	12.957	-49.633
10/23/17	PRB_coal	19 FortUnion S352	1132	16643	250	3.375	13.227	-50.405
10/23/17	PRB_coal	19 FortUnion S352	1132	16642	250	3.441	13.443	-52.116
10/23/17	polish brown coal	22 PL-4/384	146.7	16649	25	48.876	-18.223	-56.975
10/23/17	polish brown coal	22 PL-4/384	146.7	16650	25	40.837	-18.306	-56.904
10/23/17	polish brown coal	23 PL-11/384	105.9	16652	25	27.698	-12.464	-56.136
10/23/17	polish brown coal	23 PL-11/384	105.9	16653	25	29.074	-12.436	-56.401
11/2/17	CIT_tree	24 green bark	441	16715	25	9.993	-59.077	-53.943
11/2/17	CIT_tree	24 green bark	441	16714	250	121.417	-59.085	-50.315
10/28/17	CIT_tree	25 leaves	289.3	16684	50	11.843	-70.131	-48.837
10/28/17	CIT_tree	25 leaves	289.3	16683	250	69.371	-70.031	-47.718
10/29/17	CIT_grass	26 thin grass	282.6	16695	250	32.248	-60.932	-37.471
10/29/17	CIT_grass	27 wide grass	355.3	16688	25	3.233	-52.918	-42.021
10/29/17	CIT_grass	27 wide grass	355.3	16686	250	16.493	-53.019	-51.91
10/28/17	CIT_tree	28 inner wood	107.4	16678	25	21.355	-32.089	-49.833
10/28/17	CIT_tree	28 inner wood	107.4	16679	125	90.541	-31.909	-47.206
11/2/17	CIT_tree	29 outer wood	111.2	16713	250	22.986	-32.101	-55.274
10/28/17	IODP-337_coal	31_15R2	195.8	16680	250	8.446	7.209	-47.24

Table 6.4 continued from previous page

Date	Type	Sample_ID	Amount (mg)	Analysis #	Injection size (uL)	CO_2 area (Vs)	$\delta^{13}C$ (‰)	$\delta^{18}O$ (‰)
11/1/17	IODP-337_coal	32 22R5	564.1	16708	25	1.113	28.023	-50.794
11/2/17	IODP-337_coal	32 22R5	564.1	16725	250	5.953	28.57	-52.979
11/2/17	IODP-337_coal	32 22R5	564.1	16724	250	6.969	28.981	-52.307
11/1/17	IODP-337_coal	32 22R5	564.1	16707	250	8.71	27.526	-49.7
11/2/17	IODP-337_coal	32 22R5	564.1	16723	250	6.701	28.576	-52.403
10/28/17	IODP-337_coal	33_25R	402.5	16682	50	15.155	18.812	-47.512
10/28/17	IODP-337_coal	33_25R	402.5	16681	250	81.867	18.847	-47.732
10/29/17	PRB_coal	34 S939	1151.6	16696	250	1.877	5.262	-38.735
10/29/17	IODP-337_coal	35_15R3	856.9	16693	25	0.97	14.767	-33.452
10/29/17	IODP-337_coal	35_15R3	856.9	16692	250	9.735	14.345	-37.19
11/2/17	SBB_seds	39_SBB_BC1_0-10cm	784.2	16719	25	0.362	-10.658	-49.542
11/2/17	SBB_seds	39 SBB-BC1 0-10cm	784.2	16718	250	2.543	-10.475	-50.196
10/18/17	wood	4_USC_bamboo	2.4	16597	250	13.832	-27.667	-54.822
11/1/17	CIT_tree	41 minor stems	243.6	16710	25	11.54	-48.563	-53.148
11/1/17	CIT_tree	41 minor stems	243.6	16709	250	167.038	-48.059	-47.364
11/2/17	CIT_tree	42 major stems	371.1	16712	25	42.089	-36.615	-54.841
10/19/17	lignin	5_USC_Lignin	5.9	16608	50	11.29	-20.582	-54.254
10/19/17	lignin	5_USC_Lignin	5.9	16607	250	64.33	-20.606	-55.506
10/19/17	wood	8_HU-1_beech	8	16601	250	37.045	-26.377	-56.426
10/19/17	wood	9_HU-2_Tinea	10.2	16602	250	31.526	-22.636	-56.425
10/19/17	wood	9_HU-2_Tinea	10.2	16606	250	53.084	-22.974	-56.222
10/12/17	DM	DM-P-2		16544	125	36.365	-12.02	-51.755
10/12/17	DM	DM-P-2		16543	250	89.623	-11.94	-51.013

Table 6.4 continued from previous page

Date	Type	Sample_ID	Amount (mg)	Analysis #	Injection size (uL)	CO_2 area (Vs)	$\delta^{13}C$ (‰)	$\delta^{18}O$ (‰)
10/12/17	DM	DM-P-2		16542	250	106.774	-11.983	-50.703
10/13/17	PRB_coal	PRB-S352		16558	25	3.285	22.785	-52.858
10/13/17	PRB_coal	PRB-S352		16559	250	25.392	22.376	-55.135
10/13/17	PRB_coal	PRB-S352		16560	1000	7.536	22.722	-53.751
10/17/17	PRB_coal	PRB-S352_CO_2		16580	250	0.492	-36.893	-50.552
10/13/17	PRB_coal	PRB-S939		16566	100	9.015	4.138	-54.456
10/13/17	PRB_coal	PRB-S939		16567	250	10.971	4.787	-54.019
10/13/17	PRB_coal	PRB-S939		16565	250	17.811	3.922	-53.737

Table 6.4: Individual iodomethane measurements by GC-combustion-IRMS

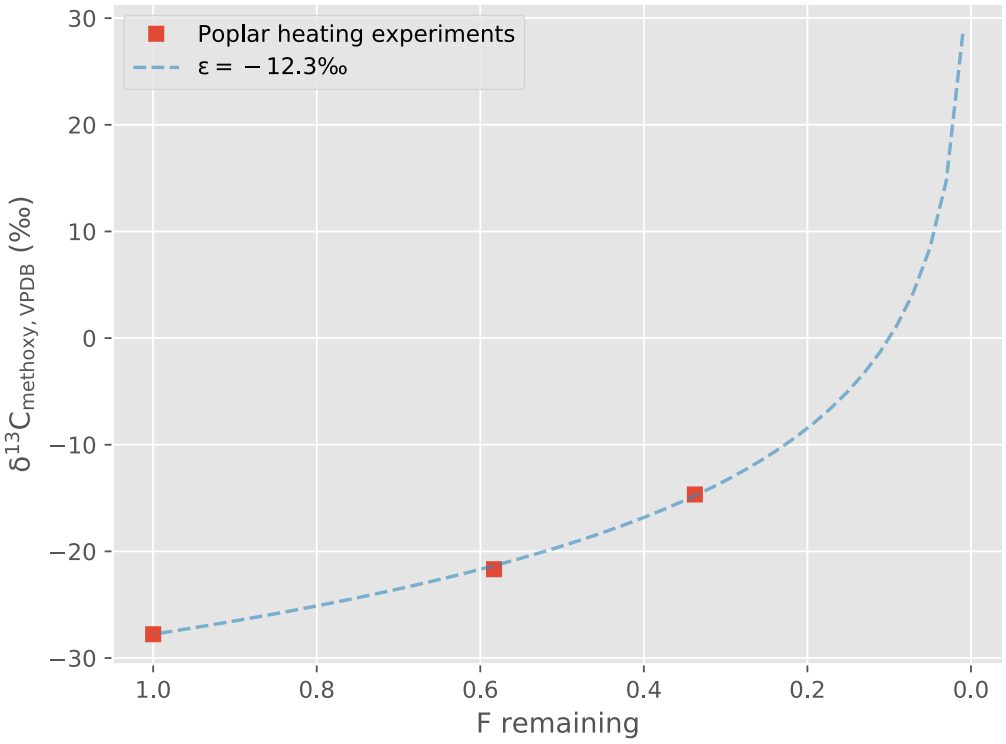

Figure 6.4: A Rayleigh model for the poplar thermal stress experiments

Date	Type	sample_ID	Amount (mg)	moles_CH_3I	wt.% methoxyl	$\delta^{13}C$	$\delta^{13}C$ (1σ s.e.)	$\delta^{18}O$	$\delta^{18}O$ (1σ s.e.)	$\delta^{13}C$ (bulk)	$\delta^{13}C$ (bulk) (1σ s.d.)
1/31/16	wood	USC_bamboo	63	2.23E-04	24.382	-30.36	0.01			-27.04	0.06
4/12/16	IODP-337_coal	18R2	11400	2.47E-04	0.067	23.46	0.15			-24.40	0.30
6/12/16	IODP-337_coal	18R2	5500	1.52E-04	0.086	29.69	0.15	26.62	0.02	-24.40	0.30
6/12/16	IODP-337_coal	15R3	2500	1.20E-04	0.149	20.57	0.15	18.95	0.01	-25.00	0.20
9/29/16	IODP-337_coal	18R2	2745	1.93E-04	0.218	22.49	0.15	32.80	0.01	-24.40	0.30
10/2/16	IODP-337_coal	22R5	3275	6.63E-05	0.063	16.69	0.15	23.52	0.02	-25.20	0.50
10/5/16	IODP-337_coal	15R7	2349	9.67E-05	0.128	-13.98	0.15	31.59	0.02	-24.80	0.30
10/6/16	IODP-337_coal	15R4	2592	1.18E-04	0.142	6.73	0.15	34.05	0.01	-24.30	0.20
10/11/16	polish brown coal	PL-11/384	527	1.14E-03	6.684	-13.59	0.15	33.43	0.01	-21.20	0.30
10/12/16	polish brown coal	PL-4/384	110	3.41E-04	9.612	-20.50	0.15	32.27	0.07	-22.90	0.10
12/16/16	wood	USC_poplar	125	1.84E-04	22.847	-27.77	0.15	18.56	0.01	-26.04	0.04
12/17/16	PRB_coal	SWL	2425	3.73E-05	0.048	-11.21	0.15	17.12	0.02	-24.70	0.09
7/1/17	DM	DM-P-1	66	1.42E-04	6.698	-21.67	0.01	30.28	0.02		
7/1/17	DM	DM-P-2	94	2.06E-04	6.849	-14.67	0.02	25.18	0.01		
7/23/17	PRB_coal	PRB_S352	7240	1.01E-04	0.043	-2.02	0.01	24.48	0.04	-24.10	0.10
7/23/17	SJB_coal	SJB_D395	6697	1.71E-05	0.008						
7/24/17	SJB_coal	SJB_S057	1516	7.45E-06	0.015						
7/24/17	PRB_coal	PRB_S939	9380	1.22E-04	0.040	-21.45	0.00	23.07	0.00	-24.90	0.10

Table 6.5: Individual iodomethane measurements by reflux reaction + offline sealed-tube combustion

References

Anhäuser, T., Greule, M., Polag, D., Bowen, G.J., Keppler, F., 2017. Mean annual temperatures of mid-latitude regions derived from δ^2H values of wood lignin methoxyl groups and its implications for paleoclimate studies. Science of The Total Environment 574, 1276–1282. doi:10.1016/j.scitotenv.2016.07.189

Anhäuser, T., Greule, M., Zech, M., Kalbitz, K., McRoberts, C., Keppler, F., 2015. Stable hydrogen and carbon isotope ratios of methoxyl groups during plant litter degradation. Isotopes in

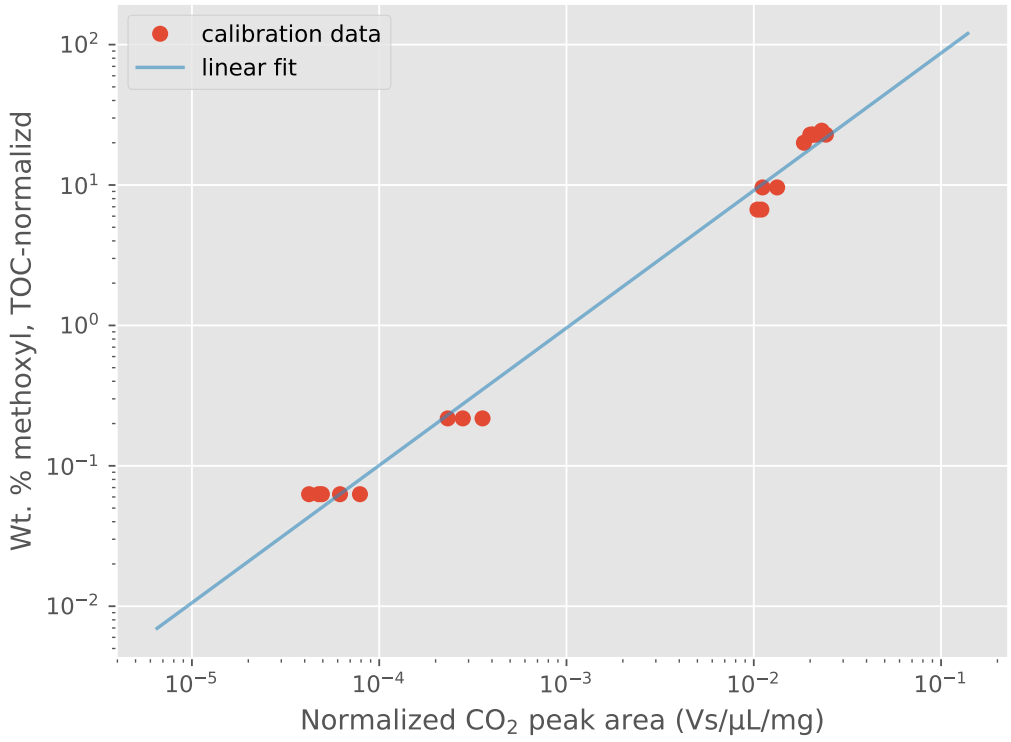

Figure 6.5: Calibration line used to relate CH_3I peak areas measured by GC-combustion-IRMS to true methoxyl concentrations obtained by offline reflux condense procesures.

Environmental and Health Studies 1–12. doi:10.1080/10256016.2015.1013540

Benner, R., Fogel, M.L., Sprague, E.K., Hodson, R.E., 1987. Depletion of 13 C in lignin and its implications for stable carbon isotope studies. Nature. doi:10.1038/329708a0

Clayton, C.J., 1991. Effect of Maturity on Carbon Isotope Ratios of Oils and Condensates. Organic Geochemistry 17, 887–899.

Clayton, C.J., Bjorøy, M., 1994. Effect of maturity on 13C12C ratios of individual compounds in North Sea oils. Organic Geochemistry.

Donnelly, M.I., Dagley, S., 1980. Production of methanol from aromatic acids by Pseudomonas putida. Journal of bacteriology 142.

Drobniak, A., Mastalerz, M., 2006. Chemical evolution of Miocene wood: Example from the Belchatow brown coal deposit, central Poland. International Journal of Coal Geology 66, 157–178. doi:10.1016/j.coal.2005.06.004

Feakins, S.J., Ellsworth, P.V., da Silveira Lobo Sternberg, L., 2013. Lignin methoxyl hydrogen isotope ratios in a coastal ecosystem. Geochimica et Cosmochimica Acta 121, 54–66. doi:10.1016/j.gca.2013.07.012

Feakins, S.J., Rincon, M., Pinedo, P., 2012. Analytical challenges in the quantitative determination of 2H/ 1H ratios of methyl iodide. Rapid Commun. Mass Spectrom. 27, 430–436.

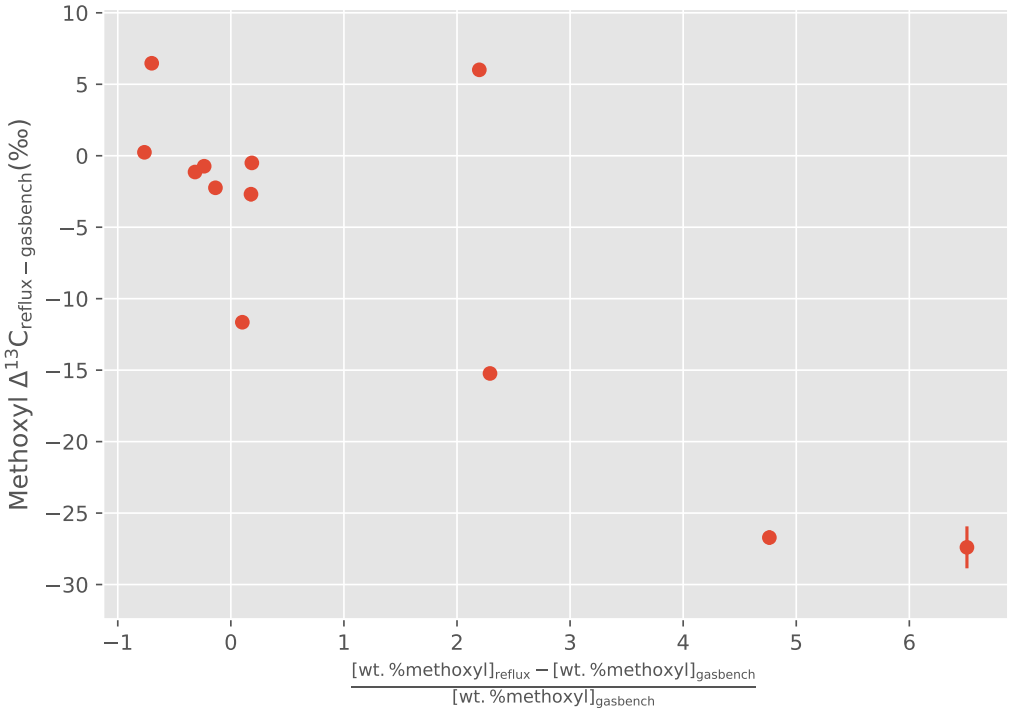

Figure 6.6: Discrepancies and agreements in measured vs. predicted methoxyl content, and methoxyl δ^{13}C, for samples measured by both methods.

doi:10.1002/rcm.6465

Flores, R.M., 1986. Styles of coal deposition in Tertiary alluvial deposits, Powder River Basin, Montana and Wyoming. Geological Society of America Special Publications.

Flores, R.M., Rice, C.A., Stricker, G.D., Warden, A., 2008. Methanogenic pathways of coal-bed gas in the Powder River Basin, United States: the geologic factor. International Journal of Coal Geology

Gori, Y., Wehrens, R., Greule, M., Keppler, F., Ziller, L., La Porta, N., Camin, F., 2012. Carbon, hydrogen and oxygen stable isotope ratios of whole wood, cellulose and lignin methoxyl groups of Picea abiesas climate proxies. Rapid Commun. Mass Spectrom. 27, 265–275. doi:10.1002/rcm.6446

Greule, M., Mosandl, A., Hamilton, J.T.G., Keppler, F., 2009. A simple rapid method to precisely determine 13C/ 12C ratios of plant methoxyl groups. Rapid Commun. Mass Spectrom. 23, 1710–1714. doi:10.1002/rcm.4057

Greule, M., Mosandl, A., Hamilton, J.T.G., Keppler, F., 2008. A rapid and precise method for determination of D/H ratios of plant methoxyl groups. Rapid Commun. Mass Spectrom. 22, 3983–3988. doi:10.1002/rcm.3817

Gross, D., Bechtel, A., Harrington, G.J., 2015. Variability in coal facies as reflected by organic petrological and geochemical data in Cenozoic coal beds offshore Shimokita (Japan) - IODP Exp. 337. International Journal of Coal Geology 152, 63–79. doi:10.1016/j.coal.2015.10.007

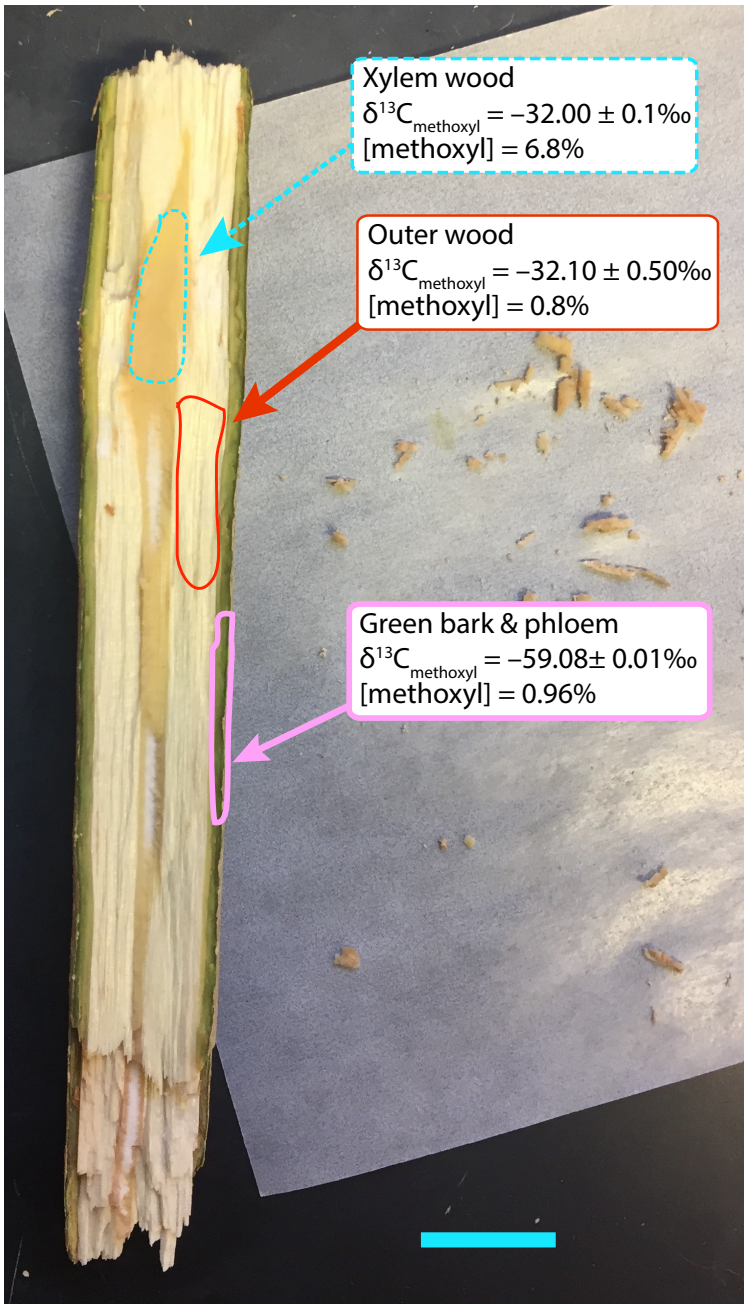

Figure 6.7: Methoxyl sampling sites, concentrations, and δ^{13}C values from a living Jacaranda branch.

Guo, H., Yu, Z., Liu, R., Zhang, H., Zhong, Q., Xiong, Z., 2012. Methylotrophic methanogenesis governs the biogenic coal bed methane formation in Eastern Ordos Basin, China. Appl Microbiol Biotechnol 96, 1587–1597. doi:10.1007/s00253-012-3889-3

Hatcher, P.G., Breger, I.A., Earl, W.L., 1981. Nuclear magnetic resonance studies of ancient buried wood—I. Observations on the origin of coal to the brown coal stage. Organic Geochemistry 3, 49–55. doi:10.1016/0146-6380(81)90013-9

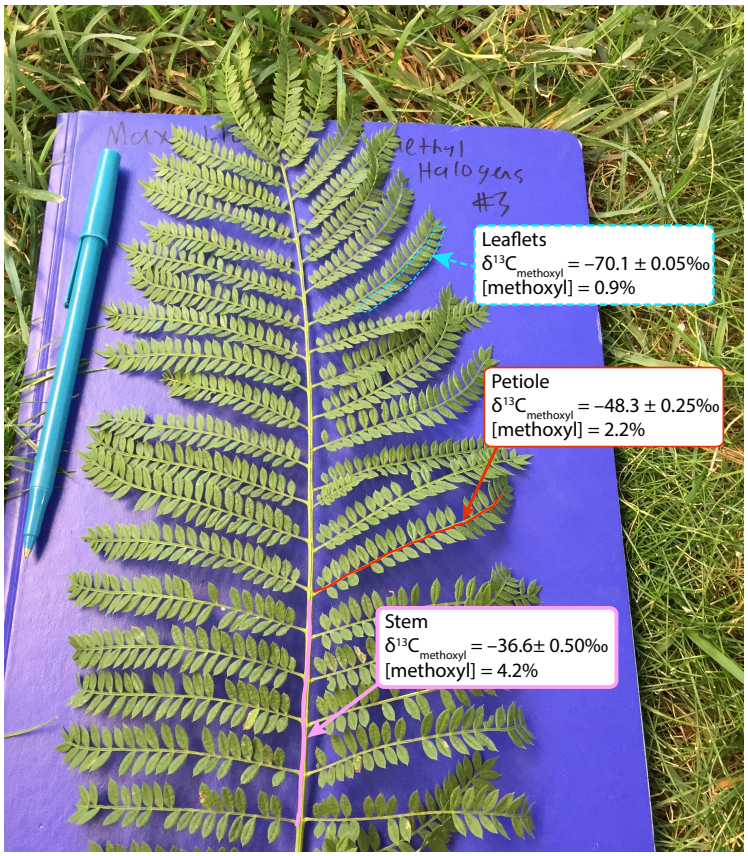

Figure 6.8: Methoxyl sampling sites, concentrations, and δ^{13}C values from the compound leaf of a living Jacaranda tree.

Hatcher, P.G., Breger, I.A., Szeverenyi, N., Maciel, G.E., 1982. Nuclear magnetic resonance studies of ancient buried wood—II. Observations on the origin of coal from lignite to bituminous coal. Organic Geochemistry 4, 9–18. doi:10.1016/0146-6380(82)90003-1

Hatcher, P.G., Clifford, D.J., 1997. The organic geochemistry of coal: from plant materials to coal. Organic Geochemistry 27, 251–274. doi:10.1016/S0146-6380(97)00051-X

Head, I.M., Jones, D.M., Larter, S.R., 2003. Biological activity in the deep subsurface and the origin of heavy oil. Nature 426, 344–352. doi:10.1038/nature02134

Hoefs, J., Frey, M., 1976. The isotopic composition of carbonaceous matter in a metamorphic profile from the Swiss Alps. Geochimica et Cosmochimica Acta 40, 945–951. doi:10.1016/0016-7037(76)90143-5

Inagaki, F., Hinrichs, K.-U., Kubo, Y., the IODP Expedition 337 Scientists, 2016. IODP Expedition 337: Deep Coalbed Biosphere off Shimokita – Microbial processes and hydrocarbon system associated with deeply buried coalbed in the ocean. Sci. Dril. 21, 17–28. doi:10.5194/sd-21-17-2016

Inagaki, F., Hinrichs, K.U., Kubo, Y., Bowles, M.W., Heuer, V.B., Hong, W.L., Hoshino, T., Ijiri, A., Imachi, H., Ito, M., Kaneko, M., Lever, M.A., Lin, Y.S., Methé, B.A., Morita, S., Morono, Y., Tanikawa, W., Bihan, M., Bowden, S.A., Elvert, M., Glombitza, C., Gross, D., Harrington, G.J.,

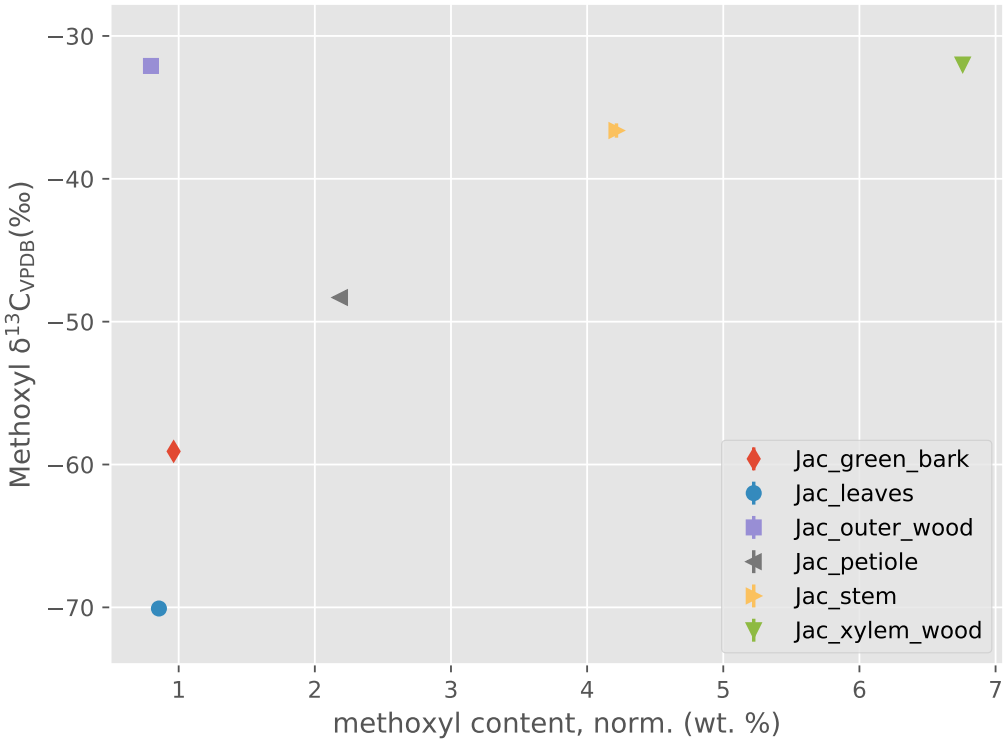

Figure 6.9: Covariation in methoxyl content and δ^{13}C values of specific tissues within a single Jacaranda tree.

Hori, T., Li, K., Limmer, D., Liu, C.H., Murayama, M., Ohkouchi, N., Ono, S., Park, Y.S., Phillips, S.C., Prieto-Mollar, X., Purkey, M., Riedinger, N., Sanada, Y., Sauvage, J., Snyder, G., Susilawati, R., Takano, Y., Tasumi, E., Terada, T., Tomaru, H., Trembath-Reichert, E., Wang, D.T., Yamada, Y., 2015. Exploring deep microbial life in coal-bearing sediment down to 2.5 km below the ocean floor. Science 349, 420–424. doi:10.1126/science.aaa6882

Keppler, F., Harper, D.B., Kalin, R.M., Meier-Augenstein, W., Farmer, N., Davis, S., Schmidt, H.-L., Brown, D.M., Hamilton, J.T.G., 2007. Stable hydrogen isotope ratios of lignin methoxyl groups as a paleoclimate proxy and constraint of the geographical origin of wood. New Phytologist 176, 600–609. doi:10.1111/j.1469-8137.2007.02213.x

Keppler, F., Kalin, R.M., Harper, D.B., McRoberts, W.C., Hamilton, J.T.G., 2004. Carbon isotope anomaly in the major plant C1 pool and its global biogeochemical implications. Biogeosciences 1, 123–131.

Kotarba, M.J., Lewan, M.D., 2004. Characterizing thermogenic coalbed gas from Polish coals of different ranks by hydrous pyrolysis. Organic Geochemistry 35, 615–646.

Krueger, D.A., Krueger, H.W., 1983. Carbon isotopes in vanillin and the detection of falsified natural vanillin. J. Agric. Food Chem. 31, 1265–1268. doi:10.1021/jf00120a030

Martini, A.M., Walter, L.M., Ku, T.C.W., Budai, J.M., McIntosh, J.C., Schoell, M., 2003. Microbial

production and modification of gases in sedimentary basins: A geochemical case study from a Devonian shale gas play, Michigan basin. AAPG Bulletin 87, 1355–1375. doi:10.1306/031903200184

Mayumi, D., Mochimaru, H., Tamaki, H., Yamamoto, K., Yoshioka, H., Suzuki, Y., et al., 2016. Methane production from coal by a single methanogen. Science 354, 222–225. doi:10.1126/science.aaf8821

Meyers, P.A., 1994. Preservation of Elemental and Isotopic Source Identification of Sedimentary Organic-Matter. Chemical Geology 114, 289–302.

Meyers, P.A., Simoneit, B.R.T., 1999. Effects of extreme heating on the elemental and isotopic compositions of an Upper Cretaceous coal. Organic Geochemistry 30, 299–305. doi:10.1016/S0146-6380(99)00015-7

Mischel, M., Esper, J., Keppler, F., Greule, M., Werner, W., 2016. ?2H, ?13C and ?18O from whole wood, ?-cellulose and lignin methoxyl groups in Pinus sylvestris: a multi-parameter approach 1–17. doi:10.1080/10256016.2015.1056181

Penger, J., Conrad, R., Blaser, M., 2012. Stable carbon isotope fractionation by methylotrophic methanogenic archaea. Applied and environmental...

Redding, C.E., Schoell, M., Monin, J.C., Durand, B., 1980. Hydrogen and carbon isotopic composition of coals and kerogens. Physics and Chemistry of

Riechelmann, D.F.C., Greule, M., Treydte, K., Esper, J., Keppler, F., 2016. Palaeogeography, Palaeoclimatology, Palaeoecology. Palaeogeography, Palaeoclimatology, Palaeoecology 445, 60–71. doi:10.1016/j.palaeo.2016.01.001

Schimmelmann, A., Sessions, A.L., Mastalerz, M., 2006. Hydrogen isotopic (D/H) composition of organic matter during diagenesis and thermal maturation. Annu. Rev. Earth Planet. Sci. 34, 501–533. doi:10.1146/annurev.earth.34.031405.125011

Schink, B., Zeikus, J.G., 1982. Microbial ecology of pectin decomposition in anoxic lake sediments. Microbiology.

Schmidt, H.-L., 2003. Fundamentals and systematics of the non-statistical distributions of isotopes in natural compounds. Naturwissenschaften 90, 537–552. doi:10.1007/s00114-003-0485-5

Stahl, W.J., 1977. Carbon and Nitrogen Isotopes in Hydrocarbon Research and Exploration. Chemical Geology 20, 121–149.

Strapoc, D., Mastalerz, M., Dawson, K., Macalady, J., Callaghan, A.V., Wawrik, B., Turich, C., Ashby, M., 2011. Biogeochemistry of Microbial Coal-Bed Methane. Annu. Rev. Earth Planet. Sci. 39, 617–656. doi:10.1146/annurev-earth-040610-133343

Summons, R.E., Franzmann, P.D., Nichols, P.D., 1998. Carbon isotopic fractionation associated with methylotrophic methanogenesis. Organic Geochemistry 28, 465–475. doi:10.1016/S0146-6380(98)00011-4

Welte, C.U., 2016. A microbial route from coal to gas. Science 354, 184–184. doi:10.1126/science.aai8101

Whiticar, M.J., 1999. Carbon and hydrogen isotope systematics of bacterial formation and oxidation of methane. Chemical Geology 161, 291–314.

Whiticar, M.J., 1996. Stable isotope geochemistry of coals, humic kerogens and related natural gases. International Journal of Coal Geology 32, 191–215.

Wilson, A.T., Grinsted, M.J., 1977. 12C/13C in cellulose and lignin as palaeothermometers. Nature 265, 133–135. doi:10.1038/265133a0

Zeisel, S., 1885. Über ein Verfahren zum quantitativen Nachweise von Methoxyl. Monatshefte für Chemie 6, 989–997. doi:10.1007/BF01554683

Zhuang, G.-C., Elling, F.J., Nigro, L.M., Samarkin, V., Joye, S.B., Teske, A., Hinrichs, K.-U., 2016. Multiple evidence for methylotrophic methanogenesis as the dominant methanogenic pathway in hypersalinesediments from the Orca Basin, Gulf of Mexico. Geochimica et Cosmochimica Acta 187, 1–20. doi:10.1016/j.gca.2016.05.005

INDEX

F

figures, 13, 17, 20, 30, 32, 42, 77, 82, 87, 90, 91, 109–113, 119, 121, 123, 126–128, 130, 134, 135, 138–145, 147, 148, 164, 167, 172, 173, 175, 177–186, 189, 190, 192, 193, 215, 216, 223, 227–232

T

tables, 25, 28, 29, 41, 50–54, 73, 79, 85, 98, 101–104, 151–153, 188, 189, 212–214, 226, 227